DEPARTMENT OF CHEMISTRY, UNIVERSITY OF JYVÄSKYLÄ
RESEARCH REPORT No. 189

ELECTRONIC AND VIBRATIONAL SPECTROSCOPIC STUDIES OF GOLD-NANOCLUSTERS

BY
JAAKKO KOIVISTO

Academic Dissertation
for the Degree of
Doctor of Philosophy

To be presented, by permission of the Faculty of Mathematics and Natural Sciences of the University of Jyväskylä, for public examination in auditorium KEM4 of the University of Jyväskylä on January 8, 2016 at 12 noon.

UNIVERSITY OF JYVÄSKYLÄ

Copyright ©, 2016
University of Jyväskylä
Jyväskylä, Finland
ISBN 978-951-39-6516-7
ISSN 0357-346X

Abstract

Koivisto Jaakko
Electronic and vibrational spectroscopic studies of gold-nanoclusters.
Jyväskylä: University of Jyväskylä, 2015, 63 p.
(Department of Chemistry, University of Jyväskylä Research Report,
ISSN 0357-346X, 189)
ISBN(print): 978-951-39-6515-0
ISBN(electronic): 978-951-39-6516-7

Gold nanoclusters are a peculiar new material with properties between that of bulk metal and single atoms. They show size-dependent evolution of optical and electronic properties sensitive to the change of single atom or single electron in the system. Understanding the relationship between structure and properties is important to both fundamental scientific question of the role of the quantum size effects in small metal-clusters, and to application of nanoclusters in *e.g.* photonics, nanoelectronics, and heterogeneous catalysis.

In this thesis four spectroscopic studies of monolayer-protected gold-nanoclusters are presented. The optical gap of the $Au_{144}(PET)_{60}$ and $(Au/Ag)_{144}(PET)_{60}$ (PET: phenylethylthiolate) nanoclusters were measured by absorption spectroscopy in the infra-red (IR) region in order to validate the proposed Au_{144}-cluster model, and to measure the effect of the silver content to the optical gap of the cluster. For pure gold Au_{144} optical gap of 2200 cm^{-1}(0.27 eV) was measured in good agreement with the gap calculated from the model with density functional theory (DFT). For bimetallic Au/Ag-clusters the gap was found in the range 1150–2100 cm^{-1}(0.16–0.20 eV), indicating the gap is only moderately affected by doping Au with Ag.

The structure of the $Au_{144}(PET)_{60}$ single crystals was studied with IR-microscopy. The IR-spectrum of the single crystals were found to be significantly broadened compared to the reference PET and $Au_{144}(PET)_{60}$ in solution. The inhomogeneous broadening was explained via randomly packed structure of the ligands on the cluster surface in the crystals.

The model-structure proposed for the $Au_{68}(m\text{MBA})_{32}$ -cluster (mMBA: *meta*-mercaptobenzoic acid) obtained from combination of transmission electron microscopy and DFT was verified with IR-spectroscopy. The measured optical gap (2500 cm^{-1}, 0.31 eV) of the cluster was smaller than excpected for the cluster size, which is explained by the disordered structure of the cluster.

In order to quantify the dependence of the solubility of $Au_{102}(p\text{MBA})_{44}$-nanocluster ($p$MBA: *para*-mercaptobenzoic acid) on the protonation state of the pMBA ligands,

we measured the number of protonated ligands on the cluster at different pH and the acid constant pK_a using acid-base and IR-titration. The pK_a was measured to be 6.18, two units higher than for free *p*MBA. The cluster was found to be insoluble in water when less than fifth, and truly water-soluble when more than half of the ligands are in deprotonated state.

Preface

The work presented in this thesis was done at the Department of Physical Chemisty of University of Jyväskylä during the years 2011 to 2015. The work was funded by the LASKEMO graduate school during the entire period, for which I'm grateful.

First I would like to thank professor Mika Pettersson for offering me the possibility to do my pHD studies on the subject. His guidance help in the various aspects of optical spectroscopy and science in general have been invaluable during the years.

Half of the results presented here would not exist without collaboration. Special thanks to Prof. Hannu Häkkinen and Dr. Sami Malola for performing and explaining the many theoretical aspects of gold-cluster research. I would also like to thank the organic chemistry Tanja Lahtinen and Kirsi Salorinne for gold particle synthesis, and answering intriquing scientific questions such as "Does this dissolve in carbon tetrachloride?". The support of Eero Hulkko, Satu Mustalahti, and my office-mates Heikki Häkkänen and Heli Lehtivuori has been valuable in the lab. Xi Chen, Serena Donnini, and Gerrit Groenhof are aknowledged for the molecular dynamics simulations. I'm also grateful for all the foreign collaborators, Chanaka Kumara and Amal Dass from the University of Mississippi, Maia Azubel, Roger Kornberg, and their co-workers from Stanford University, and Hironori Tsunoama and Tatsuya Tsukuda from Hokkaido University.

I'm grateful to Prof. Tapani Pakkanen and Dr. Stefan Knoppe for reviewing my thesis and offering their comments on it.

I would like to thank my co-workers for making Nanoscience Center and the department of Chemistry a great working environment. It has been a privilige to work there for these years. Of course all work and no play makes Jaakko a dull boy, and I'm therefore grateful for the conversations in the coffee room, where no topic is too strange to be entertained.

Jyväskylä, December 2015

Jaakko Koivisto

Author's address Jaakko Koivisto
Department of Chemistry
Nanoscience Center
University of Jyväskylä
Finland
e-mail: jaakko.m.koivisto@jyu.fi

Supervisor Prof. Mika Pettersson
Department of Chemistry
Nanoscience Center
University of Jyväskylä
Finland

Co-Supervisor Prof. Hannu Häkkinen
Department of Physics
Department of Chemistry
Nanoscience Center
University of Jyväskylä
Finland

Reviewers Prof. Tapani Pakkanen
Department of Chemistry
University of Eastern Finland
Finland

Dr. Stefan Knoppe
Department of Chemistry
Katholieke Universiteit Leuven
Belgium

Opponent Prof. Thomas Bürgi
Department of Physical Chemistry
University of Geneva
Switzerland

List of Publications

Publications included in the thesis:

I **J. Koivisto**, S. Malola, C. Kumara, A. Dass, H. Häkkinen, and M. Pettersson. "Experimental and Theoretical Determination of the Optical Gap of the $Au_{144}(SC_2H_4Ph)_{60}$ Cluster and the $(Au/Ag)_{144}(SC_2H_4Ph)_{60}$ Nanoalloys.", *Journal of Physical Chemistry Letters*, **2012**, *3* p. 3076.

II **J. Koivisto**, K. Salorinne, S. Mustalahti, T. Lahtinen, S. Malola, H. Häkkinen, and M. Pettersson. "Vibrational Perturbations and Ligand-Layer Coupling in a Single Crystal of $Au_{144}(SC_2H_4Ph)_{60}$ Nanocluster.", *Journal of Physical Chemistry Letters*, **2014**, *5*, p. 387.

III M. Azubel, **J. Koivisto**, S. Malola, D. Bushnell, G.L. Hura, A.L. Koh, H. Tsunoyama, T. Tsukuda, M. Pettersson, H. Häkkinen, and R.D. Kornberg. "Electron microscopy of gold nanoparticles at atomic resolution.", *Science*, **2014**, *345*, p. 909.

IV **J. Koivisto**, X. Chen, S. Donnini, T. Lahtinen, H. Häkkinen, G. Groenhoff, and M. Pettersson. "Experimental and computational determination of the protonation states of the water-soluble $Au_{102}(p\text{MBA})_{44}$-nanocluster.", *Manuscript to be submitted*

Authors contribution

The author has performed all IR– and UV/Vis–spectroscopy measurements and analysis of the experimental results in articles **I** – **IV**. The author has written the first draft of articles **I**, **II**, and **IV**, and the spectroscopy section of article **III**.

Publications the author has contributed to which are not included in the thesis:

A1 E. Hulkko, O. Lopez-Acevedo, **J. Koivisto**, Y. Levi-Kalisman, R.D. Kornberg, M. Pettersson, and H. Häkkinen. "Electronic and Vibrational Signatures of the $Au_{102}(p\text{MBA})_{44}$ cluster.", *Journal American Chemical Society*, **2011**, *133*, p. 3752.

A2 K. Salorinne, T. Lahtinen, **J. Koivisto**, E. Kalenius, M. Nissinen, M. Pettersson, and H. Häkkinen. "Nondestructive Size Determination of Thiol-Stabilized Gold Nanoclusters in Solution by Diffusion Ordered NMR-Spectroscopy.", *Analytical Chemistry*, **2013**, *85*, p. 3489.

A3 K. Salorinne, T. Lahtinen, S. Malola, **J. Koivisto**, and H. Häkkinen. "Solvation Chemistry of Water-Soluble Thiol-Protected Gold Nanocluster Au_{102} from DOSY NMR-Spectroscopy and DFT-calculations.", *Nanoscale*, **2014**, *6*, p. 7823.

A4 S. Mustalahti, P. Myllyperkiö, T. Lahtinen, K. Salorinne, S. Malola, **J. Koivisto**, H. Häkkinen, and M. Pettersson. "Ultrafast Electronic Relaxation and Vibrational Cooling Dynamics of $Au_{144}(SC_2H_4Ph)_{60}$ Nanocluster Probed by Transient Mid-IR Spectroscopy.", *Journal of Physical Chemical C*, **2014**, *118*, p. 18233.

A5 S. Mustalahti, P. Myllyperkiö, S. Malola, T. Lahtinen, K. Salorinne, **J. Koivisto**, H. Häkkinen, and M. Pettersson. "Molecule-like Photodynamics of $Au_{102}(p\text{MBA})_{44}$ nanocluster.", *ACS Nano*, **2015**, *9*, p. 2328.

A6 S. Mustalahti, P. Myllyperkiö, T. Lahtinen, S. Malola, K. Salorinne, T.R. Tero, **J. Koivisto**, H. Häkkinen, and M. Pettersson. "Photodynamics of a Molecular Water-Soluble Nanocluster Identified as $Au_{130}(p\text{MBA})_{50}$.", *Journal Physical Chemical C*, **2015**, *119*, p. 20224.

A7 V. Marjomäki, T. Lahtinen, M. Martikainen, **J. Koivisto**, S. Malola, K. Salorinne, M. Pettersson, and Hannu Häkkinen. "Site-specific targeting of enterovirus capsid by functionalized monodisperse gold nanoclusters.", *Proceedings of the National Academy of Science U.S.A.*, **2014**, *111*, p. 1277.

CONTENTS

Abbreviations

MPC	Monolayer protected cluster
FTIR	Fourier-transform infra-red
NIR	Near infra-red
FIR	Far infra-red
UV	Ultra-violet
vis	Visible
*m*MBA	*meta*-mercaptobenzoic acid
*p*MBA	*para*-mercaptobenzoic acid
PET	Phenylethylthiolate, HSC_2H_4Ph
TEM	Transmission electron microscope
SEM	Scanning electron microscope
STEM	Scanning transmission electron microscope
NMR	Nuclear magnetic resonance
DCM	Dichloromethane
HOMO	Highest occupied molecular orbital
LUMO	Lowest unoccupied molecular orbital
DFT	Density functional theory
DOS	Density of states
PLDOS	Projected local density of states
FCC	Face centered cubic
HCP	Hexagonal close packing
MD	Marks decahedron
MI	Mackay icosahedron
MD	Molecular dynamics

1 Introduction

Gold has the atomic number 79, atomic weight 196.97 g/mol, density 19.30 g/cm^3, electrical resistivity of 22.14 nΩ m, and redox potential of +1.83 V.[1]

When presented as a list, the properties of metallic gold are quite unimpressive. However, no other metal invokes the feeling that gold does. Gold has a special importance in most cultures due to its peculiar colour and scarcity. It is attributed to wealth and power, and their symbols such as crowns and scepters are often made of gold. Gold is frequently referred to in everyday language with phrases like "golden opportunity", "worth its weight in gold", and "Fermi golden rule". Success is linked to gold with golden medals bestowed to winners in olympics and Nobel-prize laurates. Historically gold was used for thousands of years for defining value, first as physical currency in commerce, and later as the gold-standard where the value of paper-currency was fixed to weight in gold. Due to the high oxidation potential of gold, it can be found in metallic state, generally called gold nuggets. These can grow into staggering sizes, largest ones weighting over 60 kg.[2] Gold is very scarce with mass abundancy of 3.1×10^{-7} % in earth's crust. Only about 180 000 tons of gold have been extracted from earth during the history of humankind. For comparison, the annual production of metallic sodium is ~100 000 tons/year.[3] Industrially gold is used mainly for jewelry, which accounts for approximately 50 % of annual consumption. It is also used in electronics due to it's high conductivity and resistance to oxidation, and in space-technology due to the high reflectance of thermal radiation.

Gold nanoparticles have been used for almost two thousand years, without even knowing they existed, for the production of ruby-red glass.[4,5] The most famous example are the dichroic properties of the famous 4 th century Lycurgus cup has been proven to originate from combination of silver and gold nanoparticles.[6] The scientific studies of gold particles started over a millenia later with with studies from leading scientists of the mid 19 th century like Louis Joseph Gay-Lussac and Michael Faraday.[4,7]

1.1 General Properties of Bulk and Nanoscopic Metals

Metals in every day life have several characteristic properties like high electrical and thermal conductivity. They have specific "metallic" luster due to high reflectance of electromagnetic radiation at visible light wavelengths (380–750 nm).[4,8] As single metal atoms present completely different properties from the bulk, such as optical spectrum composed of sharp transitions lines, it is not surprising that the size evolution from single atom to bulk metal exhibits peculiar properties at intermediate sizes. These include enhanced stability and increased ionization potential of certain 'magic-sizes',[9,10] collective oscillation of the electron cloud at specific frequency (localized surface plasmon resonance, LSPR)[11–15] structures not conforming to the bulk metal packing-motif,[16–18] and molecular-like charging.[19,20]

The properties of metals as a function of size can be separated into three regions: (macroscopic/bulk) properties are determined only by the element; (nanoparticle) the properties change monotonically when the size changes; (nanocluster) the properties are governed by quantized energy levels. In the first case the properties are not size dependent. In the second case the particles do show properties arising from the finite size of the system, and when the general trend and the particle size is known, the new properties can be predicted. If two particles with diameters of d_1 and d_2 exhibit plasmon resonance at wavelengths λ_1 and λ_2, the plasmon of a third particle with diameter between d_1 and d_2 will always be between λ_1 and λ_2. In the last case 'every atom counts', and the properties of the cluster can change radically when the cluster size changes by single atom, or when the electrical charge of the cluster changes. As even very minor changes in the system may lead into entirely different properties, the behaviour of the clusters in this regime cannot be accurately predicted, and they have to be measured or calculated for every different size and structure.

The transition between the last two regions is hard to pinpoint, as it varies between different metals, and different properties may not revert back to bulk properties at same size,[14,21] For monolayer protected gold clusters the size region of transition from molecular to bulk properties is well known. The electronic properties converge back to bulk-like between 130 and 144 gold atoms,[20,22–26] The geometrical arrangement of gold atoms transitions from icosahedral back to FCC-packing found in bulk gold between the range 144–187 gold atoms. The Au_{187} is also the first cluster size exhibiting a measurable plasmon resonance band,[27] although plasmon-like transitions have been reported for the Au_{144} cluster also based on DFT-calculations.[28]

1.1.1 Quantization of Energy Levels: Metallic vs. Molecular

The properties of bulk metal systems and the evolution to molecular systems can be understood by considering the results of the standard particle in a box -model from elementary quantum mechanics. The valence electrons of the metal atoms are loosely bound by the nuclei, and can be approximated as free-electrons in one dimensional box of length L. The Schrödinger equation of the system is written as

$$-\frac{\hbar^2}{2m_e}\frac{\mathrm{d}^2\Psi}{\mathrm{d}x^2} + V(x)\Psi = E\Psi \tag{1.1}$$

where $\hbar$ is the reduced planck's constant, m_e is the electron mass.[29,30] The potential $V(x)$ is 0 when $0 \leq x \leq L$, and infinite elsewhere. The Schrödinger equation is solved by wavefunctions Ψ of the form $\Psi_n = C\sin(n\pi x/L)$ inside the box, where C is a constant, and n is the principal quantum number which can take integer values $n = 1, 2, 3, \ldots$ (fig. 1.1A). The energy of the state described by the wavefunction Ψ_n is given by the equation

$$E_n = \frac{n^2h^2}{8m_eL^2}, \quad n = 1, 2, 3, \ldots \tag{1.2}$$

and the separation between the energy levels is

$$\delta = E_{n+1} - E_n = (2n-1)\frac{h^2}{2mL^2} \tag{1.3}$$

The above can be easily extented to three dimensional systems by replacing the derivative $\frac{\mathrm{d}^2}{\mathrm{d}x^2}$, the principal quantum number n^2, and the box length L with their three dimensional equivalents $\nabla^2 = \frac{\mathrm{d}^2}{\mathrm{d}x^2}+\frac{\mathrm{d}^2}{\mathrm{d}y^2}+\frac{\mathrm{d}^2}{\mathrm{d}z^2}$, $\boldsymbol{n}^2 = n_x^2+n_y^2+n_z^2$, and $\boldsymbol{L}^2 = L_x^2+L_y^2+L_z^2$.[31] This simple model shows the main behaviour of the energy levels with respect to the size of the system. The evergy level separation and the size of the system L are related by inverse squared relationship, and the separation depends strongly on the system size. As the system size increases ($L \to \inf$) the energy level separation gets smaller ($\delta \to 0$), and for any macroscopic system the energy levels form a continuous band with $\delta = 0$ (fig. 1.1B left). The energy levels are then populated according to the Pauli exclusion principle. For metals the populated levels are called valence band and the unoccupied levels conduction band. In room temperature the thermal energy k_BT excites small population of the valence band electrons to the unoccupied states in the conduction band, which then gives rise to the systems metallic properties such as high electrical conductivity, plasmon resonance, Mie scattering, or reflectivity at optical frequencies.[8,11,32] Due to the thermally excited population and the high density of states, the occupancy of the orbitals changes smoothly from occupied to unoccupied. The energy of the level which is half occupied is called the fermi level E_f.[33]

A nanoscopic system, for which the system size L is in the order of only few nanometers or less, will have a non-zero energy level separation δ significantly larger than the

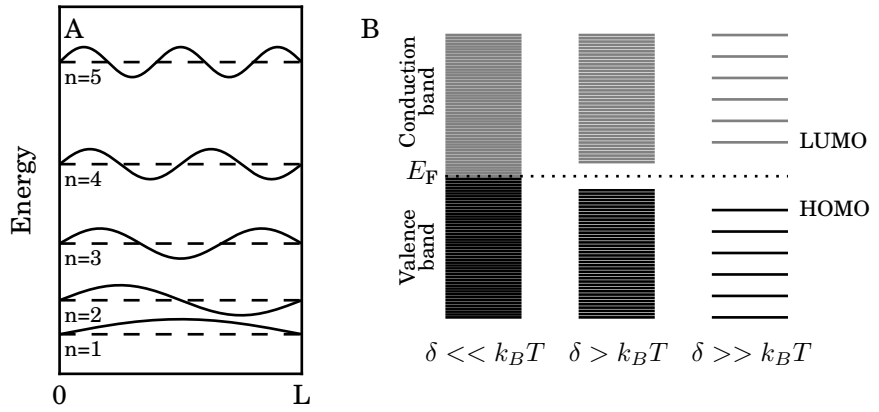

Figure 1.1: A: Wavefunctions Ψ_n and the relative energies of the solutions of the Schrödinger equation (eq. 1.1). **B**: General energy levels of metallic, semiconducting, and molecular systems. The energy level spacing δ is given eq. 1.3.

thermal energy k_BT, causing completely different behaviour. In this case the energy levels are well separated from one another and can be considered as single orbitals instead of bands. Again, the orbitals are populated according to the Pauli exclusion principle, but the thermal energy is too small to change the populations of the highest occupied molecular orbital (HOMO) and the lowest unoccupied molecular orbital (LUMO). The electrons are strongly localized in the occupied orbitals, inhibiting any collective motions of the electron cloud such as SPR. Instead, the optical properties are described by single electron excitations from occupied orbital to unoccupied orbital, with lowest possible transition energy being the energy difference between the HOMO and LUMO -levels, called HOMO-LUMO gap. For molecules the fermi level doesn't co-incide with any existing energy level of the system, but resides inside the HOMO-LUMO gap.

The intermediate case is when δ is sufficiently small that the valence and conduction bands fuse together, but there is a non-zero gap between the two bands. In this case the material is called semi-conducting.[34,35]

1.1.2 Electronic Shell Structure and the Superatom model

If we substitute $V(x)$ in eq. 1.1 with the spherical Coulomb potential created by the positively charged nucleus,

$$V(Z,r) = \frac{1}{4\pi\varepsilon_0}\frac{Ze^2}{r} \tag{1.4}$$

and add the electron-electron repulsion term, the solutions of the Schrödinger equation gives the well known series of atomic orbitals[30,36]

$$1s^2 \mid 2s^2\ 2p^6 \mid 3s^2\ 3p^6\ 3d^{10} \mid 4s^2\ \ldots \tag{1.5}$$

where the superscript indicates the maximum amount of electrons in the orbital, and the vertical line indicates strong electronic shell closing at the corresponding electron configuration. The first number is the principal quantum number n, and the letters s, p, d, ... denote the orbital angular momentum $l = 0, 1, 2, \ldots$.[30,36] The exceptional stability of nobel-gas atoms is attributed to the shell closing of the 1st (He, $2e^-$), 2nd (Ne, $10e^-$), 3rd (Ar, $18e^-$), *etc.* electronic shells.

In molecules and cluster the potential is created by the sum of the positive potentials created by every nucleus, which are screened by the core electrons of the atoms. For metal cluster the potential can be approximated by a constant potential well which terminates at the edge of the cluster, so called Jellium-model,[37] and the valence electrons are delocalized over the whole cluster. Using this model the energy levels can be again calculated, giving new series

$$1S^2 \mid 1P^6 \mid 1D^{10} \mid 2S^2\ 1F^{14} \mid 2P^6\ 1G^{18} \mid 2D^{10}\ 3S^2\ 1H^{22} \mid 1I^{26}\ 2F^{14}\ 3P^6 \mid \ldots \tag{1.6}$$

Contrary to the atomic orbitals, in superatoms the principal quantum number n is not used, and the labels 1D refers to the first orbital with overal angular momentum similar to that of the d-orbitals, *etc.*. With this order of orbitals the shell closing occurs when the system has $n_e = 2, 8, 18, 34, 58, 92, 138, \ldots$ electrons in the superatoms orbitals.[38] Depending on the shape of the spherical potential, the orbitals shift in energy,[10,39] and the major shell closing can occur also with 20 (1D and 2S shift closer to each other), 40 (1F and 2P), *etc.*. Also, unlike for single atoms where the potential is always spherical, for clusters the potential can deviate towards ellipsoidal due to the shape of the cluster.[10,37,40] This leads into additional splitting of the orbitals, which is required to explain the weaker shell closings such as $n_e = 12, 14, 26, \ldots$.[41]

The free electrons which fill the superatom orbitals come from the loosely bound valence electrons of the metal-atoms, *e.g.* 6s in gold, 5s in silver, 3s and 3p in aluminium *etc.*.[38,42] These can be widthdrawn from the metallic core by the ligands attached to the clusters, or localized in covalent bonds, depending on the type of ligand used. With this formulation the number of electrons in the superatom orbitals n_e can be calculated by

$$n_e = N v_a - M - z \tag{1.7}$$

where N is the amount of metal atoms, v_a is the number of valence electrons for the metal, M is the amount of electron widthdrawing ligands, and z is the overall charge.[38] Using the above equation electronic properties of small clusters can be explained via the occupations of the superatomic orbitals. For Al_{13}, $Al_{13}{}^-$, Al_{14} clusters we get $n_e = 13 \times 3 - 0 - 0 = 39$, $n_e = 13 \times 3 - 0 + 1 = 40$, and $n_e = 14 \times 3 - 0 - 0 = 42$,

explaining the halogen-like properties of Al_{13}, inertness of Al_{13}^-, and alkaline earth atom -like properties of Al_{14} around the shell closing of 2P superatom orbital (40 e^-).[42] Exceptionally stable ligand-protected clusters, such as $Au_{11}(PPh_3)_8Cl_3$ and $[Au_{25}(SR)_{18}]^-$, can be interpreted as nobel-gas -like superatoms, as we are left with $n_e = 11 \times 1 - 3 - 0 = 8$ and $n_e = 25 \times 1 - 18 + 1 = 8$ electrons which fill the 1S and 1P orbitals. Geometry and compositions of the cluster also have to be considered, as evident by the differences between the halogen-like unprotected al_{13} and the neutral form of the $Au_{25}(SR)_{18}$ ($n_e = 25 \times 1 - 18 - 0 = 7$) cluster. Although it should be noted that the neutral and positive forms are less stabile than the negatively charged form.[43] Especially larger particles are no longer stabilized by any electronic shell closings, but instead form stable geometric constructions such as Mackay icosahedra,[44,45] FCC-polyhedra,[21,46] or Wulff-constructions.[47]

1.2 Monolayer Protected Noble-Metal Clusters

All nanoscopic metal clusters or particles are meta-stable with respect to the bulk metal structure. In other words, they are not thermodynamically stable.[4,48] This means the clusters prefer to aggregate back into larger and larger particles if they come into contact with one another.[49] As a result, experimental work on unprotected clusters (naked clusters) is limited to gas phase or clusters immobilized on surfaces. In solution, unprotected clusters quickly aggregate back to bulk metal, making proper control of the samples impossible. The aggregation can be stopped by adding a protective layer of ligands on the cluster surface. Commonly, such species are called monolayer protected clusters (MPC). The purpose of the ligand-layer is two-fold: the ligands should completely envelope the metal-core of the cluster to prohibit two metal cores from coming into contact, and it should also passivate the surface atoms to form electronically stable system.[50] Depending of the metal composition of the cluster, different functional groups can be used to attach the ligands to the metal. For gold cluster, these include tri-coordinated phosphines (PR_3, R = organic fragment), citric acid ($C_6H_8O_7$), halogens, terminal alkyne ($C{\equiv}C{-}R$), or organic thiols (SR) and it's selenium and tellurium analogs (SeR, TeR).[4,31,48,51–55]

The stability of geometrically and electronically stable MPCs is remarkable. They can be stored in refrigerator as solid or in solution for extended periods, in case of $Au_{102}(p\text{MBA})_{44}$ atleast up to two years, and they can also be dried and dissolved at will without degradation of the sample. Overall they can be handled like regular chemicals. Most importantly, certain "magic" sized clusters can be synthetized as extremely monodisperse samples. Currently more than 40 different discrete cluster sizes ranging from Au_7 to Au_{333} have been identified for gold alone.[48] The synthesis of gold nanoparticles depends on the desired size, size distribution, and the ligand used to passivate the particle, for example Turkevich synthesis for citrate,[51,52] and

Brust synthesis for thiol protected clusters.[56,57] The latter is the most commonly used synthesis method for monodisperse MPCs. Briefly, the synthesis consists of reduction of $HAuCl_4$ salt dissolved in water in the presence of thiols using $NaBH_4$ as the reduction agent. First the gold salt, the thiols, and tetraoctylammonium bromide salt are mixed, and the thiols reduce the Au(III) ions to Au(I) forming $(-Au-SR-)_n$ polymer. This polymer is then reduced to metallic Au(0) using $NaBH_4$, the end result being metallic Au(0) cluster core with thiols attached to the surface.

1.2.1 Core: Physical Properties

The electronic structure of the cluster is mainly governed by the structure and composition of the cluster. The shape of the metal core in the cluster determines the shape of the positive potential well, which then, as established in chapters 1.1.1 and 1.1.2, determines the energy levels of the system, and the valence electrons of the metal atoms fill the superatom orbitals. Properties such as electronic absorption,[58–62] and optical activity,[63–65] photoelectron spectra,[10,66] and electrochemical response,[19,67] are therefore direct result of the cluster core structure.

The ligands have little effect on the electronic structure aside from the widthdrawing or localizing part of the free electrons. DFT calculations made on the same structures using different ligand molecules, give similar electronical structure as the calculations done with the real ligand.[68] Also, the electronic spectrum of the cluster does not change radically in ligand exchange as long as the cluster core structure stays intact.[69,70]

1.2.2 Ligand Shell: Chemical Properties and Size selectivity

The ligand-layer of the cluster carries larger importance than just protecting the metals from aggregating. As the ligand-layer envelopes the clusters metal core, only the ligand layer is in contact with the environment, providing the chemical interface through which the cluster interacts with the surrounding medium. Therefore the chemical properties of the ligands determine much of the chemical properties of the cluster, such as solubility and reactivity.

Solubility of the cluster can be approximated simply by the solubility of the ligands, water-soluble ligands resulting in water soluble clusters and organic soluble ligands resulting in organic soluble clusters.[56,57,71] Size of the resulting cluster does however, play small but important part in the solubility of the different cluster sizes protected by the same ligand in different solvents. The different solubilities can be exploited in post-synthesis fractioning of different cluster sizes, *e.g.* $Au_{144}(PET)_{60}$ and the smaller $Au_{25}(PET)_{18}$ can be separated using acetone since $Au_{25}(PET)_{18}$ is acetone soluble

while $Au_{144}(PET)_{60}$ is not.[72] *p*MBA-clusters of different size can be separated similarly based on their solubility in water:methanol mixtures, with larger clusters having lower solubility in methanol causing them to precipitate out from the solution at lower methanol concentrations than smaller clusters.[73,74]

Ligand-layer can induce formation of chiral MPCs either by using chiral ligands (*e.g.* glutathione), or by the chiral arrangement of achiral ligands on the cluster surface.[65,75,76]

The ligand-layer also affects the physical properties of the cluster, as certain ligands stabilize different cluster sizes or core structures more effectively. Large ligands such as glutathione promotes formation of small clusters with core sizes in the range from Au_{10} to Au_{39}.[75,77–79] Smaller, less sterically hindered ligands such as phenylethylthiolate (PET, HSC_2H_4Ph) or straigth chained alkanethiolates can form numerous stable clusters sizes both large and small.[27,58,80,81] The monodisperse clusters which can be made using PET as a ligand is especially rich: $Au_{20}(PET)_{16}$,[82] $Au_{25}(PET)_{18}$,[83] $Au_{38}(PET)_{24}$,[84–86] $Au_{40}(PET)_{24}$,[86] $Au_{130}(PET)_{50}$,[87] $Au_{137}(PET)_{56}$,[88] $Au_{144}(PET)_{60}$,[72] $Au_{333}(PET)_{79}$.[89] Some cluster sizes show high degree of selectivity and can only be formed when using certain ligands, $Au_{102}(SR)_{44}$ using *para*-mercaptobenzoic acid or thiophenol.[73,90] or $Au_{133}(SPh-tBu)_{52}$ with the thiophenyl-tertbutyl.[91,92]

1.2.3 Bimetallic alloy clusters

The properties of the clusters can be further controlled by alloying two different metals together in the same cluster.[93] The emergent properties of the cluster is then determined by the elements, their relative amounts, and the arrangement of the atoms. The structure of the alloyed nanoclusters is governed by the relative bond strength, surface energies, atomic size, and ligand interactions.[93] The bond strengths of A-A, B-B, and A-B determine whether the elements form phases (A-A and B-B bonds dominate), or mixed structures (A-B bond dominates). The metals which have high surface energy (Gibbs free energy per surface area) go to the center of the cluster and the metals with low surface energy go to the surface.[48] Ligands used to passivate the surface of MPCs may have stronger interactions with one of the metals, which leads that metal to gravitate towards the surface of the cluster. Generally alloying metals which have similar packing, surface energy, chemical properties, and redox-potential is easier, *e.g.* Au/Ag[87] or Pd/Pt,[94] than metals where the mismatch of properties is large, *e.g.* Au/Co.[95]

Introduction of the new metal to the system modifies the system properties, and it can be used to modify or enhance the cluster properties, such as electronic absorption[87,96,97] or photoluminescence.[95,98,99] Doping known gold-cluster structures with single palladium atoms have been demonstrated for $PdAu_{24}(SR)_{18}$,[100,101] $Pd_2Au_{36}(SR)_{24}$,[102] and

$PdAu_{12}(PR_3)_8Cl_4$,[103,104] and in every case the cluster stability was increased compared to the monometallic analog. Increased catalytic activity of silver-doped gold-clusters relative to the silver content has been also demonstrated.[105]

1.3 Structure and Properties of selected MPCs

In this section we will briefly describe the structure and earlier results on the clusters used in the experimental studies presented in this thesis.

1.3.1 $Au_{102}(p\text{MBA})_{44}$

The exact crystal structure of the $Au_{102}(p\text{MBA})_{44}$-cluster is known from single-crystal XRD, solved in 2007 by Jadzinsky *et.al.*[106] The arrangement of the gold atoms can be separated into three distinct structures, shown in fig. 1.2A. The center of the cluster is formed by 49-atom Marks (2,1,2) decahedron (MD), which is extended at the poles by two 20-atom caps. Final 13 gold atoms are located on the equator of the cluster in a chiral arrangement, resulting in approximately spherical shape for the gold-framework. The structure formed by the MD and the caps is highly symmetrical (D_{5h} point group), but the arrangement of the equatorial atoms lowers the symmetry of the whole cluster to C_2 point group. The ligands bind to the cluster surface via the thiol-group, with every thiol binding with two gold atoms (fig. 1.2B). The structure of the protecting ligands follows the same chiral C_2 arrangement as the equatorial Au-atoms, resulting in 22 symmetry independent ligands (fig. 1.2C and D).[107] Alternatively the cluster can be described by a core of 79 Au-atoms decorated with 19 short $Au(p\text{MBA})_2$ and 2 long $Au_2(p\text{MBA})_3$ staple-motifs.[53] The cluster diameter is approximately 1.6 nm and 2.6 nm for the core gold-atoms and the whole cluster with the ligand-layer, respectively. For $Au_{102}(p\text{MBA})_{44}$-cluster the superatom model gives $n_e = 102 - 44 = 58$ free electrons corresponding with the closing of the superatom 1G shell. According to DFT-calculation of the orbitals and projected local density of states (PLDOS), the HOMO-levels have mixed G- and P-character and the first LUMO-levels consists mainly of H-type orbitals, as expected from the superatom shell ordering in eq. 1.6. Computational HOMO-LUMO gap of the cluster is 0.55 eV. Experimental HOMO-LUMO gap was measured by Hulkko *et.al.* to be 0.45 ± 0.05 eV using FTIR-spectroscopy.[69] The circular dichroism spectra of the different chiral enantiomers were measured by Knoppe *et.al.*[108] Femtosecond dynamics of the cluster have been investigated in two separate studies, both of which found the cluster to show molecular behaviour.[24,109] The $Au_{102}(p\text{MBA})_{44}$-cluster has been shown to undergo ligand exchange with molecules containing reactive thiol-groups,[110] including exposed cysteine residue in proteins and thiol-modified DNA-strands.[73]

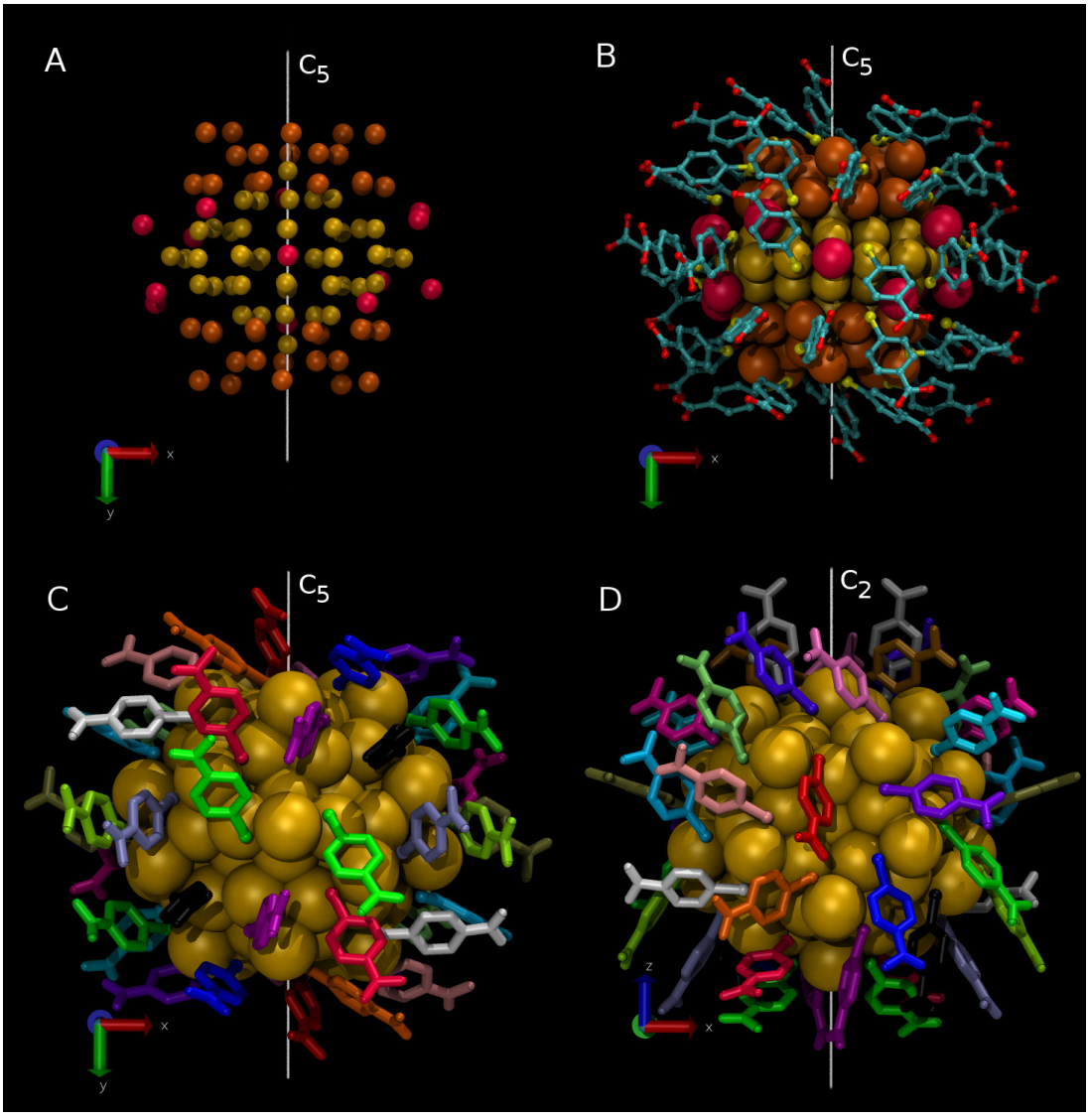

Figure 1.2: Structure of the $Au_{102}(p\text{MBA})_{44}$-cluster. **A**: Structure of the gold-framework viewed through the cluster C_2-axis showing the Mackay decahedron (yellow), 20-atom caps at the poles (orange), and the 13 chiral equatorial gold-atoms (red). **B**: Arrangement of the ligands with respect to the core gold-atoms (colour scheme, Au: same as in fig. A, C: cyan, S: yellow, O: red, H: not shown). **C**: Structure of the ligand-layer showing the symmetry related *p*MBA with the same colour. **D**: Same as **C** after 90° rotation viewed through the C_5-axis of the core.

1.3.2 $Au_{144}(SR)_{60}$

Clusters with 140 to 150 gold atoms and approximately 60 protecting ligands have been reported in several studies during the last two decades.[67,111,112] The early assignments were based on broad LDI- or MALDI-MS peaks, and more recently the formula $Au_{144}(SR)_{60}$ was identified by ESI-MS.[72,96,113] The optical and electronic properties reported in both the old literature and the new studies made on confirmed $Au_{144}(SR)_{60}$ samples agree well with each other, indicating they are indeed the same cluster size.

The structure of the cluster has not been solved via single crystal XRD. Instead, a structure proposal[114] based on the known XRD structures of similar sized $Pd_{145}(CO)_{60}(PEt_3)_{30}$ and $Pd_{164-x}Pt_x(CO)_{72}(PPh_3)_{20}$ ($x \approx 7$)[94,115] is used. Starting from the center of the cluster the gold-atoms can be grouped into four shells as illustrated in fig. 1.3A. The first two are concentric 12 and 42 atom icosahedral shells, which together form 54 atom Mackay icosahedron. The third shell is formed by placing 3 atom triangles on every face of the icosahedron, forming a 60 atom rhombicosidodecahedron. The final 30 atoms are placed to the center of the square formed by two adjanced triangles in the third shell, resulting in icosidodecahedron. All four shells have highly symmetrical icosahedral symmetry (I_h point group). The 60 thiols groups bind to the outer two shells (fig. 1.3B and C), with third shell gold-atoms bonding to one and fourth shell gold-atoms to two thiol groups, forming 30 short $Au(SR)_2$ staple motifs. Due to bond length and angle constraints, the staples are arranged in a chiral pattern in the cluster surface, bringing the final symmetry of the cluster to the icosahedral rotation group I. Similar structure differing by the arrangement of the staple motifs has been proposed by Bahena *et.al.* based on electron diffraction.[116]

The superatom model gives $n_e = 144 - 60 = 84$ free electrons, which is 8 electrons short of closing the 1H shell. The electrochemical properties of the cluster have been measured using voltammetry and can be described by quantized charging of metal-like system, *i.e.* no HOMO-LUMO gap was observed,[67,112] consistent with open shell system. Femtosecond studies of cluster dynamics also indicate the cluster electronic structure to be metallic.[23,24]

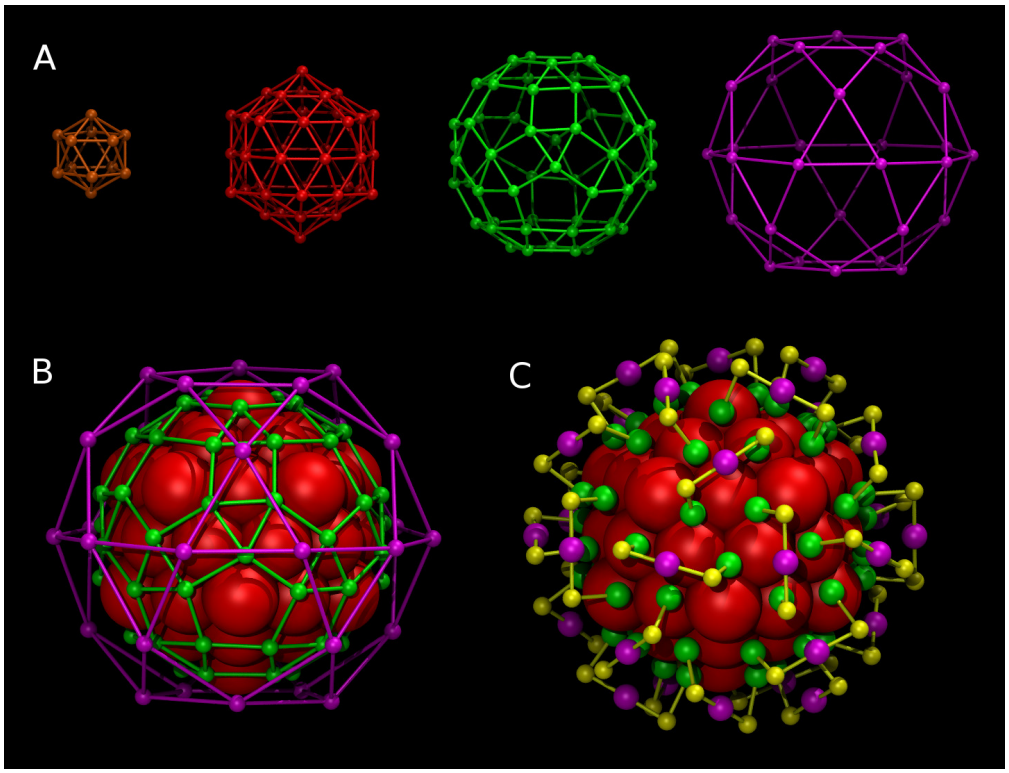

Figure 1.3: **A**: Shell structure of the proposed $Au_{144}(SR)_{60}$ model. From left to right: inner icosahedron (Au_{12}, brown), outer icosahedron (Au_{42}, red) rhombicosidodecahedron (Au_{60}, green), icosidodecahedron (Au_{30}, violet). **B**: Packing of the outer two layers on the icosahedron surface. **C**: Chiral arrangement of the staple motifs and the sulfur atoms (yellow) on the cluster surface. All images are viewed through the C_3 axis of the I point group.

2 Experimental Methods

This chapter will shortly introduce the main experimental methods used in this work by the author, including the Au-cluster sample preparation, basic description of vibrational and electronic spectroscopy, and acid-base titration.

2.1 Basics of experimental absorption spectroscopy

Energy units

In experimental and computational spectroscopy several different units are used to measure the energy of the electronic, vibrational, or rotational energy levels, and to present the spectrum of the system. Commonly used units are: frequency ν for rotational spectroscopy, wavelength λ for electronic absorption and photoluminescene, wavenumber $\tilde{\nu}$ or ω for vibrational spectroscopy, and electron volt eV for computational results and processes in deep UV- and X-ray regions. The different units are related by

$$E = h\nu = \frac{hc}{\lambda} = hc\tilde{\nu} \tag{2.1}$$

where h is the planck's constant. Electron volt eV is simply a multiple of Joules, 1 eV $= 1.602 \cdot 10^{-19}$ J, the energy given to single electron by electric field of 1 V.

Beer-Lambert law

Measuring the attenuation of electromagnenic radiation as it passes the measured system at different wavelengths gives the absorption spectrum of the system. For quantitative analysis the physical properties of the system must be connected to the spectrum. The absorbance A, or optical density, of a sample at wavelength λ is related to the sample properties via Beer-Lambert law

$$A(\lambda) = \log_{10} \frac{I(\lambda)}{I_0(\lambda)} = \varepsilon(\lambda)cl \tag{2.2}$$

where I and I_0 are the light intensity detected with and without the sample, c and l are the sample concentration and optical path length, and ε is the molar absorption coefficient of the molecule.

2.2 Vibrational spectroscopy

Every molecule vibrates, and the frequencies of the vibrations are characteristic to the molecule. In vibrational spectroscopy, transitions between the vibrational levels are used to determine the structure or the environment of the molecule.

The potential well of the oscillation can be described near the bottom as classical harmonic motion

$$U(r) = \frac{1}{2}k(r - r_e)^2 \tag{2.3}$$

where k is the spring constant and r_e is the equilibrium geometry. For classical oscillator the vibration energy is given in wavenumbers by

$$\omega = \frac{1}{2\pi c}\sqrt{\frac{k}{\mu}} \tag{2.4}$$

where μ is the reduced mass of the oscillating bodies. For molecules the spring constant k is associated with the bond strength, with stronger bonds oscillating at higher energies than weak, and the mass of the bodies is given by the atomic masses of the oscillating atoms. Quantum mechanical oscillator can only exist in discrete vibrational levels $v = 0, 1, 2, 3, \ldots$, described by the vibrational wavefunction Ψ_v, and as a result the vibrational energy of the system is also quantized with energies

$$E_v = \omega(v + 1/2) \tag{2.5}$$

with separation of ω between the vibrational levels.

Harmonic oscillator model fails to accurately model the behaviour of real molecules. Therefore more realistic model of anharmonic Morse potential[117] is frequently used

$$U(r) = D_e\left(e^{-2a(r-r_e)} - 2e^{-a(r-r_e)}\right) \tag{2.6}$$

where D_e is the potential well depth, r_e is the bond length at equilibrium, and parameter a describes the force constant of the oscillator. For anharmonic oscillator the vibrational energies are given by the series

$$G(v) = \omega_e(v + 1/2) - \omega_e\chi_e(v + 1/2)^2 + \omega_e\gamma_e(v + 1/2)^3 + \ldots \tag{2.7}$$

where χ_e, γ_e, *etc.* are the anharmonic constants accounting for the difference from the standard harmonic oscillator energies. Generally anharmonicity constants higher than the second order term $\omega_e\chi_e$ are ignored. The anharmonicity of the potential well leads to converging separation of vibrational energy levels.

The intensity of the transition is proportional to the transition dipole moment between vibrational wavefunctions ψ_v^i and ψ_v^f, which is defined as

$$\boldsymbol{R_v} = \int \psi_v^{f*}\boldsymbol{\mu}\psi_v^i \mathrm{d}Q \tag{2.8}$$

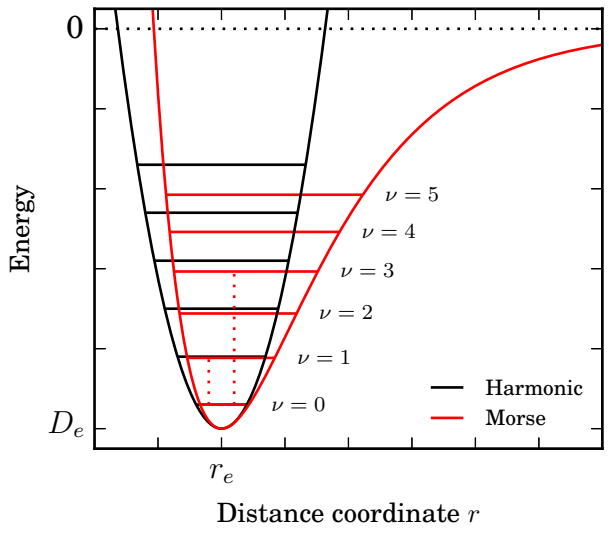

Figure 2.1: Harmonic and anharmonic potential wells as given by equations 2.3 and 2.6 respectively. Fundamendal $\nu : 1 \leftarrow 0$ and second overtone $\nu : 3 \leftarrow 0$ transitions are shown as dotted vertical lines.

where Q is the vibration coordinate expressed as deviation from the equilibrium. The variation of the dipole moment with respect to the molecular vibration can be written as Taylor expansion

$$\boldsymbol{\mu} = \boldsymbol{\mu}_e + \left(\frac{\mathrm{d}\boldsymbol{\mu}}{\mathrm{d}Q}\right)_e Q + \frac{1}{2!}\left(\frac{\mathrm{d}^2\boldsymbol{\mu}}{\mathrm{d}Q^2}\right)_e Q^2 + \frac{1}{3!}\left(\frac{\mathrm{d}^3\boldsymbol{\mu}}{\mathrm{d}Q^3}\right)_e Q^3 + \dots \tag{2.9}$$

where μ_e is the dipole moment at equilibrium. After substituting the Taylor expansion to the equation 2.8 we are left with

$$\boldsymbol{R_v} = \boldsymbol{\mu}_e \int \psi_v^{f*}\psi_v^i \mathrm{d}Q + \left(\frac{\mathrm{d}\boldsymbol{\mu}}{\mathrm{d}Q}\right)_e \int \psi_v^{f*} Q \psi_v^i \mathrm{d}Q + \frac{1}{2!}\left(\frac{\mathrm{d}^2\boldsymbol{\mu}}{\mathrm{d}Q^2}\right)_e \int \psi_v^{f*} Q^2 \psi_v^i \mathrm{d}Q + \dots \tag{2.10}$$

The first term is non-zero only if $\psi_v^i = \psi_v^f$, which does not represent a transition. The second and higher terms are non-zero if the derivative of the dipole moment with respect to the vibration coordinate Q and the wavefunction integral are both non-zero. These requirements create selection rules for vibrational absorption spectroscopy. The former means that only vibrations where the dipole moment of the molecule changes during the vibration can be excited by the external electric field, while the latter is true only when the vibrational quantum number v changes by 1. The energy ω of the transition $v \to v + 1$ is given by applying eq. 2.7

$$\omega = G(v+1) - G(v) \tag{2.11}$$

2.3 Electronic spectroscopy

Electronic spectroscopy considers transitions between two states of the molecules electron cloud. In the process the molecule absorbs a photon which excites electron from the lower energy electronic orbital to higher energy orbital. The photon is provided by outside electromagnetic field, and the absorption is seen as depletion of the radiation corresponding with the energy difference between the states.[30,36]

For vast majority of small and medium size molecules the electronic transitions happen at energies corresponding with the ultraviolet- or visible-region of electromagnetic spectrum. Due to this electronic spectroscopy is commonly called ultraviolet/visible (UV/Vis)-spectroscopy, even though the method is not bound to any single region of the electromagnetic spectrum. Larger systems which have small separation of electronic energy levels, such as metal cluster, can also have transitions in the near- middle- or far-IR regions.

As the molecular wavefunctions are eigenfunctions of the three dimensional Hamiltonian of the molecule, the shape and the allowed energy levels of the electronic wavefunctions depend on the shape and composition of the molecule. Therefore the transitions and the resulting spectrum is specific to the measured system.

The electronic transition moment $\boldsymbol{R_e}$ is defined as coupling of the initial and final electronic state wavefunctions ψ_e^i and ψ_e^f by outside electric field[36]

$$\boldsymbol{R_e} = \int \psi_e^{f*} \boldsymbol{\mu} \psi_e^i \mathrm{d}\tau. \tag{2.12}$$

$\boldsymbol{\mu}$ is the dipole moment operator $\boldsymbol{\mu} = \sum q_i \boldsymbol{r_i}$, where q_i and $\boldsymbol{r_i}$ are the charge and position of element i, respectively. For atomic orbitals (1.5) the transition is allowed, *i.e.* $R_e \neq 0$, only if the total angular momentum J is unchanged or changes by one, leading to the selection rule $\Delta J = 0, \pm 1$.[36,118] Similar rules apply also for the superatomic orbitals. The transition probability is proportional to the square of the transition moment $|\boldsymbol{R_e}^2|$, and the transition energy is given by the energy difference between the initial and final states $\Delta E = E_{\psi_e^f} - E_{\psi_e^i}$.

2.4 Acid-base titration

Monoprotic Brønsted acid HA dissociates in water according to the reaction

$$\mathrm{HA\,(s) + H_2O\,(l) \overset{K_a}{\rightleftharpoons} A^-(aq) + H_3O^+(aq)} \tag{2.13}$$

The acid dissociation constant of the reaction is given by the regular equation

$$K_a = \frac{[\mathrm{H_3O^+}][\mathrm{A^-}]}{[\mathrm{HA}]} \tag{2.14}$$

and the pH of the resulting solution is defined as usual by equation

$$pH = -\log_{10}[\mathrm{H_3O^+}] \tag{2.15}$$

When strong base is added to the solution it neutralizes the excess $\mathrm{H_3O^+}$ ions via reaction

$$\mathrm{MOH(s) + H_3O^+(aq) \longrightarrow M^+(aq) + H_2O(l)} \tag{2.16}$$

The base is added to the acid solution until all of the original acid has been neutralized, and the change of the pH of the solution is measured as function of the addition of the base. During the addition the $[\mathrm{H_3O^+}]$ concentration of the solution changes according to the equation[119] (fig. 2.2A)

$$[\mathrm{H_3O^+}]^3 + \left(\frac{M_b V_b}{V_b + V_a} + K_a\right)[\mathrm{H_3O^+}]^2 + \left(K_a \frac{M_b V_b - M_a V_a}{V_b + V_a} - K_w\right)[\mathrm{H_3O^+}] - K_a K_w = 0 \tag{2.17}$$

where V_a and M_a are initial volume and concentration of acid, V_b and M_b are the volume and concentration of base added to the solution, K_a is defined by eq. 2.14, and K_w is the autoionization constant of the solvent, for water $K_w = [\mathrm{H_3O^+}][\mathrm{OH^-}]$. The titration can be done also in reverse by titrating base with strong acid, in this case the acid constant and $\mathrm{H_3O^+}$ concentration in eq. 2.17 are substituted by the base constant K_b and $\mathrm{OH^-}$ concetration.

For weak acids ($K_a > 1$) the acid dissociation constant 2.14 can be rearranged into Henderson-Hasselbalch equation, which gives approximate pH of the solution when the pH is close to the pK_a of the acid:

$$pH = pK_a + \log_{10}\frac{[\mathrm{A^-}]}{[\mathrm{HA}]} \tag{2.18}$$

where $pK_a = -\log_{10} K_a$. In case of multiple pK_a points which can interact with each other, the Henderson-Hasselbalch equation is modified by the Hill-coefficient n.

$$n(pH - pK_a) = \log_{10}\frac{[\mathrm{A^-}]}{[\mathrm{HA}]} \tag{2.19}$$

By subsituting $[\mathrm{A^-}]$ and $[\mathrm{HA}]$ with the respective fraction of species $\alpha_{\mathrm{A^-}} = \frac{[\mathrm{A^-}]}{[\mathrm{HA}][\mathrm{A^-}]}$ and $\alpha_{\mathrm{HA}} = \frac{[\mathrm{HA}]}{[\mathrm{HA}][\mathrm{A^-}]}$ and rearranging the equation, we get fraction of protonated and deprotonated species as function of pH with equations (fig. 2.2B)

$$\alpha_{HA} = \frac{1}{1 + 10^{n(pH - pK_a)}} \tag{2.20}$$

$$\alpha_{A^-} = \frac{10^{n(pH - pK_a)}}{1 + 10^{n(pH - pK_a)}} \tag{2.21}$$

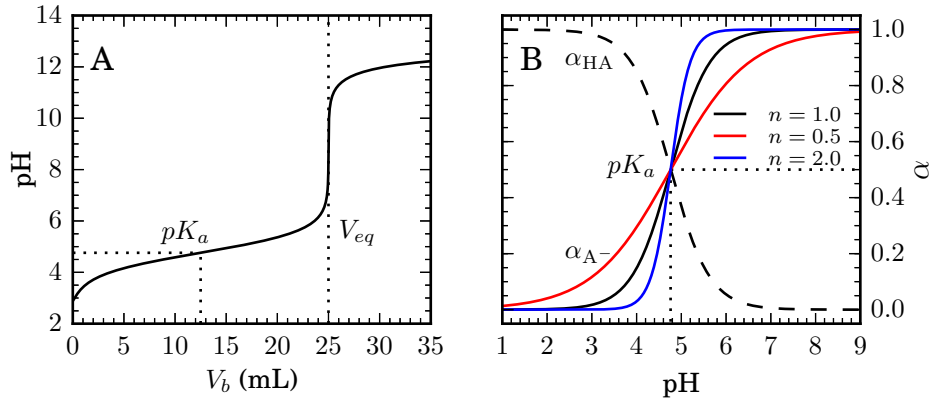

Figure 2.2: **A**: Titration curve of 25 mL of 0.10 mol/L acetic acid ($pK_a = 4.76$) being titrated with 0.10 mol/L strong base, as given by equation 2.17. **B**: Fraction of protonated and deprotonated species for the titration curve in fig. **A** as function of pH (eq. 2.20 and 2.21). The cooperative and anti-cooperative Hill-coefficient is observed as different slope of the curve, steeper slope if $n > 1$ and more shallow slope if $n < 1$. For clarity, only the fracion of deprotonated species α_{A^-} if plotted for different Hill-coefficients.

The Hill-coefficient n describes the behaviour of the equilibrium of single pK_a point with respect to the protonation state of another protonable functional group. Three types of behaviour are identified: non-interacting ($n = 1$), in which case the protonation of different groups does not affect the protonation of the observed group. Cooperative ($n > 1$), if one group is protonated/deprotonated, the other groups are easier to protonate/deprotonate. Anti-cooperative ($n < 1$), if one group is protonated/deprotonated, the other groups are harder to protonate/deprotonate. The anti-cooperative behaviour can be though as splitting of the identical pK_a's found in the system into numerous different pK_a's which are too closely spaced to be resolved in any measurements.

The protonation state of system can be measured in addition to the basic titration experiments using any experimental technique which can differentiate between the protonated and deprotonated states of the molecule, such as NMR- or FTIR-spectroscopy.

2.5 Sample preparation

Solid-state IR-measurements of the Au-clusters were measured from samples drop-cast on IR-transparent CaF_2 or BaF_2 window. The sample was dissolved in water ($Au_{102}(p\text{MBA})_{44}$ and $Au_{68}(m\text{MBA})_{32}$ samples), toluene or dichloromethane (PET-protected cluster samples). 5–20 µL of the solution was pipetted to the window and either dried in vacuum (water-solutions), or let dry in normal pressure (toluene and

DCM -solutions).

The IR-measurements of solvated clusters was measured using home-made absorption cuvette with changeable windows and variable path-length. We used 2 mm CaF_2 windows and path lengths between 10–80 µm, depending on the sample concentration and solvent absorbance. All liquid-IR measurement were performed using deuterated solvents (D_2O, MeOD-d4, DCM-d2, DMSO-d6), while the solvent was chosen by the solubility of the measured substance. The IR-measurements of single crystals were performed on crystals deposited on gold-mirror (reflection geometry), or CaF_2-window (transmission geometry). The crystals were transferred with standard loops using high-viscosity FOMBLIN-Y oil or ethanol, where the former resulted in less damage to the crystals in transfer. The $Au_{144}(PET)_{60}$ crystals were grown by slow vapour diffusion from toluene solution using acetonitrile as the antisolvent. All IR-measurements were done with 2 or 4 cm^{-1} resolution and processed with Happ-Genzel apodization function before Fourier-Transform.

Electronic absorption spectra were measured from solvated samples using regular 1 or 10 mm quartz-cuvettes, or the same cuvette as used in the IR-measurements.

3 Results and Discussion

3.1 Optical properties of $Au_{144}(PET)_{60}$ cluster

3.1.1 Optical gap in solution, dropcast layer, and in single crystal

The Au_{144}-cluster has been studied intensively during the last two decades, however the electronic transitions in the IR-region have not been studied before. Early electrochemical and computational studies of the Au_{144}-cluster showed that the HOMO-LUMO gap for the cluster is less than 0.05 eV,[20,26,120] *i.e.* the cluster can be considered metallic. However, the HOMO and LUMO orbitals have mainly S and H angular momentum characters respectively, making the HOMO-LUMO transitions forbidden.[120] Due to this the first allowed optical transitions may be seen at higher energies in the mid-IR or NIR-regions. The IR-spectrum of the $Au_{144}(PET)_{60}$ (PET: Phenylethyl thiolate) cluster was measured dissolved in deuterated DCM (DCM-d2), dropcast on CaF_2-window, and from single crystals deposited on gold-mirror or CaF_2-window. Measurements in

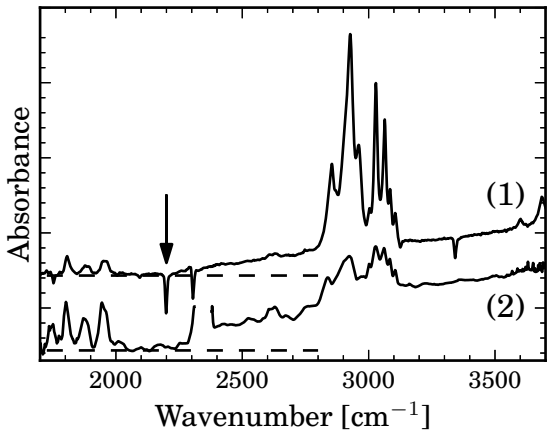

Figure 3.1: IR-spectrum of $Au_{144}PET_{60}$ cluster solvated in DCM-d2 (**1**) and in single crystal (**2**). Reprinted with permission from *J. Phys. Chem. Lett.*, 2014, 5, p. 387. Copyright ©2014, American Chemical Society.

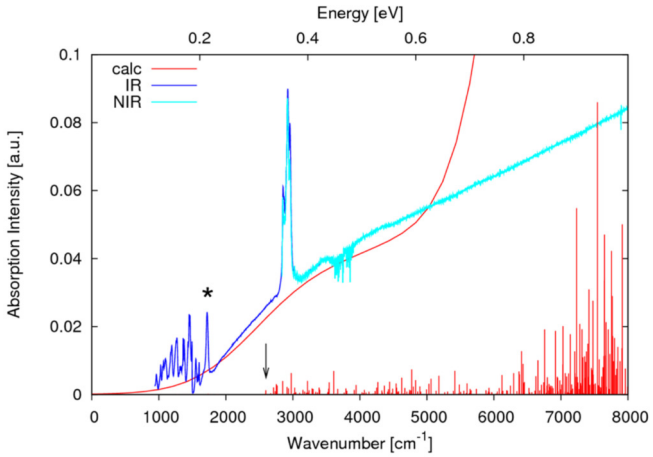

Figure 3.2: IR-spectrum of $Au_{144}(PET)_{60}$ cluster in solid state, and the computational spectra. Reprinted with permission from *J. Phys. Chem. Lett.*, 2012, 3, p. 3076. Copyright ©2012, American Chemical Society.

all three phases show the onset of smooth electronic absorption in the mid-IR region (fig. 3.1) at 2100 cm^{-1} (0.26 eV), 1500 cm^{-1} (0.19 eV), and 2100 cm^{-1} (0.26 eV) for the three samples respectively.

The optical gap obtained for the solvated and single crystal samples agrees well with the transitions from the HOMO(H) and first LUMO(H) to the LUMO+2(I) -level According to the PLDOS of the computational $Au_{144}(SH)_{60}$ orbitals, the HOMO, LUMO, and LUMO+1 levels consist of 5 H-type orbitals with less than 0.05 eV separation in energy. Due to the small energy gap the first LUMO levels can have fractional population at room temperature, making transitions from LUMO possible. The optical gap of the dropcast sample is slightly lower (fig. 3.2) than in solution and single crystal. This difference can be rationalized by the different sample morphology of the dropcast sample. During the drying of the dropcast sample microcrystals with sizes similar to the mid-IR wavelengths can form in the sample. These would then cause Mie-scattering[32] of the incident IR-beam, and the loss of signal is registered as absorbtion by the spectrometer, which may give slight error to the optical gap values measured from solid samples. The calculated spectrum predicts a significant rise in absorption at 6000 cm^{-1}(0.74 eV) which was not observed experimentally for any measured system. This discrepancy between the measured and calculated spectrum could not be explained.

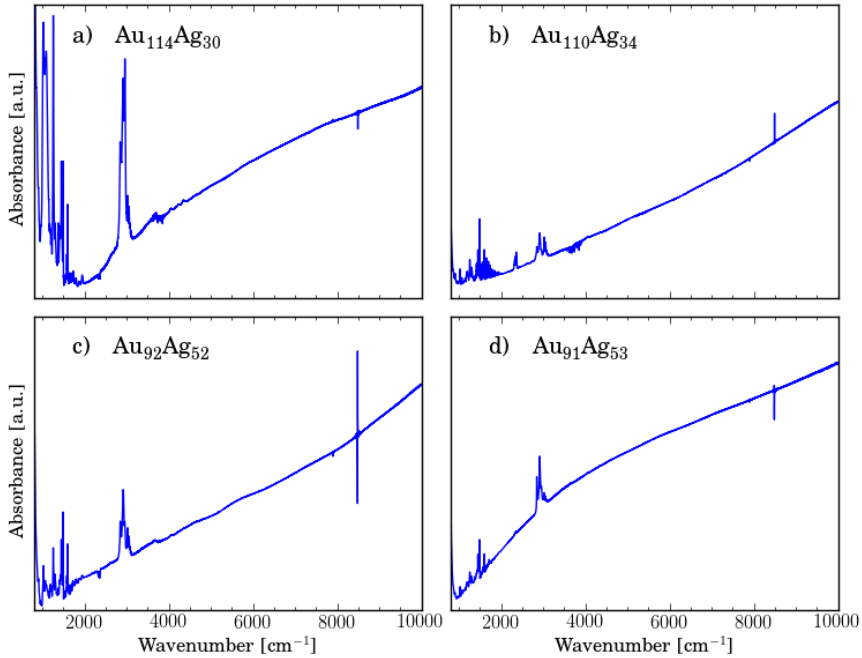

Figure 3.3: Measured IR/NIR-spectrum of the $(Au/Ag)_{144}(PET)_{60}$ clusters. Reprinted with permission from *J. Phys. Chem. Lett.*, 2012, 3, p. 3076. Copyright ©2012, American Chemical Society.

3.1.2 Variation of the optical gap due to silver-content

The effect of replacing gold atoms with silver in the Au_{144} cluster on the optical gap of the cluster was studied for four silver-doped clusters containing up to 60 silver atoms. According to the ESI-MS analysis, these samples were monodisperse with respect to the total amount of metal atoms in the system, but the amount of silver atoms in the samples formed a gaussian distribution.[96] According to later analysis, these clusters may have contained also Au_{137}-clusters.[88] The Au/Ag -cluster samples are labeled by the composition at the peak of the distribution, which are $Au_{114}Ag_{30}PET_{60}$, $Au_{110}Ag_{34}PET_{60}$, $Au_{91}Ag_{53}PET_{60}$, and $Au_{90}Ag_{54}PET_{60}$. The fact that up to 60 gold atoms, but no more, could be exchanged to silver suggests that the silver is selectively incorporated into the third 60-atom rhombicosidodecahedral layer of the cluster (fig. 1.3). DFT-studies of the system also found this to be energetically the most favorable arrangement.[121,122] Same prediction can be made from the surface energies of gold (97 meV/Å^2) and silver (78 meV/Å^2).[48,93]

The four silver-doped cluster samples were measured in the mid-IR and NIR-regions from dropcast films of the sample on CaF_2-window (fig. 3.3). Compared to the pure gold $Au_{144}(PET)_{60}$ cluster measured also as dropcast film, the electronic absorption

edge of the $Au_{114}Ag_{30}(PET)_{60}$ sample is found at slightly higher energy (2100 cm^{-1}, 0.26 eV), while the other three are slighly lower ($Au_{110}Ag_{34}(PET)_{60}$: 1200 cm^{-1}/0.15 eV, $Au_{91}Ag_{53}(PET)_{60}$: 1300 cm^{-1}/0.16 eV, $Au_{90}Ag_{54}(PET)_{60}$: 1000 cm^{-1}/0.12 eV). All values are within 600 cm^{-1} (0.07 eV) of the pure gold Au_{144}, and within 1100 cm^{-1} (0.14 eV) of each other, indicating the cluster optical gap is not significantly altered by the addition of silver. A change in the shape of the absorption band is observed between the different samples, with $Au_{110}Ag_{34}$ and $Au_{92}Ag_{52}$ giving a smooth rise from the absorption edge up to 10000 cm^{-1}, while for $Au_{114}Ag_{30}$ and $Au_{91}Ag_{53}$ a wide absorption peak is forming around 4000 cm^{-1} (0.50 eV). The spectrum of four different $Au_{144-x}Ag_x$ (x = 30, 58, and 60) clusters were calculated (fig. 3.4) and compared with the experimental spectra. For the three clusters which have the silver atoms in the third layer the absorption edge is at around 1500-1600 cm^{-1} (approx. 0.19 eV) after the convolution with convolution with gaussian function with 0.10 eV width. The optical gap of all measured and calculated Au_{144} and $AuAg_{144}$ systems are presented in table 3.1. In the cluster with silver dispersed in all three inner layers the electronic states are more closely spaced, leading into smoother spectrum, and the absorption edge is found at significantly lower energy at 1150 cm^{-1} (0.14 eV). The difference of the shape of the experimental spectra can be attributed due to the different distribution of silver atoms in the samples, or to different morphology of the measured films which may contribute to scattering as explained in the case of Au_{144} films earlier. They can also be explained by the presence of of the Au_{137}-cluster, which was reported in the same samples afterwards.[88]

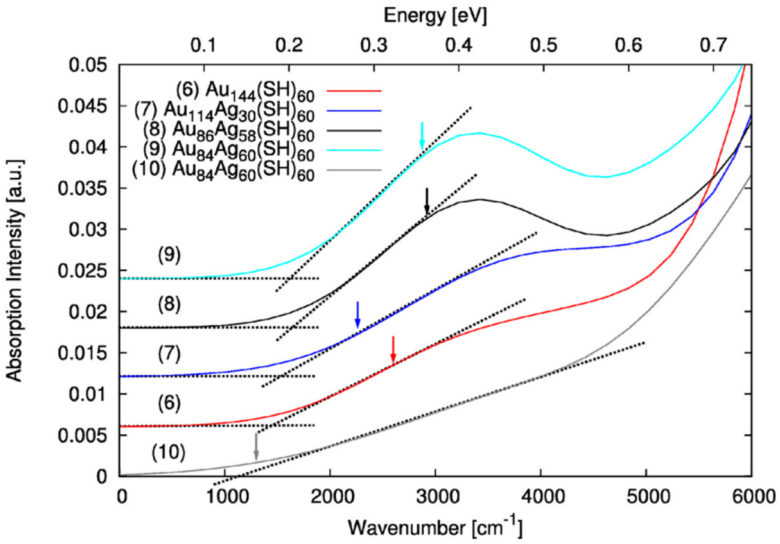

Figure 3.4: Calculated spectra of $Au_{144}(PET)_{60}$ and $(Au/Ag)_{144}(PET)_{60}$ clusters. In the structures (7), (8), and (9) the Ag-atoms are distributed in the third layer of the proposed Au_{144} structure, while in (10) 30 are placed in the inner Mackay icosahedron and 30 in the third layer (fig. 1.3). Reprinted with permission from *J. Phys. Chem. Lett.*, 2012, 3, p. 3076. Copyright ©2012, American Chemical Society.

Table 3.1: Measured and calculated optical gaps of the $Au_{144}(PET)_{60}$ and silver doped $(Au/Ag)_{144}(PET)_{60}$ derivatives. The experimental spectra are presented in fig. 3.1 and fig. 3.3, and the calculated spectra in fig. 3.4. The calculated gaps are taken after convolution with gaussian function with 0.10 eV linewidth. The values in parenthesis are without convolution. Adapted with permission from *J. Phys. Chem. Lett.*, 2012, 3, p. 3076. Copyright ©2012, American Chemical Society.

Sample	exp./calc.	optical Gap (eV)	optical Gap (cm^{-1})
1a: $Au_{144}PET_{60}$ (solv.)	exp.	0.273 ± 0.013	2200 ± 100
1b: $Au_{144}PET_{60}$ (film.)	exp.	0.186 ± 0.013	1500 ± 100
1c: $Au_{144}PET_{60}$ (cryst.)	exp.	0.273 ± 0.013	2200 ± 100
2: $Au_{114}Ag_{30}PET_{60}$	exp.	0.260 ± 0.025	2100 ± 200
3: $Au_{110}Ag_{34}PET_{60}$	exp.	0.149 ± 0.025	1200 ± 200
4: $Au_{91}Ag_{53}PET_{60}$	exp.	0.161 ± 0.025	1300 ± 200
5: $Au_{90}Ag_{54}PET_{60}$	exp.	0.124 ± 0.013	1000 ± 100
6: $Au_{144}(SH)_{60}$	calc.	0.175 (0.323)	1410 (2600)
7: $Au_{114}Ag_{30}(SH)_{60}$	calc.	0.186 (0.281)	1500 (2260)
8: $Au_{86}Ag_{58}(SH)_{60}$	calc.	0.200 (0.362)	1610 (2920)
9: $Au_{84}Ag_{60}(SH)_{60}$	calc.	0.200 (0.357)	1610 (2880)
10: $Au_{84}Ag_{60}(SH)_{60}$	calc.	0.143 (0.161)	1150 (1300)

3.1.3 Vibrational signatures of $Au_{144}(PET)_{60}$ single crystal

Solving the crystal structure of the $Au_{144}(SR)_{60}$ cluster is a long standing challenge in the gold-cluster field. We managed to grow high quality hexagonal $Au_{144}(PET)_{60}$ single crystals approximately 100x100x20 μm in size using slow-vapour diffusion from toluene/acetonitrile solvent system. Despite the apparent high quality of the crystals, they did not diffract beoynd 5 Å resolution. Since the XRD-measurements failed, we measured the IR-spectrum of the single crystals in order to gain insight into the properties and packing of the $Au_{144}(PET)_{60}$ crystals. The IR-spectrum of $Au_{144}(PET)_{60}$ -cluster and reference PET are presented in fig. 3.5. The free PET and the cluster in solution are very similar, corresponding very well to the earlier vibrational studies of similar systems,[123–126] with largest differences being the disappearance of the S−H stretching mode at 2540 cm^{-1} (not shown) and red-shift of the CH_2 scissor, wagging, and twisting modes of the aliphatic chain. Two new, very weak peaks are observed in the C−H stretching region at 2871 and 2981 cm^{-1}. Overall, the intensity of the aliphatic $-C_2H_4-$ chain vibrations are increased compared to the phenyl-ring vibrations. The vibrational modes of the phenyl-ring are unperturbed by the linking. The spectrum obtained from single crystal is similar to the solution state spectrum with respect to peak positions, however significant differences are observed in peak intensities and lineshape. The single crystal spectrum is characterized by significant broadening of peaks, and the intensity differences between peaks are smaller. The peak broadening is evident when looking the normally sharp phenyl ring C−C stretching peaks at 1600 cm^{-1} and 1500 cm^{-1}. Majority of the peaks in the fingerprint region overlap too much for quantitative analysis, but in the C−H stretching region the peaks were sufficiently well defined to be analyzed using multi-peak fitting. The region 2780–3130 cm^{-1} was fitted using set of 9 or 11 Gaussian and/or Lorentzian functions, and the peak positions and width are shown in table 3.3. The positions of the phenyl-ring vibrations shift only by 2 cm^{-1} at maximum, while the aliphatic peaks show up to 6 cm^{-1} shifts. In crystal the peak width is increased by 50–200 % compared to the neat PET and solvent spectra, and the peak shape changes from Lorentzian to Gaussian indicating inhomogeneous broadening mechanism in the crystal. This is in contrast to regular case, in which the crystal gives sharper and more defined peaks than in solution due long-range order in the crystal and lack of solvent dynamics.[127]

We argue the inhomogeneous broadening of the ligand vibrational modes are caused by inhomogeneous packing of the ligands in the crystal, *i.e.* the ligands are not packed in well ordered, periodic fashion. If we consider close packing of spherical particles, cavities are left between the spheres. For a 3 nm particle such as $Au_{144}(PET)_{60}$ these can be as large as 1.25 nm, which is about the same size as the PET molecule length. As a result the ligands which are next to the neighbouring cluster see different environment than the ones pointing towards the cavities. We also believe the flexibility of the aliphatic chain and the lack of strong coordinating interactions such as hydrogen

Table 3.2: Observed vibrational modes of the PET-molecule in neat liquid, and $Au_{144}(PET)_{60}$ cluster in solution and in single crystal. Adapted with permission from *J. Phys. Chem. Lett.*, 2014, 5, p. 387. Copyright ©2014, American Chemical Society.

Symmetry[a]	Notation/Assignment			$\tilde{\nu}_{obs}$ (cm^{-1})		
(C_{2v}/C_s)	Herzberg	Wilson	Gardner	PET (l)	Au_{144}[b]	Au_{144}[c]
A_1	ν_1	ν_{20a}	$\mathscr{M}_2$	3084.7 m	3084.8 m	3084.1 m
A_1	ν_2	ν_{7a}	$\mathscr{M}_3$	3062.0 m	3062.0 m	3060.7 m
A_1	ν_3	ν_2	$\mathscr{M}_1$	3105.7 w	3105.7 w	3103.9 m
A_1	ν_4	ν_{13}	$\mathscr{M}_4$	1604.0 m	1603.8 m	~1604 m
A_1	ν_5	ν_{8a}	$\mathscr{M}_7$	1496.9 s	1496.2 s	1497.7 m
A_1	ν_6	ν_{19a}	$\mathscr{M}_8$	1199.4 w	1196.8 w	1196.8 m
A_1	ν_7	ν_{9a}	$\mathscr{M}_5$	1179.0 w	1179.0 w	1179.0 m
A_1	ν_8	ν_{18a}	$\mathscr{M}_6$	1030.6 w	1030.6 w	1030.6 w
A_1	ν_9	ν_{12}	$\mathscr{M}_9$	1004.1 w	1005.7 w	1002.7 w
A_1	ν_{10}	ν_1	$\mathscr{M}_{10}$	804.9 w	–	~806 sh
A_1	ν_{11}	ν_{6a}	$\mathscr{M}_{11}$	489.8 m	–	–
A_2	ν_{12}	ν_{17a}	$\mathscr{M}_{12}$	970.8 w	–	~966 w,sh
A_2	ν_{13}	ν_{10a}	$\mathscr{M}_{13}$	845.5 w	–	841.6 m
A_2	ν_{14}	ν_{16a}	$\mathscr{M}_{14}$	–	–	–
B_1	ν_{15}	ν_5	$\mathscr{M}_{15}$	983 w,sh	–	982.7 w
B_1	ν_{16}	ν_{17b}	$\mathscr{M}_{16}$	910.3 w	–	914.1 m
B_1	ν_{17}	ν_{10b}	$\mathscr{M}_{17}$	732.1 s	–	–
B_1	ν_{18}	ν_4	$\mathscr{M}_{18}$	698.0 s	–	–
B_1	ν_{19}	ν_{11}	$\mathscr{M}_{19}$	559.9 m	–	–
B_1	ν_{20}	ν_{16b}	$\mathscr{M}_{20}$	–	–	–
B_2	ν_{21}	ν_{20b}	$\mathscr{M}_{21}$	3026.9 m	3028.3 m	3026.4 m
B_2	ν_{22}	ν_{7b}	$\mathscr{M}_{22}$	3001.8 w	3001.8 w	3000.1 m
B_2	ν_{23}	ν_{8b}	$\mathscr{M}_{23}$	1584.4 w	1584.1 w	1583.8 m
B_2	ν_{24}	ν_{19b}	$\mathscr{M}_{24}$	1453.3 s	1453.3 s	1453.3 m
B_2	ν_{25}	ν_3	$\mathscr{M}_{25}$	1322.7 w	1309.1 w	1309.1 m
B_2	ν_{26}	ν_{14}	$\mathscr{M}_{26}$	1292 w,sh	1278 w,sh	~1279 m
B_2	ν_{27}	ν_{15}	$\mathscr{M}_{27}$	1157.5 w,sh	1157.5 w	1157.5 m
B_2	ν_{28}	ν_{18b}	$\mathscr{M}_{28}$	1076.3 w	1072.0 w	1072.0 m
B_2	ν_{29}	ν_{9b}	$\mathscr{M}_{29}$	622.0 w	–	–
B_2	ν_{30}	ν_{6b}	$\mathscr{M}_{30}$	–	–	–
A'	ν_{31}	S-CH_2 sym. str.		2933.2 m	2927.5 m	2930.4 m
A'	ν_{32}	Ph-CH_2 sym. str.		2849.0 m	2852.2 m	2835.6 m
A'	ν_{33}	S-CH_2 scissor		~1447, sh	~1414 w	~1414 w
A'	ν_{34}	Ph-CH_2 scissor		~1428, w	~1433 w	~1433 w
A'	ν_{35}	CH_2-wag		1279.3 m	1262.1 m	~1265 m
A''	ν_{36}	S-CH_2 asym. str.		2963.8 m	2961.6 m	2962.4 m
A''	ν_{37}	Bz-CH_2 asym. str.		2908.2 m	2905.0 m	2897.2 m
A''	ν_{38}	CH_2-twist		1236.6 m	~1220 w	~1220 w
A''	ν_{39}	CH_2-rock		751.0 s	–	~750 m

s: strong, m: medium, w: weak, sh: shoulder.
S: adjacent to the sulfur, Ph: adjacent to the phenyl-ring.
[a] C_{2v} for $\nu_1 - \nu_{30}$, C_s for $\nu_{31} - \nu_{39}$.
[b] solvated in DCM-D2, [c] in single crystal.

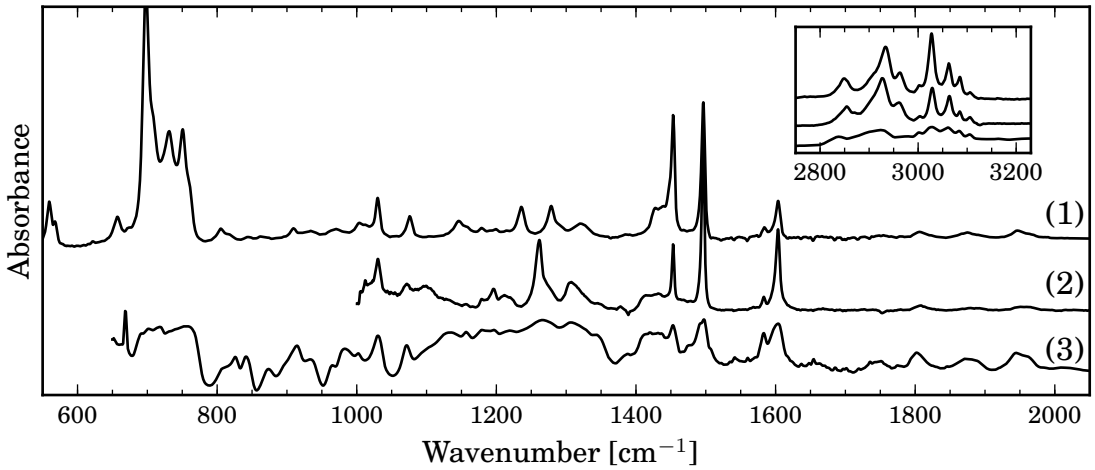

Figure 3.5: IR-spectrum of neat PET thin film (1), $Au_{144}(PET)_{60}$ solvated in DCM-d2 (2), and $Au_{144}(PET)_{60}$ single crystals (3). Reprinted with permission from *J. Phys. Chem. Lett.*, 2014, 5, p. 387. Copyright ©2014, American Chemical Society.

bonds in the PET molecule contribute to the disorder of the ligand packing. This proposed disorder of the ligand layer explains the behaviour of the X-ray diffraction obtained from these crystals. The crystals diffract strongly at small 2θ angles indicating ordered long-range structure, but the diffraction pattern disappears quickly at large 2θ angles regardless of the exposure time. We also measured the IR-spectrum of $Au_{25}(PET)_{18}$ crystals which are known to make well-defined single crystals.[61] In the obtained spectrum (fig. 3.7) C – H stretching region the peaks, for which $Au_{144}(PET)_{60}$ show only broadened features, are resolved into well defined peaks in the $Au_{25}(PET)_{18}$ crystal. The resolved peaks can be correlated with the known orientations of the ligands in the crystal, *i.e. trans-gauche* isomerism of the aliphathic chain.

The characteristic pattern of combination and overtone vibrations of monosubstituted benzene[128,129] is observed between 1650–2000 cm^{-1} for all samples, but the intensity relative to the fundamentals is significantly increased in the crystal (fig. 3.6A). A number of new peaks are found in the region 2000–2700 cm^{-1}, and they are also attributed to combination and overtones which are usually too weak to be observed experimentally.[123,124] Increase of combination and overtone intensity is usually caused by changes in electrical or mechanical anharmonicty, or intensity transfer between vibrational modes,[36,130] Electrical anharmonicity is caused by the nonlinear variation of the dipole moment with respect to the vibration, *i.e.* $Q^2, Q^3, ...$ terms in eq. 2.9, while mechanical anharmonicity is caused by the anharmonic shape of the potential energy function as shown in fig. 2.1. Mechanical anharmonicity alters both transitions energies and intensities, while electrical anharmonicty only alters the intensities. The overtones and combinations at 1650–2000 cm^{-1} show a small redshift of *c.a.* 5 cm^{-1} between the

solvent and crystal spectra of $Au_{144}(PET)_{60}$, ruling out any significant contribution from mechanical anharmonicity. Potential large change in electrical anharmonicity of the ligand vibrations would presumably be caused by either the proximity of the gold core, or the packing in the crystals, or both. The first option alone can be ruled out since the $Au_{144}(PET)_{60}$ solution does not display significant increase in the overtone and combination intensity. The second option would be also observable in IR-spectra of simple molecules recorded in single crystals, but hasn't been reported in, *e.g.* for single crystal benzene. The last option would imply high degree of coupling of the electrical structure of the adjanced Au_{144} -cores by the PET molecules. This also seems dubious as PET is not conductive molecule. Vibrational coupling between the different vibrational modes can also lead into intensity transfer between different peaks, while the sum of all the peak intensities remain unchanged by the process. Unfortunately the experimental data of the $Au_{144}(PET)_{60}$ was insufficient for quantitative analysis of the peak intensities between the spectra in different states, and the origin of the overtone and combination vibrations could not be attributed to any proposed theory.

In later studies, using *para*-iodine tetrafluorobenzene as sample system, we measured the absorption coefficient in both CCl_4 -solution and in single crystals. Qualitatively the IR-spectrum of the crystals showed similar relative increase in the benzene-ring overtone and combination vibrations compared to the solution spectrum. However, the absorption coefficient of the fundamentals in the crystal dropped significantly while the overtone and combination absorption coefficient remained the same in both phases. Any anharmonic effects can be ruled out as per above, while the significant change in total vibrational absorption cannot be attributed to intensity transfer between modes. Most probable explanation for this is that the measured crystal was too thick, and the fundamental peaks are truncated due to saturation, while for the overtones and combinations the signal stays in the linear region. It is possible that similar effect is also responsible for the intensity changes in the much thinner $Au_{144}(PET)_{60}$ crystals.

Table 3.3: Peak fitting parameters, center X_0 and full width half maximum (FWHM), for neat PET and $Au_{102}(p\text{MBA})_{44}$ in C-H stretching region. Adapted with permission from *J. Phys. Chem. Lett.*, 2014, 5, p. 387. Copyright ©2014, American Chemical Society.

Assignment	X_0 (cm^{-1})			FWHM (cm^{-1})		
	PET (l)	$Au_{144}{}^a$	$Au_{144}{}^b$	PET	$Au_{144}{}^a$	$Au_{144}{}^b$
Ph–CH_2 s.	2849.0	2852.2	2835.6	21.4	27.0	38.0
Ph–CH_2 as.	2908.2	2905.0	2897.2	34.2	37.3	46.6
S–CH_2 s.	2933.2	2927.5	2930.4	24.6	26.4	34.3
S–CH_2 as.	2963.8	2961.6	2962.4	15.2	20.3	19.5
X	—	2871.5	2868.0	—	7.5	21.2
Y	—	2981.2	2981.2	—	7.2	27.1
$\mathscr{M}_{22}$	3001.8	3001.8	3000.1	8.7	8.9	12.5
$\mathscr{M}_{21}$	3026.9	3028.3	3026.4	13.5	13.8	32.1
$\mathscr{M}_3$	3062.0	3063.1	3060.7	12.9	13.9	24.8
$\mathscr{M}_2$	3084.7	3084.8	3084.1	9.3	8.0	13.8
$\mathscr{M}_1$	3105.7	3105.1	3103.9	5.0	7.7	14.6

s: symmetric stretch, as: anti-symmetric stretch.

S: adjacent to the sulfur, Ph: adjacent to the phenyl-ring.

^{a} solvated in DCM-D2, ^{b} in single crystal.

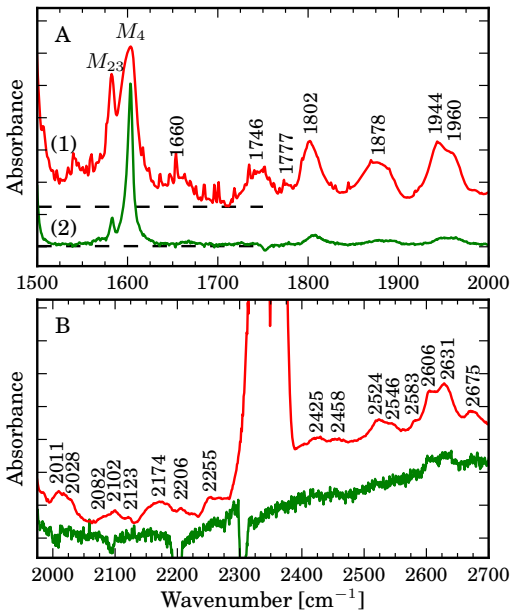

Figure 3.6: Overtone and combination vibrations of the phenyl-ring modes of $Au_{144}(PET)_{60}$ cluster. (Green) solvated, (Red) single crystal. Reprinted with permission from *J. Phys. Chem. Lett.*, 2014, 5, p. 387. Copyright ©2014, American Chemical Society.

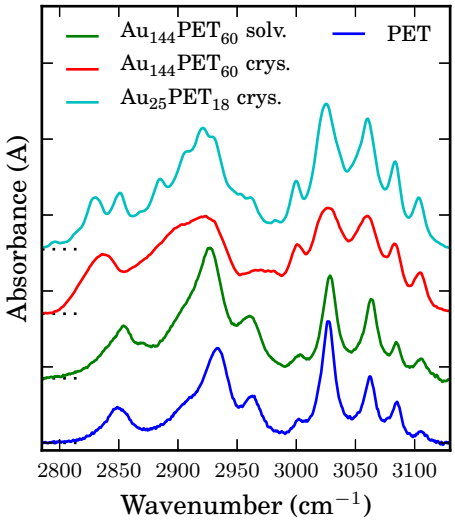

Figure 3.7: C-H stretching region of the PET-protected crystals. The well ordered $Au_{25}(PET)_{18}$ crystal shows narrow peaks as expected.

3.2 Structure Determination of $Au_{68}(m\text{MBA})_{32}$

Brust synthesis of water-soluble gold-clusters using *meta*-mercaptobenzoic acid (*mMBA*, also called 3MBA) was performed using 2:1 ligand:gold ratio, yielding a monodisperse gold cluster of approximately 1.4 nm in diameter in electron microscope images. The exact mass of the cluster could not be accurately measured by ESI-MS due to fragmentation and poor resolution, and the obtained peaks could be explained by compositions $[Au_{71}(m\text{MBA})_{27}]^{n-}$, $[Au_{68}(m\text{MBA})_{31}]^{n-}$, $[Au_{68}(m\text{MBA})_{32}]^{n-}$ $[Au_{65}(m\text{MBA})_{35}]^{n-}$, $[Au_{62}(m\text{MBA})_{39}]^{n-}$, where $n = 5, 6, 7, 8$. Of these the compositions with 71, 65, or 62 gold atoms were ruled out by combination of thermogravimetric analysis and X-ray photoelectron spectroscopy. Large crystals of the material were obtained, but the X-ray diffraction extended only up to 5 Å resolution.

3.2.1 Single particle reconstruction electron density map

Transmission electron microscope (TEM) image of an three-dimensional object represents the projection of the electron density in the object to a two-dimensional space.[131–133] If sufficient amount of images representing different orientations of the original object can be acquired, the original 3D-structure can be reconstructed using iterative methods. In this method similar images are grouped into class averages, which represent the projections of the object from different angles.[134] These are then used to calculate a intial model for the object, and the projections of the model is compared to the experimental data. The process is repeated until the model and experimental data converge.

The $Au_{68}(m\text{MBA})_{32}$ samples were imaged using aberration corrected-TEM, using $\sim 800\ e^-/\text{Å}^2$ electron dose to avoid radiation damage.[135] Images of 939 clusters were selected from the TEM-images and used in the particle reconstruction. In fig. 3.8A example for three class-averages of the cluster are shown. The reconstruction yields electron density map, which has 68 peaks (fig. 3.8). Due to the very high electron density of gold vs. any other atom in the system (79(Au) vs. 6(C), 8(O), 16(S)), and the ESI-MS results, the peaks are assumed to arise from the positions of the gold atoms.

3.2.2 Electronic spectroscopy of $Au_{68}(m\text{MBA})_{32}$

The low-energy electronic transitions were studied by measuring the IR- and NIR-spectrum from 900 cm^{-1} to 7000 cm^{-1} of the unknown sample dropcasted on CaF_2-window and dried in vacuum. The measured region (fig. 3.9a) contains both the

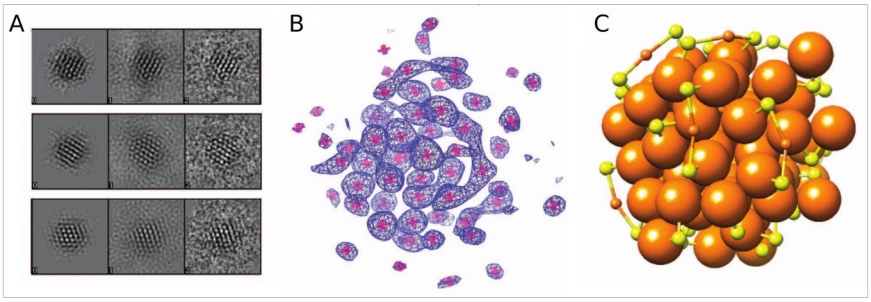

Figure 3.8: **A**: Electron micrographs of the $Au_{68}(m\text{MBA})_{32}$-cluster. (Left) Back-projection from the reconstruction, (Middle) class average, (Right) original images. **B**: Electron density map of the reconstruction. Red crosses indicate maxima in the map. **C**: Structure of the full $Au_{68}(m\text{MBA})_{32}$-cluster with the SH ligands after relaxation by DFT. Adapted from *Science*, 2014, 345, p. 909. Reprinted with permission from AAAS.

vibrational signatures of the *m*MBA-ligand at 2900–3600 cm^{-1}, and below 1700 cm^{-1}, and the electronic signatures of the Au_{68} cluster core above 3600 cm^{-1}. For vibrations the expected C−H and O−H stretching at 2900-3600 cm^{-1}, symmetric and asymmetric $-CO_2^-$ stretching at 1400 cm^{-1} and 1550 cm^{-1}, and the benzene ring mode at 1600 cm^{-1} were observed. The pH of the sample was not measured, however the absence of the carbonyl strething peak indicates the ligand layer is in completely deprotonated form. The region 2900–3600 cm^{-1}lost approximately third of it's intensity when the sample was illuminated with the IR-beam in dry conditions for 90 minutes (fig. 3.10A). The loss of signal is consistent with evaporation of water adsorbed on the sample, as seen earlier with $Au_{102}(p\text{MBA})_{44}$-cluster.[69] This is further proven by taking the difference between the first (0 min) and the last spectrum (90 min), and plotting it's second derivative (dashed and solid black lines in fig. 3.10A). The difference spectrum shows broad asymmetric absorbance centered around 3400 cm^{-1}, and the derivative shows four distinct peaks at 3600, 3500, 3200, and 3000 cm^{-1}, consistent with water in different hydrogen bonding states. Above 3600 cm^{-1} three absorption peaks at 4200 cm^{-1}, 5250 cm^{-1}, and a split peak at 6100 cm^{-1} attributed to the electronic transitions are observed. The peak around 2500 cm^{-1} required further analysis, as the thiol-group (−SH) stretching vibration is generally around the observed energy. However, since the the ligands bind to the cluster via the thiol-group sulfur, it's very unlikely there exists any free thiol-groups in the cluster. Also, the broadness of the peak (FWHM $\approx$ 250 cm^{-1}) is very large for a single vibrational peak, therefore this peak was attributed to electronic transition. To prove this, we removed the vibrational signatures of the *m*MBA ligand from the spectrum (fig. 3.11). This was achieved by taking the spectrum of a larger *m*MBA protected cluster which showed smooth electronic absorbance spectrum, from which the electronic absorbance was

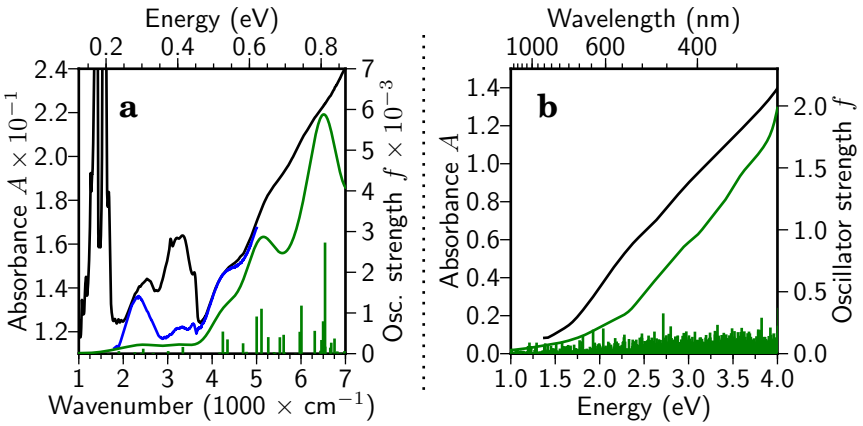

Figure 3.9: Absorption spectrum of the $Au_{68}(m\text{MBA})_{32}$ -sample in (**a**) IR/NIR-region, and in visible region (**b**). Black and green represent experimental and computational spectrum, and blue in fig. **a** is the experimental without the vibrational contribution of the *m*MBA ligand. From *Science*, 2014, 345, p. 909. Reprinted with permission from AAAS.

then removed by fitting a 5th degree polynomial function to the spectrum at points where there is no vibrational absorbance. The obtained spectrum of *m*MBA attached to gold is then removed from the IR-spectrum of Au_{68}-sample. After the procedure the known vibrational peaks at 2900–3600 cm^{-1} are reduced very close to the baseline, while the known electronic peaks are left unchanged. The unknown peak at 2500 cm^{-1} persists after the procedure, further reinforcing it's assignment as electronic transition. As the lowest electronic transition this peak energy of 2500 cm^{-1} (0.31 eV) is also the optical gap for the Au_{68}-cluster. The absorption spectrum in the visible region was measured from sample dissolved in H_2O. In the visible region (fig. 3.9b) of the absorption spectrum the onset of gold intraband $d-d$ transitions can be seen at 1.6 eV (750 nm),[62] but otherwise the spectrum is quite featureless.

The electronic transitions of the Au_{68}-cluster with the added ligand-layer consisting of 31, 32, or 34 ligands were calculated using LR-TDDFT with Perdew-Burke-Ernzerhof (PBE) exchange-correlation functional implemented in the GPAW-software package. For the calculations the *m*MBA ligands were exchanged to thiol-groups to reduce computational effort. The positions of the gold-atoms were taken from the single particle reconstruction. The calculated spectra in the IR/NIR-region are presented in fig. 3.12. Every spectrum gives three to five electronic absorption peaks below 7000 cm^{-1} (0.90 eV) with slightly different peak positions and intensities. Lowest optical gap of 2000 cm^{-1} (0.25 eV) is found for the $Au_{68}(SH)_{32}$ structure with -2 charge state, and the highest gap of 3900 cm^{-1} (0.48 eV) for the $Au_{68}(SH)_{31}$ ver.2 cluster. The best agreement with respect to the peak positions and intensities is given by the $Au_{68}(SH)_{32}$ -structure in neutral state, which gives good agreement with

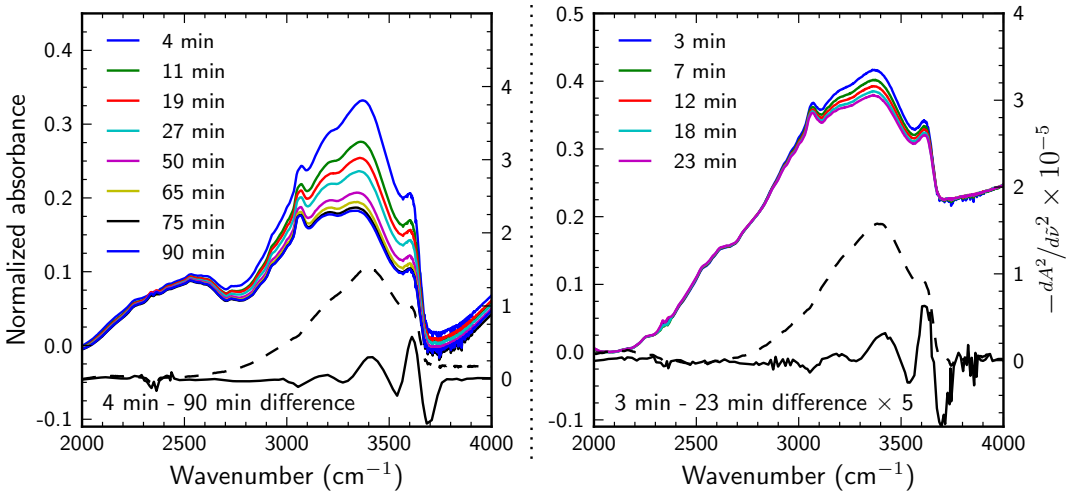

Figure 3.10: Evaporation of adsorbed H_2O from the Au68- (left) and larger *m*MBA-cluster (right) samples. From *Science*, 2014, 345, p. 909. Reprinted with permission from AAAS.

experimental peaks at 2500 cm^{-1}, 4200 cm^{-1}, 5250 cm^{-1}. The fourth peak is found at slightly higher energy at 6500 cm^{-1} than the experimental value of 6100 cm^{-1}. The computational spectrum gives a peak also at 3400 cm^{-1}, where a feature is observed also in the experimental spectrum. This region overlaps with the vibrational absorbance of water, and cannot be considered reliable. The second best agreement is given by the spectrum of the same structure with -2 charge, for which the peak at 6000 cm^{-1} gives better agreement. Other features including the too low optical gap and the absence of the peak at 4200 cm^{-1} leads us to select the neutral form of the proposed $Au_{68}(SH)_{32}$ structure as the best structure based on the spectroscopic evidence. It should be noted that due to the large amount of possible structures it is unlikely to find the exact conformation of the ligand layer without sampling unreasonable amount of model structures. Also, the models are constructed using thiol groups instead of the full *m*MBA molecule, so all intralayer ligand-ligand interactions, such as π–π stacking or hydrogen bonding which may stabilise the cluster, are absent. The optical gap of the $Au_{68}(m\text{MBA})_{32}$ is lower than expected, being slightly smaller than that of much larger $Au_{102}(p\text{MBA})_{44}$ (0.45 eV), and significantly smaller than the optical gap of almost identical size $Au_{67}(SR)_{35}$ -cluster (0.74 eV). The very small optical gap can be explained by the unsymmetric structure found in the clusters core, which causes splitting of the energy levels and lowers the HOMO-LUMO gap of the cluster.

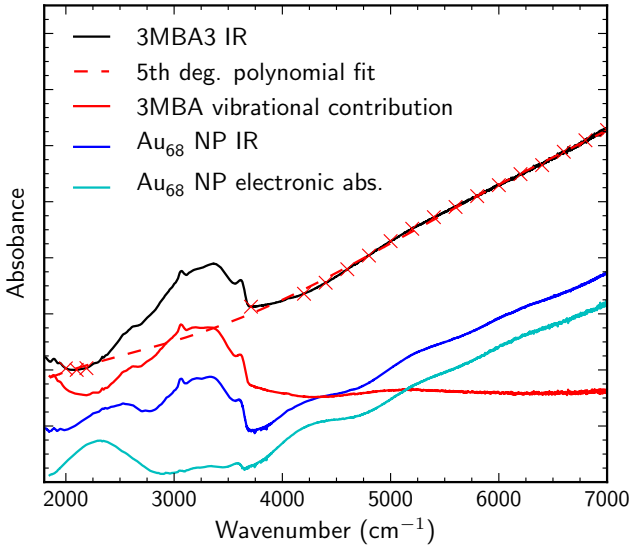

Figure 3.11: Removal of the features originating from the *m*MBA ligand vibrations. 5th. degree polynom is fitted to the spectrum of large *m*MBA particle which is then removed from the spectrum to give the vibrational spectrum. The vibrations of *m*MBA are then removed from the Au_{68} -spectrum to yield the electronic transitions. From *Science*, 2014, 345, p. 909. Reprinted with permission from AAAS.

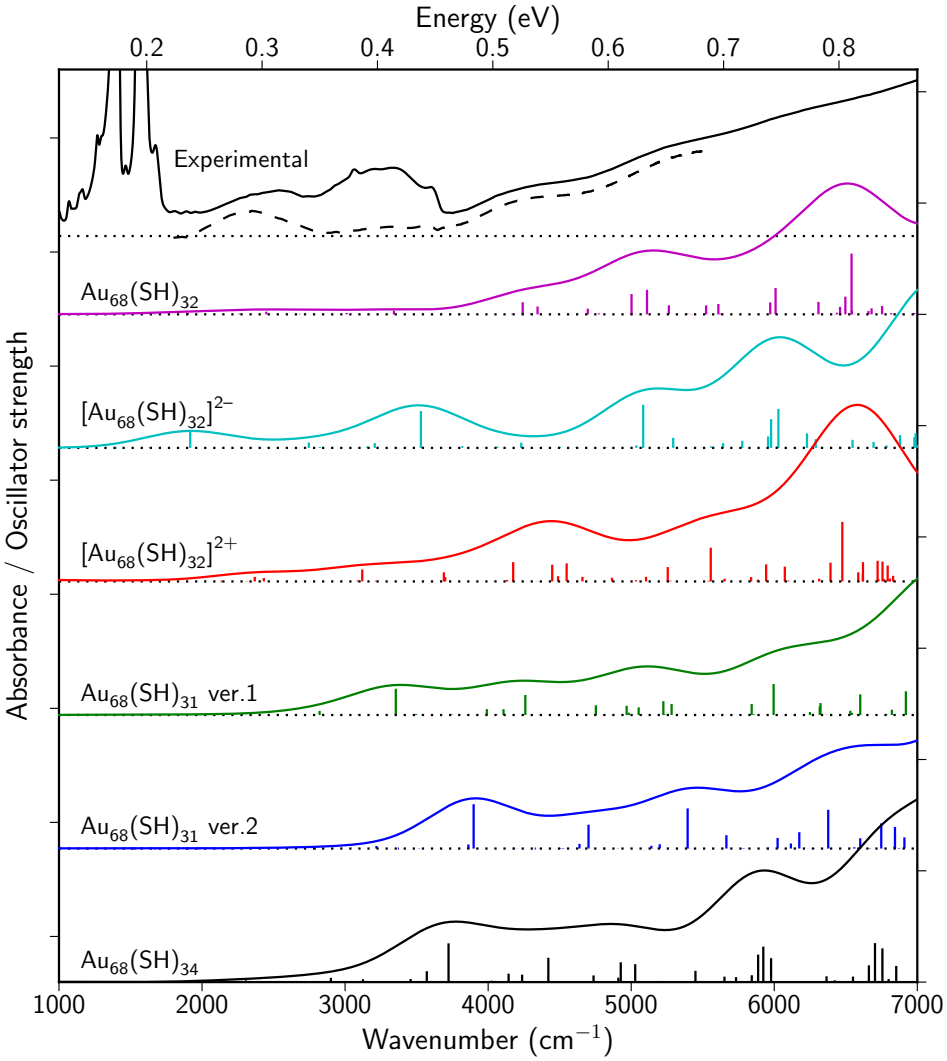

Figure 3.12: Computational spectra of the best proposed $Au_{68}(m\text{MBA})_{32}$-cluster structures. From *Science*, 2014, 345, p. 909. Reprinted with permission from AAAS.

3.3 Protonation states of $Au_{102}(p\text{MBA})_{44}$ cluster

The crystal structure of the water-soluble $Au_{102}(p\text{MBA})_{44}$-cluster shows the cluster as fully protonated species.[106] The *p*MBA-molecule, however, is only water-soluble in deprotonated state, meaning the cluster must also be in deprotonated form in solution.[74] Despite the importance of the ligands in the interactions with the surrounding medium, basic information of the protonation behaviour of the ligands in the $Au_{102}(p\text{MBA})_{44}$-cluster remained unknown. In paper **IV** we investigated the protonation states of the $Au_{102}(p\text{MBA})_{44}$-cluster using combination of acid-base-titration, IR-spectroscopy, and molecular dynamics simulations.

3.3.1 Vibrational signatures of protonated and deprotonated *p*MBA

Distinguishing the two different protonation states of the carboxylic acid group from IR-spectrum is trivial (fig. 3.13). The protonated acid exhibits a strong absorption at 1680–1800 cm^{-1} due to the stretching of the C=O double bond, while the deprotonated acid has two strong peaks at 1380–1410 cm^{-1} and 1520-1540 cm^{-1} for the symmetric and asymmetric stretching of the delocalized double bond of the $-CO_2^-$ group. The C–C stretching vibrations of the *para*-substituted benzene ring are observed between 1600–1390 cm^{-1} for both species. The spectrum of protonated *p*MBA is very similar after linking to the Au_{102} -cluster. This is also the case for the deprotonated *p*MBA, except for a blueshift of the carboxylate group vibrations in the spectrum of the $Au_{102}(p\text{MBA})_{44}$-cluster. This shift was attributed to lower degree of hydrogen bonding of the carboxylates in the cluster compared to the free *p*MBA, since in the cluster the neighbouring ligands perturb the environment. The vibrations observed in MeOD-d4 of D_2O-solutions are presented in table 3.4.

The IR-spectrum of $Au_{102}(p\text{MBA})_{44}$-cluster was measured in D_2O-solution at different pH (fig. 3.13B). The values given by the pH-meter for the D_2O-solutions were converted to the corresponding values in regular water using the equation $pH = 0.936pH^* + 0.412$.[136] At high pH the spectrum shows only the signatures of the deprotonated *p*MBA, but when the pH is lowered using DCl the protonated *p*MBA starts forming between pH 7.3 and 7.8. In neutral and slightly acidic conditions the cluster shows both protonation states of the *p*MBA-ligand. When the pH is lowered to acidic, the cluster precipitates out of the solution. At this point (pH $\approx$ 5 when $c \approx 1$ mmol/L) majority of the ligands are protonated, but a small fraction is still seen in deprotonated form.

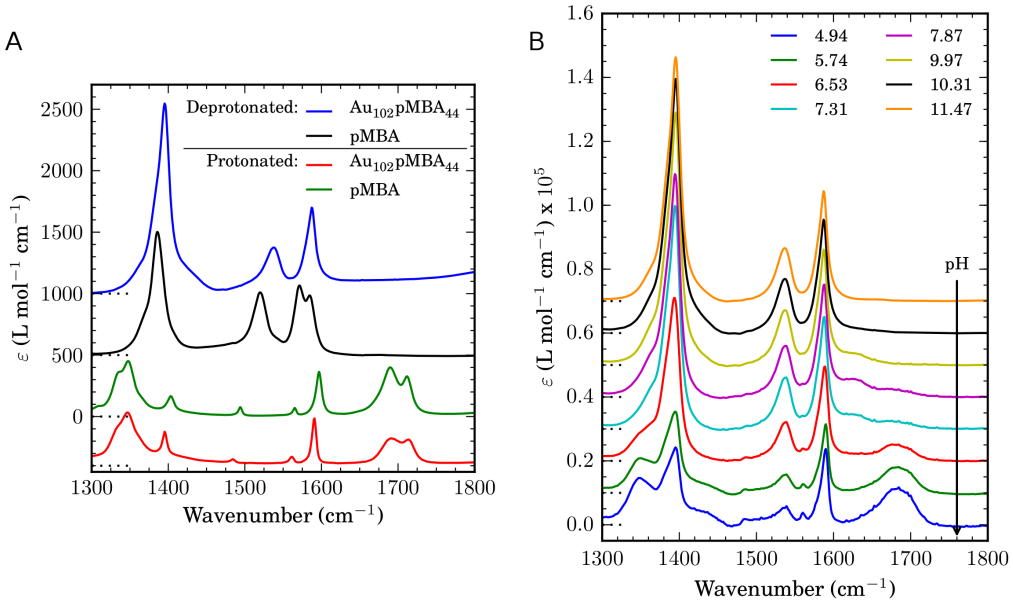

Figure 3.13: **A**: IR-spectrum of free pMBA molecule and $Au_{102}(pMBA)_{44}$-cluster in protonated and deprotonated forms. **B**: IR-spectrum of $Au_{102}(pMBA)_{44}$-cluster at different pH.

3.3.2 Titration curves of $Au_{102}(pMBA)_{44}$

The pK_a of the ligands was investigated by standard acid-base titration of $Au_{102}(pMBA)_{44}$ solution, and analyzing the amount of protonated and deprotonated pMBA from the IR-spectra measured at different pH.

The acid-base titration of $Au_{102}(pMBA)_{44}$ was done in pure water and in 50% methanol-solution to reduce the precipitation at low pH observed in pure water. In both solvents we get a titration curve which can be interpreted as anti-cooperative titration of monoprotic weak acid. The titration curves were fitted using eq. 2.20 to extract the pK_a and Hill coefficient n. The curve shows single equivalence point and single pK_a point at 6.18 ± 0.05 in H_2O and 7.19 ± 0.07 in 50% MeOH. In both cases the protonation behaviour is strongly anti-cooperative (H_2O: $n = 0.63 \pm 0.04$, 50% MeOH: $m = 0.53 \pm 0.03$).

The standard acid-base titration can only resolve different pK_a points which are approximately 2.0 units apart from each other, or the solvent autoionization constant. Therefore we also analyzed the protonation state of the cluster from the IR-spectra. The analysis was performed as follows. Consider two peaks a and b corresponding with two different species in the same system. The absorbance of the peaks are given by

Table 3.4: Observed vibrations of protonated and deprotonated *p*MBA.

	Protonated		**Deprotonated**	
	Exp. in MeOD-d4		**Exp. in D_2O**	
Assignment	Sol.[a]	Au_{102}[b]	Sol.[a]	Au_{102}[b]
C=O str.	1712.4 vs	1713.9 vs	–	–
	1690.0 vs	1691.0 vs	–	–
-CO_2^- as. str.	–	–	1520.3 s	1538.2 s
-CO_2^- s. str.	–	–	1386.1 s	1395.7 s
9a/$\mathscr{M}_4$	1597.0 s	1590.7 s	1584.9 s	1587.7 s
9b/$\mathscr{M}_{23}$	1565.3 m	1561.6 m	1571.4 s	1581.6 m,sh
18a/$\mathscr{M}_5$	1494.2 m	1485.2 m	1483.3 w	*N.O.*
18b/$\mathscr{M}_{24}$	1403.7 m	1395.5 m	1384.0 m	1384.9 m
OH-wag	~1350[c]	~1350[c]	–	–

vs: very strong, s: strong, m: medium, w: weak, sh: shoulder.
[a] Free *p*MBA solvated in MeOD-d4 or D_2O.
[b] $Au_{102}(p\text{MBA})_{44}$ cluster solvated in MeOD-d4 or D_2O.
[c] Several peaks in 1300 – 1370 cm^{-1} due to HDO impurity and H-bonding.
N.O.: Not observed.

Beer-Lambert law

$$A_a = \varepsilon_a C_a l \tag{3.1}$$

$$A_b = \varepsilon_b C_b l \tag{3.2}$$

If a and b correspond with protonated and deprotonated ligands, we can write the cluster concentration and the amount of ligands using these concentrations.

$$C_{\mathrm{Au_{102}}} = \frac{C_a + C_b}{44} \tag{3.3}$$

$$N_a = \frac{C_a}{C_{\mathrm{Au_{102}}}} = \frac{44 C_a}{C_a + C_b} \tag{3.4}$$

$$N_b = \frac{C_b}{C_{\mathrm{Au_{102}}}} = \frac{44 C_b}{C_a + C_b} \tag{3.5}$$

Since the optical path length is constant for both peaks, the ratio of absorbance depends on the concentrations C_a and C_b and the absorbance coefficients ε_a and ε_b

$$\frac{A_a}{A_b} = \frac{\varepsilon_a c_a \cancel{l}}{\varepsilon_b c_b \cancel{l}} = \alpha \frac{c_a}{c_b} \tag{3.6}$$

where the ratio of absorbance coefficients is $\alpha = \varepsilon_a/\varepsilon_b$. By substituting eq. 3.6 into eqs. 3.4 and 3.5 we get

$$N_a = \frac{44C_a}{C_a + \alpha C_a \frac{A_b}{A_a}} = \frac{44\cancel{C_a}}{\cancel{C_a}(1 + \alpha \frac{A_b}{A_a})} = \frac{44}{1 + \alpha \frac{A_b}{A_a}} \tag{3.7}$$

$$N_b = \frac{44C_b}{\frac{C_b A_a}{\alpha A_b} + C_b} = \frac{44\cancel{C_b}}{\cancel{C_b}(\frac{A_a}{\alpha A_b} + 1)} = \frac{44}{1 + \frac{A_a}{\alpha A_b}} \tag{3.8}$$

This way we need accurate concentration data only to determine the ratio of two peaks from the spectra of protonated and deprotonated forms, not for every measured IR-spectra. Here we chose the asymmetric stretching and carbonyl stretching peaks for deprotonated and protonated peaks. The area of the carbonyl peak was determined by fitting of the peak with gaussian function. For the asymmetric stretching peak the fitting procedure overestimated the peak area due to variation of the baseline. Instead the area was numerically integrated after baseline removal. The amount of protonated ligands of four different measurement sets at different pH given by the above equations are presented in fig. 3.14. The results were fitted with eq. 2.20 as earlier, giving $\mathrm{pK_a} = 5.98 \pm 0.13$ and $n = 0.78 \pm 0.14$. The obtained values are within errors the same as obtained from regular titration, but the values from regular titrations are taken as more reliable due to more repetitions and less noise in the measured data. From the IR-titration curve we can see that the last ligands deprotonate around pH 7.5 – 8.0. At pH 5 where the cluster starts precipitating, approximately fifth of the ligands are still deprotonated, indicating the minimum amount necessary for water-solubility. The IR-spectra were also measured in solid-state by drying the sample from solutions at different pH. The acquired spectra follows the trend seen in the solvent-state IR, indicating the protonation state of the cluster in the solution is preserved when the sample is dried. In addition, during the measurements the samples which were dried from pH below 6 did not redissolve in neutral water without the addition of base. We speculate that at this point, corresponding with less than half of the ligand-layer in deprotonated state, the hydrophobic interactions start to dominate and while the cluster stays in solution, it is no longer truly water-soluble.

3.3.3 Distribution of deprotonated ligands at equilibrium

Since the 22 (44) different protonations cannot be resolved in the experimental data, it is very challenging if not impossible to determine the $\mathrm{pK_a}$ of individual ligands experimentally. Instead, we modeled the $Au_{102}(p\text{MBA})_{44}$-cluster using constant pH molecular dynamics using GROMACS -software package,[137–141] near the experimental $\mathrm{pK_a}$ (6.20) in order to get information of the preferred protonation states of the different ligands. The simulation models the protonation via λ-dynamics approach[142,143] in which the existance of the proton is described with additional degree of freedom λ

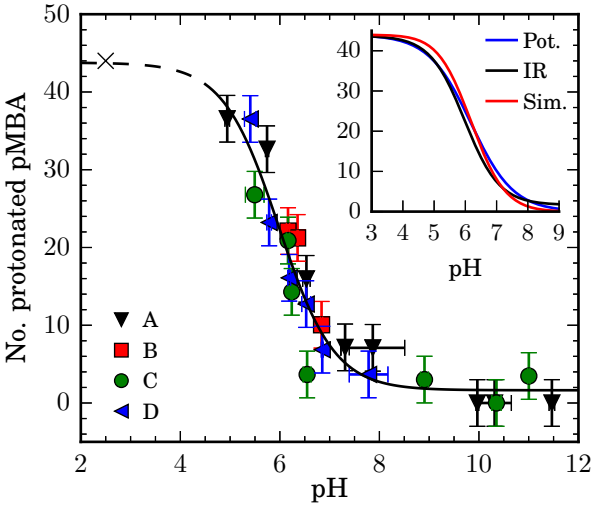

Figure 3.14: IR-titration curve of the $Au_{102}(p\text{MBA})_{44}$-cluster. A, B, C, and D refer to different measurement sets. Additionally, the fully protonated form at pH 2.5 from the XRD-data is plotted. Inset shows the potentiometric-, IR-, and simulated titration curves.

($\lambda = 0$: protonated, $\lambda = 1$: deprotonated). The number of protons in the system was fixed into 22, forcing the system to sample the case pH = pK_a, to prevent charge fluctuations in the system.[144]

The individual pK_a's of the ligands were estimated from the free energy of the deprotonation

$$\Delta G^i = -RT \ln[\frac{p^i_{A^-}}{p^i_{AH}}] + RT \ln 10 \text{pH} \tag{3.9}$$

where the propabilities of being protonated ($p^i_{A^-}$) or deprotonated (p^i_{HA}) calculated as the time-average of the λ-values ($p^i_{A^-} = \langle\lambda_i\rangle$, $p^i_{AH} = \langle 1 - \lambda_i\rangle$). The final pK_a values are then given by

$$pK^i_a = \frac{1}{\ln 10 RT} \Delta G^i \tag{3.10}$$

where R is the molar gas constant, and T is the temperature.

Simulations at pH 6.20 from 32 different starting configurations, differing in the initial λ values, were performed up to 2.5 ns. Each simulation converges towards qualitatively similar pattern of protonated and deprotonated ligands (fig. 3.15), suggesting the cluster has a preferred protonation distribution at pH 6.20. The mean λ values calculated from all 32 simulations are presented in table 3.5 along with the pK_a shift, the actual pK_a, and the number of protonation transitions during the simulation. The λ and pK_a values are also illustrated on the cluster model in fig. 3.16. The ligands are numbered according to the scheme by Salorinne *et.al.*,[145] which labels the 22 symmetry

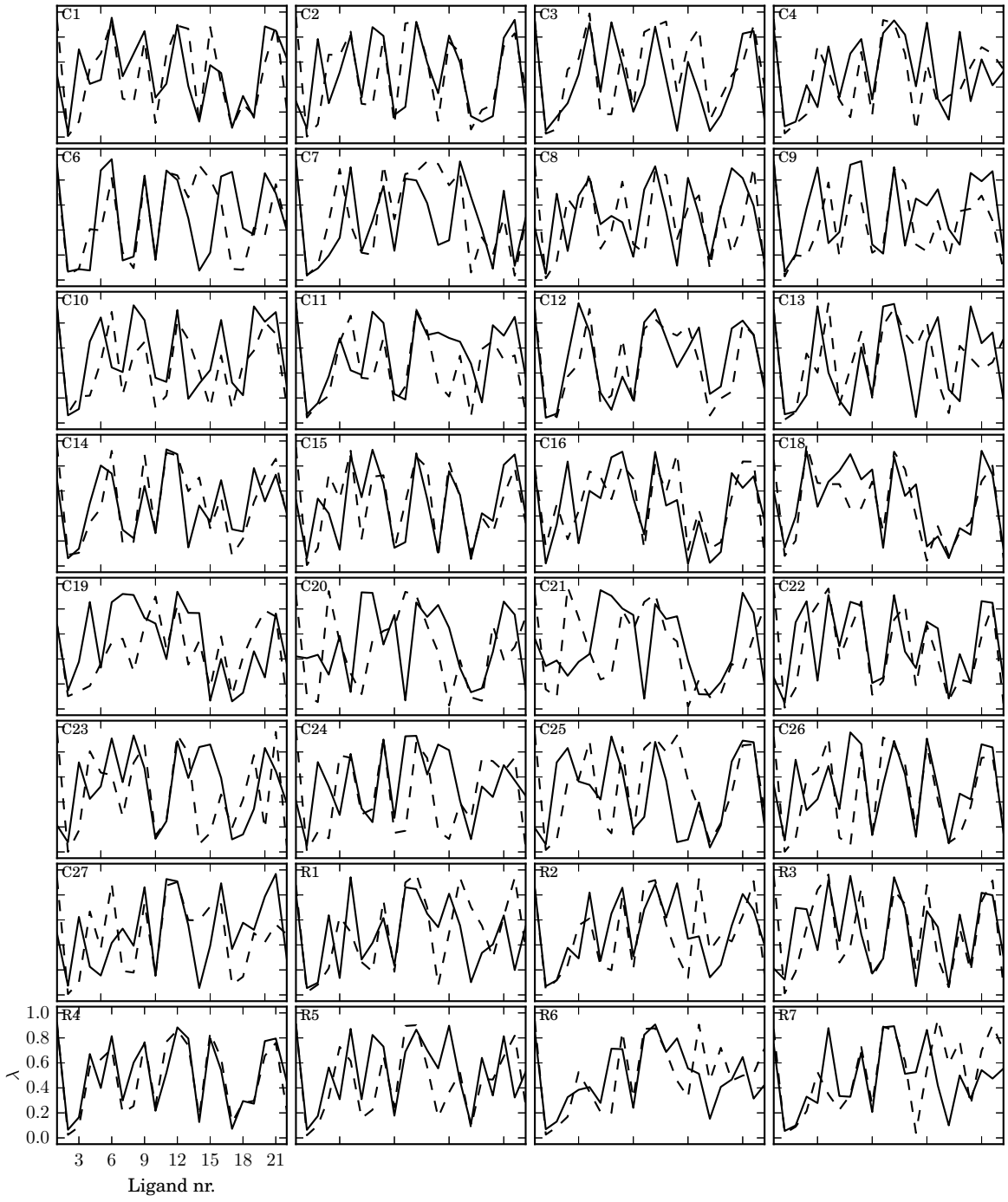

Figure 3.15: Average λ-values of individual ligands after 2.5 ns simulation for 32 different initial distributions of λ-values. is shown by the dots. Solid and dashed lines refer to both symmetry related halves of the ligands, with solid line being for ligands 1–22 and dashed for 1*–22*.

independent ligands based on their NMR-shifts (fig. 3.17). One half of the ligands are numbered 1–22, and the other half 1*–22*, 1* being the C_2 related pair of ligand 1 etc..

Ligands which are related by the C_2-symmetry of the cluster have similar λ and pK_a, indicating the simulation models the intrisic symmetry of the cluster. The ligands show a distinct preference towards adopting either the protonated, deprotonated, or neither state, depending on their positions on the cluster (fig. 3.16). Therefore, at the simulation pH 6.20, a non-uniform surface charge distribution of neutral and negative patches develop on the cluster. The standard deviation of the lambda values $\Delta\lambda_{avg} = 0.19$ is quite high, due to the short simulation time of 2.5 ns per run. This can be improved by increasing the simulation time, for example, smaller dataset simulated up to 8 ns gives $\Delta\lambda_{avg} = 0.10$. Ligands at both poles of the C_5 -axis of the core, which are related by the main C_2 symmetry, prefer the deprotonated state (fig. 3.16A). The poles of the C_2 axis show different protonation states, with one end adapting weakly deprotonated state (fig. 3.16B) and the other end adapting strongly protonated state (fig. 3.16C). The individual pK_a's of the ligands are in the range 5.18 – 7.58, all of which are higher than the reference pK_a (4.16) of free *p*MBA. The increase in pK_a can be explained by considering the change in the *p*MBA environment when attached to the cluster surface. Hydrogen bonding to the carboxylate group stabilizes the deprotonated form, lowering the pK_a, and in the simulations the average number of hydrogen bonds to the carboxylate drops from 4.1 in free *p*MBA to 3.6 in the cluster, in line with the observed blueshift in IR-spectrum. It is also assumed that the repulsive interactions between deprotonated ligands contribute to the lowering of the pK_a. If the pK_a's are assumed to be independent of pH, we get macroscopic $pK_a = 6.20$, in good agreement with the experimental values, and Hill-coefficient of 0.82. The simulated Hill-coefficient is sligtly larger than the value obtained from the potentiometric titration, but within the error of the value obtained from IR-titration.

Table 3.5: Protonation state λ_{avg}(mean), pK_a shift and pK_a, and number of transitions in the MD simulations.

Ligand	λ_{avg}(mean)	ΔpK_a [a]	pK_a [b]	$N_{\text{trans.}}$
1/1*	$0.91 \pm 0.06/0.67 \pm 0.25$	-1.01/-0.32	5.18/5.88	125/249
2/2*	$0.09 \pm 0.08/0.04 \pm 0.04$	1.03/1.38	7.23/7.58	118/64
3/3*	$0.13 \pm 0.08/0.34 \pm 0.26$	0.83/0.30	7.04/6.50	165/266
4/4*	$0.45 \pm 0.25/0.48 \pm 0.22$	0.09/0.04	6.29/6.24	364/332
5/5*	$0.60 \pm 0.14/0.44 \pm 0.24$	-0.17/0.10	6.03/6.30	339/277
6/6*	$0.71 \pm 0.21/0.73 \pm 0.22$	-0.38/-0.42	5.82/5.78	259/192
7/7*	$0.26 \pm 0.14/0.41 \pm 0.20$	0.45/0.16	6.65/6.36	430/437
8/8*	$0.32 \pm 0.18/0.67 \pm 0.29$	0.33/-0.31	6.53/5.89	304/193
9/9*	$0.76 \pm 0.10/0.72 \pm 0.14$	-0.50/-0.41	5.70/5.79	261/232
10/10*	$0.28 \pm 0.19/0.27 \pm 0.21$	0.41/0.44	6.61/6.64	327/337
11/11*	$0.67 \pm 0.29/0.55 \pm 0.30$	-0.31/-0.09	5.89/6.11	243/261
12/12*	$0.88 \pm 0.05/0.89 \pm 0.04$	-0.87/-0.91	5.33/5.29	183/162
13/13*	$0.70 \pm 0.12/0.59 \pm 0.16$	-0.36/-0.16	5.84/6.04	330/318
14/14*	$0.43 \pm 0.29/0.35 \pm 0.28$	0.12/0.26	6.32/6.46	233/177
15/15*	$0.49 \pm 0.30/0.60 \pm 0.26$	0.02/-0.18	6.22/6.02	271/242
16/16*	$0.59 \pm 0.21/0.54 \pm 0.19$	-0.15/-0.07	6.05/6.13	315/337
17/17*	$0.19 \pm 0.16/0.18 \pm 0.19$	0.62/0.67	6.82/6.87	197/174
18/18*	$0.40 \pm 0.20/0.36 \pm 0.18$	0.17/0.25	6.37/6.45	272/292
19/19*	$0.41 \pm 0.17/0.46 \pm 0.24$	0.16/0.08	6.36/6.28	354/320
20/20*	$0.75 \pm 0.14/0.61 \pm 0.16$	-0.47/-0.20	5.72/6.00	288/326
21/21*	$0.66 \pm 0.21/0.75 \pm 0.19$	-0.29/-0.48	5.91/5.72	251/238
22/22*	$0.36 \pm 0.14/0.32 \pm 0.23$	0.24/0.32	6.45/6.52	409/291

[a] pK_a shift with respect to the center pK_a 6.20.
[b] $6.20 + \Delta pK_a$.

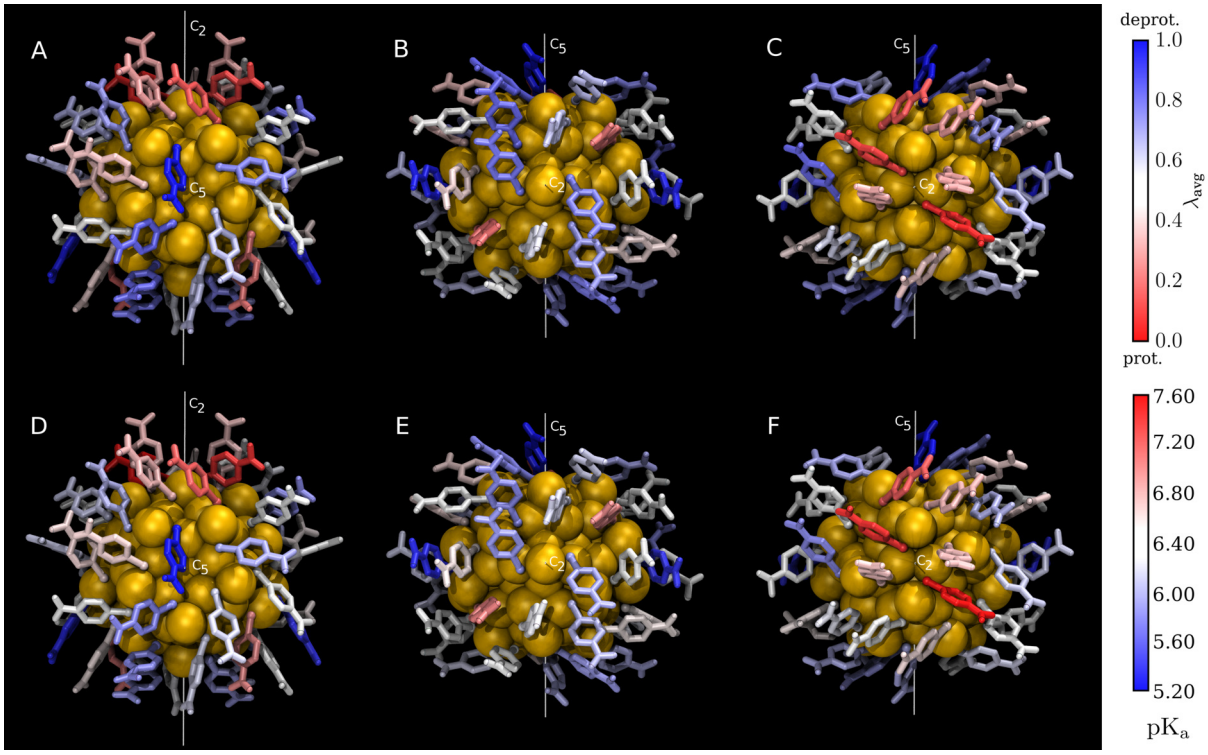

Figure 3.16: Mean λ_{avg} -values of the 44 ligands from constant pH MD at pH 6.20. **A**: Viewed through the C_5 axis of the core. **B**: Same as **A** viewed through the C_2 axis. **C**: Same as **B** from the other end of the C_2 axis. **D, E, F**: Same as **A, B**, and **C** with the pK_a -values of the 44 ligands.

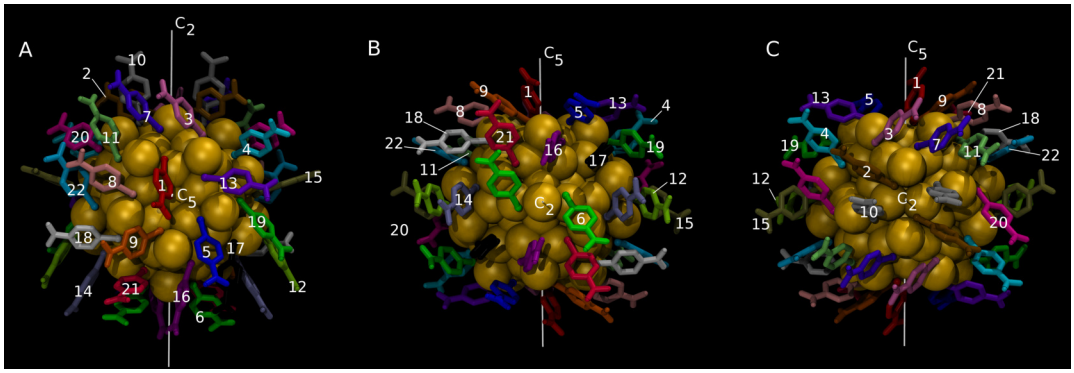

Figure 3.17: Ligand labeling scheme of $Au_{102}(p\text{MBA})_{44}$. Viewed along the same axes as in fig. 3.16

4 Conclusions

Optical gap of $Au_{144}(PET)_{60}$ cluster (2200 cm^{-1}, 0.27 eV) and silver doped derivatives (1000–2100 cm^{-1}, 0.12–0.26 eV) were determined using FTIR-spectroscopy. The silver-doping introduced only minor changes in the optical gap region of the cluster. When measuring the optical gap in IR-region, spectra in solution state or single crystals should be preferred over dropcast films.

The of $Au_{144}(PET)_{60}$ cluster single crystals were found to exhibit significant inhomogeneous broadening in the peaks attributed to the vibrations of the PET-ligands. The broadening of the peaks was explained by inhomogeneous packing of the ligands in the crystal, *i.e.* the ligands do not form well ordered structures due to the large size of the cluster core compared to the ligands, and lack of coordinating interactions between the PET molecules. We believe changing the ligand from PET into more rigid and coordinating ligand might yield better long-range order in the crystals.

The core-structure of water-soluble $Au_{68}(m\text{MBA})_{32}$ -cluster was determined using combination of TEM single-particle reconstruction, IR-spectroscopy, and DFT-calculations. IR- and optical spectra of the cluster were measured, and the resulting spectra compared with the calculated spectra of cluster models based on the experimental Au-atom positions. Good agreement in both the optical gap (2500 cm^{-1}, 0.31 eV) and the first electronic transitions in the IR-region were found for the model. The optical gap is smaller than expected for the small size, but can be explained by the low symmetry structure of the cluster core. The obtained low symmetry strcuture is peculiar compared to the highly symmetric structures of other known gold clusters, and it indicates that clusters do not need to adapt symmetric geometrical structures in order to be stable.

The macroscopic pK_a 6.18 of the $Au_{102}(p\text{MBA})_{44}$ cluster was measured using acid-base and IR-titration, *ca.* 2 units higher than the free *p*MBA molecule. This pK_a shift is explained by decrease of hydrogen bonding of the carboxylate group in the cluster compared to the free *p*MBA. The solubility of the cluster depends on the protonation state of the cluster, with the cluster being soluble in methanol in fully protonated state, and water-soluble if more than one quarter of the ligands are deprotonated. The protonation behaviour was measured to be $Au_{102}(p\text{MBA})_{44}$ anti-cooperative. Molecular dynamics simulations at pH 6.20 revealed the individual pK_a's of the ligads to be in the range 5.18–7.58, depending on the position, which leads into an non-uniform charge distribution on the cluster surface. As the charge distribution governs the interactions

of the particles with the solvent, it may also be possible to fine-tune the surface charge distribution using ligand-exchange and pH of the solution.

References

[1] D. R. Lide (ed.), *CRC Handbook of Chemistry and Physics*, CRC Press, Boca Raton, FL, **2005**.

[2] D. Tout-Smith, "Gold Nugget 'Welcome Stranger' (1869) in Museum Victoria Collections", **2010**.

[3] A. Klemm, G. Hartmann, and L. Lange, "Sodium and Sodium Alloys", in *Ullmann's Encyclopedia of Industrial Chemistry*, Wiley-VCH Verlag GmbH & Co. KGaA, **2000**, ISBN 9783527306732.

[4] C. Louis and O. Pluchery, *Gold Nanoparticles for Physics, Chemistry and Biology*, Imperial College Press, 1st ed., **2012**, ISBN 978-1-84816-806-0.

[5] W. Weyl, *Coloured Glasses*, The Society of Glass Technology, **1951**.

[6] G. L. Hornyak, C. J. Patrissi, E. B. Oberhauser, C. R. Martin, J.-C. Valmalette, L. Lemaire, J. Dutta, and H. Hofmann, "Effective medium theory characterization of Au/Ag nanoalloy-porous alumina composites", *Nanostructured Materials*, *9*(1–8), **1997**, pp. 571.

[7] M. Faraday, "The Bakerian Lecture: Experimental Relations of Gold (and Other Metals) to Light", *Philosophical Transactions of the Royal Society of London*, *147*, **1857**, pp. 145.

[8] U. Kreibig and M. Vollmer, *Optical Properties of Metal Clusters*, Springer-Verlag, **1995**, ISBN 3-540-57836-6.

[9] W. D. Knight, K. Clemenger, W. A. de Heer, W. A. Saunders, M. Y. Chou, and M. L. Cohen, "Electronic Shell Structure and Abundances of Sodium Clusters", *Physical Review Letters*, *52*(24), **1984**, pp. 2141.

[10] W. A. de Heer, "The physics of simple metal clusters: experimental aspects and simple models", *Reviews of Modern Physics*, *65*(3), **1993**, p. 611.

[11] S. M. Morton, D. W. Silverstein, and L. Jensen, "Theoretical Studies of Plasmonics using Electronic Structure Methods", *Chemical reviews*, *111*(6), **2011**, pp. 3962.

[12] W. A. de Heer, K. Selby, V. Kresin, J. Masui, M. Vollmer, A. Chatelain, and W. D. Knight, "Collective dipole oscillations in small sodium clusters", *Physical Review Letters*, *59*(16), **1987**, pp. 1805.

[13] S. Fedrigo, W. Harbich, and J. Buttet, "Collective dipole oscillations in small silver clusters embedded in rare-gas matrices", *Physical Review B*, *47*(16), **1993**, pp. 10706.

[14] S. Fedrigo, W. Harbich, J. Belyaev, and J. Buttet, "Evidence for electronic shell structure of small silver clusters in the optical absorption spectra", *Chemical Physics Letters*, *211*(2), **1993**, pp. 166.

[15] K. Selby, M. Vollmer, J. Masui, V. Kresin, W. A. de Heer, and W. D. Knight, "Surface plasma resonances in free metal clusters", *Physical Review B*, *40*(8), **1989**, p. 5417.

[16] P. Gruene, D. M. Rayner, B. Redlich, A. F. G. van der Meer, J. T. Lyon, G. Meijer, and A. Fielicke, "Structures of Neutral Au_7, Au_{19}, and Au_{20} Clusters in the Gas Phase", *Science*, *321*(5889), **2008**, pp. 674.

[17] A. Fielicke, A. Kirilyuk, C. Ratsch, J. Behler, M. Scheffler, G. von Helden, and G. Meijer, "Structure Determination of Isolated Metal Clusters via Far-Infrared Spectroscopy", *Physical Review Letters*, *93*(2), **2004**, p. 23401.

[18] A. Fielicke, C. Ratsch, G. von Helden, and G. Meijer, "Isomer selective infrared spectroscopy of neutral metal clusters", *The Journal of chemical physics*, *122*(9), **2005**, p. 91105.

[19] R. W. Murray, "Nanoelectrochemistry: Metal Nanoparticles, Nanoelectrodes, and Nanopores", *Chemical reviews*, *108*(7), **2008**, pp. 2688.

[20] T. Laaksonen, V. Ruiz, P. Liljeroth, and B. M. Quinn, "Quantised charging of monolayer-protected nanoparticles", *Chemical Society Reviews*, *37*(9), **2008**, pp. 1836.

[21] D. Reinhard, B. D. Hall, D. Ugarte, and R. Monot, "Size-independent fcc-to-icosahedral structural transition in unsupported silver clusters: An electron diffraction study of clusters produced by inert-gas aggregation", *Physical Review B*, *55*(12), **1997**, pp. 7868.

[22] S. Mustalahti, P. Myllyperkiö, T. Lahtinen, S. Malola, K. Salorinne, T.-R. Tero, J. Koivisto, H. Häkkinen, and M. Pettersson, "Photodynamics of a Molecular Water-Soluble Nanocluster Identified as $Au_{130}(p\text{MBA})_{50}$", *Journal of Physical Chemistry C*, *119*(34), **2015**, pp. 20224.

[23] S. Mustalahti, P. Myllyperkiö, T. Lahtinen, K. Salorinne, S. Malola, J. Koivisto, H. Häkkinen, and M. Pettersson, "Ultrafast Electronic Relaxation and Vibrational Cooling Dynamics of $Au_{144}(SC_2H_4Ph)_{60}$ Nanocluster Probed by Transient Mid-IR Spectroscopy", *The Journal of Physical Chemistry C*, *118*(31), **2014**, pp. 18233.

[24] C. Yi, M. A. Tofanelli, C. J. Ackerson, and K. L. Knappenberger, "Optical properties and electronic energy relaxation of metallic $Au_{144}(SR)_{60}$ nanoclusters.", *Journal of the American Chemical Society*, *135*(48), **2013**, pp. 18222.

[25] C. Yi, H. Zheng, L. M. Tvedte, C. J. Ackerson, and K. L. Knappenberger Jr., "Nanometals: Identifying the Onset of Metallic Relaxation Dynamics in Mono layer-Protected Gold Clusters Using Femtosecond Spectroscopy", *Journal of Physical Chemistry C*, *119*(11), **2015**, pp. 6307.

[26] J. F. Hicks, D. T. Miles, and R. W. Murray, "Quantized Double-Layer Charging of Highly Monodisperse Metal Nanoparticles", *Journal of the American Chemical Society*, *124*(44), **2002**, pp. 13322.

[27] Y. Negishi, T. Nakazaki, S. Malola, S. Takano, Y. Niihori, W. Kurashige, S. Yamazoe, T. Tsukuda, and H. Häkkinen, "A Critical Size for Emergence of Nonbulk Electronic and Geometric Structures in Dodecanethiolate-Protected Au Clusters", *Journal of the American Chemical Society*, *137*(3), **2015**, pp. 1206.

[28] S. Malola, L. Lehtovaara, J. Enkovaara, and H. Häkkinen, "Birth of the Localized Surface Plasmon Resonance in Monolayer-Protected Gold Nanoclusters", *ACS Nano*, **2013**.

[29] F. Michael D, *Elements of Quantum Mechanics*, Oxford University Press, **2001**, ISBN 978-0195141955.

[30] P. Atkins and J. De Paula, *Physical Chemistry*, Oxford University Press, 8th ed., **2006**, ISBN 9780198700722.

[31] R. Jin, "Quantum sized, thiolate-protected gold nanoclusters", *Nanoscale*, *2*(3), **2010**, pp. 343.

[32] G. Mie, "Beiträge zur Optik trüber Medien, speziell kolloidaler Metallösungen", *Annalen der Physik*, *330*(3), **1908**, pp. 377.

[33] C. Kittel and H. Kroemer, *Thermal Physics*, W.H.Freeman, **1980**, ISBN 0716710889.

[34] D. A. Neamen, *Semiconductor physics and devices: Basic Principles*, McGraw Hill, 3rd ed., **2003**, ISBN 0-07-232107-5.

[35] R. L. Johnston, *Atomic and Molecular Clusters*, Taylor & Francis, 1st ed., **2002**, ISBN 0-748-40930-0.

[36] J. M. Hollas, *Modern Spectroscopy*, Wiley Interscience, 4th ed., **2008**, ISBN 978-0-470-84416-8.

[37] M. Brack, "The physics of simple metal clusters: self-consistent jellium model and semiclassical approaches", *Reviews of Modern Physics*, *65*(3), **1993**, pp. 677.

[38] M. Walter, J. Akola, O. Lopez-Acevedo, P. D. Jadzinsky, G. Calero, C. J. Ackerson, R. L. Whetten, H. Grönbeck, and H. Häkkinen, "A unified view of ligand-protected gold clusters as superatom complexes", *Proceedings of the National Academy of Sciences*, *105*(27), **2008**, pp. 9157.

[39] M. G. Mayer and J. Jensen, "Elementary Theory of Nuclear Shell Structure", *Angewandte Chemie*, *68*(10), **1956**, p. 360.

[40] S. M. Reimann, M. Brack, and K. Hansen, "Modified Nilsson model for large sodium clusters", **1993**.

[41] K. Clemenger, "Ellipsoidal shell structure in free-electron metal clusters", *Phys.Rev.B*, *32*(2), **1985**, pp. 1359.

[42] J. U. Reveles, S. N. Khanna, P. J. Roach, and A. W. Castleman, "Multiple valence superatoms", *Proceedings of the National Academy of Sciences*, *103*(49), **2006**, pp. 18405.

[43] M. A. Tofanelli and C. J. Ackerson, "Superatom Electron Configuration Predicts Thermal Stability of $Au_{25}(SR)_{18}$ Nanoclusters", *Journal of the American Chemical Society*, *134*(41), **2012**, pp. 16937.

[44] K. H. Kuo, "Mackay, Anti-Mackay, Double-Mackay, Pseudo-Mackay, and Related Icosahedral Shell Clusters", *Structural Chemistry*, *13*(3-4), **2002**, pp. 221.

[45] A. L. Mackay, "A dense non-crystallographic packing of equal spheres", *Acta Crystallographica*, *15*(9), **1962**, pp. 916.

[46] A. S. Barnard and L. A. Curtiss, "Predicting the Shape and Structure of Face-Centered Cubic Gold Nanocrystals Smaller than 3 nm", *ChemPhysChem*, *7*(7), **2006**, pp. 1544.

[47] L. D. Marks, "Experimental studies of small particle structures", *Reports on Progress in Physics*, *57*(6), **1994**, p. 603.

[48] T. Tsukuda and H. Häkkinen, *Protected Metal Clusters: From Fundamentals to Applications*, Elsevier, **2015**.

[49] H. Häkkinen and M. Manninen, "How "Magic" is a Magic Metal Cluster?", *Physical Review Letters*, *76*(10), **1996**, p. 1599.

[50] H. Häkkinen, M. Walter, and H. Grönbeck, "Divide and Protect: Capping Gold Nanoclusters with Molecular Gold–Thiolate Rings", *The Journal of Physical Chemistry B*, *110*(20), **2006**, pp. 9927.

[51] J. Turkevich, P. C. Stevenson, and J. Hillier, "A study of the nucleation and growth processes in the synthesis of colloidal gold", *Discussions of the Faraday Society*, *11*, **1951**, pp. 55.

[52] J. Kimling, M. Maier, B. Okenve, V. Kotaidis, H. Ballot, and A. Plech, "Turkevich Method for Gold Nanoparticle Synthesis Revisited", *The Journal of Physical Chemistry B*, *110*(32), **2006**, pp. 15700.

[53] H. Häkkinen, "The gold-sulfur interface at the nanoscale", *Nature Chemistry*, *4*(6), **2012**, pp. 443.

[54] L. C. McKenzie, T. O. Zaikova, and J. E. Hutchison, "Structurally similar triphenylphosphine-stabilized undecagolds, $Au_{11}(PPh_3)_7Cl_3$ and $[Au_{11}(PPh_3)_8Cl_2]Cl$, exhibit distinct ligand exchange pathways with glutathione.", *Journal of the American Chemical Society*, *136*(38), **2014**, pp. 13426.

[55] Y. Negishi, W. Kurashige, and U. Kamimura, "Isolation and Structural Characterization of an Octaneselenolate-Protected Au_{25} Cluster", *Langmuir*, *27*(20), **2011**, pp. 12289.

[56] M. Brust, M. Walker, D. Bethell, D. J. Schiffrin, and R. Whyman, "Synthesis of thiol-derivatised gold nanoparticles in a two-phase Liquid-Liquid system", *Journal of the Chemical Society, Chemical Communications*, (7), **1994**, pp. 801.

[57] M. Brust, J. Fink, D. Bethell, D. J. Schiffrin, and C. Kiely, "Synthesis and reactions of functionalised gold nanoparticles", *Journal of the Chemical Society, Chemical Communications*, (16), **1995**, pp. 1655.

[58] M. M. Alvarez, J. T. Khoury, T. G. Schaaff, M. N. Shafigullin, I. Vezmar, and R. L. Whetten, "Optical Absorption Spectra of Nanocrystal Gold Molecules", *The Journal of Physical Chemistry B*, *101*(19), **1997**, pp. 3706.

[59] T. G. Schaaff, M. N. Shafigullin, J. T. Khoury, I. Vezmar, R. L. Whetten, W. G. Cullen, P. N. First, C. Gutierrez-Wing, J. Ascensio, and M. Jose-Yacaman, "Isolation of Smaller Nanocrystal Au Molecules: Robust Quantum Effects in Optical Spectra", *The Journal of Physical Chemistry B*, *101*(40), **1997**, pp. 7885.

[60] C. M. Aikens, "Effects of Core Distances, Solvent, Ligand, and Level of Theory on the TDDFT Optical Absorption Spectrum of the Thiolate-Protected Au_{25} Nanoparticle", *The Journal of Physical Chemistry A*, *113*(40), **2009**, pp. 10811.

[61] M. Zhu, C. M. Aikens, F. J. Hollander, G. C. Schatz, and R. Jin, "Correlating the Crystal Structure of A Thiol-Protected Au_{25} Cluster and Optical Properties", *Journal of the American Chemical Society*, *130*(18), **2008**, pp. 5883.

[62] R. B. Wyrwas, M. M. Alvarez, J. T. Khoury, R. C. Price, T. G. Schaaff, and R. L. Whetten, "The colours of nanometric gold", *The European Physical Journal D - Atomic, Molecular, Optical and Plasma Physics*, *43*(1), **2007**, pp. 91.

[63] O. Lopez-Acevedo, H. Tsunoyama, T. Tsukuda, H. Häkkinen, and C. M. Aikens, "Chirality and Electronic Structure of the Thiolate-Protected Au_{38} Nanocluster", *Journal of the American Chemical Society*, *132*(23), **2010**, pp. 8210.

[64] M. R. Provorse and C. M. Aikens, "Origin of Intense Chiroptical Effects in Undecagold Subnanometer Particles", *Journal of the American Chemical Society*, *132*(4), **2010**, pp. 1302.

[65] S. Knoppe and T. Bürgi, "Chirality in Thiolate-Protected Gold Clusters", *Accounts of Chemical Research*, *47*(4), **2014**, pp. 1318.

[66] K. J. Taylor, C. L. Pettiette-Hall, O. Cheshnovsky, and R. E. Smalley, "Ultraviolet photoelectron spectra of coinage metal clusters", *The Journal of chemical physics*, *96*(4), **1992**, pp. 3319.

[67] S. Chen, R. S. Ingram, M. J. Hostetler, J. J. Pietron, R. W. Murray, T. G. Schaaff, J. T. Khoury, M. M. Alvarez, and R. L. Whetten, "Gold Nanoelectrodes of Varied Size: Transition to Molecule-Like Charging", *Science*, *280*(5372), **1998**, pp. 2098.

[68] Y. Gao, N. Shao, and X. C. Zeng, "Ab Initio Study of Thiolate-Protected Au_{102} Nanocluster", *ACS Nano*, *2*(7), **2008**, pp. 1497.

[69] E. Hulkko, O. Lopez-Acevedo, J. Koivisto, Y. Levi-Kalisman, R. D. Kornberg, M. Pettersson, and H. Häkkinen, "Electronic and vibrational signatures of the $Au_{102}(p\text{-MBA})_{44}$ cluster.", *Journal of the American Chemical Society*, *133*(11), **2011**, pp. 3752.

[70] S. Knoppe, S. Michalet, and T. Bürgi, "Stabilization of Thiolate-Protected Gold Clusters Against Thermal Inversion: Diastereomeric $Au_{38}(SCH_2CH_2Ph)_{24-2x}(R\text{-BINAS})_x$", *Journal of Physical Chemistry C*, *117*(29), **2013**, pp. 15354.

[71] C. J. Ackerson, P. D. Jadzinsky, and R. D. Kornberg, "Thiolate Ligands for Synthesis of Water-Soluble Gold Clusters", *Journal of the American Chemical Society*, *127*(18), **2005**, pp. 6550.

[72] H. Qian and R. Jin, "Ambient Synthesis of $Au_{144}(SR)_{60}$ Nanoclusters in Methanol", *Chemistry of Materials*, *23*(8), **2011**, pp. 2209.

[73] Y. Levi-Kalisman, P. D. Jadzinsky, N. Kalisman, H. Tsunoyama, T. Tsukuda, D. A. Bushnell, and R. D. Kornberg, "Synthesis and Characterization of $Au_{102}(p\text{-MBA})_{44}$ Nanoparticles", *Journal of the American Chemical Society*, *133*(9), **2011**, pp. 2976.

[74] K. Salorinne, T. Lahtinen, S. Malola, J. Koivisto, and H. Häkkinen, "Solvation chemistry of water-soluble thiol-protected gold nanocluster Au_{102} from DOSY NMR spectroscopy and DFT calculations.", *Nanoscale*, *6*(14), **2014**, pp. 7823.

[75] T. G. Schaaff, G. Knight, M. N. Shafigullin, R. F. Borkman, and R. L. Whetten, "Isolation and Selected Properties of a 10.4 kDa Gold:Glutathione Cluster Compound", *The Journal of Physical Chemistry B*, *102*(52), **1998**, pp. 10643.

[76] N. Nishida, H. Yao, and K. Kimura, "Chiral Functionalization of Optically Inactive Monolayer-Protected Silver Nanoclusters by Chiral Ligand-Exchange Reactions", *Langmuir*, *24*(6), **2008**, pp. 2759.

[77] Y. Negishi, K. Nobusada, and T. Tsukuda, "Glutathione-Protected Gold Clusters Revisited: Bridging the Gap between Gold(I)-Thiolate Complexes and Thiolate-Protected Gold Nanocrystals", *Journal of the American Chemical Society*, *127*(14), **2005**, pp. 5261.

[78] Y. Shichibu, Y. Negishi, T. Tsukuda, and T. Teranishi, "Large-Scale Synthesis of Thiolated Au_{25} Clusters via Ligand Exchange Reactions of Phosphine-Stabilized Au_{11} Clusters", *Journal of the American Chemical Society*, *127*(39), **2005**, pp. 13464.

[79] Y. Negishi, Y. Takasugi, S. Sato, H. Yao, K. Kimura, and T. Tsukuda, "Magic-Numbered Aun Clusters Protected by Glutathione Monolayers (n = 18, 21, 25, 28, 32, 39): Isolation and Spectroscopic Characterization", *Journal of the American Chemical Society*, *126*(21), **2004**, pp. 6518.

[80] N. K. Chaki, Y. Negishi, H. Tsunoyama, Y. Shichibu, and T. Tsukuda, "Ubiquitous 8 and 29 kDa Gold:Alkanethiolate Cluster Compounds: Mass-Spectrometric Determination of Molecular Formulas and Structural Implications", *Journal of the American Chemical Society*, *130*(27), **2008**, pp. 8608.

[81] M. M. Alvarez, J. T. Khoury, T. G. Schaaff, M. Shafigullin, I. Vezmar, and R. L. Whetten, "Critical sizes in the growth of Au clusters", *Chemical Physics Letters*, *266*(1-2), **1997**, pp. 91.

[82] M. Zhu, H. Qian, and R. Jin, "Thiolate-Protected Au_{20} Clusters with a Large Energy Gap of 2.1 eV", *Journal of the American Chemical Society*, *131*(21), **2009**, pp. 7220.

[83] M. Zhu, E. Lanni, N. Garg, M. E. Bier, and R. Jin, "Kinetically Controlled, High-Yield Synthesis of Au_{25} Clusters", *Journal of the American Chemical Society*, *130*(4), **2008**, pp. 1138.

[84] H. Qian, M. Zhu, U. N. Andersen, and R. Jin, "Facile, Large-Scale Synthesis of Dodecanethiol-Stabilized Au_{38} Clusters", *The Journal of Physical Chemistry A*, *113*(16), **2009**, pp. 4281.

[85] H. Qian, W. T. Eckenhoff, Y. Zhu, T. Pintauer, and R. Jin, "Total Structure Determination of Thiolate-Protected Au_{38} Nanoparticles", *Journal of the American Chemical Society*, *132*(24), **2010**, pp. 8280.

[86] S. Knoppe, J. Boudon, I. Dolamic, A. Dass, and T. Bürgi, "Size Exclusion Chromatography for Semipreparative Scale Separation of $Au_{38}(SR)_{24}$ and $Au_{40}(SR)_{24}$ and Larger Clusters", *Analytical Chemistry*, *83*(13), **2011**, pp. 5056.

[87] V. R. Jupally and A. Dass, "Synthesis of $Au_{130}(SR)_{50}$ and $Au_{130-x}Ag_x(SR)_{50}$ nanomolecules through core size conversion of larger metal clusters.", *Physical chemistry chemical physics : PCCP*, *16*(22), **2014**, pp. 10473.

[88] V. R. Jupally, A. C. Dharmaratne, D. Crasto, A. J. Huckaba, C. Kumara, P. R. Nimmala, N. Kothalawala, J. H. Delcamp, and A. Dass, "$Au_{137}(SR)_{56}$ nanomolecules: composition, optical spectroscopy, electrochemistry and electrocatalytic reduction of CO_2.", *Chemical communications (Cambridge, England)*, *50*(c), **2014**, pp. 9895.

[89] H. Qian, Y. Zhu, and R. Jin, "Atomically precise gold nanocrystal molecules with surface plasmon resonance", *Proceedings of the National Academy of Sciences*, **2012**.

[90] M. Rambukwella, L. Sementa, G. Barcaro, A. Fortunelli, and A. Dass, "Organosoluble $Au_{102}(SPh)_{44}$ Nanomolecules: Synthesis, Isolation, Compositional Assignment, Core Conversion, Optical Spectroscopy, Electrochemistry, and Theoretical Analysis", *The Journal of Physical Chemistry C*, *119*(44), **2015**, pp. 25077.

[91] A. Dass, S. Theivendran, P. R. Nimmala, C. Kumara, V. R. Jupally, A. Fortunelli, L. Sementa, G. Barcaro, X. Zuo, and B. C. Noll, "$Au_{133}(SPh-tBu)_{52}$ Nanomolecules: X-ray Crystallography, Optical, Electrochemical, and Theoretical Analysis", *Journal of the American Chemical Society*, *137*(14), **2015**, pp. 4610.

[92] C. Zeng, Y. Chen, K. Kirschbaum, K. Appavoo, M. Y. Sfeir, and R. Jin, "Structural patterns at all scales in a nonmetallic chiral $Au_{133}(SR)_{52}$ nanoparticle", *Science Advances*, *1*(2), **2015**.

[93] R. Ferrando, J. Jellinek, and R. L. Johnston, "Nanoalloys: from theory to applications of alloy clusters and nanoparticles.", *Chemical reviews*, *108*(3), **2008**, pp. 845.

[94] E. G. Mednikov, M. C. Jewell, and L. F. Dahl, "Nanosized (μ12-Pt)$Pd_{164-x}Pt_x(CO)_{72}(PPh_3)_{20}$ (x $\approx$ 7) Containing Pt-Centered Four-Shell 165-Atom Pd-Pt Core with Unprecedented Intershell Bridging Carbonyl Ligands: Comparative Analysis of Icosahedral Shell-Growth Patterns with Geometrically Related Pd_{145}", *Journal of the American Chemical Society*, *129*(37), **2007**, pp. 11619.

[95] L. E. Marbella, C. M. Andolina, A. M. Smith, M. J. Hartmann, A. C. Dewar, K. A. Johnston, O. H. Daly, and J. E. Millstone, "Gold-Cobalt Nanoparticle Alloys Exhibiting Tunable Compositions, Near-Infrared Emission, and High T2 Relaxivity", *Advanced Functional Materials*, *24*(41), **2014**, pp. 6532.

[96] C. Kumara and A. Dass, "$(AuAg)_{144}(SR)_{60}$ alloy nanomolecules", *Nanoscale*, *3*(8), **2011**, pp. 3064.

[97] M. J. Hartmann, H. Häkkinen, J. E. Millstone, and D. S. Lambrecht, "Impacts of Copper Position on the Electronic Structure of $[Au_{25-x}Cu_x(SH)_{18}]^-$ Nanoclusters", *The Journal of Physical Chemistry C*, *119*(15), **2015**, pp. 8290.

[98] Y. Negishi, T. Iwai, and M. Ide, "Continuous modulation of electronic structure of stable thiolate-protected Au_{25} cluster by Ag doping", *Chemical Communications*, *46*(26), **2010**, pp. 4713.

[99] C. M. Andolina, A. C. Dewar, A. M. Smith, L. E. Marbella, M. J. Hartmann, and J. E. Millstone, "Photoluminescent Gold–Copper Nanoparticle Alloys with Composition-Tunable Near-Infrared Emission", *Journal of the American Chemical Society*, *135*(14), **2013**, pp. 5266.

[100] Y. Negishi, W. Kurashige, Y. Niihori, T. Iwasa, and K. Nobusada, "Isolation, structure, and stability of a dodecanethiolate-protected Pd_1Au_{24} cluster", *Physical Chemistry Chemical Physics*, *12*(23), **2010**, pp. 6219.

[101] K. A. Kacprzak, L. Lehtovaara, J. Akola, O. Lopez-Acevedo, and H. Häkkinen, "A density functional investigation of thiolate-protected bimetal $PdAu_{24}(SR)_{18}^z$ clusters: doping the superatom complex", *Physical Chemistry Chemical Physics*, *11*(33), **2009**, pp. 7123.

[102] Y. Negishi, K. Igarashi, K. Munakata, W. Ohgake, and K. Nobusada, "Palladium doping of magic gold cluster $Au_{38}(SC_2H_4Ph)_{24}$: formation of $Pd_2Au_{36}(SC_2H_4Ph)_{24}$ with higher stability than $Au_{38}(SC_2H_4Ph)_{24}$", *Chemical Communications*, *48*(5), **2012**, pp. 660.

[103] M. Laupp and J. Strähle, "$[(Ph_3PAu)_6(dppeAu_2)(AuCl)_4Pd]$, an Icosahedral Au_{12} Cluster with a Central Pd Atom", *Angewandte Chemie International Edition in English*, *33*(2), **1994**, pp. 207.

[104] M. Walter and M. Moseler, "Ligand-Protected Gold Alloy Clusters: Doping the Superatom", *The Journal of Physical Chemistry C*, *113*(36), **2009**, pp. 15834.

[105] N. K. Chaki, H. Tsunoyama, Y. Negishi, H. Sakurai, and T. Tsukuda, "Effect of Ag-Doping on the Catalytic Activity of Polymer-Stabilized Au Clusters in Aerobic Oxidation of Alcohol", *The Journal of Physical Chemistry C*, *111*(13), **2007**, pp. 4885.

[106] P. D. Jadzinsky, G. Calero, C. J. Ackerson, D. A. Bushnell, and R. D. Kornberg, "Structure of a Thiol Monolayer-Protected Gold Nanoparticle at 1.1 Å Resolution", *Science*, *318*, **2007**, p. 430.

[107] O. A. Wong, C. L. Heinecke, A. R. Simone, R. L. Whetten, and C. J. Ackerson, "Ligand symmetry-equivalence on thiolate protected gold nanoclusters determined by NMR spectroscopy", *Nanoscale*, *4*(14), **2012**, pp. 4099.

[108] S. Knoppe, O. A. Wong, S. Malola, H. Häkkinen, T. Bürgi, T. Verbiest, and C. J. Ackerson, "Chiral Phase Transfer and Enantioenrichment of Thiolate-Protected Au_{102} Clusters", *Journal of the American Chemical Society*, *136*(11), **2014**, pp. 4129.

[109] S. Mustalahti, P. Myllyperkiö, S. Malola, T. Lahtinen, K. Salorinne, J. Koivisto, H. Häkkinen, and M. Pettersson, "Molecule-like photodynamics of $Au_{102}(p\text{MBA})_{44}$ nanocluster.", *ACS nano*, *9*(3), **2015**, pp. 2328.

[110] C. L. Heinecke, T. W. Ni, S. Malola, V. Mäkinen, O. A. Wong, H. Häkkinen, and C. J. Ackerson, "Structural and theoretical basis for ligand exchange on thiolate monolayer protected gold nanoclusters.", *Journal of the American Chemical Society*, *134*(32), **2012**, pp. 13316.

[111] T. G. Schaaff, M. N. Shafigullin, J. T. Khoury, I. Vezmar, and R. L. Whetten, "Properties of a Ubiquitous 29 kDa Au:SR Cluster Compound", *The Journal of Physical Chemistry B*, *105*(37), **2001**, pp. 8785.

[112] B. M. Quinn, P. Liljeroth, V. Ruiz, T. Laaksonen, and K. Kontturi, "Electrochemical Resolution of 15 Oxidation States for Monolayer Protected Gold Nanoparticles", *Journal of the American Chemical Society*, *125*(22), **2003**, pp. 6644.

[113] K. Salorinne, T. Lahtinen, J. Koivisto, E. Kalenius, M. Nissinen, M. Pettersson, and H. Häkkinen, "Nondestructive size determination of thiol-stabilized gold nanoclusters in solution by diffusion ordered NMR spectroscopy", *Analytical Chemistry*, *85*(7), **2013**, pp. 3489.

[114] O. Lopez-Acevedo, J. Akola, R. L. Whetten, H. Grönbeck, and H. Häkkinen, "Structure and Bonding in the Ubiquitous Icosahedral Metallic Gold Cluster $Au_{144}(SR)_{60}$", *The Journal of Physical Chemistry C*, *113*(13), **2009**, pp. 5035.

[115] N. T. Tran, D. R. Powell, and L. F. Dahl, "Nanosized $Pd_{145}(CO)_x(PEt_3)_{30}$ Containing a Capped Three-Shell 145-Atom Metal-Core Geometry of Pseudo Icosahedral Symmetry", *Angewandte Chemie International Edition*, *39*(22), **2000**, pp. 4121.

[116] D. Bahena, N. Bhattarai, U. Santiago, A. Tlahuice, A. Ponce, S. B. H. Bach, B. Yoon, R. L. Whetten, U. Landman, and M. Jose-Yacaman, "STEM Electron Diffraction and High-Resolution Images Used in the Determination of the Crystal Structure of the $Au_{144}(SR)_{60}$ Cluster", *The Journal of Physical Chemistry Letters*, *4*(6), **2013**, pp. 975.

[117] P. M. Morse, "Diatomic Molecules According to the Wave Mechanics. II. Vibrational Levels", *Physical Review*, *34*(1), **1929**, pp. 57.

[118] T. Softley, *Atomic Spectra*, Oxford University Press, **1994**, ISBN 9780198556886.

[119] D. A. Morales, "Mathematical modeling of titration curves", *Journal of Chemometrics*, *16*(5), **2002**, pp. 247.

[120] O. Lopez-Acevedo, J. Rintala, S. Virtanen, C. Femoni, C. Tiozzo, H. Grönbeck, M. Pettersson, and H. Häkkinen, "Characterization of Iron-Carbonyl-Protected Gold Clusters", *Journal of the American Chemical Society*, *131*(35), **2009**, pp. 12573.

[121] S. Malola and H. Häkkinen, "Electronic Structure and Bonding of Icosahedral Core–Shell Gold–Silver Nanoalloy Clusters $Au_{144-x}Ag_x(SR)_{60}$", *The Journal of Physical Chemistry Letters*, *2*(18), **2011**, pp. 2316.

[122] S. Malola, L. Lehtovaara, and H. Häkkinen, "TDDFT Analysis of Optical Properties of Thiol Monolayer-Protected Gold and Intermetallic Silver–Gold $Au_{144}(SR)_{60}$ and $Au_{84}Ag_{60}(SR)_{60}$ Clusters", *The Journal of Physical Chemistry C*, *118*(34), **2014**, pp. 20002.

[123] J. E. Bertie, Y. Apelblat, and C. D. Keefe, "Infrared intensities of liquids. Part XXIII. Infrared optical constants and integrated intensities of liquid benzene-d1 at 25°C", *Journal of Molecular Structure*, *550–551*(0), **2000**, pp. 135.

[124] J. E. Bertie, Y. Apelblat, and C. D. Keefe, "Infrared intensities of liquids XXV: Dielectric constants, molar polarizabilities and integrated intensities of liquid toluene at 25°C between 4800 and 400 cm^{-1}", *Journal of Molecular Structure*, *750*(1), **2005**, pp. 78.

[125] H. Wolff and J. Szydlowski, "Vibrational spectra and rotational isomerism of ethanethiol and ethanethiol-d1", *Canadian Journal of Chemistry*, *63*(7), **1985**, pp. 1708.

[126] A. M. Gardner and T. G. Wright, "Consistent assignment of the vibrations of monosubstituted benzenes", *The Journal of chemical physics*, *135*(11), **2011**, p. 114305.

[127] J. L. Hollenberg and D. A. Dows, "Absolute Infrared Intensities in Crystalline Benzene", *The Journal of chemical physics*, *37*(6), **1962**, pp. 1300.

[128] Y. Kakiuti, "Binary Combination Bands of the Out-of-Plane CH Vibrations of Benzene Derivatives", *The Journal of chemical physics*, *25*(4), **1956**, pp. 777.

[129] A. I. Pavlyuchko, E. V. Vasilyev, and L. A. Gribov, "Calculations of molecular IR spectra in the overtone and combination frequency regions", *Journal of Applied Spectroscopy*, *78*, **2011**, pp. 639.

[130] T. L. Brown, "Vibronic Contribution to the Infrared Intensities of Benzene", *The Journal of chemical physics*, *43*(8), **1965**, pp. 2780.

[131] D. J. De Rosier and A. Klug, "Reconstruction of Three Dimensional Structures from Electron Micrographs", *Nature*, *217*(5124), **1968**, pp. 130.

[132] W. Hoppe, H. J. Schramm, M. Sturm, N. Hunsmann, and J. Gassman, "3-Dimensional Electron-Microscopy of Individual Biological Objects Part 1. Methods", *Zeitschrift fur Naturforschung Section A - A Journal of Physical Sciences*, *31*(6), **1976**, pp. 645.

[133] R. A. Crowther, L. A. Amos, J. T. Finch, D. J. De Rosier, and A. Klug, "Three Dimensional Reconstructions of Spherical Viruses by Fourier Synthesis from Electron Micrographs", *Nature*, *226*(5244), **1970**, pp. 421.

[134] J. Frank, "Single-Particle Imaging of Macromolecules by Cryo-Electron Microscopy", *Annual Review of Biophysics and Biomolecular Structure*, *31*(1), **2002**, pp. 303.

[135] R. F. Egerton, P. Li, and M. Malac, "Radiation damage in the TEM and SEM", *Micron*, *35*(6), **2004**, pp. 399.

[136] A. Krężel and W. Bal, "A formula for correlating pK_a values determined in D_2O and H_2O", *Journal of Inorganic Biochemistry*, *98*(1), **2004**, pp. 161.

[137] S. Donnini, F. Tegeler, G. Groenhof, and H. Grubmüller, "In Silico Titration of Biomolecules: Explicit Solvent Constant pH Molecular Dynamics", *Biophysical Journal*, *100*(3), **2011**, p. 613a.

[138] S. Donnini, F. Tegeler, G. Groenhof, and H. Grubmüller, "Constant pH molecular dynamics in explicit solvent with λ-dynamics", *Journal of Chemical Theory and Computation*, *7*, **2011**, pp. 1962.

[139] H. J. C. Berendsen, D. van der Spoel, and R. van Drunen, "GROMACS: a message-passing parallel molecular dynamics implementation", *Computer Physics Communications*, *91*, **1995**, pp. 43.

[140] E. Lindahl, B. Hess, and D. van der Spoel, "Gromacs 3.0: a package for molecular simulation and trajectory analysis", *Journal of Molecular Modeling*, *7*(8), **2001**, pp. 306.

[141] D. van der Spoel, E. Lindahl, B. Hess, G. Groenhof, A. E. Mark, and H. J. C. Berendsen, "Gromacs: Fast, flexible, and free", *Journal of Computational Chemistry*, *26*(16), **2005**, pp. 1701.

[142] X. Kong and B. C. L., "λ-dynamics: A new approach to free energy calculations", *Journal of Chemical Physics*, *105*, **1996**, pp. 2414.

[143] B. Tidor, "Simulated annealing on free energy surfaces by a combined molecular dynamics and monte carlo approach", *Journal of Physical Chemistry*, *97*, **1993**, pp. 1069.

[144] S. Donnini, R. T. Ullmann, G. Groenhof, and H. Grubmüller, "Charge-neutral constant pH molecular dynamics simulations using a parsimonious proton buffer", *Manuscript in preparation.*

[145] K. Salorinne, S. Malola, O. A. Wong, C. O. Rithner, X. Chen, C. J. Ackerson, and H. Häkkinen, "Solution structure of a water-soluble gold nanoparticle $Au_{102}(p\text{MBA})_{44}$", *Nature Communications*, DOI: 10.1038/ncomms10401, **2015**.

Article I

Experimental and Theoretical Determination of the Optical Gap of the $Au_{144}(SC_2H_4Ph)_{60}$ Cluster and the $(Au/Ag)_{144}(SC_2H_4Ph)_{60}$ Nanoalloys.

I

Reprinted with permission from

J. Koivisto, S. Malola, C. Kumara, A. Dass, H. Häkkinen, and M. Pettersson.
Journal of Physical Chemistry Letters, **2012**, *3*, p. 3076.
Copyright © 2012, American Chemical Society.

THE JOURNAL OF PHYSICAL CHEMISTRY Letters

Letter

pubs.acs.org/JPCL

Experimental and Theoretical Determination of the Optical Gap of the $Au_{144}(SC_2H_4Ph)_{60}$ Cluster and the $(Au/Ag)_{144}(SC_2H_4Ph)_{60}$ Nanoalloys

Jaakko Koivisto,[†] Sami Malola,[†] Chanaka Kumara,[‡] Amal Dass,[‡] Hannu Häkkinen,[†,§] and Mika Pettersson*,[†]

[†]Department of Chemistry and [§]Department of Physics, Nanoscience Center, University of Jyväskylä, P.O. Box 35, FI-40014, Finland
[‡]Department of Chemistry and Biochemistry, University of Mississippi, Oxford, Mississippi 38677, United States

Supporting Information

ABSTRACT: $Au_{144}PET_{60}$ and $Au_{144-x}Ag_xPET_{60}$ (PET = SC_2H_4Ph, phenylethylthiolate, and $30 \leq x \leq 53$) clusters were studied by optical spectroscopy and linear response time-dependent density functional theory. Spectra of thin dry films were measured in order to reveal the onset for electronic absorption. The optical gap of the $Au_{144}PET_{60}$ cluster was determined at 0.19 ± 0.01 eV, which agrees well with the computed energy for the first optical transition at 0.32 eV for a model cluster $Au_{144}(SH)_{60}$ when the line width of individual transitions is taken into account. The optical gaps for the $Au_{144-x}Ag_xPET_{60}$ alloy clusters were observed in a range of 0.12−0.26 eV, in good agreement with the calculations giving 0.16−0.36 eV for the lowest-energy optical transitions for corresponding $Au_{144-x}Ag_x(SH)_{60}$ models. This indicates that the gap is only moderately affected by doping Au with Ag. This work constitutes the first accurate determination of the fundamental spectroscopic gap of these compounds.

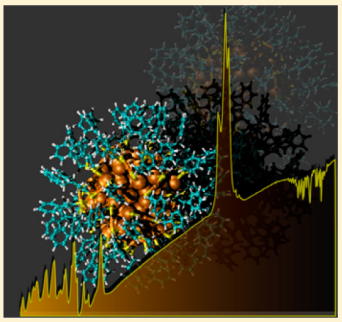

SECTION: Spectroscopy, Photochemistry, and Excited States

Downloaded by UNIV OF JYVASKYLA on September 3, 2015 | http://pubs.acs.org
Publication Date (Web): October 9, 2012 | doi: 10.1021/jz301261x

Over the past few years, tremendous progress has taken place in experimental and theoretical studies of atomically and compositionally precise thiol-stabilized gold nanoclusters in the size range of 1−3 nm. Stimulated by the seminal synthesis work of Brust, Schiffrin, and collaborators,[1] the field has now progressed to a state where numerous compounds $Au_x(SR)_y$ have been identified by means of high-precision mass spectrometric techniques, and their physical and chemical properties have been analyzed extensively. Like their larger, colloidal counterparts,[2] these well-defined building blocks of nanomaterials are expected to have a wide range of potential applications in the areas of site-specific bioconjugate labeling and sensing, drug delivery and medical therapy, molecular electronics, and gold nanoparticle catalysis.[3−10] From a more fundamental point of view, these compounds are also extremely interesting because they bridge the gap between molecular metal-containing complexes and colloidal, "metallic" nanoparticles. Most importantly, some of them have by now been structurally characterized via single-crystal X-ray diffraction,[11−15] hence opening the door for detailed investigations on structure−function relationships.

Concerning the electronic properties, it is of high current interest to understand the transition from molecular (i.e, discrete electron states) to "metallic" plasmonic behavior, and its correlation to the size dependence of the fundamental spectroscopic gap of well-defined cluster compounds. The quantum gap can be determined either from electrochemistry[16,17] or from optical spectroscopy.[13,15] Previously, the optical gap has been determined for $Au_{38}(SR)_{24}$ and $Au_{25}(SR)_{18}^{-1}$ clusters at 0.9 and 1.3 eV, respectively.[13,15] For larger clusters, the gap gets smaller, and the onset for absorption moves to the mid-IR region that is rather challenging to study experimentally. Recently, an accurate determination of the optical gap in this region (0.47 eV) succeeded for $Au_{102}(p\text{-MBA})_{44}$.[18] The next known stable size of clusters was long referred to as having a 28−29 kDa gold core mass, but the recent high-resolution mass spectrometry has given compositions of $Au_{144/146}(SR)_{59/60}$[19,20] and $Au_{144}(SR)_{60}$.[21,22] It has been known for a long time that these clusters are already "metallic" in the sense that electrochemistry does not reveal any central quantum gap but only classical double-layer charging.[16,17] Existence of the fundamental optical gap has been unclear however. An added interest comes from the recent report where mixed silver−gold clusters with the total count of metal atoms of 144 and thiolates of 60 were shown to have enhanced plasmonic absorption due to silver doping.[22]

In this work, we measured the optical spectrum of pure $Au_{144}PET_{60}$ (PET = SC_2H_4Ph, phenylethylthiolate) (**1**) and gold−silver alloy clusters $Au_{114}Ag_{30}PET_{60}$ (**2**), $Au_{110}Ag_{34}PET_{60}$ (**3**), $Au_{92}Ag_{52}PET_{60}$ (**4**), and $Au_{91}Ag_{53}PET_{60}$ (**5**) in the IR and NIR regime, utilizing samples from an earlier work by some of us.[22] It should be emphasized that the binary alloy samples are

Received: August 24, 2012
Accepted: October 5, 2012
Published: October 9, 2012

 © 2012 American Chemical Society

Downloaded by UNIV OF JYVASKYLA on September 3, 2015 | http://pubs.acs.org
Publication Date (Web): October 9, 2012 | doi: 10.1021/jz301261x

not exact compounds but contain a distribution of clusters having varying amounts of Au and Ag atoms while the total number of metal atoms is 144 and the stated composition reflects the maximum of the distribution. For details, see ref 22. To gain theoretical insight, we calculated the optical absorption spectra using linear response time-dependent density functional theory (LR-TDDFT) for the following cluster models: $Au_{144}(SH)_{60}$ (**6**), $Au_{114}Ag_{30}(SH)_{60}$ (**7**), $Au_{86}Ag_{58}(SH)_{60}$ (**8**), and $Au_{84}Ag_{60}(SH)_{60}$ (**9**,**10**). The theoretical model structures **6**−**10** are visualized in the Supporting Information (SI) (Figure S1). Our LR-TDDFT calculations are based on previously published DFT-optimized structures of the $Au_{144}(SH)_{60}$ and $Au_{144-x}Ag_x(SH)_{60}$ clusters.[23,24] The model structure for $Au_{144}(SH)_{60}$ reproduces the experimental features of the powder X-ray diffraction of the 28−29 kDa compounds very well and is considered currently as the "standard model" in the absence of the single-crystal structure for this compound. The gold core of $Au_{144}(SH)_{60}$ consists of a 114-atom symmetric cluster related to the icosahedral symmetry, having atomic layers of 12, 42, and 60 atoms. The 60 surface Au atoms are passivated by 30 HS−Au−SH units in a chiral arrangement (see SI Figure S1). In models **7**−**9**, the silver atoms are located in the 60-atom surface layer of the gold core, whereas in **10**, 30 silver atoms are evenly distributed in the inner 54-atom part of the core and the other 30 are located at the 60-atom surface layer. Figure 1 shows the measured and calculated spectrum of

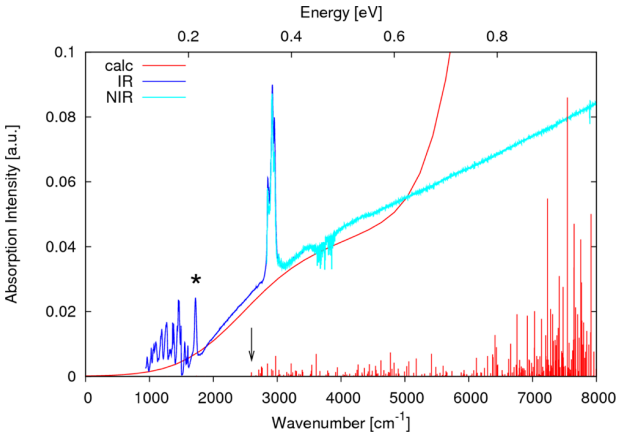

Figure 1. Absorption spectrum of a thin film of $Au_{144}PET_{60}$. The experimental spectrum is shown in blue/cyan, and the theoretical spectrum is shown in red as a stick spectrum and with a smooth envelope function constructed by convoluting the stick spectrum with a Gaussian function of width corresponding to 0.1 eV. The negative signal in the experimental spectrum at ∼3500 cm^{-1} is due to water vapor. The peak marked with (∗) is due to an impurity.

the all-gold compound **1**. The calculated spectrum is represented as a stick spectrum and additionally with a smooth envelope function that was obtained by convoluting the stick spectrum with a Gaussian function with a width of 0.10 eV. The experimental spectrum shows sharp vibrational transitions of the ligand layer below 2000 and at ∼3000 cm^{-1}. The broad electronic absorption has an onset at ∼1500 cm^{-1} (0.19 eV), after which it increases continuously toward higher energies. The derivative of absorption is smallest at ∼5000 cm^{-1}, after which it increases. Vibrational signatures of the cluster agree well with the known transitions of the PhC_2H_4S ligand used in the synthesis of these samples. For comparison, the IR spectrum of the ligand is presented in Figure S2 (SI). In cluster samples, additional peaks were found that were attributed to an impurity assigned to phthalates, which are known to solvate out from the polymer materials, especially if strong solvents such as DCM are involved. These impurities do not contribute to the broad electronic spectra. Calculations predict the absorption edge for more intensive transitions to be at 0.32 eV, giving only negligible transitions below it. If the line width of individual transitions (0.10 eV) is taken into account, the apparent onset for absorption shifts down in energy. As a result, the calculated results are in good agreement with the experimental spectra in the gap region. The used line width is consistent with typical widths for electronic transitions for similar systems like $Au_{25}(SR)_{18}$ and $Au_{38}(SR)_{24}$ clusters.[13,25,26] The line width is determined by the dephasing time, which for electronic transitions in the condensed phase is typically very short due to rapid fluctuations of solute−solvent coordinates.[27] As the measurements are done at room temperature, thermal effects will also contribute in smearing out the discrete transitions due to dynamics in the atomic structure of the clusters.[28]

Going to higher energies, the spacing between the calculated transitions is much smaller than the expected bandwidth, and individual transitions should not be resolved, as is observed experimentally. Remarkably, above ∼6000 cm^{-1}, a set of much stronger transitions is predicted by calculations, but just below the onset of strong transitions, the resulting total absorption produces nearly a plateau at ∼5000 cm^{-1}, also observed experimentally. On the other hand, the rise in absorption above 6000 cm^{-1} is much weaker experimentally.

It is important to note that the measured optical gap does not represent the HOMO−LUMO gap because of selection rules. Previously, it was found[23] that for $Au_{144}(SCH_3)_{60}$, the average separation between states in the HOMO−LUMO region is 0.02 eV, and taking into account the line width, $Au_{144}(SCH_3)_{60}$ can be considered gapless or "metallic". The present calculations are in agreement with this conclusion as well as with the electrochemical experiments that showed gapless behavior.[16,17] Thus, our current findings establish a good agreement between electronic structure calculations, optical spectroscopy, and electrochemical experiments.

Measured spectra of the gold−silver alloy clusters are presented in Figure 2, and the estimated optical gaps are presented in Table 1. $Au_{114}Ag_{30}PET_{60}$ and $Au_{91}Ag_{53}PET_{60}$ show similar spectral shape to that of $Au_{144}PET_{60}$ having a relatively steeply rising absorption in the gap region. $Au_{110}Ag_{34}PET_{60}$ and $Au_{92}Ag_{52}PET_{60}$ show slightly different behavior, indicating more smoothly rising absorption. Figure 3 shows theoretical spectra of four different alloy clusters and the Au_{144} cluster, with the estimated optical gaps and lowest transitions summarized in Table 1. The important finding is that the predicted optical gap is very similar for all of the clusters, which is in a good agreement with the experiments, as can be seen by comparing Figures 2 and 3. On the other hand, the theoretically predicted steep rise at around 6000 cm^{-1} (0.74 eV) is not observed experimentally (see Figure 1), but the reason for this discrepancy is not clear. We have shown previously that the absorption intensity is expected to increase in the energy region where strong optically allowed transitions between "superatom electron shells" become available.[24]

The measured optical gap for all gold−silver clusters was found to be between 1000 and 2100 cm^{-1} (0.12−0.26 eV), while computationally (on the basis of stick spectra), we predict

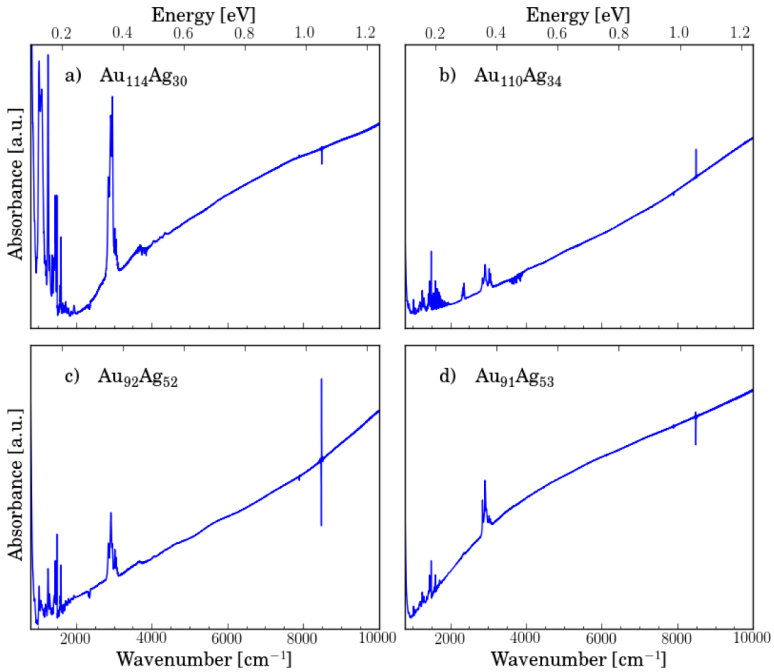

Figure 2. Absorption spectra of the cluster samples **2**–**5** measured from thin films. The spectra are constructed by combining two separate measurements in the mid-IR (800–3150 cm^{-1}) and NIR (3150–10000 cm^{-1}) regions. The interference artifact at 8500 cm^{-1} is due to the spectrometer optics. The changes in the vibrational peaks between different samples are due to presence of impurities assigned to phthalates, which are dissolved from polymer materials. They do not contribute to the electronic absorption.

Table 1. Optical Gaps Measured from Prepared Samples 1–5 and Calculated Gaps from Selected Theoretical Structures 6–10[a]

sample	exp./calc.	optical gap [eV]	optical gap [cm^{-1}]
1: $Au_{144}PET_{60}$	exp.	0.186 ± 0.013	1500 ± 100
2: $Au_{114}Ag_{30}PET_{60}$	exp.	0.260 ± 0.025	2100 ± 200
3: $Au_{110}Ag_{34}PET_{60}$	exp.	0.149 ± 0.025	1200 ± 200
4: $Au_{91}Ag_{53}PET_{60}$	exp.	0.161 ± 0.025	1300 ± 200
5: $Au_{90}Ag_{54}PET_{60}$	exp.	0.124 ± 0.013	1000 ± 100
6: $Au_{144}(SH)_{60}$	calc.	0.175 (0.323)	1410 (2600)
7: $Au_{114}Ag_{30}(SH)_{60}$	calc.	0.186 (0.281)	1500 (2260)
8: $Au_{86}Ag_{58}(SH)_{60}$	calc.	0.200 (0.362)	1610 (2920)
9: $Au_{84}Ag_{60}(SH)_{60}$	calc.	0.200 (0.357)	1610 (2880)
10: $Au_{84}Ag_{60}(SH)_{60}$	calc.	0.143 (0.161)	1150 (1300)

[a]Values for **1**–**5** have been estimated from Figures 1 and 2, and **6**–**10** are from figure 3. Values in parentheses refer to the first computational transition without convolution.

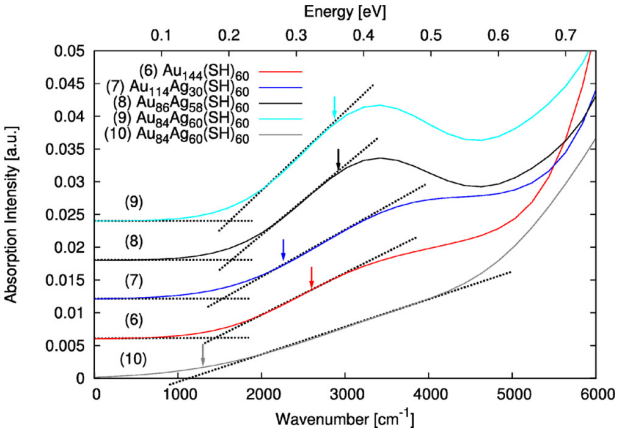

Figure 3. Computed LR-TDDFT absorption spectra of the model clusters **6**–**10** in the gap region. The spectra are constructed by convoluting the stick spectra with Gaussian line shapes. The arrows show the lowest-energy discrete transition in each case, as shown in detail in Figure S3 (SI). The dotted lines show the extrapolated gaps based on the shape of the convoluted spectra near the absorption onsets. The values for the linear onsets and the lowest optical transitions are shown in Table 1.

gaps in the range of 1300–2900 cm^{-1} (0.16–0.36 eV) depending on the cluster. We conclude that adding silver does not strongly alter the optical gap at this cluster size. However, a more careful examination reveals that there are some small but significant differences. For example, by comparing the spectra of $Au_{114}Ag_{30}$ and $Au_{91}Ag_{53}$ species, it is clear that the gap is lower for the $Au_{91}Ag_{53}$ cluster, and the other clusters seem to roughly follow this trend, but the effect is more difficult to observe from the smoother absorption edge. Similar measurements for $Au_{25-n}Ag_n(SC_{12}H_{25})_{18}$ ($0 < n < 11$) clusters by Negishi and collaborators showed that the energy of the first resolved peak increases as a function of the increasing Ag content.[29] However, simultaneously, the transitions are broadened, and as a result, for some clusters, the apparent onset for absorption seems to shift down.

Comparison of $Au_{91}Ag_{53}$ and $Au_{92}Ag_{52}$ species shows that while the onset for absorption is roughly similar in both cases, the shapes are different. One possibility is that the morphology of the samples is different, and scattering effects contribute to the shape. However, a second possibility is that in this composition range, the arrangement of silver atoms changes. In particular, as will be discussed below, according to computations, the absorption is smoother for random distribution of Ag

Downloaded by UNIV OF JYVASKYLA on September 3, 2015 | http://pubs.acs.org
Publication Date (Web): October 9, 2012 | doi: 10.1021/jz301261x

atoms in the core layers, while a more clear "bump" develops when Ag atoms are organized in the outer layer.

On the basis of our computations, the nature of the electron states around the Fermi energy will remain the same for the pure gold and the gold−silver alloy clusters of 144 metal atoms, which explains the observed similarities in the optical spectra. The projected local density of states is shown for clusters **6**, **9**, and **10** in Figure S4 (SI). Calculations show that the onset of optical absorption is the lowest for the clusters with random positions of silver atoms in the core layers like in cluster **10** and is the highest for high silver content clusters with well-separated gold and silver atomic layers (see Figure S4, SI). Random distribution of silver atoms will break the degeneracy of the electronic states, which will be, in contrast, increased if the silver atoms are located to their energetically favorable location in the outermost core layer of the cluster. Furthermore, spreading of the electronic structure will lead to a monotonously behaving "shapeless" optical absorption spectrum. This effect is seen clearly by comparing Figures S3 and S4 (SI) for clusters **9** and **10**, which both have the same composition but a different distribution of Ag atoms. In **9**, all of the Ag atoms are located in the outer layer, while in **10**, they are distributed randomly in both inner and outer layers. This illustrates an important message; the optical gap depends not only on the stoichiometry but also on the distribution of metal atoms in the cluster. This may even lead to nonmonotonous dependence of the optical gap on the cluster composition. We propose that random distribution of the silver atoms is one possible explanation for the small differences in the opening of the optical gap and also in the overall shape of the spectrum between the samples. It can be expected that these effects will be more visible in the spectrum of the clusters with high silver content.

In conclusion, we have studied the $Au_{144}PET_{60}$ cluster and $Au_{144-x}Ag_xPET_{60}$ nanoalloys by optical spectroscopy and LR-TDDFT calculations. The optical gap for the Au_{144} species was determined experimentally to be 0.19 eV, and the agreement with the calculations is very good when the bandwidth of transitions is taken into account. The optical gap for the alloy clusters was similar to that for the pure Au_{144} cluster, but a decreasing trend of the gap with increasing silver content was observed. The calculations for the optical gap of the alloy clusters were in good agreement with the experiments.

EXPERIMENTAL METHODS

The samples were synthesized and characterized by mass spectrometry and UV/vis spectroscopy, as described by some of us previously.[22] The pure gold cluster contains only a single cluster size, but the alloy clusters contain a distribution of clusters with varying amounts of silver atoms in them. However, in all of the cases, the total number of metal atoms is 144. The spectra were measured with a Nicolet Magna-IR 760 FTIR spectrometer. Samples were prepared by dropping a small amount of clusters solvated in CCl_2H_2 on a CaF_2 substrate and evaporating the solvent. For large clusters with a small optical gap, the mid-IR region contains both the vibrational signatures of the organic ligand layer and the first optical transitions of the cluster. Care was taken to establish the spectroscopic baseline accurately to make the onset for electronic transitions separate from the highest-energy vibrational bands. The optical gap was determined visually by estimating the onset for broad rising absorption from the flat baseline. The error bars for the optical gap were also estimated visually from the spectrum by considering the limits within which the determination seemed reliable.

COMPUTATIONAL METHODS

We used DFT as implemented in the real space code package GPAW.[30] For computational reasons, we replaced the phenylethane ligands with simple SH groups in our calculations. In structure optimization, we used 0.2 Å grid spacing and 0.05 eV/Å convergence criteria for the maximum forces acting on atoms in clusters. Optical spectra were calculated using linear response time-dependent DFT[31] and the Perdew−Burke−Ernzerhof (PBE) functional.[32] The GPAW setups for Au and Ag include scalar-relativistic corrections.

ASSOCIATED CONTENT

Supporting Information

The theoretical model clusters **6**−**10**, the IR spectrum of the ligand molecule phenylethylthiolate, the computed LR-TDDFT discrete absorptions of the model clusters **6**−**10**, and the projected local density of states of model clusters **6**, **9**, and **10**. This material is available free of charge via the Internet at http://pubs.acs.org.

AUTHOR INFORMATION

Corresponding Author

*E-mail: Mika.j.pettersson@jyu.fi. Tel: +358 50 3109969. Fax: +358 14 260 4756.

Notes

The authors declare no competing financial interest.

ACKNOWLEDGMENTS

H.H. and M.P. were supported by the Academy of Finland. J.K. was supported by the LASKEMO graduate school. The computations were done via a CPU grant (H.H.) at the CSC − The Finnish IT Center for Science in Espoo.

REFERENCES

(1) Brust, M.; Walker, M.; Bethell, D.; Schiffrin, D. J.; Whyman, R. Synthesis of Thiol-Derivatised Gold Nanoparticles in a Two-Phase Liquid System. *J. Chem. Soc., Chem. Commun.* **1994**, 801.

(2) Daniel, M.-C.; Astruc, D. Gold Nanoparticles: Assembly, Supramolecular Chemistry, Quantum-Size-Related Properties, and Applications toward Biology, Catalysis, and Nanotechnology. *Chem. Rev.* **2004**, *104*, 293−346.

(3) Templeton, A.; Wuelfing, M.; Murray, R. Monolayer Protected Cluster Molecules. *Acc. Chem. Res.* **2000**, *33*, 27−36.

(4) Häkkinen, H. Atomic and Electronic Structure of Gold Clusters: Understanding Flakes, Cages and Superatoms From Simple Concepts. *Chem. Soc. Rev.* **2008**, *37*, 1847−1859.

(5) Sardar, R.; Funston, A. M.; Mulvaney, P.; Murray, R. W. Gold Nanoparticles: Past, Present, and Future. *Langmuir* **2009**, *25*, 13840−13851.

(6) Jin, R. Quantum Sized, Thiolate-Protected Gold Nanoclusters. *Nanoscale* **2010**, *2*, 343−362.

(7) Ackerson, C. J.; Powell, R. D.; Hainfeld, J. F. Specific Biomolecule Labeling with Gold Clusters. *Methods Enzymol.* **2010**, *481*, 195−230.

(8) Aikens, C. Electronic Structure of Ligand-Passivated Gold and Silver Nanoclusters. *J. Phys. Chem. Lett.* **2011**, *2*, 99−104.

(9) Häkkinen, H. The Gold−Sulfur Interface at the Nanoscale. *Nat. Chem.* **2012**, *4*, 443−455.

(10) Sousa, A. A.; Morgan, J. T.; Brown, P. H.; Adams, A.; Mudiyanselage, P.; Zhang, G.; Ackerson, C. J.; Kruhlak, M. J.; Leapman, R. D. Synthesis, Characterization, and Direct Intracellular Imaging of Ultrasmall and Uniform Glutathione-Coated Gold Nanoparticles. *Small* **2012**, *8*, 2277−2286.

Downloaded by UNIV OF JYVASKYLA on September 3, 2015 | http://pubs.acs.org
Publication Date (Web): October 9, 2012 | doi: 10.1021/jz301261x

(11) Jadzinsky, P. D.; Calero, G.; Ackerson, C. J.; Bushnell, D. A.; Kornberg, R. D. Structure of a Thiol Monolayer-Protected Gold Nanoparticle at 1.1 Ångstrom Resolution. *Science* **2007**, *318*, 430−433.
(12) Heaven, M. W.; Dass, A.; White, P. S.; Holt, K. M.; Murray, R. W. Crystal Structure of the Gold Nanoparticle $[N(C_8H_{17})_4][Au_{25}(SCH_2CH_2Ph)_{18}]$. *J. Am. Chem. Soc.* **2008**, *130*, 3754−3755.
(13) Zhu, M.; Aikens, C. M.; Hollander, F. J.; Schatz, G. C.; Jin, R. Correlating the Crystal Structure of a Thiol-Protected Au_{25} cluster and Optical Properties. *J. Am. Chem. Soc.* **2008**, *130*, 5883−5885.
(14) Zhu, M.; Eckenhoff, W. T.; Pintauer, T.; Jin, R. Conversion of Anionic $[Au_{25}(SCH_2CH_2Ph)_{18}]^-$ Cluster to Charge Neutral Cluster via Air Oxidation. *J. Phys. Chem. C* **2008**, *112*, 14221−14224.
(15) Qian, H.; Eckenhoff, W. T.; Zhu, Y.; Pintauer, T.; Jin, R. Total Structure Determination of Thiolate-Protected Au_{38} Nanoparticles. *J. Am. Chem. Soc.* **2010**, *132*, 8280−8281.
(16) Hicks, J. F.; Miles, D. T.; Murray, R. W. Quantized Double-Layer Charging of Highly Monodisperse Metal Nanoparticles. *J. Am. Chem. Soc.* **2002**, *124*, 13322−13328.
(17) Quinn, B. M.; Liljeroth, P.; Ruiz, V.; Laaksonen, T.; Kontturi, K. Electrochemical Resolution of 15 Oxidation States for Monolayer Protected Gold Nanoparticles. *J. Am. Chem. Soc.* **2003**, *125*, 6644−6645.
(18) Hulkko, E.; Lopez-Acevedo, O.; Koivisto, J.; Levi-Kalisman, Y.; Kornberg, R. D.; Pettersson, M.; Häkkinen, H. Electronic and Vibrational Signatures of the Au_{102}(p-MBA)$_{44}$ Cluster. *J. Am. Chem. Soc.* **2011**, *133*, 3752−3755.
(19) Fields-Zinna, C. A.; Sardar, R.; Beasley, C. A.; Murray, R. W. Electrospray Ionization Mass Spectrometry of Intrinsically Cationized Nanoparticles, $[Au_{144/146}(SC_{11}H_{22}N(CH_2CH_3)_3^+)_x(S(CH_2)_5CH_3)_y]^{x+}$. *J. Am. Chem. Soc.* **2009**, *131*, 16266−16271.
(20) Chaki, N. K.; Negishi, Y.; Tsunoyama, H.; Shichibu, Y.; Tsukuda, T. Ubiquitous 8 and 29 kDa Gold: Alkanethiolate Cluster Compounds: Mass-Spectrometric Determination of Molecular Formulas and Structural Implications. *J. Am. Chem. Soc.* **2008**, *130*, 8608−8610.
(21) Qian, H.; Jin, R. Controlling Nanoparticles with Atomic Precision: The Case of $Au_{144}(SCH_2CH_2Ph)_{60}$. *Nano Lett.* **2009**, *9*, 4083−4087.
(22) Kumara, C.; Dass, A. $(AuAg)_{144}(SR)_{60}$ Alloy Nanomolecules. *Nanoscale* **2011**, *3*, 3064−3067.
(23) Lopez-Acevedo, O.; Akola, J.; Whetten, R. L.; Grönbeck, H.; Häkkinen, H. Structure and Bonding in the Ubiquitous Icosahedral Metallic Gold Cluster $Au_{144}(SR)_{60}$. *J. Phys. Chem. C* **2009**, *113*, 5035−5038.
(24) Malola, S.; Häkkinen, H. Electronic Structure and Bonding of Icosahedral Core−Shell Gold−Silver Nanoalloy Clusters $Au_{144-x}Ag_x(SR)_{60}$. *J. Phys. Chem. Lett.* **2011**, *2*, 2316−2321.
(25) Guo, R.; Murray, R. W. Substituent Effects on Redox Potentials and Optical Gap Energies of Molecule-like $Au_{38}(SPhX)_{24}$ Nanoparticles. *J. Am. Chem. Soc.* **2005**, *127*, 12140−12143.
(26) Toikkanen, O.; Ruiz, V.; Rönnholm, G.; Kalkkinen, N.; Liljeroth, P.; Quinn, B. M. Synthesis and Stability of Monolayer-Protected Au38 Clusters. *J. Am. Chem. Soc.* **2008**, *130*, 11049−11055.
(27) Myers, A. B. Molecular Electronic Spectral Broadening in Liquids and Glasses. *Annu. Rev. Phys. Chem.* **1998**, *49*, 267−295.
(28) Moseler, M.; Häkkinen, H.; Landman, U. Photoabsorption Spectra of Na_n^+ Clusters: Thermal Line-Broadening Mechanisms. *Phys. Rev. Lett.* **2001**, *87*, 53401.
(29) Negishi, Y.; Iwai, T.; Ide, M. Continuous Modulation of Electronic Structure of Stable Thiolate-Protected Au_{25} Cluster by Ag Doping. *Chem. Commun.* **2010**, *46*, 4713−4715.
(30) Enkovaara, J.; Rostgaard, C.; Mortensen, J. J.; Chen, J.; Dulak, M.; Ferrighi, L.; Gavnholt, J.; Glinsvad, C.; Haikola, V.; Hansen, H. A.; et al. Electronic Structure Calculations with GPAW: A Real-Space Implementation of the Projector Augmented-Wave Method. *J. Phys.: Condens. Matter* **2010**, *22*, 253202.
(31) Walter, M.; Häkkinen, H.; Lehtovaara, L.; Puska, M.; Enkovaara, J.; Rostgaard, C.; Mortensen, J. J. Time-Dependent Density-Functional Theory in the Projector Augmented-Wave Method. *J. Chem. Phys.* **2008**, *128*, 244101.
(32) Perdew, J.; Burke, K.; Ernzerhof, M. Generalized Gradient Approximation Made Simple. *Phys. Rev. Lett.* **1996**, *77*, 3865−3868.

Downloaded by UNIV OF JYVASKYLA on September 3, 2015 | http://pubs.acs.org
Publication Date (Web): October 9, 2012 | doi: 10.1021/jz301261x

Experimental and Theoretical Determination of the Optical Gap of the $Au_{144}(SC_2H_4Ph)_{60}$ Cluster and the $(Au/Ag)_{144}(SC_2H_4Ph)_{60}$ Nanoalloys

*Jaakko Koivisto[1], Sami Malola[1], Chanaka Kumara[2], Amal Dass[2], Hannu Häkkinen[1,3], and Mika Pettersson[1,]**

[1]Nanoscience Center, Department of Chemistry, P.O. Box 35, FI-40014 University of Jyväskylä, Finland.

[2]Department of Chemistry and Biochemistry, University of Mississippi, Oxford, Mississippi 38677

[3]Nanoscience Center, Department of Physics, P.O. Box 35, FI-40014 University of Jyväskylä, Finland.

Email: Mika.j.pettersson@jyu.fi, Tel: +358 50 3109969, fax: +358 14 260 4756

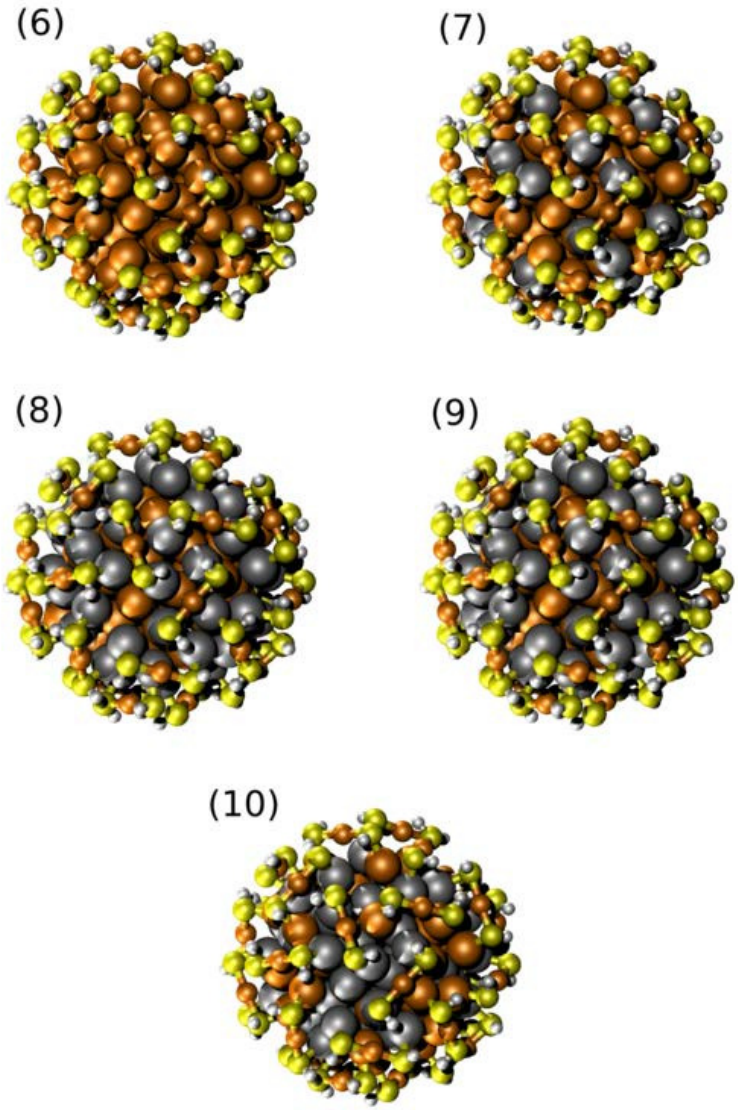

Figure S1. Structures of the considered theoretical models **6 – 10**. Gold, silver, sulfur and hydrogen are depicted as orange, grey, yellow, and white, respectively.

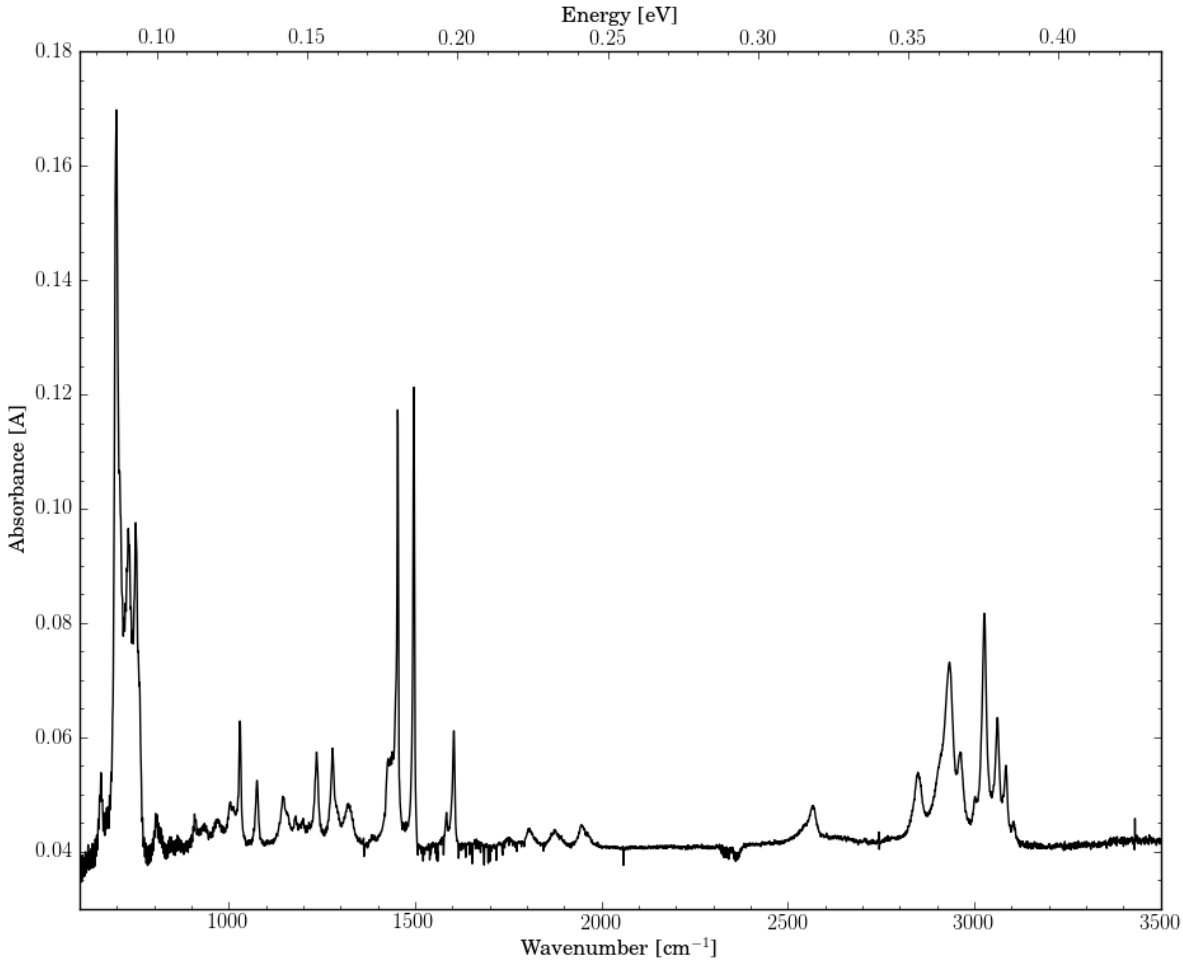

Figure S2. IR-spectrum of neat phenylethylthiolate (PhC_2H_3SH) measured in transmission geometry from thin film deposited on KBr-tablet.

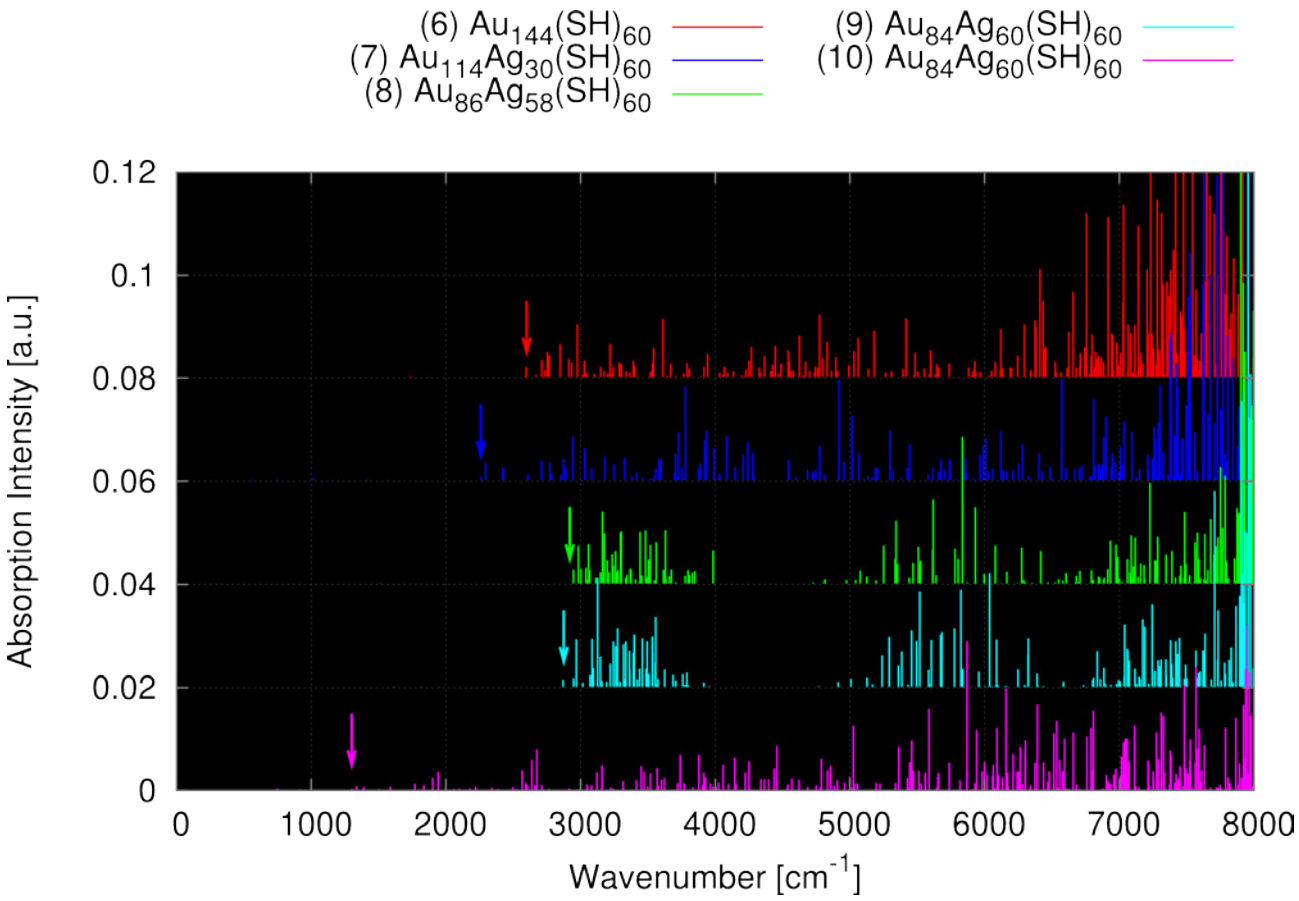

Figure S3. Calculated stick spectra of the clusters **6** – **10**. The arrow points the lowest energy transition for each cluster.

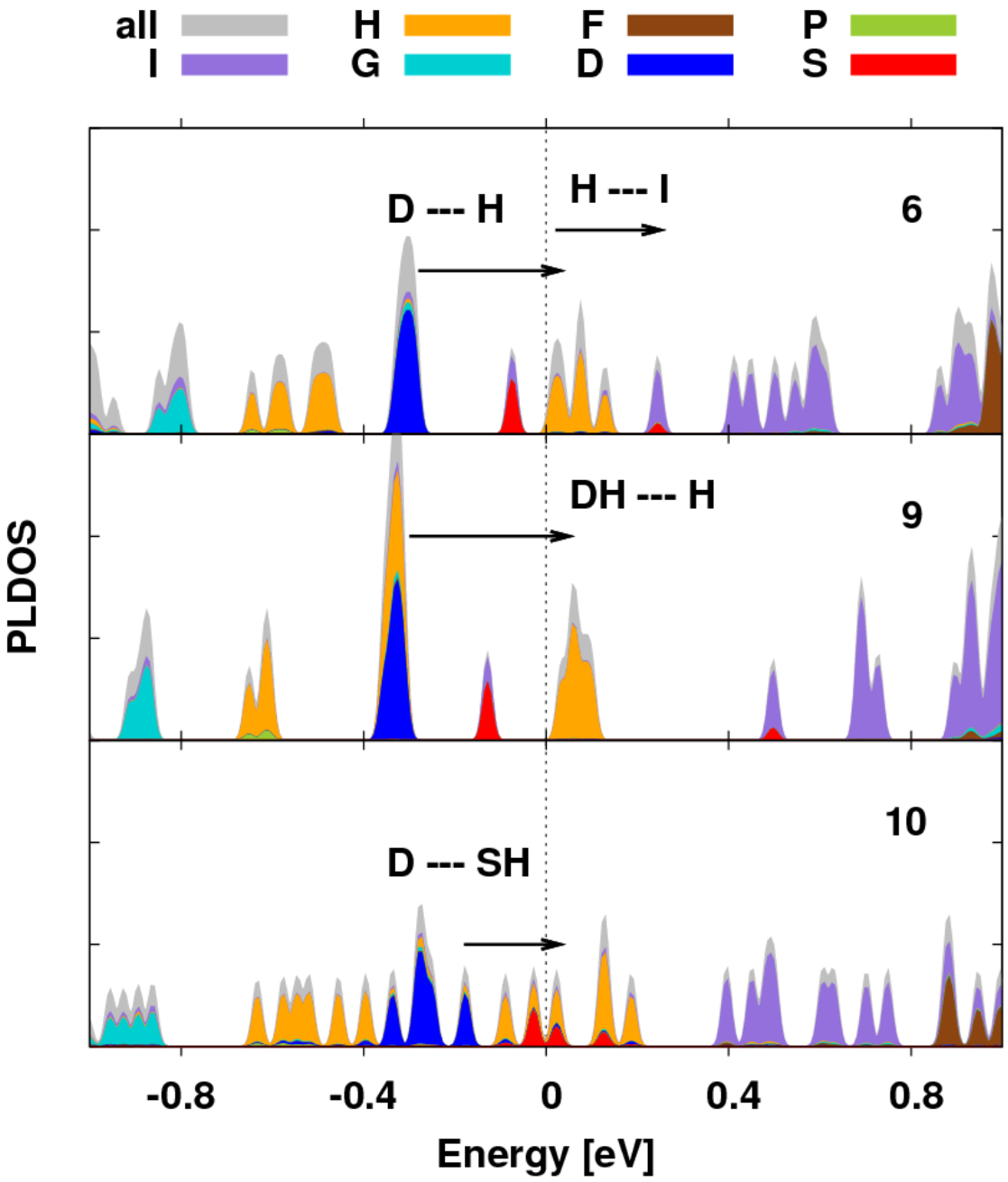

Figure S4. Projected local density of states (PLDOS) onto spherical harmonics for the model structures **6**, **9** and **10**. Projection is done about the cluster center-of-mass with a sphere radius of 8 Å up to I symmetry (L=6 angular momentum) as was shown in Ref. 24. The gray area shows the part of the DOS that cannot be described in the expansion up to L=6. Fermi level is at E=0 and the transitions that contribute to the opening of the optical gap in the structures are drawn with arrows and labeled with the corresponding symmetries.

Article II

Vibrational Perturbations and Ligand-Layer Coupling in a Single Crystal of $Au_{144}(SC_2H_4Ph)_{60}$ Nanocluster.

Reprinted with permission from

J. Koivisto, K. Salorinne, S. Mustalahti, T. Lahtinen, S. Malola, H. Häkkinen, and M. Pettersson.
Journal of Physical Chemistry Letters, **2014**, *5*, p. 387.
Copyright © 2014, American Chemical Society.

II

THE JOURNAL OF PHYSICAL CHEMISTRY Letters

Letter

pubs.acs.org/JPCL

Vibrational Perturbations and Ligand–Layer Coupling in a Single Crystal of $Au_{144}(SC_2H_4Ph)_{60}$ Nanocluster

Jaakko Koivisto,[†] Kirsi Salorinne,[†] Satu Mustalahti,[†] Tanja Lahtinen,[†] Sami Malola,[†,‡] Hannu Häkkinen,[†,‡] and Mika Pettersson*[,†]

[†]Department of Chemistry and [‡]Department of Physics, Nanoscience Center, University of Jyväskylä, FI-40014 Jyväskylä, Finland

Supporting Information

ABSTRACT: We have determined vibrational signatures and optical gap of the $Au_{144}(PET)_{60}$ (PET: phenylethylthiol, SC_2H_4Ph) nanocluster solvated in deuterated dichloromethane (DCM-D2, CD_2Cl_2) and in a single crystal. For crystals, solid-state ^{13}C NMR and X-ray diffraction were also measured. A revised value of 2200 cm^{-1} (0.27 eV) was obtained for the optical gap in both phases. The vibrational spectra of solvated $AU_{144}(PET)_{60}$ closely resembles that of neat PET, while the crystalline-state spectrum exhibits significant inhomogeneous spectral broadening, frequency shifts, intensity transfer between vibrational modes, and an increase in the overtone and combination transition intensities. Spectral broadening was also observed in the ^{13}C NMR spectrum. Changes in the intensity are explained due to vibrational coupling of the normal modes induced by the crystal packing, and the vibrational broadening is caused by ligand-environment inhomogeneity in the crystal. This indicates a pseudocrystalline state where the cluster cores are arranged in periodic fashion, while the ligand-layer molecules between the cores form amorphous structures.

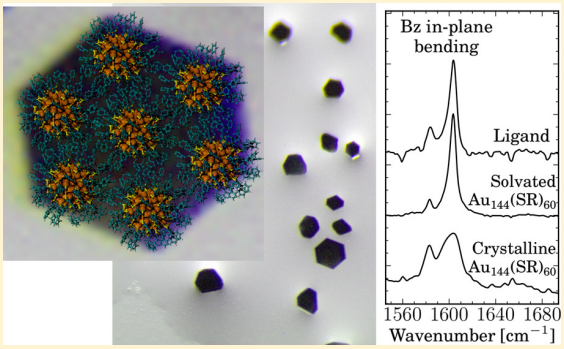

SECTION: Spectroscopy, Photochemistry, and Excited States

Downloaded by UNIV OF JYVASKYLA on September 3, 2015 | http://pubs.acs.org
Publication Date (Web): January 7, 2014 | doi: 10.1021/jz4026003

Thiol-protected nanoscopic gold-clusters have emerged as promising new materials due to their unique electronic and optical properties. Compared with larger "plasmonic nanoparticles", nanoclusters offer numerous advantages such as molecular-like HOMO–LUMO gap, discrete electrical charge states, circular dichroism, and small size, which can be exploited, for example, in nanosensors or biological labeling.[1−4] A number of robust clusters in the size range from 20 to 333 gold atoms, approximately 1–3 nm in core diameter, can be synthesized and have been identified through mass-spectroscopy, and for several clusters (Au_{25}, Au_{28}, Au_{36}, Au_{38}, Au_{102}) the total structure has been determined using single-crystal X-ray diffraction,[5−9] allowing detailed studies of the relationship between the cluster structure and properties.

$Au_{144}(SR)_{60}$ is one of the largest nanoclusters with known atomically precise formula and which can be synthesized in significant quantity as monodisperse samples.[10] The exact structure of the $Au_{144}(SR)_{60}$ cluster has not been confirmed experimentally, but from high-level DFT-simulations it is predicted to have a highly symmetrical icosahedral Au_{114} core protected by 30 $Au(SR)_2$ units.[11] In this arrangement, the cluster core is left with 84 valence electrons, which does not correspond with any known electronic shell closing number in the cluster superatom model.[12] Electrochemical studies have shown the cluster to have zero HOMO–LUMO gap, as expected for the predicted structure, making it the smallest "metallic" Au-nanocluster.[13,14] Being the first known cluster size stabilized more by it is geometric than electronic structure, it serves as an important bridge between the smaller molecular-like clusters and larger plasmonic nanoparticles in the understanding of how the cluster properties change with particle size. In particular, the emergence of localized surface plasmon resonance (LSPR), commonly attributed to the size regime between $Au_{144}(SR)_{60}$ and larger 76 Da cluster,[15,16] has been under much scrutiny. The latest computational studies indicate plasmon-like excited-states localized inside the $Au_{144}(SR)_{60}$ cluster core, giving rise to a weak absorption band around 540 nm.[17]

Infrared (IR) spectroscopy has been extensively used to characterize nanoscopic thiolate–noble-metal complexes, either as layers on flat surfaces,[18−21] or monolayers on cluster surface.[22] For gold nanoclusters, IR studies have been used to probe either the protecting ligand–molecule vibrations or the electrical transitions of the cluster core in the IR regime.[22−26] Hostetler, Stokes, and Murray studied the effect of alkanethiolate chain length on ordering of the ligands on the cluster surface and found shorter chains (C_n, $n < 6$) to form more disordered structures than the longer chains (C_n, $n \geq 6$).[22] Schaaff et al. measured the IR spectrum of alkanethiolate protected 29 kDa cluster, now assumed to be $Au_{144}(SR)_{60}$, and

Received: December 1, 2013
Accepted: January 3, 2014
Published: January 3, 2014

 © 2014 American Chemical Society

acquired similar results.[23] More recently, the optical gap of $Au_{102}(SR)_{44}$ and $Au_{144}(PET)_{60}$ and the vibrational spectrum of $Au_{144}(PET)_{60}$ measured from thin dropcasted films were reported.[24−26]

Several research groups have acquired single crystals of $Au_{144}(SR)_{60}$ with either straight-chained aliphatic thiolates or *para*-mercaptobenzoic acid (*p*-MBA, HSPhCOOH) ligands;[23,27] however, the determination of the $Au_{144}(PET)_{60}$ structure with single-crystal X-ray diffraction has so far proved to be unsuccessful. In this situation, it is valuable to obtain structural information by other methods. Here we report the vibrational IR spectrum and the optical gap of $Au_{144}(PET)_{60}$ solvated in DCM-D2 ($C_2D_2Cl_2$) and in a single crystal and the ^{13}C NMR spectra of a crystalline solid. The results are compared with the X-ray diffraction pattern of $Au_{144}(PET)_{60}$ single crystal.

Electronic absorption edge for $Au_{144}(PET)_{60}$ in solution and in crystal phase is shown in Figure 1. A revised value of 2200 cm^{-1} (0.27 eV) was obtained for $Au_{144}(PET)_{60}$ optical gap, slightly higher than the value of 1500 cm^{-1} (0.19 eV) previously obtained.[25] We believe this discrepancy is caused by the dropcast sample preparation in the previous measurements, in which microcrystals with dimensions similar to mid-IR wavelengths (5−10 μm) can form in the drying process, ultimately causing Mie scattering at these wavelengths, making it difficult to locate the onset of a continuous absorption accurately. The optical gap is identical both in solution and in a crystal, indicating that the electronic states associated with the first optical transitions are not perturbed by either solvent or intercluster interactions. This is expected because according to TDDFT simulation of the electronic transitions the lowest energy states of $Au_{144}(PET)_{60}$ cluster are localized mainly inside the cluster core.[11]

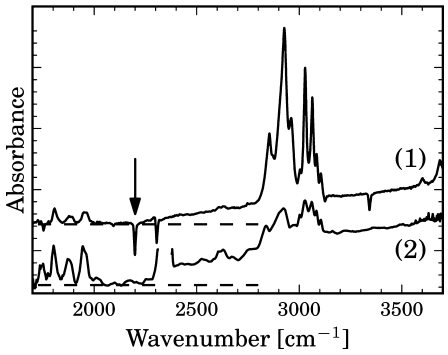

Figure 1. Optical gap of $Au_{144}(PET)_{60}$ in DCM-D2 (**1**) and in single crystal (**2**) is observed at 2200 cm^{-1} (0.27 eV). Baseline and the onset of electronic absorption are denoted with dashed line and arrow, respectively.

The vibrational spectrum of the $Au_{144}(PET)_{60}$ ligand layer differs significantly between the solution state and crystal state clusters (Figure 2). To analyze the differences in more detail, we identified fundamental IR transitions (Tables S1 and S2 in the Supporting Information), and the C−H stretching peaks of all three systems were analyzed by multipeak fitting (Figure 3, Table 1). In the vibrational analysis, we have considered the phenyl and ethyl parts of the PET molecule separately; that is, when considering the phenyl ring vibrations the ethyl chain is approximated with point mass and vice versa. With these approximations, the phenyl ring has C_{2v} and the ethyl chain has C_s symmetry, respectively. In solution the ligand IR spectrum closely resembles that of neat PET molecules; however, changes can be seen in the CH_2 wag (1280 cm^{-1}) and CH_2 twist (1237 cm^{-1}) and C−H stretching modes (2800 − 3000 cm^{-1}) of the C_2H_4-moiety.[28] Notably the CH_2 wag and twist modes have red-shifted ca. 15 cm^{-1}, and the CH_2 wag mode intensity is strongly reduced. Two new peaks are observed in the aliphatic C−H-stretching region at 2872 and 2981 cm^{-1} (Figure 3B, marked as X and Y in Table 1), and the C−H-stretching modes have undergone slight broadening (2−5 cm^{-1}). Also, the intensity of C_2H_4 vibrations is increased in comparison with phenyl-ring modes. No significant change is observed in the phenyl vibrations in DCM-D2 solution. The spectrum of $Au_{144}(PET)_{60}$ cluster in a single crystal differs markedly from the spectrum in solution or in thin dropcast film.[26] In a single crystal, all ligand vibrations are significantly broadened compared with both neat PET and solvated $Au_{144}(PET)_{60}$. The broadening is especially evident in the sharp C−C stretching vibrations of the phenyl ring (M_4, M_7, M_{24} in Gardner−Wright notation; see Table S1 in the Supporting Information and figure 5 in ref 29) and in the C−H-stretching region, with some peaks more than doubling their width. For phenyl-ring C−H stretching modes, downshifts ranging from 0.5 to 2.4 cm^{-1} are observed, which are consistent with the T-shaped benzene dimer formation,[30] and the peak shape changes from Lorentzian to Gaussian shape indicating inhomogeneous broadening mechanism (Figure 3B,C). In

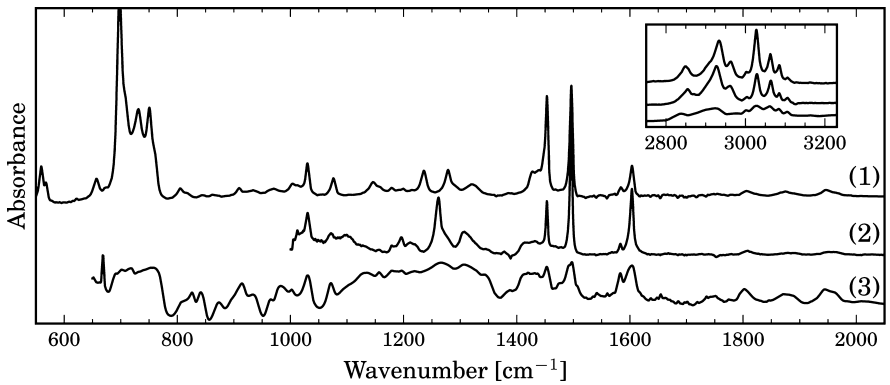

Figure 2. Overall IR spectra of neat PET (**1**), $Au_{144}(PET)_{60}$ in DCM-D2 (**2**), and $Au_{144}(PET)_{60}$ single crystal (**3**). The spectrum of **2** has been truncated at 1000 cm^{-1} due to solvent and CaF_2-window absorption. The spectra have been smoothed using four-point mean smoothing.

Downloaded by UNIV OF JYVASKYLA on September 3, 2015 | http://pubs.acs.org
Publication Date (Web): January 7, 2014 | doi: 10.1021/jz4026003

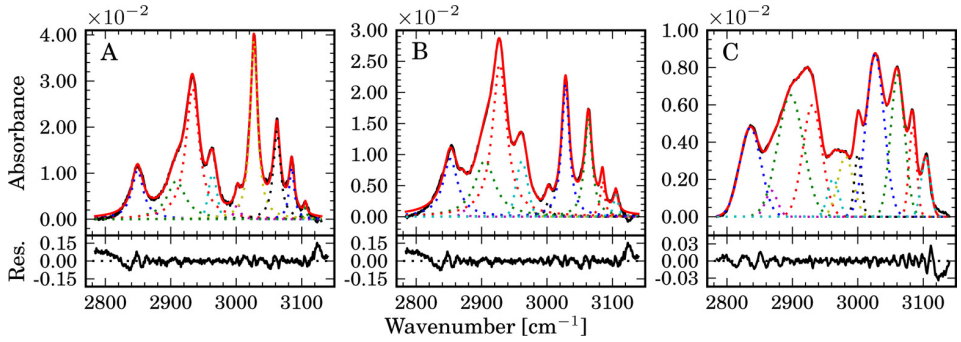

Figure 3. Fit results and the fit residual of CH stretching region of neat PET (A), $Au_{144}(PET)_{60}$ in DCM-D2 (B), and in single crystal (C). Fit parameters are presented in Table 1

Table 1. Peak Fitting Parameters, Center X_0 and Full Width Half-Maximum (fwhm), for Neat PET and $Au_{144}(PET)_{60}$ in C−H Stretching Region

	X_0 [cm^{-1}]			fwhm [cm^{-1}]		
assignment[a]	PET (1)	Au_{144}[b]	Au_{144}[c]	PET	Au_{144}[b]	Au_{144}[c]
Ph−CH_2 s	2849.0	2852.2	2835.6	21.4	27.0	38.0
Ph−CH_2 as	2908.2	2905.0	2897.2	34.2	37.3	46.6
S−CH_2 s	2933.2	2927.5	2930.4	24.6	26.4	34.3
S−CH_2 as	2963.8	2961.6	2962.4	15.2	20.3	19.5
X		2871.5	2868.0		7.5	21.2
Y		2981.2	2981.2		7.2	27.1
M_{22}	3001.8	3001.8	3000.1	8.7	8.9	12.5
M_{21}	3026.9	3028.3	3026.4	13.5	13.8	32.1
M_3	3062.0	3063.1	3060.7	12.9	13.9	24.8
M_2	3084.7	3084.8	3084.1	9.3	8.0	13.8
M_1	3105.7	3105.1	3103.9	5.0	7.7	14.6

[a]s: symmetric stretch; as: antisymmetric stretch. S: adjacent to the sulfur; Ph: adjacent to the phenyl-ring. [b]Solvated in DCM-D2. [c]In single crystal.

addition, several new peaks are observed in the fingerprint region below 1000 cm^{-1}. The observed effects on the $Au_{144}(PET)_{60}$ ligand-layer IR signal are contrary to the conventional situation where molecules in the crystal phase give sharper and more defined peaks than in solution due to the decrease in structural degrees of freedom in the crystal and lack of solvent interactions.[31,32] The hexagonal shapes of the acquired $Au_{144}(PET)_{60}$ crystals and their X-ray diffraction pattern indicate FCC (face-centered-cubic)- or HCP (hexagonal-close-packed)-type packing of the clusters (Figure S1 in the Supporting Information). The FCC packing of large nanoparticles (diameter >5 nm) has been previously observed.[33] It is probable that the $Au_{144}(PET)_{60}$ cluster represents a borderline case where the core size starts to govern the cluster packing. Assuming that the clusters are spherical and have a radius of 3.1 nm,[34] the empty space in the lattice becomes substantial compared with the size of a single ligand molecule. As a result, when the clusters are packed next to each other in the crystal lattice, the ligand molecules that are situated toward the neighboring cluster are affected by both the intra- and intercluster interactions, while the ligands pointing toward the empty space in the crystal lattice are affected only by the adjacent ligands in the cluster. We argue that this inhomogeneity of the ligand environment caused by the crystal packing is responsible for the inhomogeneous broadening of the vibrational modes.

The apparent disorder of the ligands in the $Au_{144}(PET)_{60}$ crystal also explains the difficulties in obtaining the structure solution from single-crystal X-ray diffraction studies. The $Au_{144}(PET)_{60}$ crystals diffract strongly at small 2θ angles, indicating ordered macroscopic structure of the $Au_{144}(PET)_{60}$ clusters in the crystal lattice, but the diffraction pattern quickly disappears at larger 2θ angles, yielding no information of the ligand layer structure. The lack of high resolution (only up to 5.3 Å) reflections even with substantially longer exposure times suggests that the ligand layer is highly disordered and the strong low-resolution reflections are mainly attributed to the ordered Au core. To confirm the disordered nature of the ligand layer, we measured solid-state NMR ^{13}C CP/MAS -spectra from the crystalline $Au_{144}(PET)_{60}$. The spectrum (Figure S2 in the Supporting Information) shows multiple chemical shifts for the ethylene (C-1 and C-2) and aromatic C-3 carbons at 35−50 and 135−145 ppm regions, respectively, indicating different chemical environments for the PET ligands on the cluster surface. Aromatic C-4, C-5, and C-6 carbons are farther away from the cluster surface and are less affected by the surface structure, giving rise to single chemical shift at 128 ppm. The different ligand environments cannot be accurately determined due to limited resolution and peak overlapping. A more detailed NMR analysis of the $Au_{144}(PET)_{60}$ cluster is currently underway.

The characteristic pattern of the overtone and combination transitions of the monosubstituted benzene is observed between 1650 and 2000 cm^{-1} for all measured systems (Figure 4A). For the crystalline $Au_{144}(PET)_{60}$, numerous new broad features at 2000 to 2800 cm^{-1} and several sharp peaks at 800 to 1000 cm^{-1} can be clearly seen (Figure 4B). Similar features have been observed in previous experimental[35,36] and computational studies[37,38] of related systems and are assigned to benzene overtones and combinations. The peak positions and assignments for crystalline $Au_{144}(PET)_{60}$ are presented in Table S3 in the Supporting Information. In neat PET and solvated $Au_{144}(PET)_{60}$, the peaks at 1650 to 2000 cm^{-1} region are weak and have similar intensity in both spectra, but in the crystal phase they have significantly gained intensity compared with the fundamental transitions. Also, for the neat PET, only the fundamental S−H stretching mode at 2567 cm^{-1}, and for the solvated $Au_{144}(PET)_{60}$, only the two combinations at 2606 and 2629 cm^{-1}, can be seen in Figure 4B. The increase in the intensity of the overtone and combination transitions is usually caused by increased anharmonicity of the vibration or coupling with other vibrations. The peaks at the 1650−2000 cm^{-1} region exhibit red shift of ca. 5 cm^{-1} when transitioning from solvated

Downloaded by UNIV OF JYVASKYLA on September 3, 2015 | http://pubs.acs.org
Publication Date (Web): January 7, 2014 | doi: 10.1021/jz4026003

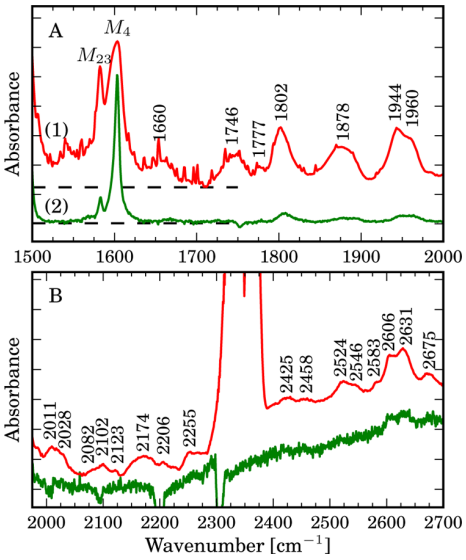

Figure 4. Phenyl-ring overtone and combination vibrations of single crystal (**1**) and solvated (**2**) $Au_{144}(PET)_{60}$. Assignments are presented in Table S3 in the Supporting Information. Spectra in panel A have been normalized to the M_4 (1600 cm^{-1}) peak. Spectrum **2** in panel B has been multiplied three times to bring out the peaks around 2620 cm^{-1}. The negative peaks at 2000−2300 cm^{-1} are caused by the solvent, and the strong peak at 2350 cm^{-1} and sharp lines at 1500−1900 cm^{-1} are caused by gaseous CO_2 and H_2O, respectively.

clusters to the crystal phase. The significant relative intensity decrease in strong fundamentals (e.g., M_4, M_7, M_{24}) and corresponding increase in weak fundamentals (e.g., M_{12}, M_{13}, M_{15}, M_{16}) in the crystalline $Au_{144}(PET)_{60}$ to the point where all vibrations seem to have similar intensity indicate substantial transfer of oscillator strength due to vibrational coupling of the ligand-layer in the crystal.[31,39] Unfortunately, our data is insufficient for accurate quantitative analysis of the absorption intensities. For vibrations of A_2 symmetry (M_{12} and M_{13}), the intensity increase can also be explained by the ligand symmetry breaking in the crystal as A_2 vibrations are not IR-active in PET, but this would not explain the corresponding increase in the IR-active B_1 vibrations (M_{15}, M_{16}). The increase in overtone and combination intensities can be partially explained by the increase in the corresponding fundamental intensity; however, several combinations for which the fundamental intensities decrease are also amplified in the crystal, so we cannot rule out the possible contribution from mechanical or electrical anharmonicity. Altogether, the crystal spectrum indicates strong mixing of vibrations and relative redistribution of intensity between many modes. This effect should be of interest for theoretical modeling.

In summary, we have measured the IR and ^{13}C NMR solid-state spectrum and X-ray diffraction of $Au_{144}(PET)_{60}$ in a single crystal. The observed IR and NMR broadening is curious because it implies a pseudocrystalline structure where the cluster cores are arranged in a periodic crystalline fashion while the ligand layers between the clusters are in an amorphous state. Such a structure would explain the behavior of the $Au_{144}(PET)_{60}$ crystals' X-ray diffraction patterns. We believe that the flexibility of the PET ligand, in combination with the predicted spherical shape and large particle diameter, results in the ligands having a large number of possible conformations available in the crystal. Noble-metal clusters in a similar size range have been successfully crystallized and characterized using single-crystal X-ray diffraction;[9,40] however, none have been characterized with a ligand as flexible as PET. Exchanging the ligand to a more rigid molecule or one with more stabilizing intra- and intercluster weak interactions between the ligands may be useful in stabilizing the ligand layer in the crystal.[40] The first electronic transitions of $Au_{144}(PET)_{60}$ were found to be independent of the surrounding medium, confirming that the lowest molecular orbitals are strongly localized inside the cluster core. In the crystalline state, strong ligand−layer vibrational coupling is induced by the crystal packing, resulting in significant transfer of oscillator strength between the ligand vibrational modes. The observed coupling pattern where all vibrations couple strongly also indicates numerous different ligand-conformations in the crystal.

EXPERIMENTAL SECTION

$Au_{144}(PET)_{60}$ nanoclusters were prepared according to published procedure[10] from commercially available reagents. The purity of the $Au_{144}(PET)_{60}$ nanoclusters was confirmed by UV−vis and NMR analyses and in our previous study also by ESI-MS.[34] In particular, ESI-MS spectra showed only $Au_{144}(PET)_{60}$ species, and no sign of other cluster sizes such as Au_{145} or Au_{146} was observed. Single crystals of $Au_{144}(PET)_{60}$ were grown by slow vapor diffusion from toluene solution of $Au_{144}(PET)_{60}$ using acetonitrile as the antisolvent. The IR spectrum of solvated $Au_{144}(PET)_{60}$ cluster was measured in deuterated dichloromethane (DCM-D2, CCl_2D_2) using transmission geometry, 80 μm optical path, CaF_2-windows, and ∼1 mmol $Au_{144}(PET)_{60}$ concentration. Crystals were deposited on Au mirror with either ethanol or high viscosity FOMBLIN Y oil, which was then washed away with ethanol. IR spectra from the crystals were measured in reflectance geometry with a Nicolet Magna-IR 550 spectrometer and Spectra-tech IR-plan advantage IR microscope. Solution-state spectrum of $Au_{144}(PET)_{60}$ and neat PET was measured with Nicolet Magna-IR 760. All IR-spectra were recorded with 2 cm^{-1} resolution using a liquid-N_2-cooled MCT detector and processed with Happ−Genzel apodization before Fourier transform. ^{13}C CP/MAS NMR spectrum was recorded on a Bruker Avance 400 NMR spectrometer equipped with a 4 mm standard bore CP/MAS probehead, whose X channel was tuned to 100.62 MHz for ^{13}C. The other channel was tuned to 400.13 MHz for broadband ^{1}H decoupling. Approximately 5 mg of single-crystalline $Au_{144}(PET)_{60}$ was packed into the ZrO_2 HR/MAS rotor, which was closed with a Kel-F cap. The spinning rate was 10 kHz. The ^{13}C CP/MAS NMR experiment for the sample was carried out under Hartmann−Hahn conditions with TPPM decoupling. The contact time used was 2 ms, and the relaxation delay was 4 s. The FID was processed by exponential apodization function with line broadening of 20 Hz prior to FT. The ^{13}C chemical shift was calibrated using glycine's carbonyl peak at 176.03 ppm as an external standard.

ASSOCIATED CONTENT

Supporting Information

Tables of the observed vibrational modes, X-ray diffraction patterns, and ^{13}C NMR spectrum. This material is available free of charge via the Internet at http://pubs.acs.org.

Downloaded by UNIV OF JYVASKYLA on September 3, 2015 | http://pubs.acs.org
Publication Date (Web): January 7, 2014 | doi: 10.1021/jz4026003

AUTHOR INFORMATION

Corresponding Author

*E-mail: mika.j.pettersson@jyu.fi.

Notes

The authors declare no competing financial interest.

ACKNOWLEDGMENTS

J.K. and S.M. thank LASKEMO and NGS-NANO graduate schools, respectively, for funding. This work was supported by the Academy of Finland. We thank Elina Sievänen for her help with NMR and Elina Kalenius for help with ESI-MS measurements.

REFERENCES

(1) Murray, R. W. Nanoelectrochemistry: Metal Nanoparticles, Nanoelectrodes, and Nanopores. *Chem. Rev.* **2008**, *108*, 2688−2720.

(2) Dolamic, I.; Knoppe, S.; Dass, A.; Bürgi, T. First Enantioseparation and Circular Dichroism Spectra of Au_{38} Clusters Protected by Achiral Ligands. *Nat. Commun.* **2012**, *3*, 798.

(3) Wu, Z.; Wang, M.; Yang, J.; Zheng, X.; Cai, W.; Meng, G.; Qian, H.; Wang, H.; Jin, R. Well-Defined Nanoclusters as Fluorescent Nanosensors: A Case Study on $Au_{25}(SG)_{18}$. *Small* **2012**, *8*, 2028−2035.

(4) Ackerson, C. J.; Jadzinsky, P. D.; Jensen, G. J.; Kornberg, R. D. Rigid, Specific, and Discrete Gold Nanoparticle/Antibody Conjugates. *J. Am. Chem. Soc.* **2006**, *128*, 2635−2640.

(5) Heaven, M. W.; Dass, A.; White, P. S.; Holt, K. M.; Murray, R. W. Crystal Structure of the Gold Nanoparticle $[N(C_8H_{17})_4][Au_{25}(SCH_2CH_2Ph)_{18}]$. *J. Am. Chem. Soc.* **2008**, *130*, 3754−3755.

(6) Zeng, C.; Li, T.; Das, A.; Rosi, N. L.; Jin, R. Chiral Structure of Thiolate-Protected 28-Gold-Atom Nanocluster Determined by X-ray Crystallography. *J. Am. Chem. Soc.* **2013**, *135*, 10011−10013.

(7) Zeng, C.; Qian, H.; Li, T.; Li, G.; Rosi, N. L.; Yoon, B.; Barnett, R. N.; Whetten, R. L.; Landman, U.; Jin, R. Total Structure and Electronic Properties of the Gold Nanocrystal $Au_{36}(SR)_{24}$. *Angew. Chem., Int. Ed.* **2012**, *51*, 13114−13118.

(8) Qian, H.; Eckenhoff, W. T.; Zhu, Y.; Pintauer, T.; Jin, R. Total Structure Determination of Thiolate-Protected Au_{38} Nanoparticles. *J. Am. Chem. Soc.* **2010**, *132*, 8280−8281.

(9) Jadzinsky, P. D.; Calero, G.; Ackerson, C. J.; Bushnell, D. A.; Kornberg, R. D. Structure of a Thiol Monolayer-Protected Gold Nanoparticle at 1.1 Å Resolution. *Science* **2007**, *318*, 430.

(10) Qian, H.; Jin, R. Ambient Synthesis of $Au_{144}(SR)_{60}$ Nanoclusters in Methanol. *Chem. Mater.* **2011**, *23*, 2209−2217.

(11) Lopez-Acevedo, O.; Akola, J.; Whetten, R. L.; Gronbeck, H.; Häkkinen, H. Structure and Bonding in the Ubiquitous Icosahedral Metallic Gold Cluster $Au_{144}(SR)_{60}$. *J. Phys. Chem. C* **2009**, *113*, 5035−5038.

(12) Walter, M.; Akola, J.; Lopez-Acevedo, O.; Jadzinsky, P. D.; Calero, G.; Ackerson, C. J.; Whetten, R. L.; Grönbeck, H.; Häkkinen, H. A Unified View of Ligand-Protected Gold Clusters as Superatom Complexes. *Proc. Natl. Acad. Sci.* **2008**, *105*, 9157−9162.

(13) Hicks, J. F.; Miles, D. T.; Murray, R. W. Quantized Double-Layer Charging of Highly Monodisperse Metal Nanoparticles. *J. Am. Chem. Soc.* **2002**, *124*, 13322−13328.

(14) Quinn, B. M.; Liljeroth, P.; Ruiz, V.; Laaksonen, T.; Kontturi, K. Electrochemical Resolution of 15 Oxidation States for Monolayer Protected Gold Nanoparticles. *J. Am. Chem. Soc.* **2003**, *125*, 6644−6645.

(15) Qian, H.; Zhu, Y.; Jin, R. Atomically Precise Gold Nanocrystal Molecules with Surface Plasmon Resonance. *Proc. Natl. Acad. Sci.* **2012**, *109*, 696−700.

(16) Dass, A. Faradaurate Nanomolecules: A Superstable Plasmonic 76.3 kDa Cluster. *J. Am. Chem. Soc.* **2011**, *133*, 19259−19261.

(17) Malola, S.; Lehtovaara, L.; Enkovaara, J.; Häkkinen, H. Birth of the Localized Surface Plasmon Resonance in Monolayer-Protected Gold Nanoclusters. *ACS Nano* **2013**, *7*, 10263−10270.

(18) Nuzzo, R. G.; Dubois, L. H.; Allara, D. L. Fundamental Studies of Microscopic Wetting on Organic Surfaces. 1. Formation and Structural Characterization of a Self-Consistent Series of Polyfunctional Organic Monolayers. *J. Am. Chem. Soc.* **1990**, *112*, 558−569.

(19) Arnold, R.; Azzam, W.; Terfort, A.; Woll, C. Preparation, Modification, and Crystallinity of Aliphatic and Aromatic Carboxylic Acid Terminated Self-Assembled Monolayers. *Langmuir* **2002**, *18*, 3980−3992.

(20) Rosendahl, S. M.; Burgess, I. J. Electrochemical and Infrared Spectroscopy Studies of 4-mercaptobenzoic Acid SAMs on Gold Surfaces. *Electrochim. Acta* **2008**, *53*, 6759−6767.

(21) Parikh, A. N.; Gillmor, S. D.; Beers, J. D.; Beardmore, K. M.; Cutts, R. W.; Swanson, B. I. Characterization of Chain Molecular Assemblies in Long-Chain, Layered Silver Thiolates: A Joint Infrared Spectroscopy and X-ray Diffraction Study. *J. Phys. Chem. B* **1999**, *103*, 2850−2861.

(22) Hostetler, M. J.; Stokes, J. J.; Murray, R. W. Infrared Spectroscopy of Three-Dimensional Self-Assembled Monolayers: N-Alkanethiolate Monolayers on Gold Cluster Compounds. *Langmuir* **1996**, *12*, 3604−3612.

(23) Schaaff, T. G.; Shafigullin, M. N.; Khoury, J. T.; Vezmar, I.; Whetten, R. L. Properties of a Ubiquitous 29 kDa Au:SR Cluster Compound. *J. Phys. Chem. B* **2001**, *105*, 8785−8796.

(24) Hulkko, E.; Lopez-Acevedo, O.; Koivisto, J.; Levi-Kalisman, Y.; Kornberg, R. D.; Pettersson, M.; Häkkinen, H. Electronic and Vibrational Signatures of the $Au_{102}(p\text{-}MBA)_{44}$ Cluster. *J. Am. Chem. Soc.* **2011**, *133*, 3752−3755.

(25) Koivisto, J.; Malola, S.; Kumara, C.; Dass, A.; Häkkinen, H.; Pettersson, M. Experimental and Theoretical Determination of the Optical Gap of the $Au_{144}(SC_2H_4Ph)_{60}$ Cluster and the $(Au/Ag)_{144}(SC_2H_4Ph)_{60}$ Nanoalloys. *J. Phys. Chem. Lett* **2012**, *3*, 3076−3080.

(26) Farrag, M.; Tschurl, M.; Dass, A.; Heiz, U. Infra-Red Spectroscopy of Size Selected Au_{25}, Au_{38} and Au_{144} Ligand Protected Gold Clusters. *Phys. Chem. Chem. Phys.* **2013**, *15*, 12539−12542.

(27) Ackerson, C. J.; Jadzinsky, P. D.; Sexton, J. Z.; Bushnell, D. A.; Kornberg, R. D. Synthesis and Bioconjugation of 2 and 3 nm-Diameter Gold Nanoparticles. *Bioconjugate Chem.* **2010**, *21*, 214−218.

(28) Wolff, H.; Szydlowski, J. Vibrational Spectra and Rotational Isomerism of Ethanethiol and Ethanethiol-D1. *Can. J. Chem.* **1985**, *63*, 1708−1712.

(29) Gardner, A. M.; Wright, T. G. Consistent Assignment of the Vibrations of Monosubstituted Benzenes. *J. Chem. Phys.* **2011**, *135*, 114305.

(30) Chandrasekaran, V.; Biennier, L.; Arunan, E.; Talbi, D.; Georges, R. Direct Infrared Absorption Spectroscopy of Benzene Dimer. *J. Phys. Chem. A* **2011**, *115*, 11263−11268.

(31) Hollenberg, J. L.; Dows, D. A. Absolute Infrared Intensities in Crystalline Benzene. *J. Chem. Phys.* **1962**, *37*, 1300−1307.

(32) Bertie, J. E.; Keefe, C. D. Infrared Intensities of Liquids XXIV: Optical Constants of Liquid Benzene-H6 at 25 C Extended to 11.5 cm^{-1} and Molar Polarizabilities and Integrated Intensities of Benzene-H6 Between 6200 and 11.5 cm^{-1}. *J. Mol. Struct.* **2004**, *695*−*696*, 39−57.

(33) Stoeva, S. I.; Prasad, B. L. V.; Uma, S.; Stoimenov, P. K.; Zaikovski, V.; Sorensen, C. M.; Klabunde, K. J. Face-Centered Cubic and Hexagonal Closed-Packed Nanocrystal Superlattices of Gold Nanoparticles Prepared by Different Methods. *J. Phys. Chem. B* **2003**, *107*, 7441−7448.

(34) Salorinne, K.; Lahtinen, T.; Koivisto, J.; Kalenius, E.; Nissinen, M.; Pettersson, M.; Häkkinen, H. Nondestructive Size Determination of Thiol-Stabilized Gold Nanoclusters in Solution by Diffusion Ordered NMR Spectroscopy. *Anal. Chem.* **2013**, *85*, 3489−3492.

(35) Bertie, J. E.; Apelblat, Y.; Keefe, C. D. Infrared Intensities of Liquids XXV: Dielectric Constants, Molar Polarizabilities and Integrated Intensities of Liquid Toluene at 25°C Between 4800 and 400 cm^{-1}. *J. Mol. Struct.* **2005**, *750*, 78−93.

(36) Bertie, J. E.; Apelblat, Y.; Keefe, C. D. Infrared Intensities of Liquids. Part XXIII. Infrared Optical Constants and Integrated

Downloaded by UNIV OF JYVASKYLA on September 3, 2015 | http://pubs.acs.org
Publication Date (Web): January 7, 2014 | doi: 10.1021/jz4026003

Intensities of Liquid Benzene-D1 at 25°C. *J. Mol. Struct.* **2000**, *550*−*551*, 135−165.
(37) Kakiuti, Y. Binary Combination Bands of the Out-of-Plane CH Vibrations of Benzene Derivatives. *J. Chem. Phys.* **1956**, *25*, 777−778.
(38) Pavlyuchko, A. I.; Vasilyev, E. V.; Gribov, L. A. Calculations of Molecular IR Spectra in the Overtone and Combination Frequency Regions. *J. Appl. Spectrosc.* **2011**, *78*, 639−645.
(39) Brown, T. L. Vibronic Contribution to the Infrared Intensities of Benzene. *J. Chem. Phys.* **1965**, *43*, 2780−2787.
(40) Tran, N. T.; Powell, D. R.; Dahl, L. F. Nanosized $Pd_{145}(CO)x(PEt_3)_{30}$ Containing a Capped Three-Shell 145-Atom Metal-Core Geometry of Pseudo Icosahedral Symmetry. *Angew. Chem., Int. Ed.* **2000**, *39*, 4121−4125.

Downloaded by UNIV OF JYVASKYLA on September 3, 2015 | http://pubs.acs.org
Publication Date (Web): January 7, 2014 | doi: 10.1021/jz4026003

Supporting information for:

Vibrational Perturbations and Ligand-Layer Coupling in a Single Crystal of $Au_{144}(SC_2H_4Ph)_{60}$ -Nanocluster

Jaakko Koivisto,[†] Kirsi Salorinne,[†] Satu Mustalahti,[†] Tanja Lahtinen,[†]

Sami Malola,[†,‡] Hannu Häkkinen,[†,‡] and Mika Pettersson[*,†]

Nanoscience Center, University of Jyväskylä, FI-40014 Jyväskylä, Finland.

E-mail: mika.j.pettersson@jyu.fi

[*]To whom correspondence should be addressed
[†]Department of Chemisty
[‡]Department of Physics

Table S1: Fundamental IR-transition energies of the phenyl-ring in PET. Notation adapted from table 4 in reference S1 and table 8 in reference S2. Only the most significant contribution of pure benzene modes have been considered when relating Gardner-Wright -notation to Herzberg- and Wilson-notations. The plane of the benzene-ring is chosen as the *yz*-plane, and therefore A_1 and B_2 symmetries denote in-plane while A_2 and B_1 denote out-of-plane vibrations. The vibrational modes are illustrated in fig. 5 of reference S1.

Symmetry (C_{2v})	Notation			$\tilde{\nu}_{obs}$ [cm^{-1}]		
	Herzberg	Wilson	Gardner	PET(l)	Au_{144} [a]	Au_{144} [b]
A_1	ν_1	ν_{20a}	M_2	3084.7 m	3084.8 m	3084.1 m
A_1	ν_2	ν_{7a}	M_3	3062.0 m	3062.0 m	3060.7 m
A_1	ν_3	ν_2	M_1	3105.7 w	3105.7 w	3103.9 m
A_1	ν_4	ν_{13}	M_4	1604.0 m	1603.8 m	~1604 m
A_1	ν_5	ν_{8a}	M_7	1496.9 s	1496.2 s	1497.7 m
A_1	ν_6	ν_{19a}	M_8	1199.4 w	1196.8 w	1196.8 m
A_1	ν_7	ν_{9a}	M_5	1179.0 w	1179.0 w	1179.0 m
A_1	ν_8	ν_{18a}	M_6	1030.6 w	1030.6 w	1030.6 w
A_1	ν_9	ν_{12}	M_9	1004.1 w	1005.7 w	1002.7 w
A_1	ν_{10}	ν_1	M_{10}	804.9 w	–	~806 sh
A_1	ν_{11}	ν_{6a}	M_{11}	489.8 m	–	–
A_2	ν_{12}	ν_{17a}	M_{12}	970.8 w	–	~966 w,sh
A_2	ν_{13}	ν_{10a}	M_{13}	845.5 w	–	841.6 m
A_2	ν_{14}	ν_{16a}	M_{14}	–	–	–
B_1	ν_{15}	ν_5	M_{15}	983 w,sh	–	982.7 w
B_1	ν_{16}	ν_{17b}	M_{16}	910.3 w	–	914.1 m
B_1	ν_{17}	ν_{10b}	M_{17}	732.1 s	–	–
B_1	ν_{18}	ν_4	M_{18}	698.0 s	–	–
B_1	ν_{19}	ν_{11}	M_{19}	559.9 m	–	–
B_1	ν_{20}	ν_{16b}	M_{20}	–	–	–
B_2	ν_{21}	ν_{20b}	M_{21}	3026.9 m	3028.3 m	3026.4 m
B_2	ν_{22}	ν_{7b}	M_{22}	3001.8 w	3001.8 w	3000.1 m
B_2	ν_{23}	ν_{8b}	M_{23}	1584.4 w	1584.1 w	1583.8 m
B_2	ν_{24}	ν_{19b}	M_{24}	1453.3 s	1453.3 s	1453.3 m
B_2	ν_{25}	ν_3	M_{25}	1322.7 w	1309.1 w	1309.1 m
B_2	ν_{26}	ν_{14}	M_{26}	1292 w,sh	1278 w,sh	~1279 m
B_2	ν_{27}	ν_{15}	M_{27}	1157.5 w,sh	1157.5 w	1157.5 m
B_2	ν_{28}	ν_{18b}	M_{28}	1076.3 w	1072.0 w	1072.0 m
B_2	ν_{29}	ν_{9b}	M_{29}	622.0 w	–	–
B_2	ν_{30}	ν_{6b}	M_{30}	–	–	–

s: strong, m: medium, w: weak, sh: shoulder.
[a] solvated in DCM-D2, [b] in single crystal.

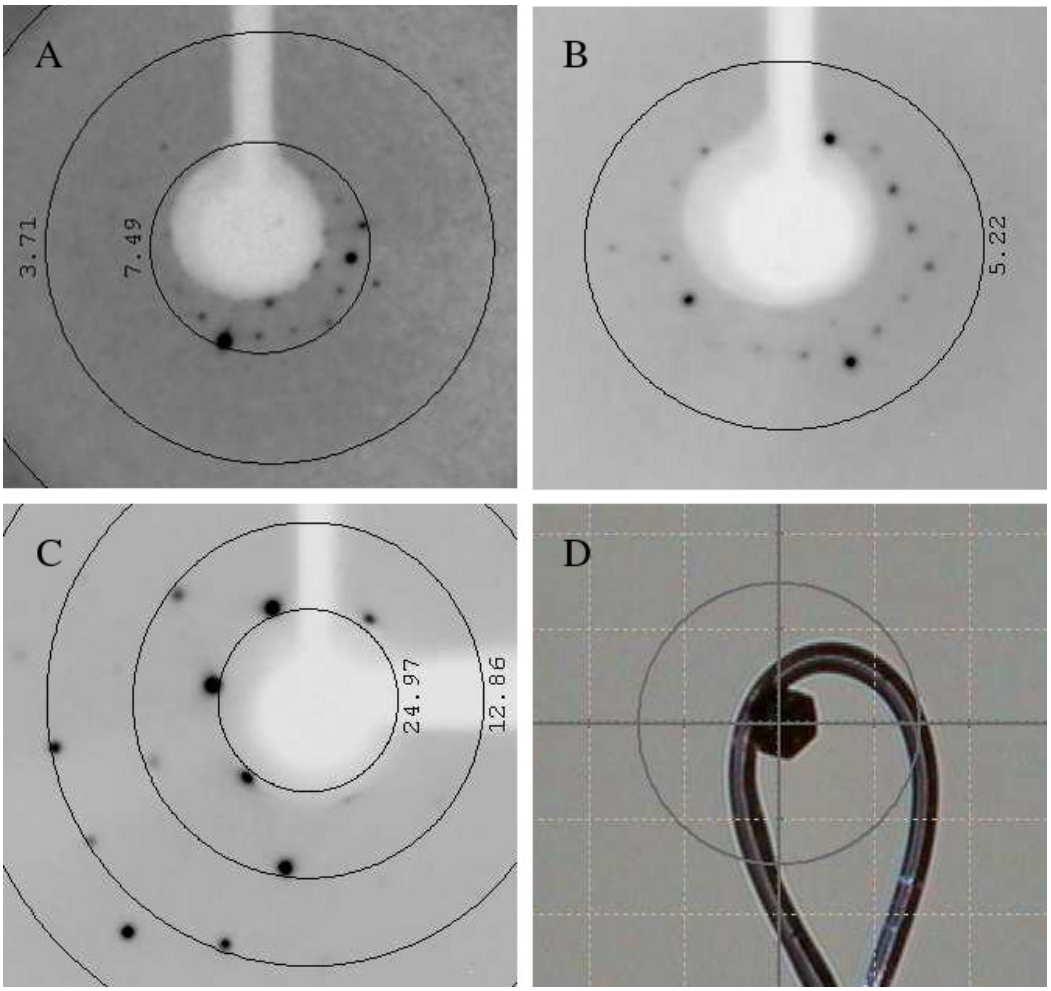

Figure S1: Diffraction patterns of $Au_{144}(PET)_{60}$ -single crystal as measured with molybdenum (fig. **A** and **B**) and copper (fig. **C**) X-ray sources using Agilent Supernova diffractometers. Measured crystal is illustrated in fig. **D**. The diffraction quickly vanishes after small 2θ-angles, but the overall hexagonal diffraction pattern is observed. The size of the unit cell was determined to be 27600 $Å^3$, indicating two particles of 3.0 nm diameter per unit cell.

Table S2: Observed fundamental vibrations of the aliphatic C_2H_4-chain.

Symmetry (C_S)	Notation	Assignment	$\tilde{\nu}_{obs}$ [cm^{-1}]		
			PET(l)	Au_{144} [a]	Au_{144} [b]
A'	ν_{31}	S-CH_2 sym. str.	2933.2 m	2927.5 m	2930.4 m
A'	ν_{32}	Ph-CH_2 sym. str.	2849.0 m	2852.2 m	2835.6 m
A'	ν_{33}	S-CH_2 scissor	~1447, sh	~1414 w	~1414 w
A'	ν_{34}	Ph-CH_2 scissor	~1428, w	~1433 w	~1433 w
A'	ν_{35}	CH_2-wag	1279.3 m	1262.1 m	~1265 m
A''	ν_{36}	S-CH_2 asym. str.	2963.8 m	2961.6 m	2962.4 m
A''	ν_{37}	Bz-CH_2 asym. str.	2908.2 m	2905.0 m	2897.2 m
A''	ν_{38}	CH_2-twist	1236.6 m	~1220 w	~1220 w
A''	ν_{39}	CH_2-rock	751.0 s	–	~750 m

s: strong, m: medium, w: weak, sh: shoulder.
S: adjacent to the sulfur, Ph: adjacent to the phenyl-ring.
[a] solvated in DCM-D2, [b] in single crystal.

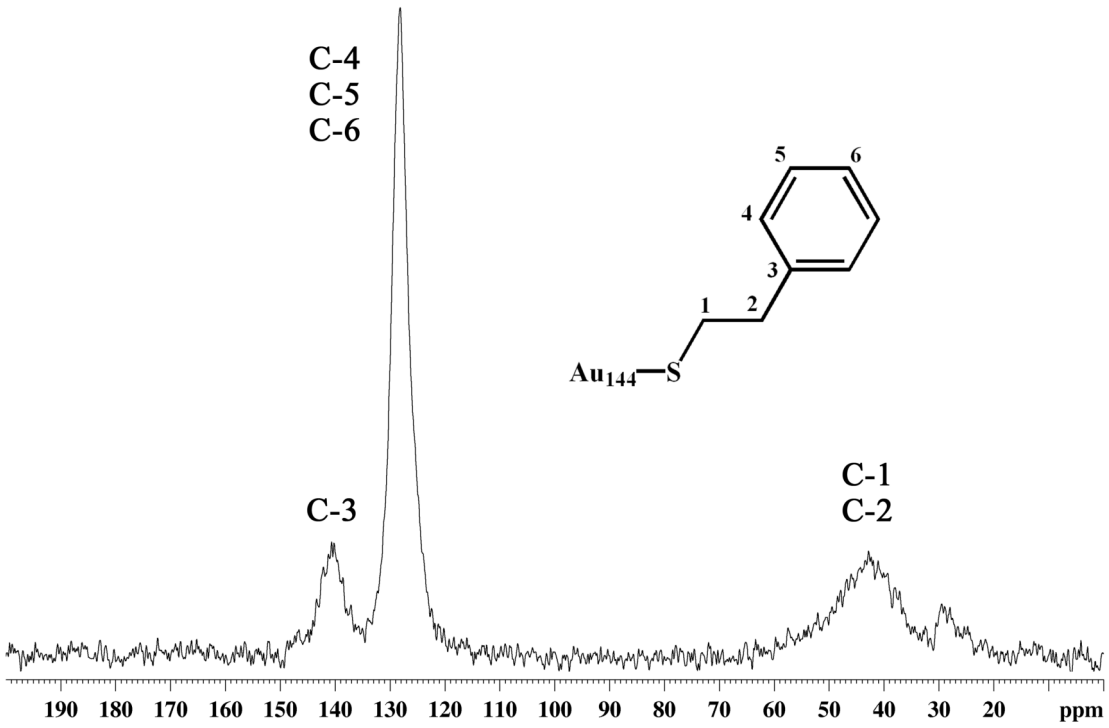

Figure S2: ^{13}C CP/MAS NMR spectrum of the crystalline $Au_{144}(PET)_{60}$ nanoclusters showing the different chemical environments of the PET ligand.

Table S3: Phenyl-ring overtone and combination mode assignments for crystalline $Au_{144}(PET)_{60}$ in the region 1600 cm^{-1} – 2700 cm^{-1}.[S2,S3]

$\tilde{\nu}_{obs}$ [cm^{-1}]	Assignment	Symmetry (C_{2v})
2675	—	—
2631	$M_4 + M_6$	$A_1 \otimes A_1 = A_1$
2606	$M_4 + M_9$	$A_1 \otimes A_1 = A_1$
2583	$M_4 + M_{15}$	$A_1 \otimes B_1 = B_1$
2546	$M_{12} + M_{23}$	$A_2 \otimes B_2 = B_1$
2524	$M_7 + M_6$ and/or $M_{24} + M_{28}$	$A_1 \otimes A_1 = A_1$ $B_2 \otimes B_2 = A_1$
2458	—	—
2425	$M_{13} + M_{23}$	$A_2 \otimes B_2 = B_1$
2255	$M_5 + M_{28}$	$A_1 \otimes B_2 = B_2$
2206	$M_5 + M_7$ and/or $M_{23} + M_{29}$	$A_1 \otimes A_1 = A_1$ $B_2 \otimes B_2 = A_1$
2174	—	—
2123	$M_{12} + M_{25}$	$A_2 \otimes B_2 = B_1$
2102	$M_6 + M_{28}$	$A_1 \otimes B_2 = B_2$
2082	—	—
2028	$M_6 + M_9$	$A_1 \otimes A_1 = A_1$
2011	$M_7 + M_{11}$	$A_1 \otimes A_1 = A_1$
1960	$2 \times M_{15}$	$B_1 \otimes B_1 = A_1$
1944	$M_{12} + M_{15}$	$A_2 \otimes B_1 = B_2$
1878	$M_{15} + M_{16}$ and/or $M_{12} + M_{16}$	$B_1 \otimes B_1 = A_1$ $A_2 \otimes B_1 = B_2$
1802	$M_{12} + M_{13}$	$A_2 \otimes A_2 = A_1$
1777	$M_{25} + M_{29}$	$B_2 \otimes B_2 = A_1$
1746	$M_{13} + M_{16}$	$A_2 \otimes B_1 = B_2$
1660	$M_{15} + M_{18}$ and/or $M_{12} + M_{18}$	$B_1 \otimes B_1 = A_2$ $B_1 \otimes A_2 = B_2$

References

(S1) Gardner, A. M.; Wright, T. G. *J. Chem. Phys.* **2011**, *135*, 114305.

(S2) Bertie, J. E.; Apelblat, Y.; Keefe, C. D. *J. Mol. Struct.* **2000**, *550–551*, 135–165.

(S3) Bertie, J. E.; Apelblat, Y.; Keefe, C. D. *J. Mol. Struct.* **2005**, *750*, 78–93.

Article III

Electron microscopy of gold nanoparticles at atomic resolution.

M. Azubel, J. Koivisto, S. Malola, D. Bushnell, G.L. Hura, A.L. Koh, H. Tsunoyama, T. Tsukuda, M. Pettersson, H. Häkkinen, and R.D. Kornberg.
Science, **2014**, *345*, p. 909.

Article not included in the electronic version of the thesis due to copyright restrictions. Available in the print version of the thesis, or from the AAAS website (DOI: 10.1126/science.1251959).

www.sciencemag.org/content/345/6199/909/suppl/DC1

Supplementary Materials for

Electron microscopy of gold nanoparticles at atomic resolution

Maia Azubel, Jaakko Koivisto, Sami Malola, David Bushnell, Greg L. Hura, Ai Leen Koh, Hironori Tsunoyama, Tatsuya Tsukuda, Mika Pettersson, Hannu Häkkinen, Roger D. Kornberg*

*Corresponding author. E-mail: kornberg@stanford.edu

Published 22 August 2014, *Science* **345**, 909 (2014)
DOI: 10.1126/science.1251959

This PDF file includes:

Materials and Methods

Synthesis

84 mM *3*-MBA (Sigma-Aldrich) and 28 mM $HAuCl_4$ (Sigma-Aldrich) solutions in 100 % (v/v) methanol were freshly prepare and mixed in a 2:1 ratio. 2.5 volumes of water were added and pH was adjusted to 13 with NaOH slowly (~ 100 mM final concentration for NaOH) until pellet was completely dissolved and solution turned from yellow to colorless. The mixture was equilibrated overnight on a rocking platform at room temperature. Methanol and water volumes were added to obtain a solution 2.72 mM *3*-MBA, 1.36 mM $HAuCl_4$, and 27% (v/v) methanol. 150 mM $NaBH_4$ freshly prepared was added in a 1.4:1 $NaHB_4$: $HAuCl_4$ ratio. Reaction proceeded for 4.5 hrs on rocking platform at room temperature. Reaction was stop by precipitating the product with 100 mM NaCl and 2 volumes of methanol, and span down for 10 min at 5,000 rpm. Supernatant was removed and pellet was washed with 75% methanol. The pellet dried on air overnight and was re-suspended in water. Yield of midsize scale (~100 ml) synthesis was in the milligram range and its solubility in the millimolar range. Aqueous solution is

stable at 4ºC for over 18 months, but particles could also be stored at room temperature as a dry pellet without affecting their solubility. Reaction product was run on a 10% glycerol, 12% polyacrylamide gel on TBE buffer for 30 min at 150 volts.

Transmission electron microscopy

For cryo-TEM, 3 µl Au_{68}NPs (1 mg/ml) applied to a glow discharged 200 mesh, Lacey carbon copper grid (SPI supplies), were frozen with a Vitrobot Mark V (FEI), after calibration of freezing parameters. The frozen-hydrated samples were imaged under low-dose conditions (~10 e−/Å^2) at a magnification of 80,000 and at a defocus range from −0.2 to −1.2 µm, using an FEI (Eindhoven, The Netherlands) Tecnai F20 FEG transmission electron microscope operating at 200 kV and equipped with 4K×4K CCD camera (Gatan US4000).

For AC-TEM, 2 µl Au_{68}NPs (2 mg/ml) were applied to a glow discharged, 400 mesh, ultrathin carbon film/holey carbon copper grid (Ted Pella, Inc.) for 30 seconds and gently blotted from the side to remove excess liquid. Dried samples were imaged using a low-dose strategy for searching and focusing. Images were recorded at ~ 800 e−/Å^2 at a magnification of 320,000 (pixel size 0.32Å), using a spherical aberration coefficient of ~ -10 µm and defocus value of ~ 1.5 nm, on an image aberration-corrected FEI (Eindhoven, The Netherlands) Titan 80-300 environmental (scanning) transmission electron microscope operating at 300kV and equipped with 2K×2K US1000XP Ultrascan CCD camera (Gatan Inc.).

Mass spectrometry

ESI mass spectra of Au_{68}NPs were collected on a homemade apparatus consisting of ESI source and TOF mass spectrometer (*28*). Au_{68}NPs (1.0 mg/mL) in 50% (v/v) methanol/water were electrosprayed at a flow rate of 1 µL/min through a stainless steel needle biased at about –3kV. To promote desolvation, charged liquid droplets were fed into a capillary heated resistively to about 180 ºC, forming desolvated cluster ions in the intact form. ESI mass spectra of $Na_nI_{n+1}^-$ cluster anions, recorded under the same condition, were used for calibration. Mass spectra collected at resolution of 400 m/Δm.

Thermal gravimetric analysis

Samples were dried in vacuum oven at 90ºC overnight and transferred into aluminum crucibles. TGA runs were recorded at a heating rate of 10^{o}C/min and temperature range of 25 - 600 ^{o}C on a Mettler Toledo TGA/SDTA 851 under a nitrogen flow of 20 ml/min.

X-ray photoelectron scattering

Dried Au_{68}NPs, mounted onto a double-size tape metal holder as powder, were analyzed with PHI 5000 VersaProbe Scanning ESCA microprobe (Physical Electronics, Chanhassen, MN) equipped with an Al (Kα) X-ray radiation source (1486.6eV, 46W) and spot size of about 200 µm

Bioconjugation

An oligodeoxyribonucleotide (500 μM**)** harboring 3ThioMC3-D modification (Integrated DNA Technologies) 5'CA GAT ATA TAA ATG CAA AAA CTG CAT AAC CAC TTT AAC TAA TAC TTT CAA/3ThioMC3-D/ 3' was reduced by treatment with 2 mM tris(2-carboxyethyl)phosphine (TCEP) for 1 h at 37 ºC. 4 μl aliquots of the reduced oligodeoxyribonucleotide at increasing concentrations (final concentration 25 μM, 50 μM, 100 μM, 200 μM) were incubated with 1 μl 1 mM Au_{68}NPs for 1 h at 37 ºC. Products were run on a 10% glycerol, 12% polyacrylamide gel on TBE buffer for 30 min at 150 volts.

A single chain fragment variable (scFv) antibody (1 mg/ml) directed against RNA polymerase II, containing a surface exposed cysteine, was reduced by treatment with 2 mM TCEP for 1 h at 37 ºC. 2 μl aliquots of the reduced scFv were incubated with 2 μl of Au_{68}NPs at increasing concentrations (final concentration 125 μM, 250 μM, 500 μM) for 1 h at 37 ºC. Products were run on a 10% glycerol, 12% SDS-polyacrilamide gel on SDS-PAGE buffer for 30 min at 150 volts.

Crystallization

Crystals were grown by the hanging drop technique in a solution containing 50 mM magnesium acetate tetrahydrate and 20% w/v polyethylene glycol 3,350 at 16ºC.

Three-dimensional reconstruction

The reconstruction was done using EMAN2 software package (*10*). Initially, 939 particles were extracted from images collected on the TITAN, using a box size of 120 x 120. Taking into consideration the relatively high signal of the individual images, particles were classified into 100 classes. The resulting reference-free class averages were used to generate an initial model. The model was iteratively refined using a projection matching approach. Only the 70% of particles having the highest cross-correlation coefficient were included in the final reconstruction. The final electron density map was subsequently converted into a format compatible with CCP4 software package (*29*) in order to perform a peak search.

SAXS

SAXS data were collected as previously described (*30*) at the SIBYLS beamline at the Advanced Light Source in Berkeley CA. Briefly, the samples were placed 1.5 m from a MAR165 CCD detector arranged co-axial with the 12 keV monochromatic beam; 1012 photons/second were impingent on the sample. The spot size at the sample was 4 × 1 mm convergent to a 100 μm spot at the detector. Buffer subtraction and raw image data were integrated by beamline software specific for this arrangement. Processing of SAXS data was conducted utilizing the Scatter package. Three concentrations were measured (1.10 mM, 0.73 mM and 0.36 mM). All three concentrations were in agreement with one another. Four exposure times were compared against one another (0.5, 1, 2 and 5 seconds) and all four were identical to within noise. SAXS were collected from Au_{68}NP in both pure water and 100 mM KCl. In both conditions most of the sample was monodispersed monomer. However in the pure water condition, signals of large multiparticle aggregates were also readily visible by their contribution to the Giunier region. These aggregates were readily dispersed by adding 100mM KCl to the same

solution as assayed by a linear Guinier region with a Radius of gration (Rg) of 7.6 Å. Aggregates are thus reversible.

Absorption spectra

Optical spectrum was measured with Perkin Elmer Lambda 850 UV/Vis -spectrometer using quartz cuvette with 1 mm optical path length. Infrared spectrum was measured using Nicolet Magna-IR 760 FTIR -spectrometer. The sample was dropcasted on CaF_2 -window and dried in vacuum.

Computational methods

For the computational modeling, we used DFT as implemented in the real-space code-package GPAW (Grid-based projector- augmented wave method) (*31*). Structure optimization was performed using local density approximation (LDA) as the exchange-correlation functional in order to get more realistic Au-Au distances. 0.2 Å grid spacing and 0.05 eV/Å convergence criterion for the maximum forces acting on atoms in clusters were used. The GPAW setups for Au include scalar-relativistic corrections. Optical absorption spectra were calculated with Perdew-Burke-Ernzerhof (PBE) functional using linear response TDDFT (*32*). In the model structures we used SH-groups instead of true *3*-MBA ligand. Ligand–ligand interactions between carboxylic acid groups of *3*-MBA were estimated using two representative ligands as a separated hydrogen-bonded ligand pair. The interactions were calculated using both PBE and LDA functionals. To model the effects of ligand-ligand interactions on the Au_{68} cluster we used two *3*-MBA ligands in the model structure of $Au_{68}(SH)_{30}(3\text{-MBA})_2$, the rest of the ligands being still modeled with SH-groups (see Fig. S9b)

Fig. S1.

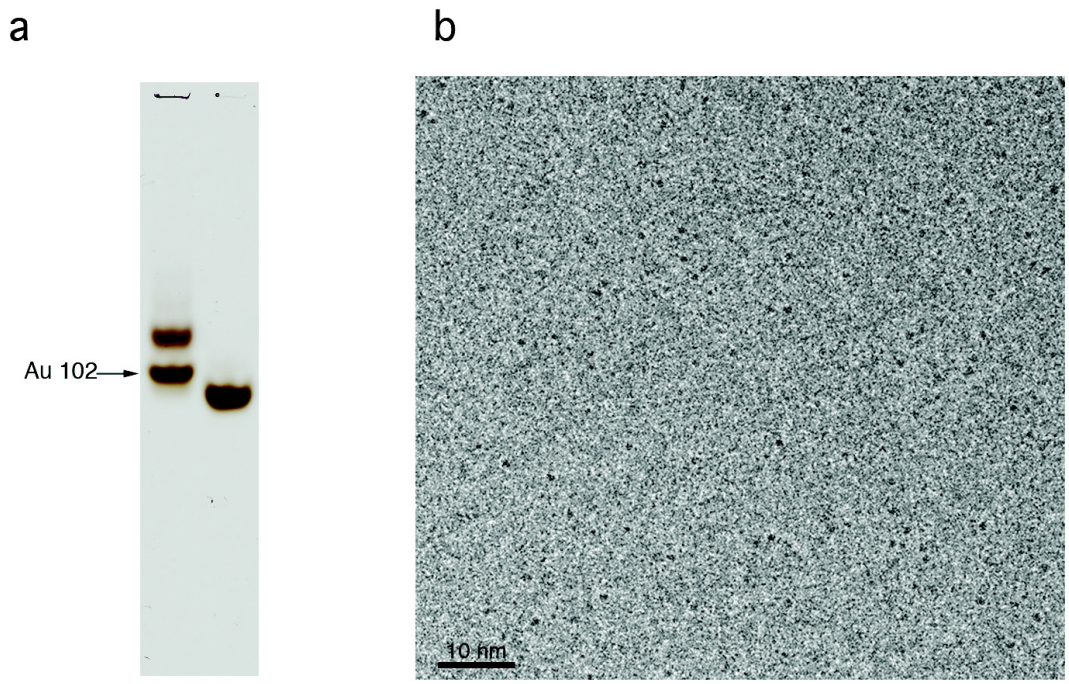

Fig. S1. Homogeneity analysis. (a) Products obtained directly from Au_{102}(*p*-MBA)$_{44}$ (left lane) and Au_{68}NP (right lane) syntheses were run in a 12% PAGE. Arrow indicates Au_{102}(*p*-MBA)$_{44}$. (b) Cryo –EM micrograph of Au_{68}NP.

Fig. S2

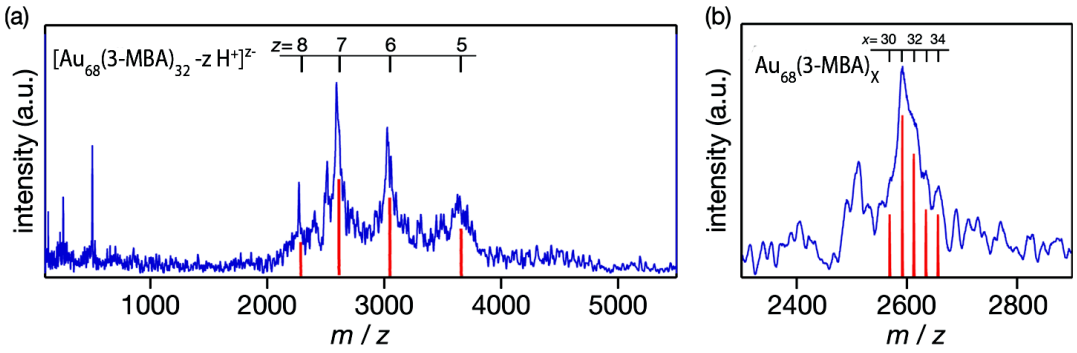

Fig. S2. ESI-MS data for the Au_{68}NP sample. a) Full spectrum b) Close-up of 7^- charge state peak.

Fig. S3

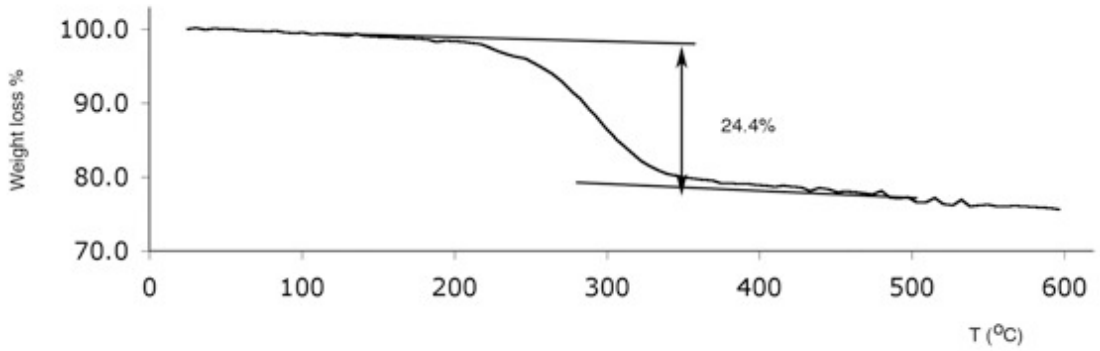

Fig. S3. TGA curve of Au_{68}NP

Fig. S4

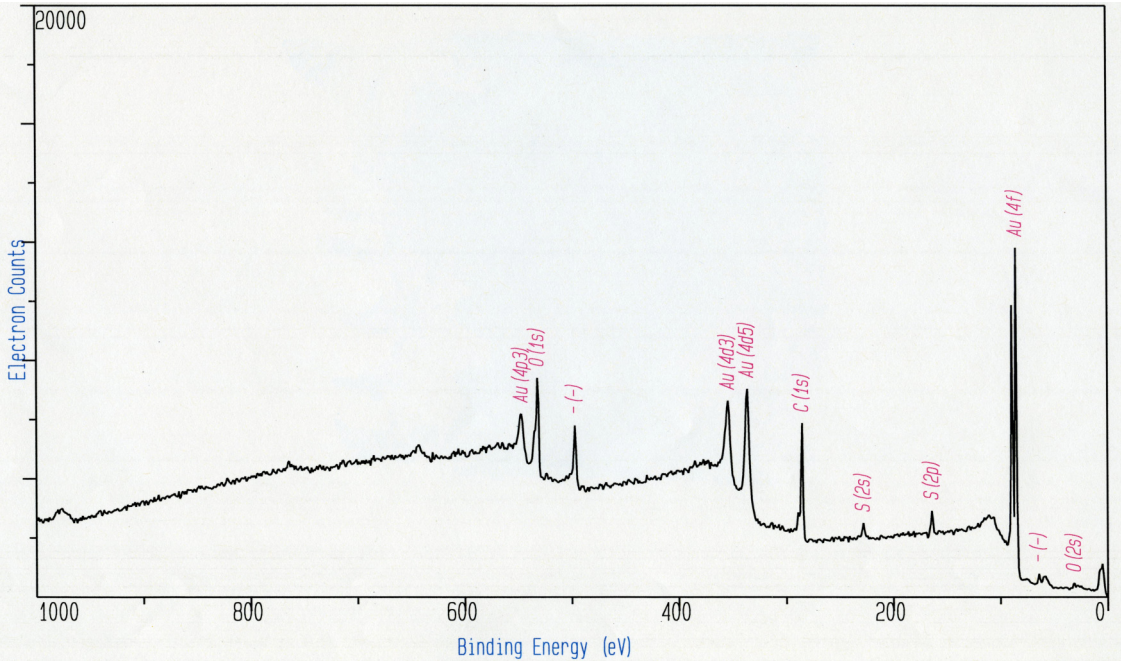

Fig S4. XPS survey spectrum for Au_{68}NP

Fig. S5

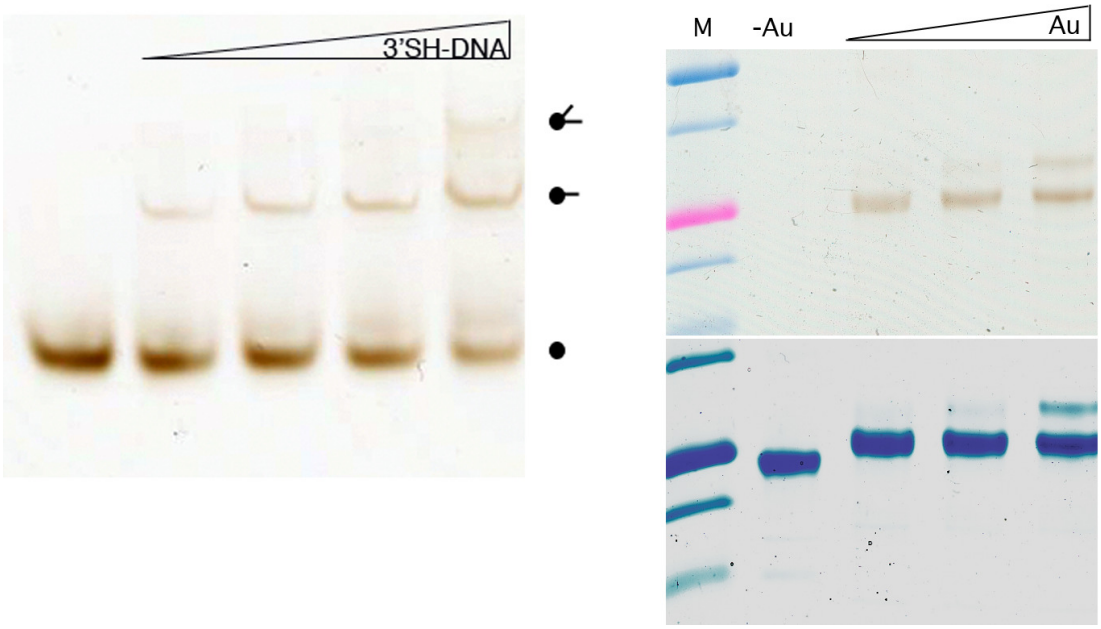

Fig S5. Bioconjugation of Au_{68}NP. (a) Increasing concentration of 3'end thiol modified oligodeoxynucleotide (3'SH-DNA) incubated with Au_{68}NP and analyzed by 12% PAGE. Diagram to the right: ball indicates free AuNPs ; ball with one or two bars indicate AuNPs conjugated to one or two, respectively, molecules of DNA. (b) Increasing concentration of Au_{68}NP incubated with scFv and analyzed by 10% SDS-PAGE, unstained (top panel) or stained with Coomassie blue (bottom panel). Left lane (M), precision plus protein standards (BioRad). Second lane from left (-Au), unlabeled scFv.

Fig S6

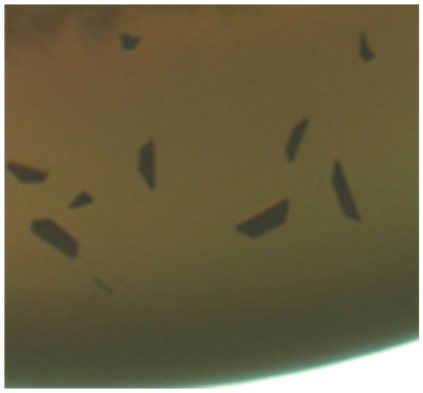

Fig S6. Crystals of Au_{68}NP imaged by light microscopy.

Fig S7

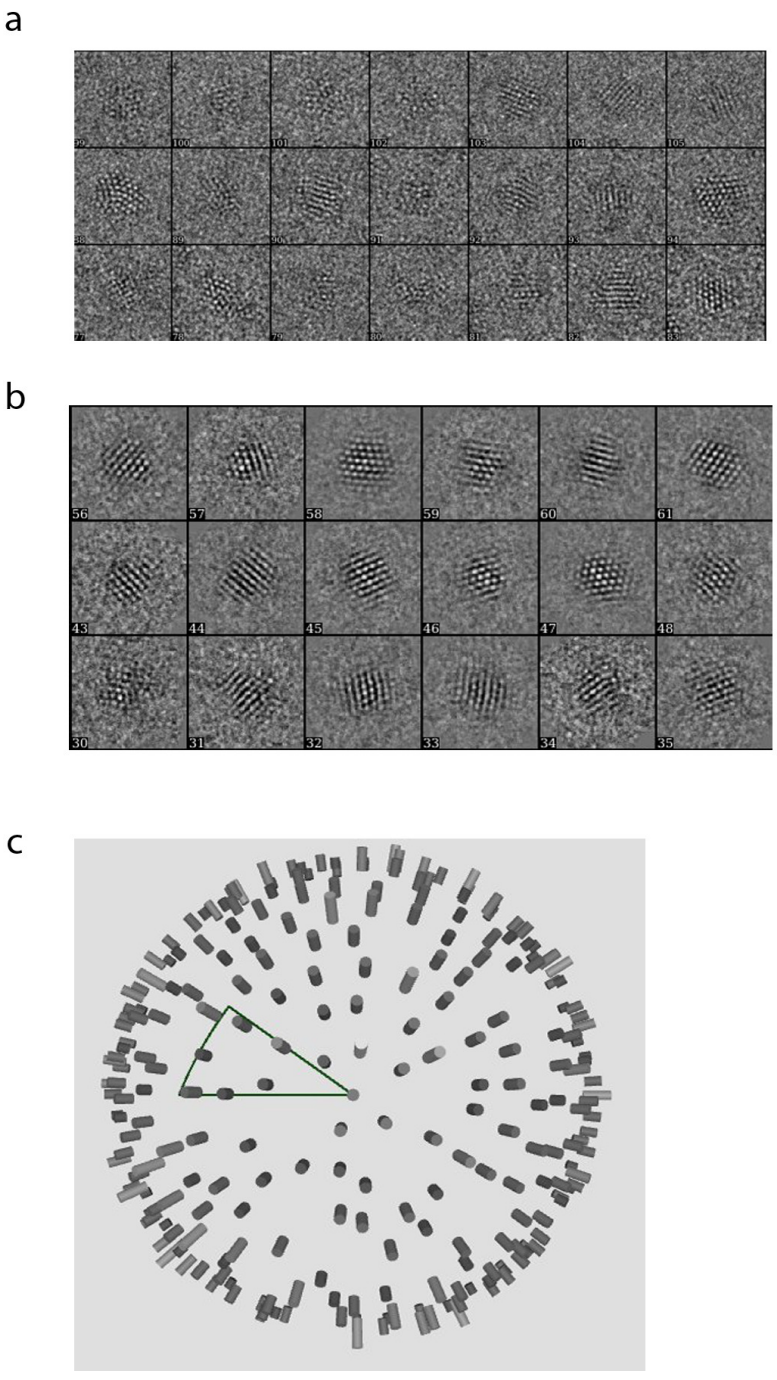

Fig S7. Single Particle reconstruction of Au_{68}NP. (a) Gallery of representative raw image particles. (b) Gallery of representative class averages. (c) Distribution of 2D projections images across the Euler space. The height of each point-bar is proportional to

the number of particles assigned to that projection. For further analysis see Fig 1a of the main text

Fig S8

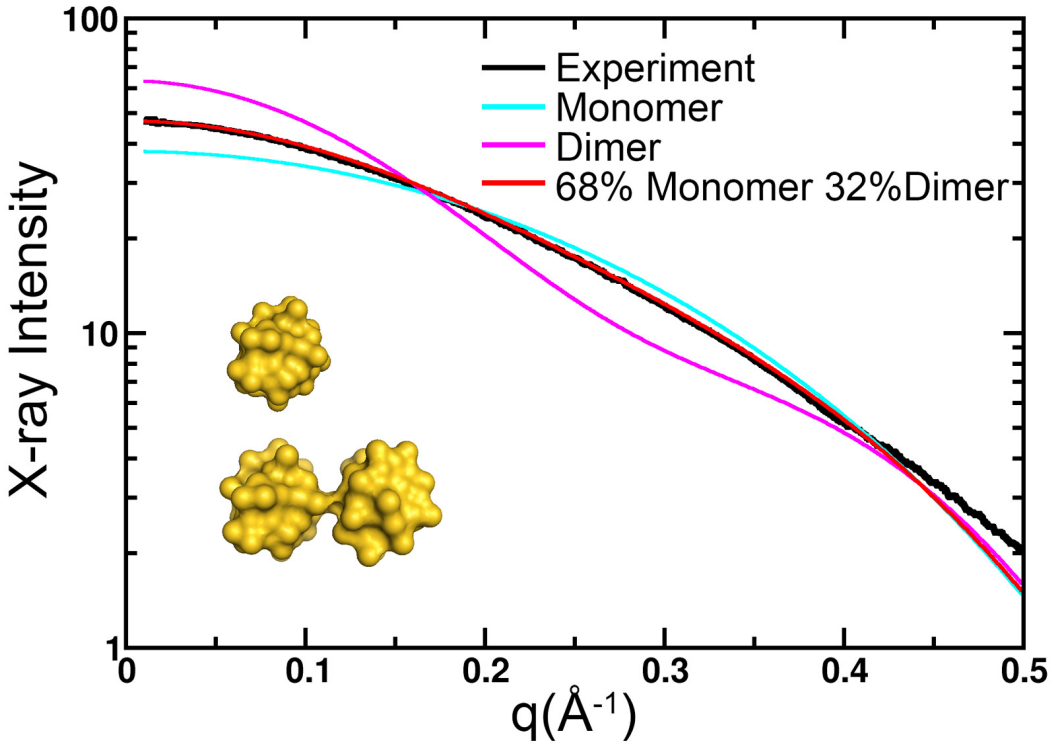

Fig S8. Small angle X-ray scattering (SAXS) from Au_{68}NPs. Using atomic coordinates of monomers and modeled dimers (bottom inset) the calculated SAXS profiles were compared against experiment. A mixture (red) with a major population of monomer (cyan) and minor population dimer (magenta) had a best fit.

Fig S9

a

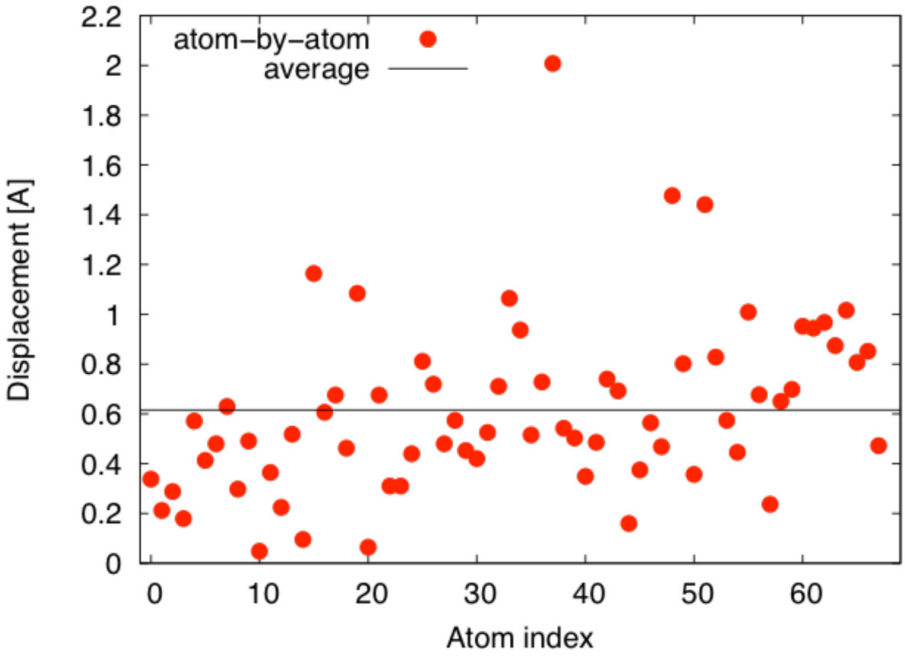
atom–by–atom
average
Displacement [A]
Atom index
0
0.2
0.4
0.6
0.8
1
1.2
1.4
1.6
1.8
2
2.2
0
10
20
30
40
50
60

b

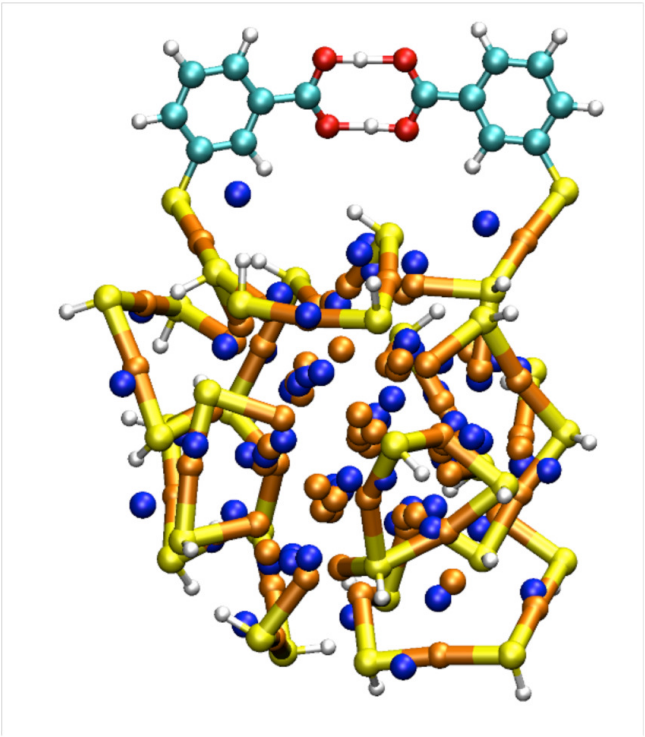

Fig S9. **AC-TEM and DFT coordinators comparison** (a) Displacements of the gold atoms observed during the DFT relaxation of the $Au_{68}(SH)_{32}$ cluster, started from the experimental positions of gold in the EM data. (b) The DFT-relaxed model structure of $Au_{68}(SH)_{30}$(*3*-MBA)$_2$ showing the special position of the Au-atoms in the double hydrogen bonded units including *3*-MBA ligands. In the model structure sulfur atoms are represented in yellow, gold in orange, carbon in light blue, oxygen in red and hydrogen in white. The experimentally determined Au atom positions are shown in blue.

Fig S10

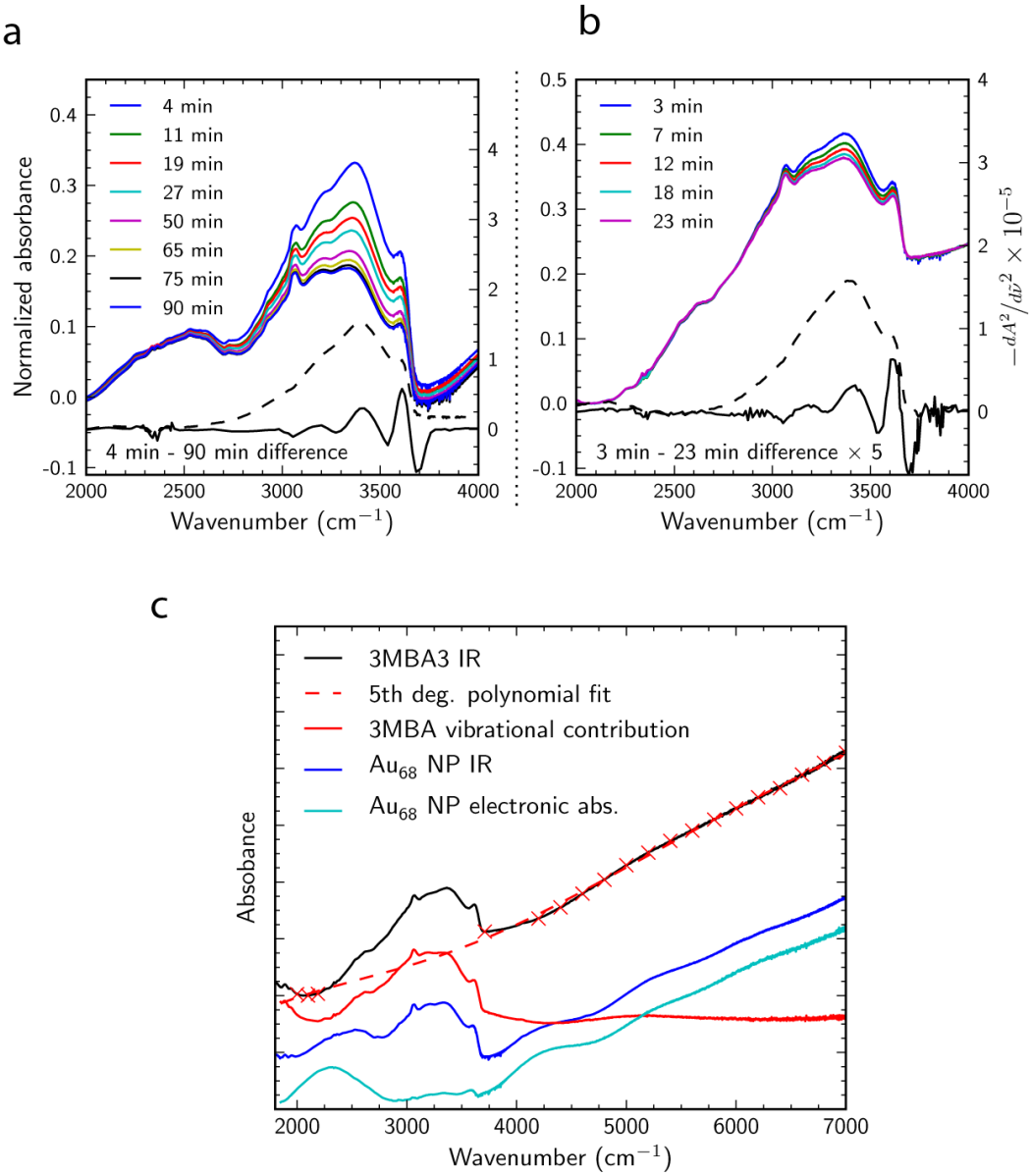

Fig S10. IR-absorption of the Au$_{68}$NP. (a) The evaporation of adsorbed water under IR-irradiation and purging with dry air in the spectrometer is observed as decrease of the OH-stretching vibration in 2500-3700 cm^{-1}. The difference between first and last measurements (4 min and 90 min) is plotted as dotted line, and its second derivative

shows four peaks consistent with water OH-stretch at various degrees of hydrogen bonding. (b) Same as Fig. (a) for a larger (Au-3MBA)NP (referred hereafter as 3MBA3) . (c) Spectra used in removing the vibrational signatures of the 3MBA-ligand from the IR-spectrum of the Au_{68}NP sample. In the fingerprint region below 1800 cm^{-1} the spectra of both Au68 and 3MBA3 are identical, except for small changes in peak width, confirming that the ligand vibrations are not significantly affected by the cluster size in dropcast samples. 5th degree polynomial was used in a fit (fit points marked with red crosses) to approximate the broad featureless electronic absorption of the larger 3MBA3 cluster. The fit was then removed from the IR-spectrum of 3MBA3 to give only the vibrational absorptions (3MBA vib.). Finally this was removed from the spectrum of Au_{68}NP to give its electronic absorption (electronic abs)

Fig S11

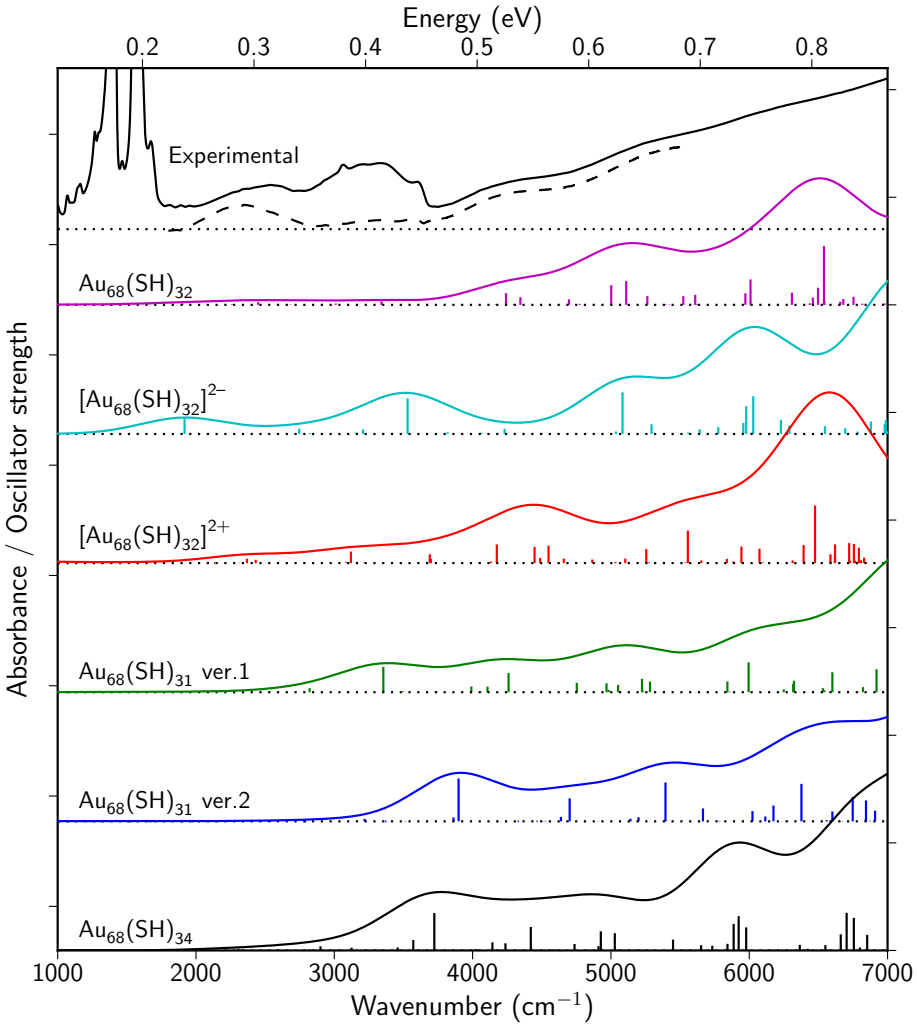

Fig S11. Absorption spectra comparison. Additional absorption spectra calculated for cluster compounds in the range of $Au_{68}(SH)_{31\text{-}34}$ do not reproduce the measured IR data (top panel) as successfully as the $Au_{68}(SH)_{32}$ structure shown in Fig. 3 of the main text.

References and Notes

1. N. L. Rosi, D. A. Giljohann, C. S. Thaxton, A. K. R. Lytton-Jean, M. S. Han, C. A. Mirkin, Oligonucleotide-modified gold nanoparticles for intracellular gene regulation. *Science* **312**, 1027–1030 (2006). Medline doi:10.1126/science.1125559

2. X. Qian, X.-H. Peng, D. O. Ansari, Q. Yin-Goen, G. Z. Chen, D. M. Shin, L. Yang, A. N. Young, M. D. Wang, S. Nie, In vivo tumor targeting and spectroscopic detection with surface-enhanced Raman nanoparticle tags. *Nat. Biotechnol.* **26**, 83–90 (2008). Medline doi:10.1038/nbt1377

3. M.-C. Daniel, D. Astruc, Gold nanoparticles: Assembly, supramolecular chemistry, quantum-size-related properties, and applications toward biology, catalysis, and nanotechnology. *Chem. Rev.* **104**, 293–346 (2004). Medline doi:10.1021/cr030698+

4. P. D. Jadzinsky, G. Calero, C. J. Ackerson, D. A. Bushnell, R. D. Kornberg, Structure of a thiol monolayer-protected gold nanoparticle at 1.1 Å resolution. *Science* **318**, 430–433 (2007). Medline doi:10.1126/science.1148624

5. M. Walter, J. Akola, O. Lopez-Acevedo, P. D. Jadzinsky, G. Calero, C. J. Ackerson, R. L. Whetten, H. Grönbeck, H. Häkkinen, A unified view of ligand-protected gold clusters as superatom complexes. *Proc. Natl. Acad. Sci. U.S.A.* **105**, 9157–9162 (2008). Medline doi:10.1073/pnas.0801001105

6. H. Häkkinen, The gold-sulfur interface at the nanoscale. *Nat. Chem.* **4**, 443–455 (2012). Medline doi:10.1038/nchem.1352

7. R. L. Whetten, J. T. Khoury, M. M. Alvarez, S. Murthy, I. Vezmar, Z. L. Wang, P. W. Stephens, C. L. Cleveland, W. D. Luedtke, U. Landman, Nanocrystal gold molecules. *Adv. Mater.* **8**, 428–433 (1996). doi:10.1002/adma.19960080513

8. Y. Levi-Kalisman, P. D. Jadzinsky, N. Kalisman, H. Tsunoyama, T. Tsukuda, D. A. Bushnell, R. D. Kornberg, Synthesis and characterization of Au_{102}(*p*-MBA)$_{44}$ nanoparticles. *J. Am. Chem. Soc.* **133**, 2976–2982 (2011). Medline doi:10.1021/ja109131w

9. J. Frank, Single-particle imaging of macromolecules by cryo-electron microscopy. *Annu. Rev. Biophys. Biomol. Struct.* **31**, 303–319 (2002). Medline doi:10.1146/annurev.biophys.31.082901.134202

10. G. Tang, L. Peng, P. R. Baldwin, D. S. Mann, W. Jiang, I. Rees, S. J. Ludtke, EMAN2: An extensible image processing suite for electron microscopy. *J. Struct. Biol.* **157**, 38–46 (2007). Medline

11. C. Zeng, H. Qian, T. Li, G. Li, N. L. Rosi, B. Yoon, R. N. Barnett, R. L. Whetten, U. Landman, R. Jin, Total structure and electronic properties of the gold nanocrystal $Au_{36}(SR)_{24}$. *Angew. Chem. Int. Ed.* **51**, 13114–13118 (2012). Medline doi:10.1002/anie.201207098

12. See supplementary materials on *Science* Online.

13. H. Häkkinen, M. Walter, H. Grönbeck, Divide and protect: Capping gold nanoclusters with molecular gold-thiolate rings. *J. Phys. Chem. B* **110**, 9927–9931 (2006). Medline doi:10.1021/jp0619787

14. E. Hulkko, O. Lopez-Acevedo, J. Koivisto, Y. Levi-Kalisman, R. D. Kornberg, M. Pettersson, H. Häkkinen, Electronic and vibrational signatures of the Au_{102}(*p*-MBA)$_{44}$ cluster. *J. Am. Chem. Soc.* **133**, 3752–3755 (2011). Medline doi:10.1021/ja111077e

15. J. Akola, M. Walter, R. L. Whetten, H. Häkkinen, H. Grönbeck, On the structure of thiolate-protected Au_{25}. *J. Am. Chem. Soc.* **130**, 3756–3757 (2008). Medline doi:10.1021/ja800594p

16. M. W. Heaven, A. Dass, P. S. White, K. M. Holt, R. W. Murray, Crystal structure of the gold nanoparticle [$N(C_8H_{17})_4$][$Au_{25}(SCH_2CH_2Ph)_{18}$]. *J. Am. Chem. Soc.* **130**, 3754–3755 (2008). Medline doi:10.1021/ja800561b

17. M. Zhu, C. M. Aikens, F. J. Hollander, G. C. Schatz, R. Jin, Correlating the crystal structure of a thiol-protected Au_{25} cluster and optical properties. *J. Am. Chem. Soc.* **130**, 5883–5885 (2008). Medline doi:10.1021/ja801173r

18. O. Lopez-Acevedo, H. Tsunoyama, T. Tsukuda, H. Häkkinen, C. M. Aikens, Chirality and electronic structure of the thiolate-protected Au38 nanocluster. *J. Am. Chem. Soc.* **132**, 8210–8218 (2010). Medline doi:10.1021/ja102934q

19. H. Qian, W. T. Eckenhoff, Y. Zhu, T. Pintauer, R. Jin, Total structure determination of thiolate-protected Au_{38} nanoparticles. *J. Am. Chem. Soc.* **132**, 8280–8281 (2010). Medline doi:10.1021/ja103592z

20. J. Koivisto, K. Salorinne, S. Mustalahti, T. Lahtinen, S. Malola, H. Häkkinen, M. Pettersson, Vibrational perturbations and ligand-layer coupling in a single crystal of $Au_{144}(SC_2H_4Ph)_{60}$ nanocluster. *J. Phys. Chem. Lett.* **5**, 387–392 (2014). doi:10.1021/jz4026003

21. P. R. Nimmala, B. Yoon, R. L. Whetten, U. Landman, A. Dass, $Au_{67}(SR)_{35}$ nanomolecules: Characteristic size-specific optical, electrochemical, structural properties and first-principles theoretical analysis. *J. Phys. Chem. A* **117**, 504–517 (2013). Medline doi:10.1021/jp311491v

22. J. A. Scholl, A. L. Koh, J. A. Dionne, Quantum plasmon resonances of individual metallic nanoparticles. *Nature* **483**, 421–427 (2012). Medline doi:10.1038/nature10904

23. D. Bahena, N. Bhattarai, U. Santiago, A. Tlahuice, A. Ponce, S. B. H. Bach, B. Yoon, R. L. Whetten, U. Landman, M. Jose-Yacaman, STEM electron diffraction and high resolution images used in the determination of the crystal structure of the $Au_{144}(SR)_{60}$ cluster. *J. Phys. Chem. Lett.* **4**, 975–981 (2013). Medline doi:10.1021/jz400111d

24. Z. Y. Li, N. P. Young, M. Di Vece, S. Palomba, R. E. Palmer, A. L. Bleloch, B. C. Curley, R. L. Johnston, J. Jiang, J. Yuan, Three-dimensional atomic-scale structure of size-selected gold nanoclusters. *Nature* **451**, 46–48 (2008). Medline doi:10.1038/nature06470

25. M. C. Scott, C.-C. Chen, M. Mecklenburg, C. Zhu, R. Xu, P. Ercius, U. Dahmen, B. C. Regan, J. Miao, Electron tomography at 2.4-ångström resolution. *Nature* **483**, 444–447 (2012). Medline doi:10.1038/nature10934

26. S. Van Aert, K. J. Batenburg, M. D. Rossell, R. Erni, G. Van Tendeloo, Three-dimensional atomic imaging of crystalline nanoparticles. *Nature* **470**, 374–377 (2011). Medline doi:10.1038/nature09741

27. B. Goris, S. Bals, W. Van den Broek, E. Carbó-Argibay, S. Gómez-Graña, L. M. Liz-Marzán, G. Van Tendeloo, Atomic-scale determination of surface facets in gold nanorods. *Nat. Mater.* **11**, 930–935 (2012). Medline doi:10.1038/nmat3462

28. Y. Negishi, K. Nobusada, T. Tsukuda, Glutathione-protected gold clusters revisited: Bridging the gap between gold(I)-thiolate complexes and thiolate-protected gold nanocrystals. *J. Am. Chem. Soc.* **127**, 5261–5270 (2005). Medline doi:10.1021/ja042218h

29. M. D. Winn, C. C. Ballard, K. D. Cowtan, E. J. Dodson, P. Emsley, P. R. Evans, R. M. Keegan, E. B. Krissinel, A. G. W. Leslie, A. McCoy, S. J. McNicholas, G. N. Murshudov, N. S. Pannu, E. A. Potterton, H. R. Powell, R. J. Read, A. Vagin, K. S. Wilson, Overview of the *CCP*4 suite and current developments. *Acta Crystallogr. D Biol. Crystallogr.* **67**, 235–242 (2011). Medline doi:10.1107/S0907444910045749

30. G. L. Hura, A. L. Menon, M. Hammel, R. P. Rambo, F. L. Poole 2nd, S. E. Tsutakawa, F. E. Jenney Jr., S. Classen, K. A. Frankel, R. C. Hopkins, S. J. Yang, J. W. Scott, B. D. Dillard, M. W. W. Adams, J. A. Tainer, Robust, high-throughput solution structural analyses by small angle x-ray scattering (SAXS). *Nat. Methods* **6**, 606–612 (2009). Medline doi:10.1038/nmeth.1353

31. J. Enkovaara, C. Rostgaard, J. J. Mortensen, J. Chen, M. Dułak, L. Ferrighi, J. Gavnholt, C. Glinsvad, V. Haikola, H. A. Hansen, H. H. Kristoffersen, M. Kuisma, A. H. Larsen, L. Lehtovaara, M. Ljungberg, O. Lopez-Acevedo, P. G. Moses, J. Ojanen, T. Olsen, V. Petzold, N. A. Romero, J. Stausholm-Møller, M. Strange, G. A. Tritsaris, M. Vanin, M. Walter, B. Hammer, H. Häkkinen, G. K. H. Madsen, R. M. Nieminen, J. K. Nørskov, M. Puska, T. T. Rantala, J. Schiøtz, K. S. Thygesen, K. W. Jacobsen, Electronic structure calculations with GPAW: A real-space implementation of the projector augmented-wave method. *J. Phys. Condens. Matter* **22**, 253202 (2010). Medline doi:10.1088/0953-8984/22/25/253202

32. M. Walter, H. Häkkinen, L. Lehtovaara, M. Puska, J. Enkovaara, C. Rostgaard, J. J. Mortensen, Time-dependent density-functional theory in the projector augmented-wave method. *J. Chem. Phys.* **128**, 244101 (2008). Medline doi:10.1063/1.2943138

Article IV

Experimental and computational determination of the protonation states of the water-soluble $Au_{102}(p\text{MBA})_{44}$-nanocluster.

By

J. Koivisto, X. Chen, S. Donnini, T. Lahtinen, H. Häkkinen, G. Groenhoff, and M. Pettersson.

Manuscript in preparation

Journal Name

ARTICLE TYPE

Cite this: DOI: 10.1039/xxxxxxxxxx

Experimental and computational determination of the protonation states of the water-soluble Au_{102}(*p*MBA)$_{44}$-nanocluster. †

Jaakko Koivisto,[a] Xi Chen,[a] Serena Donnini,[b] Tanja Lahtinen,[a] Hannu Häkkinen,[a,c] Gerrit Groenhof,[a] and Mika Pettersson[a]*

Received Date
Accepted Date

DOI: 10.1039/xxxxxxxxxx

www.rsc.org/journalname

The acid-constant pK_a of the *para*-mercaptobenzoic acid (*p*MBA) ligands in the Au_{102}(*p*MBA)$_{44}$ nanocluster was measured by using acid-base and IR-titration. The observed macroscopic $pK_a = 6.18 \pm 0.05$ is significantly more basic than free *p*MBA ($pK_a = 4.16$), and the protonation behaviour is anti-cooperative according to the Hill-coefficient $n = 0.64 \pm 0.04$. The cluster is truly water-soluble when more than 22, and insoluble when less than 7 ligands are in the deprotonated state. The cluster was modeled at pH 6.20 using constant pH molecular dynamics simulations. The pK_a values of the individual *p*MBA's are in the range of 5.18 to 7.58, depending on the positions of the ligands, generating a non-uniform charge distribution on the cluster surface. The cluster interactions with inorganic and biological environment depend on the surface charge distribution, stressing the importance of understanding the protonation state of the cluster.

Introduction

Noble metal nanoparticles have many interesting properties including optical, electrochemical, and catalytic properties which arise from the quantum confinement of electronic states as the cluster size decreases[1–5]. Water-soluble noble-metal clusters are particularly interesting due to their possible biological applications, such as drug delivery[6], local heating probes[7], or biolabeling[8–12].

Recently several authors have stressed the importance of the choice of the ligand as a driving factor on size-selective synthesis or etching of certain nanocluster sizes[13–16]. Of equal importance is the fact that while the physical properties, such as electronic and optical properties, are governed mainly by the core structure and composition, the chemical properties of the cluster, such as solubility and reactivity, result almost exclusively from the composition and structure of the ligand-layer.

Important aspect for applications of nanoscopic clusters in biology is the biocompatibility of the material. While bulk gold is well known to be biologically inactive, several authors have reported cytotoxic effects caused by small nanoclusters[17]. Nanoclusters can interact with cell membranes through electrostatics, and depending on the cluster charge state, anionic clusters permeate into the membrane inertly[18,19], while cationic clusters permeate through the membrane and induce holes in it leading to cell death[20–22]. The chemical activity of the ligands, e.g. oxidation, can also have adverse effects inside biological systems[23]. Therefore controlling the properties and the interaction of the ligand layer with the surrounding medium is of critical importance for many applications.

Water soluble particles can be created by using ligands containing strongly polar functional groups, such as aliphatic or aromatic carboxylic acids, sulfonates, or amides[18,19,24]. *meta*- and *para*-mercaptobenzoic acids (*m*MBA, *p*MBA) are frequently used for water soluble gold or silver clusters with sizes ranging from Ag_{44}(*p*MBA)$_{30}$ to Au_{459}(*p*MBA)$_{170}$[16,25–27], and in both larger plasmonic particles and 2D-surfaces[28–32]. For large particles and monolayers the behaviour of the ligand-layer has been studied extensively, including surface-enhanced Raman-scattering (SERS) enhancement and the use of the ligand protonation state as local pH-probes[28,29,33,34].

For discrete sized nanoclusters (less than 150 atoms), systematic studies of the protonation are more rare than for larger systems. Conn *et.al.* reported different solubility and stability behaviour for $[Ag_{44}(pMBA)_{30}]^{4-}$ -cluster depeding on the ligand-layer protonation[25]. Kobyashi *et.al.* demonstrated change of

* *Corresponding Author: mika.j.pettersson@jyu.fi*
[a] *Department of Chemistry, Nanoscience Center, University of Jyväskylä, FI-40014 Finland.*
[b] *Department of Biological and Environmental Sciences, University of Jyväskylä, FI-40014 Finland.*
[c] *Department of Physics, Nanoscience Center, University of Jyväskylä FI-40014, Finland.*
† Electronic Supplementary Information (ESI) available: [details of any supplementary information available should be included here]. See DOI: 10.1039/b000000x/

absorbance and photoluminescence properties of Au_8 cluster depending on the protonation state of two pyridylethyl-rings in the ligand layer[35]. The single-crystal X-ray diffraction structures reported for $Au_{102}(p\text{MBA})_{44}$ display the cluster as fully protonated after crystallization from pH 2.5[27]. Althought the X-ray does not resolve protons, no counter-cations were observed in the crystal. Therefore, it is reasonable to assume that the cluster core and the ligand-layer are neutral. In water-solution, on the other hand, the ligand-layer is partially in deprotonated form, as shown by Salorinne *et.al.* who measured the hydrodynamic radius of $Au_{102}(p\text{MBA})_{44}$ and $Au_{144}(p\text{MBA})_{60}$ in solution by diffusion ordered NMR-spectroscopy, and observed the effect of the counter-cation and solvation layer on the hydrodynamic radius of the cluster[36].

Nanoclusters protected by identical carboxylic acid ligands present a unique system in chemistry, as the cluster can be interpreted as a single molecule with charge state ranging from, *e.g.* 0–(-44) for $Au_{102}(p\text{MBA})_{44}$ -cluster and 0–(-30) for $Ag_{44}(p\text{MBA})_{30}{}^{4-}$ -cluster. In $Au_{102}(p\text{MBA})_{44}$ 22 ligands are unique in symmetry due to the C_2-axis of the cluster.[37,38] Despite the importance of the ligand layer, many important characteristics of the protonation behaviour, such as the pK_a of the acid groups, whether or not the different ligands have different pK_a values depending on the position and the protonation state of neighbouring ligands, and if the protonated and deprotonated ligands form distinct patterns on the ligand-layer, have not been studiet. The effect of the protonation of neighbouring ligands on the equilibrium of the protonation reaction is commonly characterized using the Hill-coefficient n of the equilibrium.[39] The effect of these interactions can be absent ($n = 1$), cooperative ($n > 1$), and anti-cooperative ($n < 1$). In first case the different ligands do not interact, and the state of the neighbouring ligands have no effect on the reaction equilibrium. In cooperative case the ligands adopt the protonation state of the neighbouring ligands more easily, and vice versa for anti-cooperative case. $Au_{102}(p\text{MBA})_{44}$ provides an ideal system to study this effect, since the the structure of the cluster is known in both single crystal and solution.[27,38].

The interactions of AuNPs with their environment depends crucially on the protonation state of the *p*MBA ligands. Therefore, pH determines both solubility and affinity for biomolecules. In order to exploit pH for controlling particle interactions with surroundings, we need accurate information on the protonation state of the cluster. Here we combine potentiometric acid-base titration with IR-spectroscopy to determine the ligand-layer pK_a. Furthermore, due the short intramolecular distances between the titrating sites, we expect these sites to be coupled. Therefore, whereas the macroscopic pK_a value, obtained from the titration, directly relates to the number of protons present on the particle, it does not provide information on the distribution of these charges on the surface, as different ligands cannot be distinguished experimentally. As it is the charge distribution that determines the solution properties of the particle, we also used constant pH molecular dynamics (MD) simulations to investigate the proton distribution over the ligands at the equilibrium pH.

Experimental and computational methods

Sample preparation

$Au_{102}(p\text{MBA})_{44}$ -cluster was synthetized by modified method using *p*MBA as protecting ligand, as described earlier in ref.[36]. All materials were commercial and used as received. The purity of the samples were analyzed using PAGE and UV/Vis-spectroscopy.

The water-soluble partially deprotonated $Au_{102}(p\text{MBA})_{44}$-sample was fully protonated by adding large excess of 1 M HCl. The obtained black precipitate was centrifuged, decanted, and washed twice with H_2O to remove excess HCl and NaCl. The product was dissolved in MeOH and the UV/Vis and IR-spectra were measured. The fully protonated cluster was deprotonated by dissolving it in basic H_2O.

Potentiometric titration

The pH of the $Au_{102}(p\text{MBA})_{44}$ solutions were measured using Mettler Toledo InLab Nano Ag/AgCl electrode. The pH-meter was calibrated using pH 4, 7, and 10 H_2O-based buffer-solutions. For IR-samples D_2O-solutions were used, and the apparent pH* values of D_2O-based solutions obtained with H_2O-calibrated pH-meter were converted to corresponding pH values in D_2O-solution using equation $pH = 0.936pH^* + 0.412$[40] pH values measured in MeOH-solutions used same calibration solutions and the values were used as is.

Titration samples in water were prepared by adding fully protonated $Au_{102}(p\text{MBA})_{44}$ to argonated 0.10 M NaCl solution. The solutions were made basic (between 12.0 and 10.5) by adding 1 M NaOH. For titration in MeOH the fully protonated $Au_{102}(p\text{MBA})_{44}$ was dissolved in neat MeOH. The amount of $Au_{102}(p\text{MBA})_{44}$ in different titrations ranged from 80 to 35 nmol, and the sample volume was 250 or 1000 μL. Water samples were titrated using 0.01 M HCl, and MeOH samples using 0.01 NaOH. Ionic strength of the solutions were between $I = 0.11$ and $I = 0.10$ for the water samples, $I = 0.010$ and $I = 0.005$ for the MeOH samples. Titration of *p*MBA reference was done in similar way, except that 0.05 M HCl and 0.05 M NaOH were used instead.

Infra-red titration

IR-spectra of pure *p*MBA and $Au_{102}(p\text{MBA})_{44}$ solutions were measured with a CaF_2-cuvette. Optical path was controlled using either 50 or 80 μm teflon spacer. The actual optical path was calculated from the interference pattern of the empty cuvette, being on average 5-10 % thicker than the spacer used. UV/Vis-spectra was measured with either the same IR-cuvette, or 1 mm optical path quartz-cuvette.

The IR-spectra were measured in either pure D_2O or in NaH_2PO_3/Na_2HPO_3 buffer-solution made in D_2O. The pH of the measurement solutions were adjusted using 1.0 M NaOD and 1.0 M DCl. The spectrum of H_2O impurity was subtracted by minimizing the H_2O peak at 1460 cm^{-1} (Fig. S1). Spectra measured in MeOD-d4 are presented as measured. All spectra were measured with 2 cm^{-1} resolution and processed with Happ-Genzel apodization before Fourier-transform. The sample concentration and IR-absorption coefficient were calculated with Beer-Lambert

This journal is © The Royal Society of Chemistry [year]

law from the UV/Vis- and IR-spectra. Absorption coefficient of $Au_{102}(p\text{MBA})_{44}$ in the UV/Vis-region was obtained from ref. 41. IR-spectra of $Au_{102}(p\text{MBA})_{44}$ in dried form was measured by drying the sample on CaF_2-window in vacuum.

Vibrational modes of the *p*MBA molecule were calculated using TURBOMOLE v6.5 package; TZVP basis-set, density functional theory, B3LYP exchange-correlation functional.

Molecular dynamics simulations

The titration experiments yield apparent pK_a's but do not provide information about the site-specific pK_a's of the individual *p*MBA ligands. To obtain estimates for the site-specific pK_a values, we used constant pH molecular dynamics on a $Au_{102}(p\text{MBA})_{44}$ in water. Although the constant pH approach is described in detail in[42], we will briefly summarize the main ideas of this method, before discussing the details of our $Au_{102}(p\text{MBA})_{44}$ simulations.

In the λ-dynamics approach[43,44], the Hamiltonian of a system with titratable sites (i) is expressed as

$$H(\lambda_i) = (1-\lambda_i)H_{\mathrm{R}} + \lambda_i H_{\mathrm{P}_i} + \frac{1}{2}m_\lambda \dot{\lambda_i}^2 + U^{\mathrm{dwp}}(\lambda_i) + \Delta G^{\mathrm{chem}}(\lambda_i) \quad (1)$$

where λ_i is an additional degree of freedom for titrating site i, which interpolates the system between the reactant R_i ($\lambda_i = 0$) state with site i protonated, and product P_i ($\lambda_i = 1$) state with site i deprotonated. Thus, in the reactant state R_i, the Hamiltonian H_{R_i} describes the interactions of the system with a protonated site i, while in the product state H_{P_i} describes the interactions when site i is deprotonated. The λ coordinate can be perceived as the coordinate of a particle moving between different chemical states. In this work the sites i are the carboxyl groups of the *p*MBA ligands (*i.e.*, $1 \leq i \leq 44$) In Eq. (1), m_λ is the mass and $\frac{1}{2}m_\lambda\dot{\lambda}^2$ is the kinetic energy of this "λ particle". The λ-dependent potential term $U^{\mathrm{dwp}}(\lambda)$ will serve as a biasing potential to limit the range of λ and the term $\Delta G^{\mathrm{chem}}(\lambda)$ is explained below.

To realistically describe protonation and deprotonation events at a given pH, the effect of pH and the contributions from bond breaking and formation to the deprotonation free energy are described by an additional term, which shifts the protonation equilibrium by a certain free energy ΔG^{chem}. To determine ΔG^{chem}, the equilibrium between a protonated and deprotonated acid in water is considered. ΔG^{chem} is then determined as

$$\Delta G^{\mathrm{chem}}(\lambda) = (\ln 10)\mathrm{RT}(\mathrm{pK_a} - \mathrm{pH}) - \Delta G^{\mathrm{FF}}(\lambda) \quad (2)$$

where the first term on the right side of Eq. (2) is the experimental free energy of deprotonation of the acid (*i.e.* *p*MBA), and the second term is the corresponding free energy difference obtained from a force field simulation. The pH-dependent term in Eq. (2) incorporates the dependency of the deprotonation free energy on the proton activity of the surrounding solution and was set to 6.2 in our simulations.

Finally, the biasing potential $U^{\mathrm{dwp}}(\lambda)$ restricts λ to the interval between the two physical states $\lambda = 0$ and $\lambda = 1$. Here, we use a double-well biasing potential[45] with a central barrier of 7 $\mathrm{kJmol^{-1}}$ for each λ_i.

All the simulations were performed using the costant pH MD implementation of the GROMACS Molecular Dynamics package (version 3.3)[42,46–48] in combination with a charge constraint[45]. This code is available for download from www.mpibpc.mpg.de/grubmueller/constpH.

Interactions were modeled with the Amber force field parameters described in reference 49. The starting coordinates of the $Au_{102}(p\text{MBA})_{44}$cluster were taken from the X-ray structure[27]. Half of *p*MBA ligands (i.e. 22) were protonated, while the other ligands were deprotonated, yielding a total charge of -22 e. The structure was minimized in vacuum using a steepest descent algorithm and infinite cut-offs for both Lennard-Jones and Coulomb interactions. After the minimization, the $Au_{102}(p\text{MBA})_{44}$cluster was placed in a dodecahedron box with periodic boundaries and solvated by 7569 TIP3P water molecules.[50] The system was neutralized with 168 Na^+ and 146 Cl^- ions ($\approx$ 1M NaCl). The total system containing 23783 atoms was equilibrated for 30 ns with different initial λs, prior starting the constant pH MD simulations.

The MD simulations were run at constant pressure of 1.0 bar and temperature of 300 K,[51] with time constants of 1.0 and 0.1 ps for the pressure and temperature coupling, respectively. The LINCS algorithm was used to constrain bond lengths,[52] allowing a timestep of 2 fs in the classical MD simulations. SETTLE was applied to constrain the internal degrees of freedom of the water molecules.[53] A 1.0 nm cut-off was used for non-bonded Van der Waals interactions, which were modeled by Lennard-Jones potentials. Beyond this cut-off, a dispersion correction was applied for the energy and pressure. Coulomb interactions were computed with the reaction-field method,[54] using a 1.0 nm cut-off and an infinite relative dielectric ($\varepsilon_{\mathrm{rf}} = \infty$).

Prior the λ-dynamics (constant pH) simulations, the free energies of deprotonating the carboxylic acid moiety of *p*MBA were calculated by means of thermodynamics integration (TI). These free energies are required for the force field correction ($\Delta G^{\mathrm{FF}}(\lambda)$ in equation 2).

The TI run, in which the topology was linearly interpolated between the protonated and deprotonated state, consisted of 21 simulations of 3 ns each, at fixed values of λ along the interval $[0,1]$. During the simulations the $\partial H/\partial\lambda$ was recorded, and the resulting $\partial H/\partial\lambda$ curve was integrated to yield a free energy profile of the deprotonation reaction ($\Delta G^{\mathrm{FF}}(\lambda)$). Fitting a fourth order polynomial to the free energy profiles yielded the following expression for $\Delta G^{\mathrm{FF}}(\lambda_i)$ in Eq. (2):

$$\Delta G^{\mathrm{FF}}(\lambda) = 86.4501\lambda - 217.206\lambda^2 + 80.000\lambda^3 - 51.441\lambda^4 \quad (3)$$

The reference pK_a of the carboxylate group of *p*MBA was set to 4, in line with the experimental estimate.

Five independent constant pH simulations at pH = 6.2 (*i.e.*, the apparent pK_a value from our experiments) with different initial conditions for the 44 λ_i values, were run for 8 ns each. During these simulations, the number of protons in the system was constrained to 22, using the SHAKE algorithm for the λ_i coordinates (Supporting Information). This constraint forces the system to sample at pH=pK_a, at which half of the titrating sites are protonated. The constraint also avoids charge fluctuations, which can easily lead to artefacts[55].

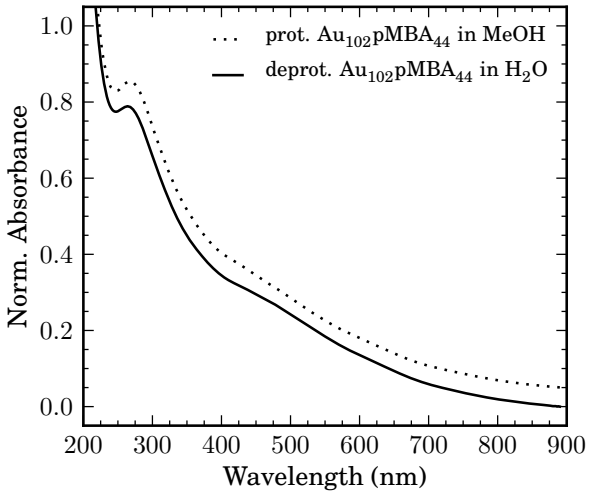

Fig. 1 UV/Vis-spectrum of $Au_{102}(pMBA)_{44}$ cluster in fully protonated and fully deprotonated states. The spectra are offset for clarity.

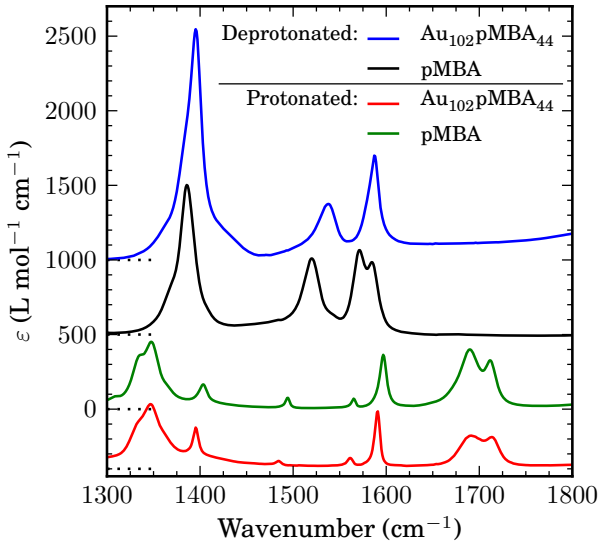

Fig. 2 IR-spectra of *p*MBA-ligand as free molecule and bound to $Au_{102}(pMBA)_{44}$ cluster in protonated and deprotonated states. The absorption coefficient values apply only to the spectra of free *p*MBA. The spectra of protonated species were measured in MeOD-d4, and the spectra of deprotonated forms measured in D_2O at pH 13 and 7 for $Au_{102}(pMBA)_{44}$ and free *p*MBA, respectively. pH 7 was chosen for the free *p*MBA in order to deprotonate the carboxylic acid, but not the thiol group.

The site-specific pK_a^i of the residues (i) were estimated directly from the probabilities of being deprotonated ($p^i_{A^-}$) and protonated (p^i_{AH}):

$$pK_a^i = \frac{1}{\ln 10 RT}\Delta G^i \tag{4}$$

with ΔG^i the free energy to deprotonate the carboxylic acid moiety of *p*MBA, which is related to these probabilities via:

$$\Delta G^i = -RT\ln[\frac{p^i_{A^-}}{p^i_{AH}}] + RT\ln 10 \mathrm{pH} \tag{5}$$

In the simulations, pH was set to 6.2. The probabilities are calculated as the time average of each λ_i coordinate:

$$\begin{aligned} p^i_{A^-} &= \langle \lambda_i \rangle \\ p^i_{AH} &= \langle 1-\lambda_i \rangle \end{aligned} \tag{6}$$

The number of hydrogen bonds between the $Au_{102}(pMBA)_{44}$-cluster and water was estimated using the g_hbond program, with cutoffs 20 degrees for the angle Hydrogen - Donor - Acceptor, and 0.3 nm for the distance Donor - Acceptor.

Results and discussion

The solubility of $Au_{102}(pMBA)_{44}$-cluster in protonated and deprotonated states was tested with various polar and nonpolar solvents. In protonated state the cluster is soluble in short alcohols and DMSO, while in deprotonated state the cluster is soluble only in water and DMSO. Both forms are insoluble in nonpolar and chlorinated solvents (See table S1 for full list of solvents in this study). The UV/Vis-spectra (fig. 1) of both forms are similar, indicating that the clusters are not degraded in the process, and the protonation state of the ligands does not significantly affect the electronic structure of the gold core.

For further analysis, the protonation state of the ligand-layer was studied using vibrational spectroscopy. Commonly surface-enchanced Raman-spectroscopy (SERS) is used when measuring the vibrational spectra of molecules adsorbed on nanoparticle surface, as the interaction of the particle surface plasmon resonance (SPR) enhances the Raman-scattering intensity by several orders of magnitude. Smaller clusters such as $Au_{102}(pMBA)_{44}$ do not supprot SPR, why we resorted to FTIR-spectroscopy instead. The IR-spectra of both protonation states are presented in fig. 2 along with the reference spectra of the bare ligand (*p*MBA). Vibrational peaks of *p*MBA and similar benzoic acid derivates have been characterized earlier in gas phase[56] and in solid state[57]. The observed IR-peaks were assigned using the earlier reports and DFT calculations of the free ligand vibrational energies in vacuum (fig. S2 and S3).

The protonated carboxylic acid group can be easily identified via the strong stretching vibration of the localized C=O double bond in the region 1670-1730 cm^{-1}. In methanol this peak is split into two peaks at 1713 cm^{-1} and 1691 cm^{-1}. After deprotonation this peak disappears and is replaced by strong symmetric and asymmetric stretching modes of the delocalized double bond of the $-CO_2^-$ group at 1396 and 1538 cm^{-1} respectively. Also, the intensity of the phenyl-ring vibration at 1582 cm^{-1} is increased significantly due to coupling with the asymmetric $-CO_2^-$ stretching mode. For the protonated $Au_{102}(pMBA)_{44}$ four of the phenyl-ring C–C stretching modes are observed at 1591 cm^{-1} (Wilson notation: 9a/Gardner-Wright notation: $\mathscr{M}_4$), 1562 cm^{-1} (9b/$\mathscr{M}_{23}$), 1485 cm^{-1} (18a/$\mathscr{M}_5$), and 1395 cm^{-1} (18b/$\mathscr{M}_{24}$)[58]. For the deprotonated $Au_{102}(pMBA)_{44}$ three of these are found at 1588 cm^{-1} (9a/$\mathscr{M}_4$), 1581 cm^{-1} (9b/$\mathscr{M}_{23}$),

This journal is © The Royal Society of Chemistry [year]

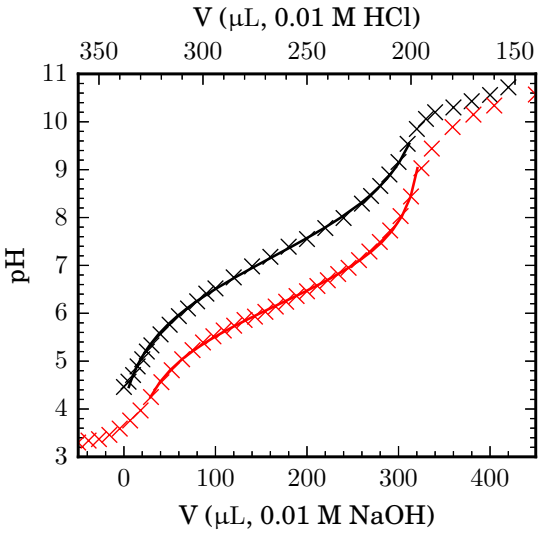

Fig. 3 $Au_{102}(pMBA)_{44}$ titration curve in H_2O (red) and 50% MeOH (black). The solid line shows the fit using the Hill-equation (eq. 7).

and 1385 cm^{-1} (18b/$\mathscr{M}_{24}$), with the 18a/$\mathscr{M}_5$ mode being obscured by H_2O impurity. The spectrum of protonated *p*MBA is very similar for both free *p*MBA and $Au_{102}(pMBA)_{44}$-cluster, only differences being the slight broadening of the C=O stretching peak and a redshift of *c.a.* 4-8 cm^{-1} of the phenyl-ring modes in the $Au_{102}(pMBA)_{44}$–spectrum. For deprotonated *p*MBA a strong blueshift (10-18 cm^{-1}) of the CO_2^- and the phenyl-ring 1560 cm^{-1} peaks is observed after the attachment to the cluster. We interpret this to originate from the hydrogen bonding environment with the solvent, because cluster-bound *p*MBA cannot form as many hydrogen bonds as free *p*MBA in solution. Our MD simulations, discussed below, support this interpretation. All analyzed IR-absorption peaks in the region 1800-1300 cm^{-1} are presented in table S2. No evidence of protonated *p*MBA is observed in the spectrum of $Au_{102}(pMBA)_{44}$ at high pH, indicating that every ligand is deprotonated. * With all ligands deprotonated, the charge of the ligand-layer is -44. With a diameter of approximately 2.2 nm[27,36], an electric field is created in the order of 10^{10} V/m. Although such strong fields could rupture bonds and result in a Coulomb explosion of the cluster, the stability of the of the $Au_{102}(pMBA)_{44}$-cluster at high pH suggests efficient screening of the ligand charges by the solvent and counter-cations. In contrast, *p*MBA-monolayers on Au-surfaces have been reported to undergo degradation at high pH[28].

The protonation-deprotonation behaviour of the $Au_{102}(pMBA)_{44}$ cluster was studied using regular acid-base pH-titration and IR-titration. Regular titration curve was measured in pure H_2O, where the cluster precipitates out of the solution at low pH (below 4), and in 50% methanol, where at lower concentrations the cluster is soluble in both protonation states. The acid-base titration curves are presented in fig. 3 and in fig. S4. The pK_a and the Hill-coefficient n were extracted from the titration data by fitting the Henderson-Hasselbalch equation

$$\alpha_{CO_2H} = A + (B-A)\frac{1}{10^{n(pH-pK_a)}+1}, \quad (7)$$

where A and B are constants defining the baseline when $pH \gg pK_a$ and $pH \ll pK_a$ respectively. In both solvents a single pK_a is observed at $pK_a = 6.18 \pm 0.05$ in H_2O, and at $pK_a = 7.19 \pm 0.07$ in 50% MeOH ($\Delta pK_a = 1.01$). The shift of pK_a to higher pH in methanol solution is consistent with earlier measurements of benzoic acid in 50% MeOH ($\Delta pK_a^{50\%} = 1.03$)[59]. The protonation behaviour is anti-cooperative in both cases as evident by the obtained Hill-coefficient of $n = 0.64 \pm 0.04$ in H_2O and $n = 0.53 \pm 0.03$ in 50% MeOH. For reference, the titration was done also for the free *p*MBA (fig. S5), obtaining $pK_a(CO_2H) = 4.16 \pm 0.06$ and $pK_a(SH) = 5.90 \pm 0.06$ in pure H_2O for the carboxylic acid and thiol groups, respectively. In 65% methanol the pK_a values are shifted to 5.46 ± 0.02 and 7.37 ± 0.01 ($\Delta pK_a(CO_2H) = 1.30$, $\Delta pK_a(SH) = 1.47$, for benzoic acid $\Delta pK_a^{65\%} = 1.50$)[59]. The pK_a observed for the $Au_{102}(pMBA)_{44}$ system is assigned to the protonation of carboxylic acid -group of the *p*MBA, despite being very close to the thiol-group pK_a of the free *p*MBA, since the $Au_{102}(pMBA)_{44}$ ligand layer does not contain any protonable thiol-groups. This assignment is confirmed by the pH-dependent IR-spectra.

In order to better quantify the exact amount of protonated and deprotonated ligands on the cluster at different pH, we measured pH-dependent IR-spectra of four different $Au_{102}(pMBA)_{44}$ samples in the pH range of 4.90 – 12.00 in solution phase (figs. 4 and S6). For pH values around the pK_a determined in the standard titration, both protonated and deprotonated *p*MBA is observed as expected. When the sample pH is increased, the intensity of the C=O stretching peak decreases and the intensities of CO_2^- stretching peaks increase. Above pH 9 only deprotonated *p*MBA is observed, indicating that the cluster is completely deprotonated.

Commonly the protonation state is analyzed using peak ratios between a peak which reacts to protonation, such as C=O and -CO_2^- stretching vibrations, with respect to a particular peak which stays identical in both states. However, such approach can only work if the reference intensity does not depend on the protonation state of the system. For most molecules, *p*MBA included, this is not the case. Instead, we calculated the number of ligands in each state from the ratio of the asymmetric CO_2^- and C=O peak areas, and the fact that for $Au_{102}(pMBA)_{44}$ the sum of the ligands must equal 44. From these assumptions we get equations for the number of protonated and deprotonated ligands

$$N_{prot} = \frac{44}{1+\frac{A_b}{RA_a}} \quad (8)$$

$$N_{deprot} = \frac{44}{1+R\frac{A_b}{A_a}} \quad (9)$$

where R is the peak area ratio determined for the free *p*MBA, and A_a and A_b are the integrated peak areas of the asymmmet-

* From the absorption coefficients of the free *p*MBA and the concentrations of $Au_{102}(pMBA)_{44}$ used in the IR-measurements, it can be deduced that two or more ligands in the protonated state would be observable in the spectrum.

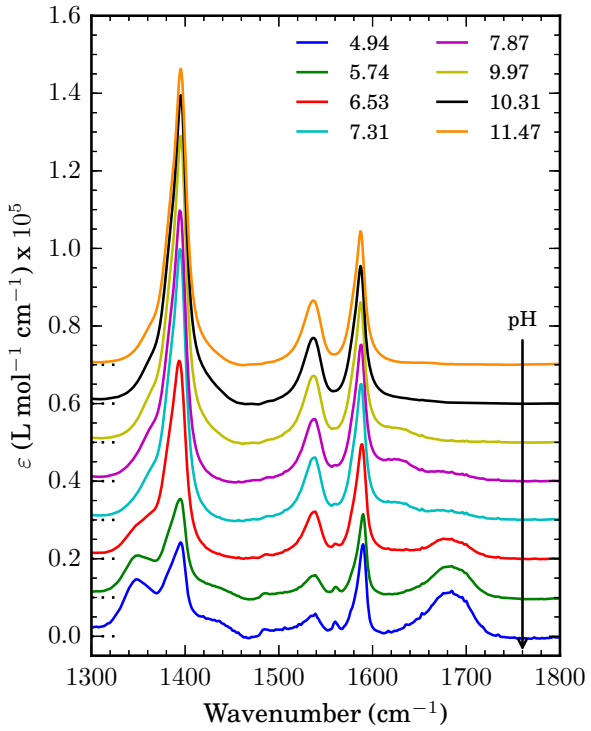

Fig. 4 pH-dependent IR-spectra of $Au_{102}(pMBA)_{44}$-cluster in D_2O. Both protonated and deprotonated forms are observed between pH 4.94 and 7.87, while above pH 7.87 only the deprotonated form can be seen. The additional absorption peak at 1625 cm^{-1} seen at pH 7.31, 7.78, and 9.97 is identified as impurity.

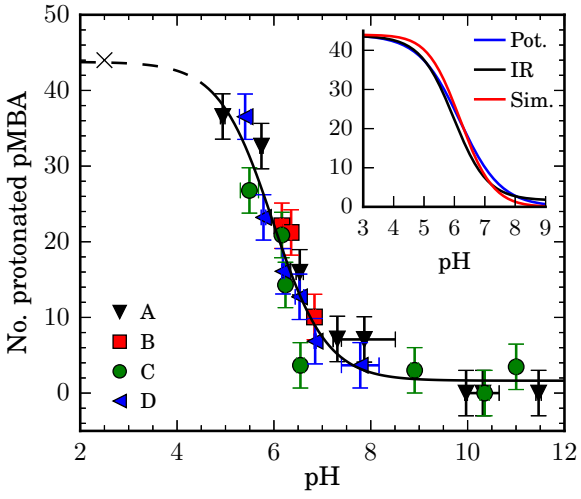

Fig. 5 Number of protonated *p*MBA-ligands on the $Au_{102}(pMBA)_{44}$ cluster at different pH. *A* refers to the measurement set in fig. 4, *B*, *C* and *D* to measurements in fig. S6. The cross at pH 2.5 indicates the fully protonated species. Error of pH is taken from the pH of the sample solution before and after the IR-measurement, and ligand number error is calculated from the error of peak areas and the ratio α. The inset shows the titration curves from the potentiometric-, IR-titration, and the MD-simulation.

ric CO_2^- and C=O stretching peaks respectively. Derivation of these equations are presented in SI. The region 1470–1750 cm^{-1} was fitted using Gaussian and Lorentzian peaks, and the area of the C=O stretching peak was obtained from the fit parameters. For the asymmetric CO_2^- peak the fitting overestimated the peak area due to water-absorbance left in the baseline. Therefore, the peak area was obtained by integrating the region 1510-1560 cm^{-1} after removing the baseline. The number of protonated ligands calculated using the peak areas and $R = 0.56 \pm 0.03$ are presented in fig. 5. Fitting of the Hill-equation to the data gives $pK_a = 5.98 \pm 0.13$ and Hill-coefficient $n = 0.78 \pm 0.14$. In the IR-measurements the cluster started to precipitate when pH was decreased below 5. This is slightly higher than what was observed in acid-base titrations, presumably because of the higher concentration of $Au_{102}(pMBA)_{44}$ used in the IR-samples. In very low concentrations (approx. 1 μmol/L) the cluster remains in solution down to pH ≈ 3. The IR-spectra were measured also of samples dried from solutions of different pH (fig. S7). The behaviour with respect to the pH is similar in solid, and the protonation state in solution is preserved when the sample is dried. When measuring the IR-spectra of the dried samples, they did not readily redissolve in pure water after the measurement when the sample was dried from solution with pH below 6. This corresponds with approximately half of the ligand layer being in protonated form. We believe this to be the borderline where the hydrophobic character of the protonated *p*MBA ligands start to dominate, and the cluster is no longer truly water soluble, instead forming a suspension of insoluble clusters.

The titration experiments yield an estimate of 6.2 for the pK_a of the $Au_{102}(pMBA)_{44}$, but do not reveal the distribution of the protons over the *p*MBAs or the site-specific pK_a values of the *p*MBAs. The anti-cooperative ($n < 1$) Hill-coefficient suggests interaction between the carboxylates of the *p*MBA ligands. To estimate how these interactions affect the site-specific pK_a values of the individual *p*MBA ligands and to investigate the distribution of the protons over the titratable sites, we performed constant pH molecular dynamics simulations at pH= 6.2 with 22 protons and 44 titratable *p*MBA sites.

32 independent simulations from different initial distributions of λ_i were performed. Regardless of the initial configuration, the simulation converged towards qualitatively similar distribution of protonated and deprotonated ligands (fig. S8). This observation suggests the cluster has a preferred protonation distribution at pH 6.20. Following equations 4-6, we estimated the site-specific pK_a values of each *p*MBA from the time-averaged λ_i's. Table S3 lists the average λ, pK_a value and number of transitions between the protonated ($\lambda = 0$) and deprotonated ($\lambda = 1$) states for each *p*MBA ligand. The number of transitions are included, because the error in the pK_a estimates depends on this number: the higher the number of transitions, the higher the accuracy of the estimate. The ligand numbering follows the scheme from recent paper by Salorinne *et.al.* [38], which numbers the 22 symmetric ligands based on their NMR-shifts (fig. S9). One half of the ligands are numbered 1–22, and the other half 1*–22*, with 1* being the C_2 related pair of ligand 1 *etc.*.

Ligands that are related by symmetry have similar λ and pK_a

This journal is © The Royal Society of Chemistry [year]

values (Table S3, fig. S8), which suggest that our simulations capture the intrinsic symmetry of the system. The pK_a's range from 5.18 to 7.58, and are all higher than 4.16, the pK_a of free *p*MBA in water. The crowded environment reduces the average number of hydrogen bonds that the carboxylates form with water, from 4.1 in solution to 3.6 in the cluster. As hydrogen bonding stabilizes the carboxylate group, this decrease in solvation increases the pK_a's (fig. S10). This is also in line with the observed blueshift of the deprotonated carboxylic acid modes in IR-spectrum (fig. 2). Despite the dielectric screening in the 1 M NaCl solution, we furthermore assume that the repulsive interaction between deprotonated carboxylate groups also contributes to increasing the pK_a.

Under the assumption that the pK_as are independent of pH, we obtained a pK_a of 6.20 and a Hill coefficient of 0.82 after fitting a Henderson-Hasselbalch curve to the computed pK_a's of Table S3. Although the assumption that the pK_a's are not dependent on the pH may not be justified if the sites are coupled,[60], the experimental pK_a value of the cluster and the anti-cooperative Hill coefficient are reproduced by the simulation. The largest deviations of the simulated titration curve from the experimental potentiometric- and IR-titration curves are 3 and 4 ligands, respectively (fig. 5 inset).

Figure 6 shows a 3D model of the cluster in which the ligands are coloured according to their λ_{avg} (upper row: A,B,C) and pK_a (lower row: D,E,F) value. At pH 6.2 the λ-coloured figures show a non-uniform distribution of the protonated and deprotonated ligands, leading into a charge distribution of slightly neutral and negative areas on the cluster surface. The C_2-symmetry related poles of the C_5 -axis, mainly ligands 1/1* and 9/9* with smaller contribution from ligands 5/5* and 13/13*, of the core prefer the deprotonated state (fig. 6A). Similar preferance to deprotonated state is seen at one end of the C_2 axis (fig. 6B), while the other end of the same axis stays protonated (fig. 6C) due to the high pK_a of ligands 2/2*, 3/3*, and 10/10*. The areas left between the strongly protonated and deprotonated patches are close to the equilibrium $\lambda \approx 0.5$. From visual inspection of the protonation states, the more tightly packed areas prefer to stay protonated while the more open areas prefer deprotonation, which is reasonable considering the effects of coulombic repulsion and the earlier H-bonding analysis. The pK_a coloured figures follow the same general features seen in the λ coloured figures, however the differences between the ligands are not so pronounced since the populations change exponentially with respect to pH and pK_a.

Next, we searched for correlation among the protonation states of the *p*MBA ligands by computing the Pearson correlation coefficient (P) of the λ trajectories for all ligand pairs (fig. 7A). Majority of the ligand-pairs show weak anti-correlation, giving rise to the observed anti-cooperative Hill coefficient. Four ligand-pairs exhibiting moderate (below -0.40) anti-correlation were identified from the correlation matrix, ligand pairs 8–11, 14–15*, 1–3, and 14*–15 (fig. 7B, C, D, E). For the first pair (fig. 7B), ligands 1 and 22 next to ligand 8 also show weak anti-correlation, while the ligands 3 and 7 next to ligand 11 show weak positive correlation, presumably to stabilize the charge distribution caused by strong correlation of the 8–11 pair. Similar patterns are observed for the other strongly anti-correlative pairs. The anti-correlation of the 14–15* and 14*–15 pairs (fig. 7C, E) is interesting as is not between neighbouring ligands. These are also the only instance where significant correlation beoynd the first neighbour is observed. It should be noted, that while the 1–3 pair shows strong anti-correlation, the symmetry related 1*–3* pair shows no correlation.

Conclusions

In this work we have studied the influence of the protonation state of the *p*MBA ligand layer to the properties of the cluster. The cluster can be protonated and deprotonated using strong acids and bases without affecting the cluster stability or the optical absorption spectrum of the cluster. The fully protonated form is insoluble in water, but soluble in short chained alcohols, while the partially and fully deprotonated cluster is water-soluble. The pK_a and Hill-coefficient of the cluster were measured via potentiometric acid-base and IR-titration, giving $pK_a = 6.18 \pm 0.05, n = 0.64 \pm 0.04$ and $pK_a = 5.98 \pm 0.13, n = 0.78 \pm 0.14$, respectively, being significantly higher than the free *p*MBA $pK_a = 4.16$. The observed pK_a shift is similar to earlier reports on carboxylic acids immobilized on nanoparticles.[29,61] For pK_a and Hill-coefficient the results from potentiometric measurements are considered more reliable than FTIR because of more repetitions. The amount of protonated and deprotonated ligands at different pH were analyzed from the IR-spectra at different pH, showing that all 44 ligands react at the observed pK_a. The water-soluble form of the cluster precipitates from water below pH 5, depending on the concentration of the particles in the solution. Based on the IR-spectra, at this pH approximately one sixth of the ligand layer (7 ± 3 ligands) is still in the deprotonated state. In the pH range 5–6 (21 to 7 deprotonated ligands) the clusters remains in solution, but when dried could not be redissolved in neutral water, indicating the hydrophobic interactions dominate over the hydrophilic interactions. This may allow, for example, tuning of the adhesion of $Au_{102}(p\text{MBA})_{44}$ -clusters to hydrophobic structures by changing the solution pH and/or solvent system, or designing receptible structures for certain cluster charge distributions. Also, the $Au_{102}(p\text{MBA})_{44}$ can be used as nanoscopic pH-probe, as long as the vibrational spectrum can be reliably measured either with IR- or Raman-spectroscopy.

Ligand specific pK_a could not be derived from the experimental data, since the different pK_a's are too closely spaced, and the shift of the pK_a values are manifested instead as the anti-cooperative Hill-coefficient. Also, it is not possible to discern the different ligands in the IR-spectrum. Constant pH molecular dynamics simulations were performed to analyze the distribution of protonated and deprotonated ligands, and the pK_a's of the individial ligands on the cluster. The simulations revealed a preference towards single pattern of protonated and deprotonated ligands, regardless of the initial conditions, when half of the ligands are in the deprotonated state. Patches of ligands which strongly prefer the protonated and deprotonated ligands form on the cluster surface, causing a non-uniform charge distribution on the cluster. The calculated pK_a of the 44 individual ligands were in the range of 5.18 to 7.58, giving macroscopic $pK_a = 6.20$ and Hill-coefficient

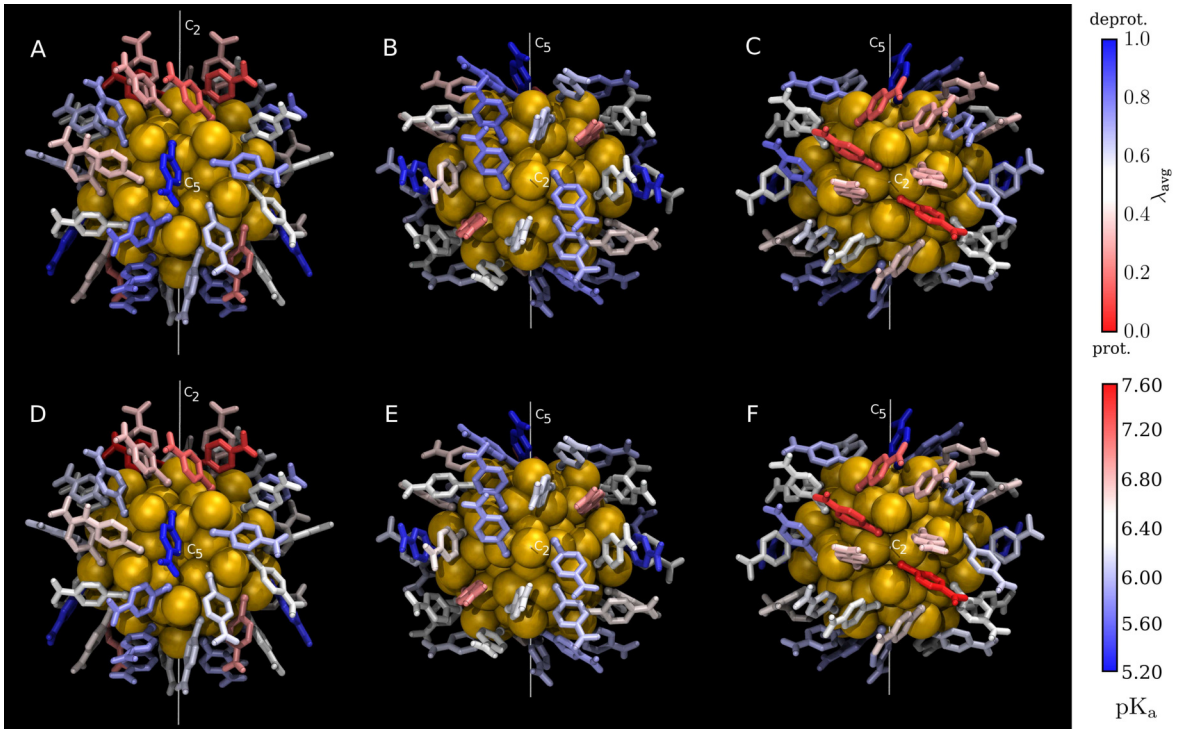

Fig. 6 A: Mean λ_{avg} -values of the 44 ligands from constant pH MD at pH 6.20 (table S3, fig. S8). Viewed through the C_5 axis of the core. B: Same as A viewed through the C_2 axis. C: Same as B from the other end of the C_2 axis. D, E, F: Same as A, B, and C with the pK_a -values of the 44 ligands.

$n = 0.82$. The pK_a value agrees well with the experimental values. The Hill-coefficient is higher than the value obtained from potentiometric titration, but within the error of the value obtained from IR-titration. Majority of the ligand-pairs show weak anti-correlation of the protonation states, with less showing weak positive correlation, and 4 pairs showing strong anti-correlation. The results give new insight to the possibilities of controlling the properties of monolayer-protected clusters protected by ligands containing protonable groups. This information can be used, for example, for controlling ligand exchange sites by using charged incoming ligands, or tuning the interactions of the cluster with charged biological or inorganic systems.

Acknowledgements

We thank Kirsi Salorinne for providing $Au_{102}(p\text{MBA})_{44}$-sample for early experiments. Sutidara Nopakun is acknowledged for pH dependent solubility studies at low concentrations. Eero Hulkko, Satu Mustalahti, and Saara Lautala are acknowledged for helpful discussions. This research is supported by the Academy of Finland (SD, GG, HH) and National Graduate School on Computational Chemistry and Spectroscopy (LASKEMO) (J.K.).

References

1 T. Tsukuda and H. Häkkinen, *Protected Metal Clusters: From Fundamentals to Applications*, Elsevier, 2015.

2 M. C. Daniel and D. Astruc, *Chemical Reviews*, 2004, **104**, 293–346.

3 T. Buergi, *Nanoscale*, 2015, **7**, 15553–15567.

4 R. W. Murray, *Chemical reviews*, 2008, **108**, 2688–2720.

5 R. Jin, *Nanoscale*, 2010, **2**, 343–362.

6 Y. Cheng, J. D. Meyers, A.-M. Broome, M. E. Kenney, J. P. Basilion and C. Burda, *Journal of the American Chemical Society*, 2011, 2583–2591.

7 D. O'Neal, L. R. Hirsch, N. J. Halas, J. Payne and J. L. West, *Cancer Letters*, 2015, **209**, 171–176.

8 V. Marjomäki, T. Lahtinen, M. Martikainen, J. Koivisto, S. Malola, K. Salorinne, M. Pettersson and H. Häkkinen, *Proceedings of the National Academy of Sciences of the United States of America*, 2014, **111**, 1277–81.

9 M. Martikainen, K. Salorinne, T. Lahtinen, S. Malola, P. Permi, H. Hakkinen and V. Marjomaki, *Nanoscale*, 2015, **7**, 17457–17467.

10 J. Z. Sexton and C. J. Ackerson, *The Journal of Physical Chemistry C*, 2010, **114**, 16037–16042.

11 C. J. Ackerson, P. D. Jadzinsky, J. Z. Sexton, D. A. Bushnell and R. D. Kornberg, *Bioconjugate chemistry*, 2010, **21**, 214–218.

12 M. A. H. Muhammed, P. K. Verma, S. K. Pal, R. C. A. Kumar, S. Paul, R. V. Omkumar and T. Pradeep, *Chemistry A European Journal*, 2009, **15**, 10110–10120.

13 Y. Chen, C. Zeng, D. R. Kauffman and R. Jin, *Nano Letters*, 2015, **15**, 3603–3609.

14 C. Zeng, Y. Chen, K. Kirschbaum, K. Appavoo, M. Y. Sfeir and R. Jin, *Science Advances*, 2015, **1**, e1500045.

15 A. Dass, S. Theivendran, P. R. Nimmala, C. Kumara, V. R. Jupally, A. Fortunelli, L. Sementa, G. Barcaro, X. Zuo and B. C.

This journal is © The Royal Society of Chemistry [year]

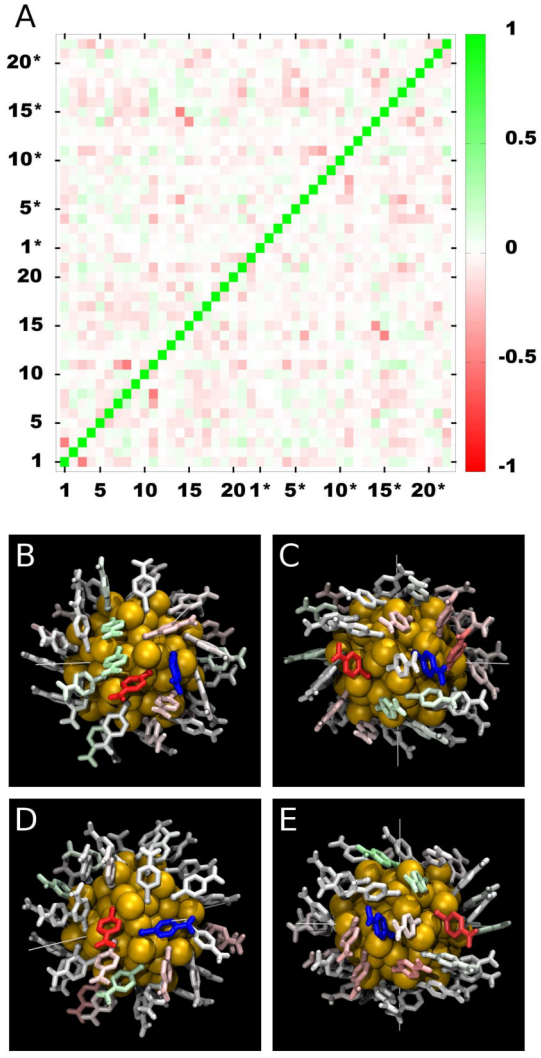

Fig. 7 A: Correlation matrix of the ligands. Positive values indicate correlation and negative values anti-correlation. B: Correlation values of ligand 8 (blue) on the cluster model. C, D, E: Same as B for ligands 14, 1, and 14*, respectively.

Noll, *Journal of the American Chemical Society*, 2015, **137**, 4610–4613.

16 C. Yi, H. Zheng, L. M. Tvedte, C. J. Ackerson and K. L. Knappenberger Jr., *Journal of Physical Chemistry C*, 2015, **119**, 6307–6313.

17 C. J. Murphy, A. M. Gole, J. W. Stone, P. N. Sisco, A. M. Alkilany, E. C. Goldsmith and S. C. Baxter, *Accounts of Chemical Research*, 2008, **41**, 1721–1730.

18 L. Becucci, R. Guidelli, F. Polo and F. Maran, *Langmuir*, 2014, **30**, 8141–8151.

19 F. Simonelli, D. Bochicchio, R. Ferrando and G. Rossi, *The Journal of Physical Chemistry Letters*, 2015, **6**, 3175–3179.

20 E. Heikkilä, H. Martinez-Seara, A. A. Gurtovenko, M. Javanainen, H. Häkkinen, I. Vattulainen and J. Akola, *The Journal of Physical Chemistry C*, 2014, **118**, 11131–11141.

21 P. R. Leroueil, S. A. Berry, K. Duthie, G. Han, V. M. Rotello, D. Q. McNerny, Baker James R., B. G. Orr and M. M. Banaszak Holl, *Nano Letters*, 2008, **8**, 420–424.

22 J. Chen, J. A. Hessler, K. Putchakayala, B. K. Panama, D. P. Khan, S. Hong, D. G. Mullen, S. C. DiMaggio, A. Som, G. N. Tew, A. N. Lopatin, J. R. Baker, M. M. B. Holl and B. G. Orr, *The Journal of Physical Chemistry B*, 2009, **113**, 11179–11185.

23 Y. Pan, A. Leifert, D. Ruau, S. Neuss, J. Bornemann, G. Schmid, W. Brandau, U. Simon and W. Jahnen-Dechent, *Small*, 2009, **5**, 2067–2076.

24 C. J. Ackerson, P. D. Jadzinsky and R. D. Kornberg, *Journal of the American Chemical Society*, 2005, **127**, 6550–6551.

25 B. E. Conn, A. Desireddy, A. Atnagulov, S. Wickramasinghe, B. Bhattarai, B. Yoon, R. N. Barnett, Y. Abdollahian, Y. W. Kim, W. P. Griffith, S. R. J. Oliver, U. Landman and T. P. Bigioni, *The Journal of Physical Chemistry C*, 2015, **119**, 11238–11249.

26 M. Azubel, J. Koivisto, S. Malola, D. Bushnell, G. L. Hura, A. L. Koh, H. Tsunoyama, T. Tsukuda, M. Pettersson, H. Hakkinen and R. D. Kornberg, *Science*, 2014, **345**, 909–912.

27 P. D. Jadzinsky, G. Calero, C. J. Ackerson, D. A. Bushnell and R. D. Kornberg, *Science*, 2007, **318**, 430.

28 A. Michota and J. Bukowska, *Journal of Raman Spectroscopy*, 2003, **34**, 21–25.

29 C. E. Talley, L. Jusinski, C. W. Hollars, S. M. Lane and T. Huser, *Analytical chemistry*, 2004, **76**, 7064–8.

30 S. M. Rosendahl and I. J. Burgess, *Electrochimica Acta*, 2008, **53**, 6759–6767.

31 M. D. Thi and K. Volka, *Journal of Molecular Structure*, 2010, **976**, 297–300.

32 S. B. Lee, K. Kim and M. S. Kim, *Journal of Raman Spectroscopy*, 1991, **22**, 811–817.

33 Y. Liu, H. Yuan, A. M. Fales and T. Vo-Dinh, *Journal of Raman Spectroscopy*, 2013, **44**, 980–986.

34 J. Kneipp, H. Kneipp, B. Wittig and K. Kneipp, *Nano Letters*, 2007, **7**, 2819–2823.

35 N. Kobayashi, Y. Kamei, Y. Shichibu and K. Konishi, *Journal of the American Chemical Society*, 2013, **135**, 16078–16081.

36 K. Salorinne, T. Lahtinen, S. Malola, J. Koivisto and H. Häkkinen, *Nanoscale*, 2014, **6**, 7823–6.

37 O. A. Wong, C. L. Heinecke, A. R. Simone, R. L. Whetten and C. J. Ackerson, *Nanoscale*, 2012, **4**, 4099–4102.

38 K. Salorinne, S. Malola, O. A. Wong, C. O. Rithner, X. Chen, C. J. Ackerson and H. Häkkinen, *Nature Communications*, 2015, **DOI: 10.1038/ncomms10401**, year.

39 A. Hill, *The Journal of Physiology*, 1910, **40**, i—-vii.

40 A. Krezel and W. Bal, *Journal of Inorganic Biochemistry*, 2004, **98**, 161–166.

41 E. Hulkko, O. Lopez-Acevedo, J. Koivisto, Y. Levi-Kalisman, R. D. Kornberg, M. Pettersson and H. Häkkinen, *Journal of the American Chemical Society*, 2011, **133**, 3752–3755.

42 S. Donnini, F. Tegeler, G. Groenhof and H. Grubmüller, *Journal of Chemical Theory and Computation*, 2011, **7**, 1962–1978.

43 X. Kong and C. L. B. III, *Journal of Chemical Physics*, 1996, **105**, 2414–2423.

44 B. Tidor, *Journal of Physical Chemistry*, 1993, **97**, 1069–1073.

45 S. Donnini, R. T. Ullmann, G. Groenhof and H. Grubmüller, *Manuscript in preparation*.

46 H. J. C. Berendsen, D. van der Spoel and R. van Drunen, *Computer Physics Communications*, 1995, **91**, 43–56.

47 E. Lindahl, B. Hess and D. van der Spoel, *Journal of Molecular Modeling*, 2001, **7**, 306–317.

48 D. van der Spoel, E. Lindahl, B. Hess, G. Groenhof, A. Mark and H. Berendsen, *Journal of Computational Chemistry*, 2005, **26**, 1701–1718.

49 E. Pohjolainen, X. Chen, S. Malola, G. Groenhof and H. Häkkinen, *Submitted to Journal of Chemical Theory and Computation*.

50 W. L. Jorgensen, J. Chandrasekhar, J. D. Madura, R. W. Impey and M. L. Klein, *Journal of Chemical Physics*, 1983, **79**, 926–935.

51 H. J. C. Berendsen, J. P. M. Postma, W. F. van Gunsteren and A. D. Nola, *Journal of Chemical Physics*, 1984, **81**, 3684–3690.

52 B. Hess, H. Bekker, H. J. C. Berendsen and J. G. E. M. Fraaije, *Journal of Computational Chemistry*, 1997, **18**, 1463–1472.

53 S. Miyamoto and P. A. Kollman, *Journal of Computational Chemistry*, 1992, **13**, 952–962.

54 I. G. Tironi, R. Sperb, P. E. Smith and W. F. van Gunsteren, *Journal of Chemical Physics*, 1995, **102**, 5451–5459.

55 J. Hub, B. L. de Groot, H. Grubmüller and G. Groenhof, *Journal of Chemical Theory and Computation*, 2014, **10**, 381–390.

56 J. Oomens and J. D. Steill, *The journal of physical chemistry. A*, 2008, **112**, 3281–3.

57 R. Li, H. Lv, X. Zhang, P. Liu, L. Chen, J. Cheng and B. Zhao, *Spectrochimica acta. Part A, Molecular and biomolecular spectroscopy*, 2015, **148**, 369–74.

58 A. M. Gardner and T. G. Wright, *The Journal of chemical physics*, 2011, **135**, 114305.

59 A. L. Bacarella, E. Grunwald, H. P. Marshall and E. L. Purlee, *The Journal of Organic Chemistry*, 1955, **20**, 747–762.

60 A. Onufriev, D. A. Case and G. M. Ullmann, *Biochemistry*, 2001, **40**, 3413–3419.

61 D. Wang, R. J. Nap, I. Lagzi, B. Kowalczyk, S. Han, B. A. Grzybowski and I. Szleifer, *Journal of the American Chemical Society*, 2011, **133**, 2192–2197.

This journal is © The Royal Society of Chemistry [year]

Supporting Information for: Experimental and Computational Determination of the Protonation States of the Water-Soluble $Au_{102}(p\text{MBA})_{44}$-nanocluster.

Jaakko Koivisto,[a] Xi Chen,[a] Serena Donnini,[b] Tanja Lahtinen,[a] Hannu Häkkinen,[a,c] Gerrit Groenhof,[a] and Mika Pettersson.[a*]

[*] *Corresponding Author: mika.j.pettersson@jyu.fi*

[a] *Department of Chemistry, Nanoscience Center, University of Jyväskylä, FI-40014 Finland.*

[b] *Department of Biological and Environmental Sciences, University of Jyväskylä, FI-40014 Finland.*

[c] *Department of Physics, Nanoscience Center, University of Jyväskylä FI-40014, Finland.*

Analysis of ligand populations from IR

For two peaks a and b arising from different species in the same measurement, the peak areas are given by Beer-Lambert law for both species

$$A_a = \varepsilon_a C_a l \tag{1}$$

$$A_b = \varepsilon_b C_b l \tag{2}$$

When one peak corresponds to the protonated and other for the deprotonated ligand, the $Au_{102}(p\text{MBA})_{44}$-concentration and the amount of ligands N_a and N_b can be expressed via these concentrations

$$C_{Au_{102}} = \frac{C_a + C_b}{44} \tag{3}$$

$$N_a = \frac{C_a}{C_{Au_{102}}} = \frac{44C_a}{C_a + C_b} \tag{4}$$

$$N_b = \frac{C_b}{C_{Au_{102}}} = \frac{44C_b}{C_a + C_b} \tag{5}$$

Since the optical path length is constant for both peaks, the ratio of absorbance depends on the concentrations C_a and C_b and the absorbance coefficients ε_a and ε_b

$$\frac{A_a}{A_b} = \frac{\varepsilon_a c_a \cancel{l}}{\varepsilon_b c_b \cancel{l}} = \alpha \frac{c_a}{c_b} \tag{6}$$

where the ratio of absorbance coefficients is $\alpha = {}^{\varepsilon_a}/_{\varepsilon_b}$. The amount of ligands in both forms can be now written without the concentration data by substituting eq. 6 into eqs. 4 and 5

$$N_a = \frac{44C_a}{C_a + \alpha C_a \frac{A_b}{A_a}} = \frac{44\cancel{C_a}}{\cancel{C_a}(1 + \alpha \frac{A_b}{A_a})} = \frac{44}{1 + \alpha \frac{A_b}{A_a}} \tag{7}$$

$$N_b = \frac{44C_b}{\frac{C_b A_a}{\alpha A_b} + C_b} = \frac{44\cancel{C_b}}{\cancel{C_b}(\frac{A_a}{\alpha A_b} + 1)} = \frac{44}{1 + \frac{A_a}{\alpha A_b}} \tag{8}$$

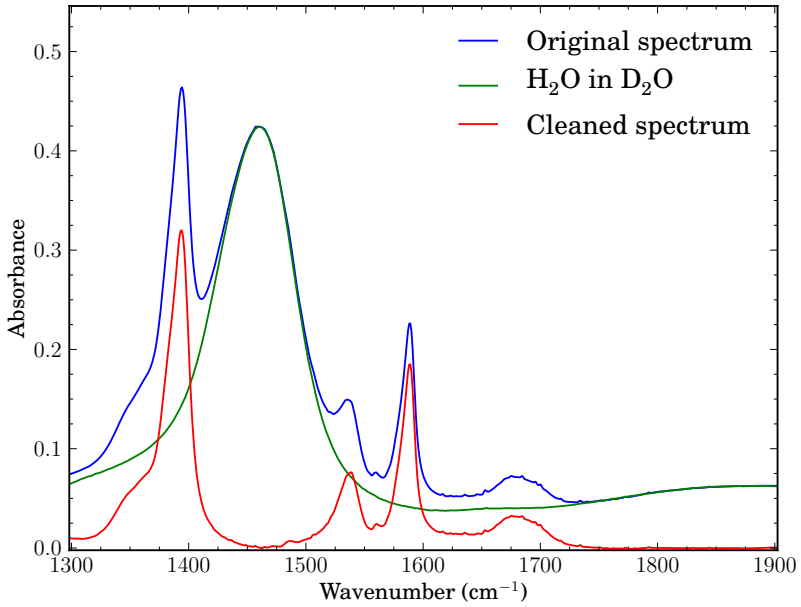

Figure S1: Example of removing the H_2O impurity from the IR-spectrum measured in D_2O. The spectrum of H_2O was fitted to the OH-bending peak at 1460 cm^{-1}, after the removal of this peak the spectrum of the measured substance remains.

Table S1: Solublity of $Au_{102}(p\text{MBA})_{44}$ cluster in fully protonated (*i.e.* $(-CO_2H)_{44}$) and fully deprotonated (*i.e.* $(-CO_2{}^-Na^+)_{44}$) states.

Solvent	Prot. Au_{102}	Deprot. Au_{102}
H_2O, pH≈6	I	S
Methanol	S	I
Ethanol	sS	I
Propan-2-ol	I	I
Ethylene glycol	S	I
Acetone	I	I
Acetonitrile	I	I
Pentane	I	I
Toluene	I	I
Dichloromethane	I	I
DMSO	S	S
CS_2	I	I

S: soluble, sS: slightly soluble, I: insoluble.

Table S2: Computational and experimental IR-absorption peaks of protonated and deprotonated *p*MBA in the range 1800 – 1300 cm^{-1}. The experimental values have been extracted from the solution-state spectra in fig. 2 in the main article. The calculated frequencies are unscaled. Phenyl-ring modes are illustrated in fig. S3, and they are labeled using Varsányay and Gardner-Wright notations.

	Protonated				**Deprotonated**			
	Calc.		**Exp. in MeOD-d4**		**Calc.**		**Exp. in D_2O**	
Mode	Vac.	2xMeOH[a]	Sol.[b]	Au_{102}[c]	Vac.	Na^+[d]	Sol.[b]	Au_{102}[c]
C=O str.[e]	1781.4	1727.1	1712.4 vs	1713.9 vs	–	–	–	–
	–	–	1690.0 vs	1691.0 vs	–	–	–	–
-CO_2^- as. str.	–	–	–	–	1684.3	1551.2	1520.3 s	1538.2 s
-CO_2^- s. str.	–	–	–	–	1336.2	1408.4	1386.1 s	1395.7 s
9a/$\mathscr{M}_4$	1636.1	1635.8	1597.0 s	1590.7 s	1614.4	1632.3	1584.9 s	1587.7 s
9b/$\mathscr{M}_{23}$	1596.2	1595.2	1565.3 m	1561.6 m	1593.7	1611.5	1571.4 s	1581.6 m,sh
18a/$\mathscr{M}_5$	1527.1	1529.9	1494.2 m	1485.2 m	1503.7	1521.6	1483.3 w	*N.O.*
18b/$\mathscr{M}_{24}$	1441.7	1439.3	1403.7 m	1395.5 m	1416.2	1429.7	1484.0 m	1384.9 m
OH-wag	1369.9	1453.1	~1350[f]	~1350[f]	–	–	–	–

vs: very strong, s: strong, m: medium, w: weak, sh: shoulder.
[a] In vacuum, two MeOH molecules hydrogen bonded to the CO_2H–group, see fig. S2A.
[b] Free *p*MBA solvated in MeOD-d4 or D_2O.
[c] $Au_{102}(pMBA)_{44}$ cluster solvated in MeOD-d4 or D_2O.
[d] In vacuum, Na^+ counter-cation next to the CO_2^-–group, see fig. S2B.
[e] In experimental spectrum this peak has split to two, see fig. 2 in main article.
[f] Several peaks in 1300 – 1370 cm^{-1} due to HDO impurity and H-bonding.
N.O.: Not observed.

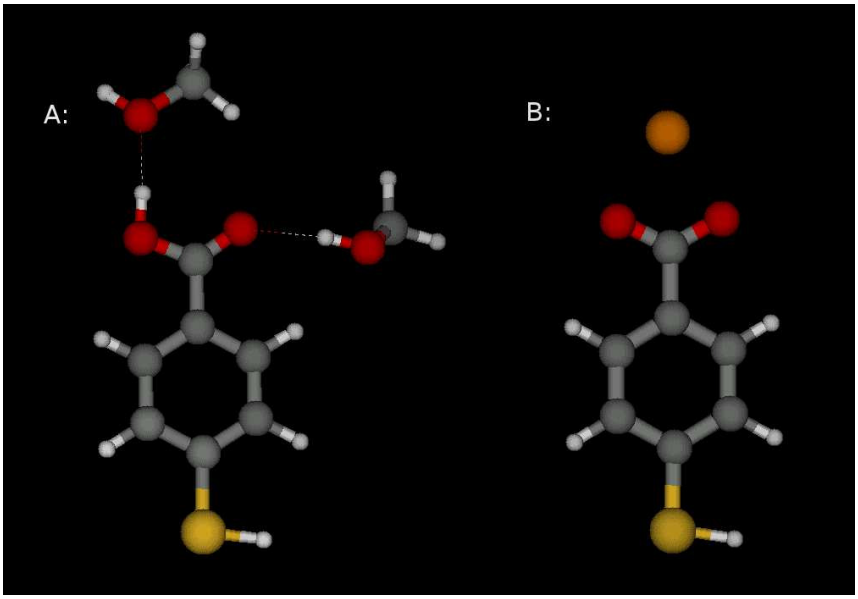

Figure S2: The relaxed structures of free *p*MBA in vacuum used for vibrational energy calculations. **A:** protonated *p*MBA with two methanol molecules hydrogen bonded to the carboxylic acid. **B:** deprotonated *p*MBA with Na^+ as counter-cation.

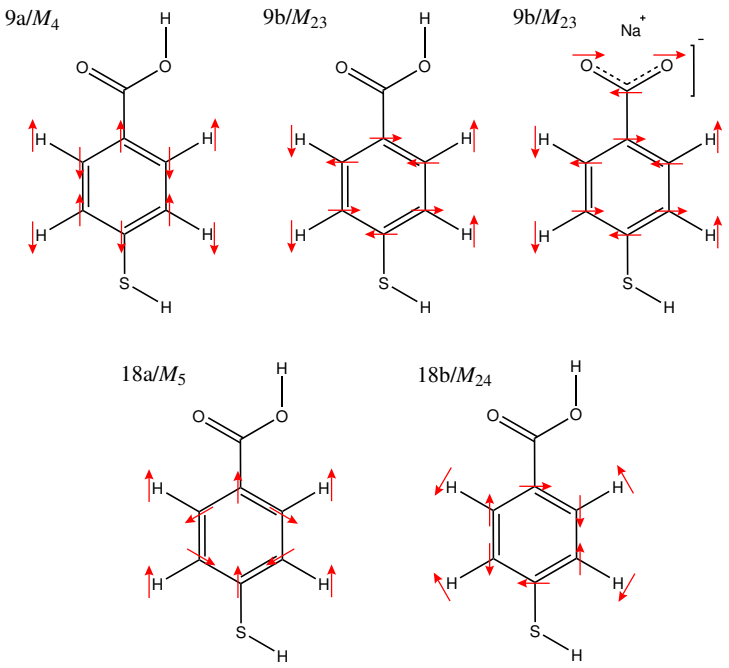

Figure S3: Selected vibrational modes of *p*MBA phenyl-ring. These modes are very similar for both protonated and deprotonated species, except for the 9b/$\mathscr{M}_{23}$ mode, which couples strongly with the asymmetric stretching mode of the deprotonated carboxylic acid group.

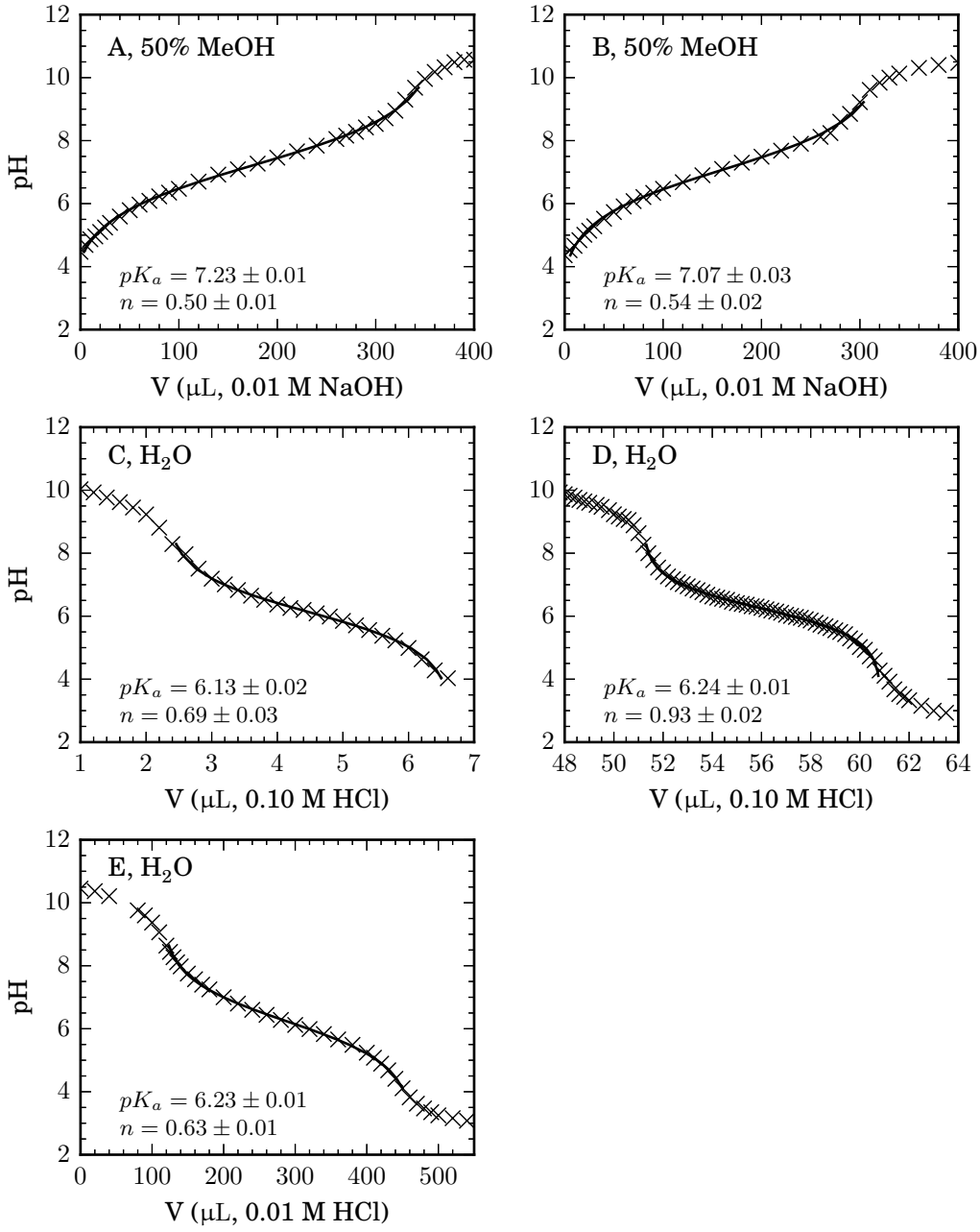

Figure S4: Extra titration curves of the $Au_{102}(p\text{MBA})_{44}$-cluster in 50 % MeOH and water.

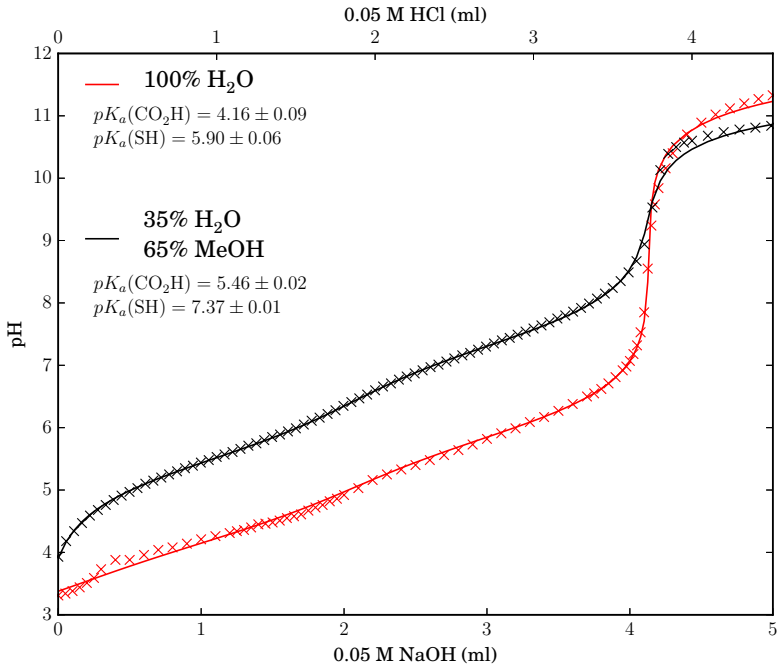

Figure S5: Titration curve of free *p*MBA in H_2O and 65% methanol. Qualitatively the behaviour is the same in both solvent systems, both curves show two distinct protonations for the carboxylic acid and thiol groups respectively. The continuous line is fitted using the quadratic equations for diprotic weak acid solution $[H_3O^+]$ concentration, using Hill-coefficient $n = 1$ for both groups. The pK_a values in 65% methanol are shifted 1.30 (CO_2H) and 1.47 (SH) units higher than in pure water.

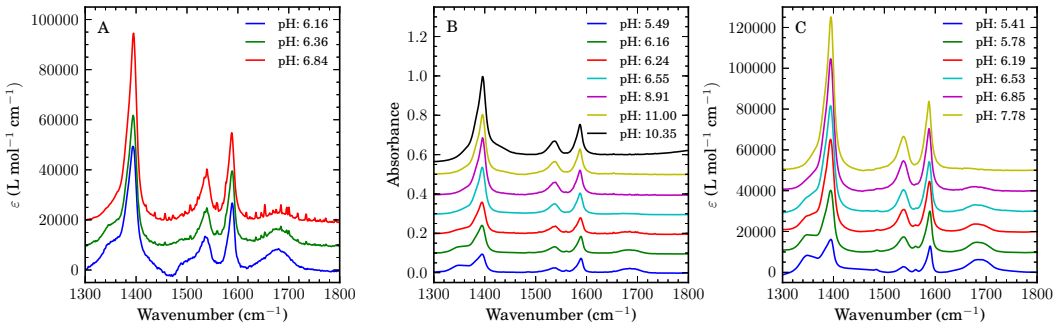

Figure S6: pH-dependent IR-spectra of other $Au_{102}(p\text{MBA})_{44}$ samples in solution.

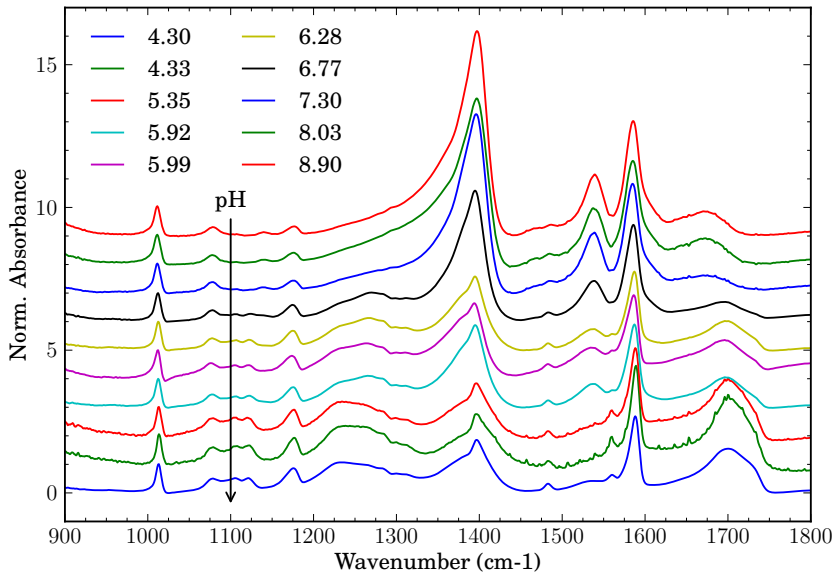

Figure S7: IR-spectra of $Au_{102}(p\text{MBA})_{44}$ dried on CaF_2 window from different pH solutions. The spectra have been normalized to the phenyl ring-breathing mode at 1013 cm^{-1}.

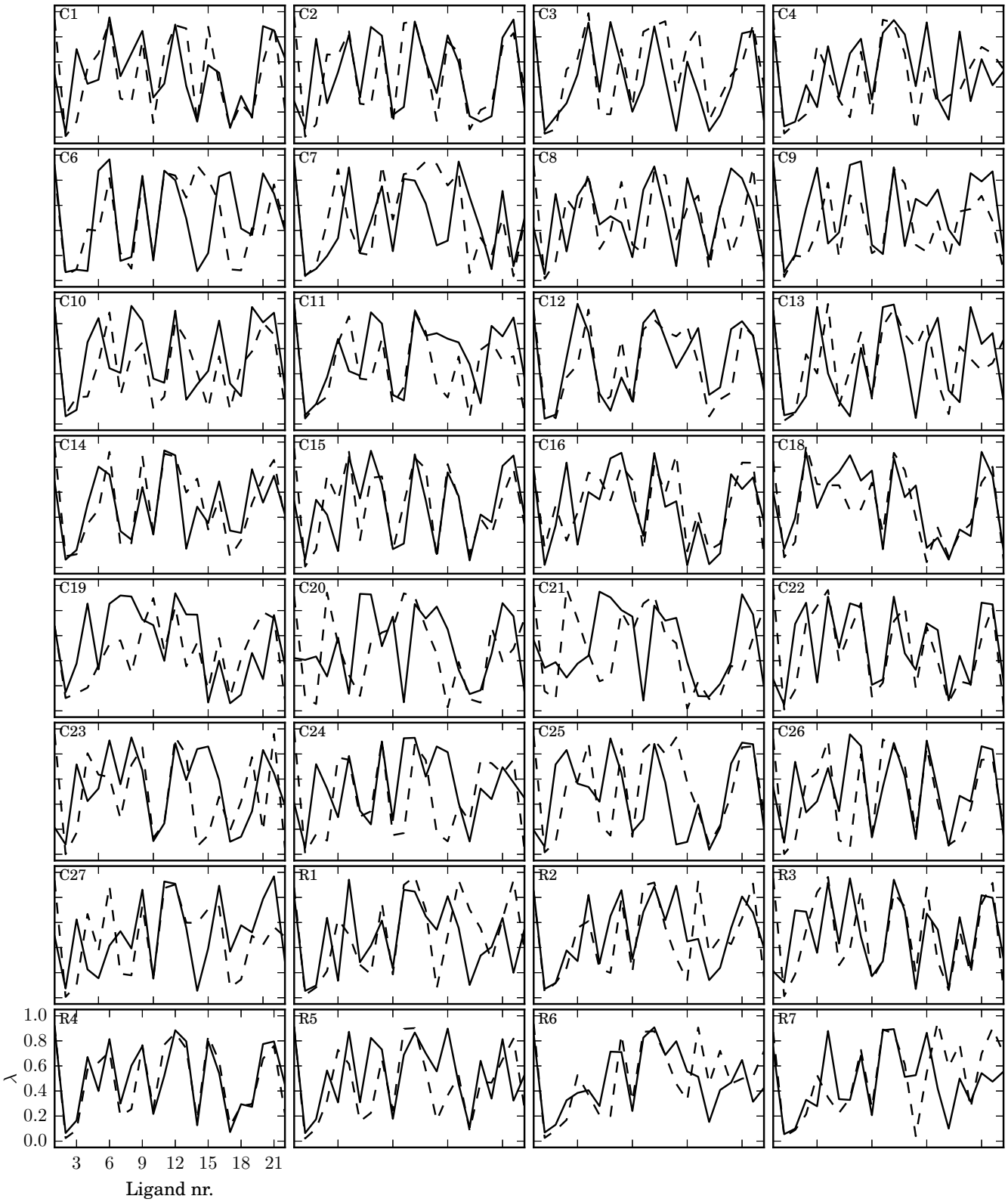

Figure S8: λ-values of individual ligands after 80 ns simulation for 32 different initial distributions of λ values. Solid and dashed lines refer to both symmetry related halves of the ligands, with solid line being for ligands 1–22 and dashed for 1*–22*. The data of R1–R7 simulations are average of two 2.5 ns runs starting from same initial conditions.

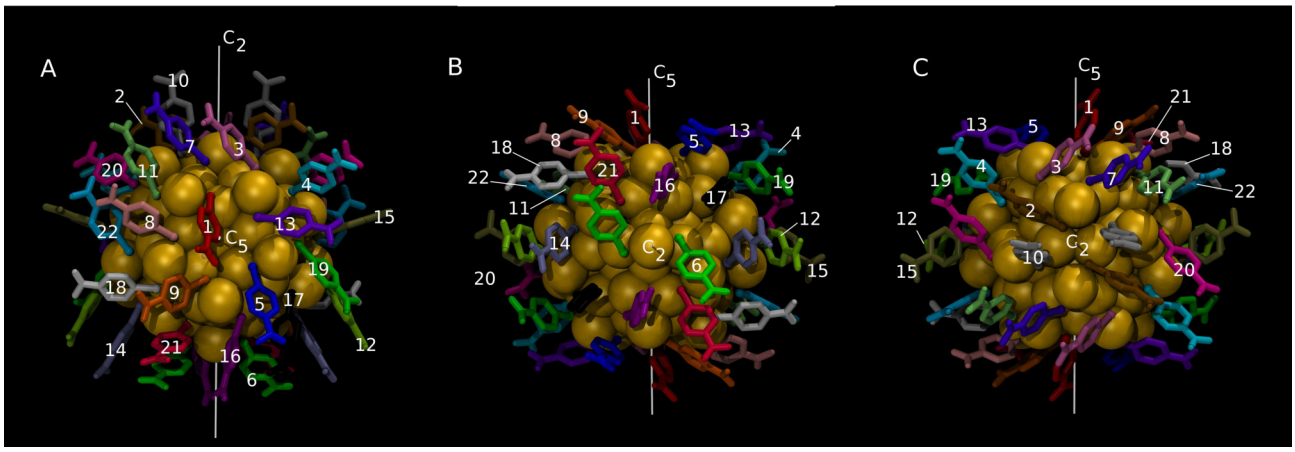

Figure S9: Numbering of the 22 symmetry independent ligands, viewed through the C_5 axis (A), and through both ends of the C_2 axis (B and C).

Table S3: Protonation state λ_{avg}(mean), pK_a shift and pK_a, and number of transitions in the total 80 ns of MD simulations. The mean λ_{avg} is calculated from the 32 different simulations in fig. S8.

Ligand	λ_{avg}(mean)	ΔpK_a [a]	pK_a [b]	$N_{\text{trans.}}$
1/1*	$0.91 \pm 0.06/0.67 \pm 0.25$	-1.01/-0.32	5.18/5.88	125/249
2/2*	$0.09 \pm 0.08/0.04 \pm 0.04$	1.03/1.38	7.23/7.58	118/64
3/3*	$0.13 \pm 0.08/0.34 \pm 0.26$	0.83/0.30	7.04/6.50	165/266
4/4*	$0.45 \pm 0.25/0.48 \pm 0.22$	0.09/0.04	6.29/6.24	364/332
5/5*	$0.60 \pm 0.14/0.44 \pm 0.24$	-0.17/0.10	6.03/6.30	339/277
6/6*	$0.71 \pm 0.21/0.73 \pm 0.22$	-0.38/-0.42	5.82/5.78	259/192
7/7*	$0.26 \pm 0.14/0.41 \pm 0.20$	0.45/0.16	6.65/6.36	430/437
8/8*	$0.32 \pm 0.18/0.67 \pm 0.29$	0.33/-0.31	6.53/5.89	304/193
9/9*	$0.76 \pm 0.10/0.72 \pm 0.14$	-0.50/-0.41	5.70/5.79	261/232
10/10*	$0.28 \pm 0.19/0.27 \pm 0.21$	0.41/0.44	6.61/6.64	327/337
11/11*	$0.67 \pm 0.29/0.55 \pm 0.30$	-0.31/-0.09	5.89/6.11	243/261
12/12*	$0.88 \pm 0.05/0.89 \pm 0.04$	-0.87/-0.91	5.33/5.29	183/162
13/13*	$0.70 \pm 0.12/0.59 \pm 0.16$	-0.36/-0.16	5.84/6.04	330/318
14/14*	$0.43 \pm 0.29/0.35 \pm 0.28$	0.12/0.26	6.32/6.46	233/177
15/15*	$0.49 \pm 0.30/0.60 \pm 0.26$	0.02/-0.18	6.22/6.02	271/242
16/16*	$0.59 \pm 0.21/0.54 \pm 0.19$	-0.15/-0.07	6.05/6.13	315/337
17/17*	$0.19 \pm 0.16/0.18 \pm 0.19$	0.62/0.67	6.82/6.87	197/174
18/18*	$0.40 \pm 0.20/0.36 \pm 0.18$	0.17/0.25	6.37/6.45	272/292
19/19*	$0.41 \pm 0.17/0.46 \pm 0.24$	0.16/0.08	6.36/6.28	354/320
20/20*	$0.75 \pm 0.14/0.61 \pm 0.16$	-0.47/-0.20	5.72/6.00	288/326
21/21*	$0.66 \pm 0.21/0.75 \pm 0.19$	-0.29/-0.48	5.91/5.72	251/238
22/22*	$0.36 \pm 0.14/0.32 \pm 0.23$	0.24/0.32	6.45/6.52	409/291

[a] pK_a shift with respect to the center pK_a 6.20.
[b] 6.20 + ΔpK_a.

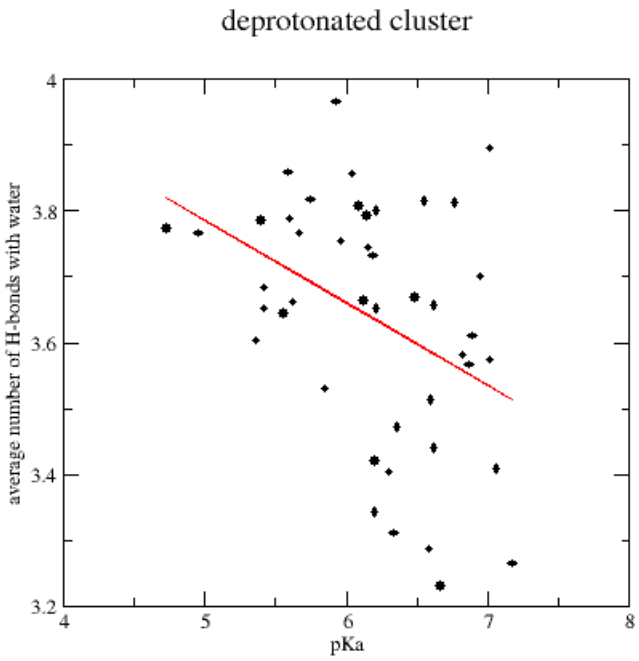

Figure S10: Average number of hydrogen bonds to the carboxylic acid group vs. the calculated pK_a.

DEPARTMENT OF CHEMISTRY, UNIVERSITY OF JYVÄSKYLÄ
RESEARCH REPORT SERIES

1. Vuolle, Mikko: Electron paramagnetic resonance and molecular orbital study of radical ions generated from (2.2)metacyclophane, pyrene and its hydrogenated compounds by alkali metal reduction and by thallium(III)trifluoroacetate oxidation. (99 pp.) 1976
2. Pasanen, Kaija: Electron paramagnetic resonance study of cation radical generated from various chlorinated biphenyls. (66 pp.) 1977
3. Carbon-13 Workshop, September 6-8, 1977. (91 pp.) 1977
4. Laihia, Katri: On the structure determination of norbornane polyols by NMR spectroscopy. (111 pp.) 1979
5. Nyrönen, Timo: On the EPR, ENDOR and visible absorption spectra of some nitrogen containing heterocyclic compounds in liquid ammonia. (76 pp.) 1978
6. Talvitie, Antti: Structure determination of some sesquiterpenoids by shift reagent NMR. (54 pp.) 1979
7. Häkli, Harri: Structure analysis and molecular dynamics of cyclic compounds by shift reagent NMR. (48 pp.) 1979
8. Pitkänen, Ilkka: Thermodynamics of complexation of 1,2,4-triazole with divalent manganese, cobalt, nickel, copper, zinc, cadmium and lead ions in aqueous sodium perchlorate solutions. (89 pp.) 1980
9. Asunta, Tuula: Preparation and characterization of new organometallic compounds synthesized by using metal vapours. (91 pp.) 1980
10. Sattar, Mohammad Abdus: Analyses of MCPA and its metabolites in soil. (57 pp.) 1980
11. Bibliography 1980. (31 pp.) 1981
12. Knuuttila, Pekka: X-Ray structural studies on some divalent 3d metal compounds of picolinic and isonicotinic acid N-oxides. (77 pp.) 1981
13. Bibliography 1981. (33 pp.) 1982
14. 6th National NMR Symposium, September 9-10, 1982, Abstracts. (49 pp.) 1982
15. Bibliography 1982. (38 pp.) 1983
16. Knuuttila, Hilkka: X-Ray structural studies on some Cu(II), Co(II) and Ni(II) complexes with nicotinic and isonicotinic acid N-oxides. (54 pp.) 1983
17. Symposium on inorganic and analytical chemistry May 18, 1984, Program and Abstracts. (100 pp.) 1984
18. Knuutinen, Juha: On the synthesis, structure verification and gas chromatographic determination of chlorinated catechols and guaiacols occuring in spent bleach liquors of kraft pulp mill. (30 pp.) 1984
19. Bibliography 1983. (47 pp.) 1984
20. Pitkänen, Maija: Addition of BrCl, B_2 and Cl_2 to methyl esters of propenoic and 2-butenoic acid derivatives and ^{13}C NMR studies on methyl esters of saturated aliphatic mono- and dichlorocarboxylic acids. (56 pp.) 1985
21. Bibliography 1984. (39 pp.) 1985
22. Salo, Esa: EPR, ENDOR and TRIPLE spectroscopy of some nitrogen heteroaromatics in liquid ammonia. (111 pp.) 1985

23. Humppi, Tarmo: Synthesis, identification and analysis of dimeric impurities of chlorophenols. (39 pp.) 1985
24. Aho, Martti: The ion exchange and adsorption properties of sphagnum peat under acid conditions. (90 pp.) 1985
25. Bibliography 1985 (61 pp.) 1986
26. Bibliography 1986. (23 pp.) 1987
27. Bibliography 1987. (26 pp.) 1988
28. Paasivirta, Jaakko (Ed.): Structures of organic environmental chemicals. (67 pp.) 1988
29. Paasivirta, Jaakko (Ed.): Chemistry and ecology of organo-element compounds. (93 pp.) 1989
30. Sinkkonen, Seija: Determination of crude oil alkylated dibenzothiophenes in environment. (35 pp.) 1989
31. Kolehmainen, Erkki (Ed.): XII National NMR Symposium Program and Abstracts. (75 pp.) 1989
32. Kuokkanen, Tauno: Chlorocymenes and Chlorocymenenes: Persistent chlorocompounds in spent bleach liquors of kraft pulp mills. (40 pp.) 1989
33. Mäkelä, Reijo: ESR, ENDOR and TRIPLE resonance study on substituted 9,10-anthraquinone radicals in solution. (35 pp.) 1990
34. Veijanen, Anja: An integrated sensory and analytical method for identification of off-flavour compounds. (70 pp.) 1990
35. Kasa, Seppo: EPR, ENDOR and TRIPLE resonance and molecular orbital studies on a substitution reaction of anthracene induced by thallium(III) in two fluorinated carboxylic acids. (114 pp.) 1990
36. Herve, Sirpa: Mussel incubation method for monitoring organochlorine compounds in freshwater recipients of pulp and paper industry. (145 pp.) 1991
37. Pohjola, Pekka: The electron paramagnetic resonance method for characterization of Finnish peat types and iron (III) complexes in the process of peat decomposition. (77 pp.) 1991
38. Paasivirta, Jaakko (Ed.): Organochlorines from pulp mills and other sources. Research methodology studies 1988-91. (120 pp.) 1992
39. Veijanen, Anja (Ed.): VI National Symposium on Mass Spectrometry, May 13-15, 1992, Abstracts. (55 pp.) 1992
40. Rissanen, Kari (Ed.): The 7. National Symposium on Inorganic and Analytical Chemistry, May 22, 1992, Abstracts and Program. (153 pp.) 1992
41. Paasivirta, Jaakko (Ed.): CEOEC'92, Second Finnish-Russian Seminar: Chemistry and Ecology of Organo-Element Compounds. (93 pp.) 1992
42. Koistinen, Jaana: Persistent polychloroaromatic compounds in the environment: structure-specific analyses. (50 pp.) 1993
43. Virkki, Liisa: Structural characterization of chlorolignins by spectroscopic and liquid chromatographic methods and a comparison with humic substances. (62 pp.) 1993
44. Helenius, Vesa: Electronic and vibrational excitations in some

biologically relevant molecules. (30 pp.) 1993

45. Leppä-aho, Jaakko: Thermal behaviour, infrared spectra and x-ray structures of some new rare earth chromates(VI). (64 pp.) 1994
46. Kotila, Sirpa: Synthesis, structure and thermal behavior of solid copper(II) complexes of 2-amino-2- hydroxymethyl-1,3-pr opanediol. (111 pp.) 1994
47. Mikkonen, Anneli: Retention of molybdenum(VI), vanadium(V) and tungsten(VI) by kaolin and three Finnish mineral soils. (90 pp.) 1995
48. Suontamo, Reijo: Molecular orbital studies of small molecules containing sulfur and selenium. (42 pp.) 1995
49. Hämäläinen, Jouni: Effect of fuel composition on the conversion of fuel-N to nitrogen oxides in the combustion of small single particles. (50 pp.) 1995
50. Nevalainen, Tapio: Polychlorinated diphenyl ethers: synthesis, NMR spectroscopy, structural properties, and estimated toxicity. (76 pp.) 1995
51. Aittola, Jussi-Pekka: Organochloro compounds in the stack emission. (35 pp.) 1995
52. Harju, Timo: Ultrafast polar molecular photophysics of (dibenzylmethine)borondifluoride and 4-aminophthalimide in solution. (61 pp.) 1995
53. Maatela, Paula: Determination of organically bound chlorine in industrial and environmental samples. (83 pp.) 1995
54. Paasivirta, Jaakko (Ed.): CEOEC'95, Third Finnish-Russian Seminar: Chemistry and Ecology of Organo-Element Compounds. (109 pp.) 1995
55. Huuskonen, Juhani: Synthesis and structural studies of some supramolecular compounds. (54 pp.) 1995
56. Palm, Helena: Fate of chlorophenols and their derivatives in sawmill soil and pulp mill recipient environments. (52 pp.) 1995
57. Rantio, Tiina: Chlorohydrocarbons in pulp mill effluents and their fate in the environment. (89 pp.) 1997
58. Ratilainen, Jari: Covalent and non-covalent interactions in molecular recognition. (37 pp.) 1997
59. Kolehmainen, Erkki (Ed.): XIX National NMR Symposium, June 4-6, 1997, Abstracts. (89 pp.) 1997
60. Matilainen, Rose: Development of methods for fertilizer analysis by inductively coupled plasma atomic emission spectrometry. (41 pp.) 1997
61. Koistinen, Jari (Ed.): Spring Meeting on the Division of Synthetic Chemistry, May 15-16, 1997, Program and Abstracts. (36 pp.) 1997
62. Lappalainen, Kari: Monomeric and cyclic bile acid derivatives: syntheses, NMR spectroscopy and molecular recognition properties. (50 pp.) 1997
63. Laitinen, Eira: Molecular dynamics of cyanine dyes and phthalimides in solution: picosecond laser studies. (62 pp.) 1997
64. Eloranta, Jussi: Experimental and theoretical studies on some

quinone and quinol radicals. (40 pp.) 1997

65. Oksanen, Jari: Spectroscopic characterization of some monomeric and aggregated chlorophylls. (43 pp.) 1998
66. Häkkänen, Heikki: Development of a method based on laser-induced plasma spectrometry for rapid spatial analysis of material distributions in paper coatings. (60 pp.) 1998
67. Virtapohja, Janne: Fate of chelating agents used in the pulp and paper industries. (58 pp.) 1998
68. Airola, Karri: X-ray structural studies of supramolecular and organic compounds. (39 pp.) 1998
69. Hyötyläinen, Juha: Transport of lignin–type compounds in the receiving waters of pulp mills. (40 pp.) 1999
70. Ristolainen, Matti: Analysis of the organic material dissolved during totally chlorine-free bleaching. (40 pp.) 1999
71. Eklin, Tero: Development of analytical procedures with industrial samples for atomic emission and atomic absorption spectrometry. (43 pp.) 1999
72. Välisaari, Jouni: Hygiene properties of resol-type phenolic resin laminates. (129 pp.) 1999
73. Hu, Jiwei: Persistent polyhalogenated diphenyl ethers: model compounds syntheses, characterization and molecular orbital studies. (59 pp.) 1999
74. Malkavaara, Petteri: Chemometric adaptations in wood processing chemistry. (56 pp.) 2000
75. Kujala Elena, Laihia Katri, Nieminen Kari (Eds.): NBC 2000, Symposium on Nuclear, Biological and Chemical Threats in the 21st Century. (299 pp.) 2000
76. Rantalainen, Anna-Lea: Semipermeable membrane devices in monitoring persistent organic pollutants in the environment. (58 pp.) 2000
77. Lahtinen, Manu: *In situ* X-ray powder diffraction studies of Pt/C, CuCl/C and Cu_2O/C catalysts at elevated temperatures in various reaction conditions. (92 pp.) 2000
78. Tamminen, Jari: Syntheses, empirical and theoretical characterization, and metal cation complexation of bile acid-based monomers and open/closed dimers. (54 pp.) 2000
79. Vatanen, Virpi: Experimental studies by EPR and theoretical studies by DFT calculations of α-amino-9,10-anthraquinone radical anions and cations in solution. (37 pp.) 2000
80. Kotilainen, Risto: Chemical changes in wood during heating at 150-260 °C. (57 pp.) 2000
81. Nissinen, Maija: X-ray structural studies on weak, non-covalent interactions in supramolecular compounds. (69 pp.) 2001
82. Wegelius, Elina: X-ray structural studies on self-assembled hydrogen-bonded networks and metallosupramolecular complexes. (84 pp.) 2001
83. Paasivirta, Jaakko (Ed.): CEOEC'2001, Fifth Finnish-Russian Seminar: Chemistry and Ecology of Organo-Element Compounds. (163 pp.) 2001
84. Kiljunen, Toni: Theoretical studies on spectroscopy and

atomic dynamics in rare gas solids. (56 pp.) 2001

85. Du, Jin: Derivatives of dextran: synthesis and applications in oncology. (48 pp.) 2001
86. Koivisto, Jari: Structural analysis of selected polychlorinated persistent organic pollutants (POPs) and related compounds. (88 pp.) 2001
87. Feng, Zhinan: Alkaline pulping of non-wood feedstocks and characterization of black liquors. (54 pp.) 2001
88. Halonen, Markku: Lahon havupuun käyttö sulfaattiprosessin raaka-aineena sekä havupuun lahontorjunta. (90 pp.) 2002
89. Falábu, Dezsö: Synthesis, conformational analysis and complexation studies of resorcarene derivatives. (212 pp.) 2001
90. Lehtovuori, Pekka: EMR spectroscopic studies on radicals of ubiquinones Q-*n*, vitamin K_3 and vitamine E in liquid solution. (40 pp.) 2002
91. Perkkalainen, Paula: Polymorphism of sugar alcohols and effect of grinding on thermal behavior on binary sugar alcohol mixtures. (53 pp.) 2002
92. Ihalainen, Janne: Spectroscopic studies on light-harvesting complexes of green plants and purple bacteria. (42 pp.) 2002
93. Kunttu, Henrik, Kiljunen, Toni (Eds.): 4th International Conference on Low Temperature Chemistry. (159 pp.) 2002
94. Väisänen, Ari: Development of methods for toxic element analysis in samples with environmental concern by ICP-AES and ETAAS. (54 pp.) 2002
95. Luostarinen, Minna: Synthesis and characterisation of novel resorcarene derivatives. (200 pp.) 2002
96. Louhelainen, Jarmo: Changes in the chemical composition and physical properties of wood and nonwood black liquors during heating. (68 pp.) 2003
97. Lahtinen, Tanja: Concave hydrocarbon cyclophane B-prismands. (65 pp.) 2003
98. Laihia, Katri (Ed.): NBC 2003, Symposium on Nuclear, Biological and Chemical Threats – A Crisis Management Challenge. (245 pp.) 2003
99. Oasmaa, Anja: Fuel oil quality properties of wood-based pyrolysis liquids. (32 pp.) 2003
100. Virtanen, Elina: Syntheses, structural characterisation, and cation/anion recognition properties of nano-sized bile acid-based host molecules and their precursors. (123 pp.) 2003
101. Nättinen, Kalle: Synthesis and X-ray structural studies of organic and metallo-organic supramolecular systems. (79 pp.) 2003
102. Lampiselkä, Jarkko: Demonstraatio lukion kemian opetuksessa. (285 pp.) 2003
103. Kallioinen, Jani: Photoinduced dynamics of $Ru(dcbpy)_2(NCS)_2$ – in solution and on nanocrystalline titanium dioxide thin films. (47 pp.) 2004
104. Valkonen, Arto (Ed.): VII Synthetic Chemistry Meeting and XXVI Finnish NMR Symposium. (103 pp.) 2004

105. Vaskonen, Kari: Spectroscopic studies on atoms and small molecules isolated in low temperature rare gas matrices. (65 pp.) 2004
106. Lehtovuori, Viivi: Ultrafast light induced dissociation of $Ru(dcbpy)(CO)_2I_2$ in solution. (49 pp.) 2004
107. Saarenketo, Pauli: Structural studies of metal complexing schiff bases , Schiff base derived *N*-glycosides and cyclophane π-prismands. (95 pp.) 2004
108. Paasivirta, Jaakko (Ed.): CEOEC'2004, Sixth Finnish-Russian Seminar: Chemistry and Ecology of Organo-Element Compounds. (147 pp.) 2004
109. Suontamo, Tuula: Development of a test method for evaluating the cleaning efficiency of hard-surface cleaning agents. (96 pp.) 2004
110. Güneş, Minna: Studies of thiocyanates of silver for nonlinear optics. (48 pp.) 2004
111. Ropponen, Jarmo: Aliphatic polyester dendrimers and dendrons. (81 pp.) 2004
112. Vu, Mân Thi Hong: Alkaline pulping and the subsequent elemental chlorine-free bleaching of bamboo (*Bambusa procera*). (69 pp.) 2004
113. Mansikkamäki, Heidi: Self-assembly of resorcinarenes. (77 pp.) 2006
114. Tuononen, Heikki M.: EPR spectroscopic and quantum chemical studies of some inorganic main group radicals. (79 pp.) 2005
115. Kaski, Saara: Development of methods and applications of laser-induced plasma spectroscopy in vacuum ultraviolet. (44 pp.) 2005
116. Mäkinen, Riika-Mari: Synthesis, crystal structure and thermal decomposition of certain metal thiocyanates and organic thiocyanates. (119 pp.) 2006
117. Ahokas, Jussi: Spectroscopic studies of atoms and small molecules isolated in rare gas solids: photodissociation and thermal reactions. (53 pp.) 2006
118. Busi, Sara: Synthesis, characterization and thermal properties of new quaternary ammonium compounds: new materials for electrolytes, ionic liquids and complexation studies. (102 pp.) 2006
119. Mäntykoski, Keijo: PCBs in processes, products and environment of paper mills using wastepaper as their raw material. (73 pp.) 2006
120. Laamanen, Pirkko-Leena: Simultaneous determination of industrially and environmentally relevant aminopolycarboxylic and hydroxycarboxylic acids by capillary zone electrophoresis. (54 pp.) 2007
121. Salmela, Maria: Description of oxygen-alkali delignification of kraft pulp using analysis of dissolved material. (71 pp.) 2007
122. Lehtovaara, Lauri: Theoretical studies of atomic scale impurities in superfluid ^{4}He. (87 pp.) 2007
123. Rautiainen, J. Mikko: Quantum chemical calculations of structures, bonding, and spectroscopic properties of some sulphur and selenium iodine cations. (71 pp.) 2007
124. Nummelin, Sami: Synthesis, characterization, structural and

retrostructural analysis of self-assembling pore forming dendrimers. (286 pp.) 2008

125. Sopo, Harri: Uranyl(VI) ion complexes of some organic aminobisphenolate ligands: syntheses, structures and extraction studies. (57 pp.) 2008
126. Valkonen, Arto: Structural characteristics and properties of substituted cholanoates and *N*-substituted cholanamides. (80 pp.) 2008
127. Lähde, Anna: Production and surface modification of pharmaceutical nano- and microparticles with the aerosol flow reactor. (43 pp.) 2008
128. Beyeh, Ngong Kodiah: Resorcinarenes and their derivatives: synthesis, characterization and complexation in gas phase and in solution. (75 pp.) 2008
129. Välisaari, Jouni, Lundell, Jan (Eds.): Kemian opetuksen päivät 2008: uusia oppimisympäristöjä ja ongelmalähtöistä opetusta. (118 pp.) 2008
130. Myllyperkiö, Pasi: Ultrafast electron transfer from potential organic and metal containing solar cell sensitizers. (69 pp.) 2009
131. Käkölä, Jaana: Fast chromatographic methods for determining aliphatic carboxylic acids in black liquors. (82 pp.) 2009
132. Koivukorpi, Juha: Bile acid-arene conjugates: from photoswitchability to cancer cell detection. (67 pp.) 2009
133. Tuuttila, Tero: Functional dendritic polyester compounds: synthesis and characterization of small bifunctional dendrimers and dyes. (74 pp.) 2009
134. Salorinne, Kirsi: Tetramethoxy resorcinarene based cation and anion receptors: synthesis, characterization and binding properties. (79 pp.) 2009
135. Rautiainen, Riikka: The use of first-thinning Scots pine (*Pinus sylvestris*) as fiber raw material for the kraft pulp and paper industry. (73 pp.) 2010
136. Ilander, Laura: Uranyl salophens: synthesis and use as ditopic receptors. (199 pp.) 2010
137. Kiviniemi, Tiina: Vibrational dynamics of iodine molecule and its complexes in solid krypton - Towards coherent control of bimolecular reactions? (73 pp.) 2010
138. Ikonen, Satu: Synthesis, characterization and structural properties of various covalent and non-covalent bile acid derivatives of N/O-heterocycles and their precursors. (105 pp.) 2010
139. Siitonen, Anni: Spectroscopic studies of semiconducting single-walled carbon nanotubes. (56 pp.) 2010
140. Raatikainen, Kari: Synthesis and structural studies of piperazine cyclophanes – Supramolecular systems through Halogen and Hydrogen bonding and metal ion coordination. (69 pp.) 2010
141. Leivo, Kimmo: Gelation and gel properties of two- and three-component Pyrene based low molecular weight organogelators. (116 pp.) 2011
142. Martiskainen, Jari: Electronic energy transfer in light-harvesting complexes isolated from *Spinacia oleracea* and from three

photosynthetic green bacteria *Chloroflexus aurantiacus*, *Chlorobium tepidum*, and *Prosthecochloris aestuarii.*(55 pp.) 2011

143. Wichmann, Oula: Syntheses, characterization and structural properties of [O,N,O,X´] aminobisphenolate metal complexes. (101 pp.) 2011
144. Ilander, Aki: Development of ultrasound-assisted digestion methods for the determination of toxic element concentrations in ash samples by ICP-OES. (58 pp.) 2011
145. The Combined XII Spring Meeting of the Division of Synthetic Chemistry and XXXIII Finnish NMR Symposium. Book of Abstracts. (90 pp.) 2011
146. Valto, Piia: Development of fast analysis methods for extractives in papermaking process waters. (73 pp.) 2011
147. Andersin, Jenni: Catalytic activity of palladium-based nanostructures in the conversion of simple olefinic hydro- and chlorohydrocarbons from first principles. (78 pp.) 2011
148. Aumanen, Jukka: Photophysical properties of dansylated poly(propylene amine) dendrimers. (55 pp.) 2011
149. Kärnä, Minna: Ether-functionalized quaternary ammonium ionic liquids – synthesis, characterization and physicochemical properties. (76 pp.) 2011
150. Jurček, Ondřej: Steroid conjugates for applications in pharmacology and biology. (57 pp.) 2011
151. Nauha, Elisa: Crystalline forms of selected Agrochemical actives: design and synthesis of cocrystals. (77 pp.) 2012
152. Ahkola, Heidi: Passive sampling in monitoring of nonylphenol ethoxylates and nonylphenol in aquatic environments. (92 pp.) 2012
153. Helttunen, Kaisa: Exploring the self-assembly of resorcinarenes: from molecular level interactions to mesoscopic structures. (78 pp.) 2012
154. Linnanto, Juha: Light excitation transfer in photosynthesis revealed by quantum chemical calculations and exiton theory. (179 pp.) 2012
155. Roiko-Jokela, Veikko: Digital imaging and infrared measurements of soil adhesion and cleanability of semihard and hard surfaces. (122 pp.) 2012
156. Noponen, Virpi: Amides of bile acids and biologically important small molecules: properties and applications. (85 pp.) 2012
157. Hulkko, Eero: Spectroscopic signatures as a probe of structure and dynamics in condensed-phase systems – studies of iodine and gold ranging from isolated molecules to nanoclusters. (69 pp.) 2012
158. Lappi, Hanna: Production of Hydrocarbon-rich biofuels from extractives-derived materials. (95 pp.) 2012
159. Nykänen, Lauri: Computational studies of Carbon chemistry on transition metal surfaces. (76 pp.) 2012
160. Ahonen, Kari: Solid state studies of pharmaceutically important molecules and their derivatives. (65 pp.) 2012

161. Pakkanen, Hannu: Characterization of organic material dissolved during alkaline pulping of wood and non-wood feedstocks (76 pp.) 2012
162. Moilanen, Jani: Theoretical and experimental studies of some main group compounds: from closed shell interactions to singlet diradicals and stable radicals. (80 pp.) 2012
163. Himanen, Jatta: Stereoselective synthesis of Oligosaccharides by *De Novo* Saccharide welding. (133 pp.) 2012
164. Bunzen, Hana: Steroidal derivatives of nitrogen containing compounds as potential gelators.(76 pp.) 2013
165. Seppälä, Petri: Structural diversity of copper(II) amino alcohol complexes. Syntheses, structural and magnetic properties of bidentate amino alcohol copper(II) complexes. (67 pp.) 2013
166. Lindgren, Johan: Computational investigations on rotational and vibrational spectroscopies of some diatomics in solid environment. (77 pp.) 2013
167. Giri, Chandan: Sub-component self-assembly of linear and non-linear diamines and diacylhydrazines, formulpyridine and transition metal cations. (145 pp.) 2013
168. Riisiö, Antti: Synthesis, Characterization and Properties of Cu(II)-, Mo(VI)- and U(VI) Complexes With Diaminotetraphenolate Ligands. (51 pp.) 2013
169. Kiljunen, Toni (Ed.): Chemistry and Physics at Low Temperatures. Book of Abstracts. (103 pp.) 2013
170. Hänninen, Mikko: Experimental and Computational Studies of Transition Metal Complexes with Polydentate Amino- and Aminophenolate Ligands: Synthesis, Structure, Reactivity and Magnetic Properties. (66 pp.) 2013
171. Antila, Liisa: Spectroscopic studies of electron transfer reactions at the photoactive electrode of dye-sensitized solar cells. (53 pp.) 2013
172. Kemppainen, Eeva: Mukaiyama-Michael reactions with α-substituted acroleins – a useful tool for the synthesis of the pectenotoxins and other natural product targets. (190 pp.) 2013
173. Virtanen, Suvi: Structural Studies Of Dielectric Polymer Nanocomposites. (49 pp.) 2013
174. Yliniemelä-Sipari, Sanna: Understanding The Structural Requirements for Optimal Hydrogen Bond Catalyzed Enolization – A Biomimetic Approach.(160 pp.) 2013
175. Leskinen, Mikko V: Remote β-functionalization of β'-keto esters (105 pp.) 2014
176. 12th European Conference on Research in Chemistry Education (ECRICE2014). Book of Abstracts. (166 pp.) 2014
177. Peuronen, Anssi: N-Monoalkylated DABCO-Based N-Donors as Versatile Building Blocks in Crystal Engineering and Supramolecular Chemistry. (54 pp.) 2014
178. Perämäki, Siiri: Method development for determination and recovery of rare earth elements from industrial fly ash. (88 pp.) 2014

179. Chernyshev, Alexander, N.: Nitrogen-containing ligands and their platinum(IV) and gold(III) complexes: investigation and basicity and nucleophilicity, luminescence, and aurophilic interactions. (64 pp.) 2014
180. Lehto, Joni: Advanced Biorefinery Concepts Integrated to Chemical Pulping. (142 pp.) 2015
181. Tero, Tiia-Riikka: Tetramethoxy resorcinarenes as platforms for fluorescent and halogen bonding systems. (61 pp.) 2015
182. Löfman, Miika: Bile acid amides as components of microcrystalline organogels. (62 pp.) 2015
183. Selin, Jukka: Adsorption of softwood-derived organic material onto various fillers during papermaking. (169 pp.) 2015
184. Piisola, Antti: Challenges in the stereoselective synthesis of allylic alcohols. (210 pp.) 2015
185. Bonakdarzadeh, Pia: Supramolecular coordination polyhedra based on achiral and chiral pyridyl ligands: design, preparation, and characterization. (65 pp.) 2015
186. Vasko, Petra: Synthesis, characterization, and reactivity of heavier group 13 and 14 metallylenes and metalloid clusters: small molecule activation and more. (66 pp.) 2015
187. Topić, Filip: Structural Studies of Nano-sized Supramolecular Assemblies. (79 pp.) 2015
188. Mustalahti, Satu: Photodynamics Studies of Ligand-Protected Gold Nanoclusters by using Ultrafast Transient Infrared Spectroscopy. (58 pp.) 2015